COPPE
Instituto Alberto Luiz Coimbra de Pós-Graduação e Pesquisa de Engenharia
UFRJ

EVALUATION OF THE ATLANTIC MERIDIONAL OVERTURNING CIRCULATION UNDER HIGH CO_2 EMISSIONS

Lívia Maria Barbosa Sancho Alvares Mendonça Cabral

Tese de Doutorado apresentada ao Programa de Pós-graduação em Engenharia Civil, COPPE, da Universidade Federal do Rio de Janeiro, como parte dos requisitos necessários à obtenção do título de Doutor em Engenharia Civil.

Orientadores: Luiz Landau
Luiz Paulo de Freitas Assad
Marcio Cataldi

Rio de Janeiro
Abril de 2020

EVALUATION OF THE ATLANTIC MERIDIONAL OVERTURNING CIRCULATION UNDER HIGH CO_2 EMISSIONS

Lívia Maria Barbosa Sancho Alvares Mendonça Cabral

TESE SUBMETIDA AO CORPO DOCENTE DO INSTITUTO ALBERTO LUIZ COIMBRA DE PÓS-GRADUAÇÃO E PESQUISA DE ENGENHARIA DA UNIVERSIDADE FEDERAL DO RIO DE JANEIRO COMO PARTE DOS REQUISITOS NECESSÁRIOS PARA A OBTENÇÃO DO GRAU DE DOUTOR EM CIÊNCIAS EM ENGENHARIA CIVIL.

Orientadores: Luiz Landau
Luiz Paulo de Freitas Assad
Marcio Cataldi

Aprovada por: Prof. Luiz Landau
Prof. Luiz Paulo de Freitas Assad
Prof. Marcio Cataldi
Prof. José Luis Drummond Alves
Profª. Leticia Cotrim da Cunha
Dr. Rogerio Neder Candella

RIO DE JANEIRO, RJ - BRASIL
ABRIL DE 2020

Cabral, Lívia Maria Barbosa Sancho Alvares Mendonça

Evaluation of the Atlantic Meridional Overturning Circulation under high CO_2 Emissions/Lívia Maria Barbosa Sancho Alvares Mendonça Cabral. – Rio de Janeiro: UFRJ/COPPE, 2020.

XXXI, 176 p.: il.; 29, 7cm.

Orientadores: Luiz Landau
Luiz Paulo de Freitas Assad
Marcio Cataldi

Tese (doutorado) – UFRJ/COPPE/Programa de Engenharia Civil, 2020.

Referências Bibliográficas: p. 147 – 176.

1. North Atlantic Deep Water. 2. Meridional Overturning Circulation. 3. Tipping Point. I. Landau, Luiz *et al.* II. Universidade Federal do Rio de Janeiro, COPPE, Programa de Engenharia Civil. III. Título.

To Léa Barbosa Sancho and Fernando Luiz Sancho

"Do. Or do not. There is no try."
- Master Yoda.

"Não vai dar tempo mas tem que dar.."
- Unknown author

"Minha paz não é mais segredo
Invadiu meus dias mais sombrios
Fez morada em mim
O amor"
- Crombie

Acknowledgments

First of all, to God. My guide, when I was in the dark. My shelter, when I was under the storm. The One who brought me to the surface many times to breathe when I was drowning and the One who made me believe enough to walk over the waters.

To you, that gave me life and taught me how to be polite, respectful, and correct. You taught me that I wouldn't need to go over anyone to achieve my goals because the peace of sleeping without having done nothing wrong is priceless. You gave me everything. I hope I can give something back to you.

To those to whom I dedicate this thesis, from the earth and heaven, you are the base of our family, and your love is what everyone searches for in life. Thanks for letting us participate in this.

To my family, thanks for understanding my absences and crazy talks! Thanks for bringing me food!

To you, who makes my heart beats faster, stronger, and happier each day I'm with you. Thanks for all the support and the healing hugs!

To whom I share the roof with, thanks for being there every step of the way, helping me even though I did not deserve it. I am very proud to call you my friend! Even from far away, I can sense you are cheering for me, as always.

To those that make life worth it. To those that warm my heart. I'm not gonna

cite any names 'cause I don't want to forget anyone - I definitely would! You know who you are! Thanks for understanding my absences. Thanks for being you, my dear friends!

To those that share the workplace every day and also occasionally, thanks for making these heavy days, lighter! And thanks for the bits of help and good suggestions, even when you didn't know you were making them!

To my advisors, thanks for embracing this challenge with me. I know it was not easy! Thanks for believing in my capacity, and thanks for supporting my requests, my doubts, and my despair sometimes! I would be very lucky to have even just one of you! Having the three of you was some experience!

To the examination board, thanks for caring and for dedicating yourselves to reading this text. Thank you for playing such an important role in helping to train doctors in a country that currently thinks that science and education mean money being thrown away.

To everyone in LAMCE that helped me in some way, even if with just a "Good morning!".

To the CGD/NCAR staff and CESM Tutorial participants and organizers, first, thank you for granting me the opportunity to meet so many people and learn from them. Thanks for the opportunity to meet some of the 'heroes' I just used to read in papers. It's weird to realize you are real people! Thanks to the CGD staff that helped me through some problems with my thesis, for your kindness and patience. For the friends I made at the Tutorial, thanks for the fun days we spent there and some illuminating discussions later! Especially thanks to the CESM chief scientist that helped me in many moments and kindly answered my doubts.

To the PFRH, thanks for granting me a scholarship so disputed and valuable. I just wish you didn't want to cancel it in the middle of the thesis.

It is very hard to sum up the role that so many people had and what they did, said, or didn't say that helped me to get here after five (and a few months) long years. So, to all of you that somehow contributed to getting me here, thank you!

Life is made up of people and moments, and they make it worth it!

Ubuntu!

Resumo da Tese apresentada à COPPE/UFRJ como parte dos requisitos necessários para a obtenção do grau de Doutor em Ciências (D.Sc.)

AVALIAÇÃO DA CIRCULAÇÃO DE REVOLVIMENTO MERIDIONAL DO ATLÂNTICO FRENTE A ALTAS EMISSÕES DE CO_2

Lívia Maria Barbosa Sancho Alvares Mendonça Cabral

Abril/2020

Orientadores: Luiz Landau
Luiz Paulo de Freitas Assad
Marcio Cataldi

Programa: Engenharia Civil

Esta tese teve como objetivo avaliar o impacto, no Sistema Climático Terrestre, do aumento contínuo do CO_2 na atmosfera. Mais especificamente, a tese se propôs a identificar pontos de inflexão na Circulação Termohalina e avaliar seus impactos principalmente no oceano Atlântico. Para atender aos objetivos propostos, resultados de duas simulações numéricas, oriundas de um modelo do sistema terrestre do estado da arte, foram utilizados. O experimento definido como controle tinha como objetivo representar o período pré-industrial com condições que não evoluíam no tempo, ou seja, sem forçantes, e é denominado de piControl. Já o experimento com condições alteradas é denominado 1pctCO_2, tem origem do ano 501 do piControl e possui como único forçante, o aumento de 1% ao ano da concentração de CO_2 na atmosfera. O experimento piControl foi validado para ser utilizado como parâmetro de comparação com o experimento 1pctCO_2 através de diversas análises e comparações com dados observados e de reanálise. No experimento 1pctCO_2, um aquecimento médio global na atmosfera de mais de 6°C foi identificado e houve uma mudança no padrão de fluxo de água doce no Atlântico Norte. Essa mudança causou impacto nas regiões de convecção profunda e em toda dinâmica associada à Circulação de Revolvimento Meridional do Atlântico (AMOC). Esse trabalho contribuiu para o conhecimento acerca dos mecanismos da dinâmica da AMOC e da Água Profunda do Atlântico Norte em toda a bacia do oceano Atlântico.

Abstract of Thesis presented to COPPE/UFRJ as a partial fulfillment of the requirements for the degree of Doctor of Science (D.Sc.)

EVALUATION OF THE ATLANTIC MERIDIONAL OVERTURNING CIRCULATION UNDER HIGH CO_2 EMISSIONS

Lívia Maria Barbosa Sancho Alvares Mendonça Cabral

April/2020

Advisors: Luiz Landau
Luiz Paulo de Freitas Assad
Marcio Cataldi

Department: Civil Engineering

This thesis aimed to evaluate the impact, in the Earth Climate System, of the continuous increase of CO_2 in the atmosphere. More specifically, the thesis proposed identifying tipping points in the Thermohaline Circulation and evaluating its impacts mainly in the Atlantic Ocean. The results from two numerical simulations, derived from a state-of-the-art Earth System Model, were used to achieve the proposed objectives. The control experiment aimed to represent the pre-industrial period with conditions that did not evolve, that is, without forcing, and it is called piControl. The experiment with altered conditions, on the other hand, is called 1pctCO_2, started from year 501 of piControl and has as its only forcing, an increase of 1% per year in the concentration of atmospheric CO_2. The piControl experiment was validated to be used as a comparison parameter with the 1pctCO_2 experiment through several analyzes and comparisons with observed and reanalysis data. In the 1pctCO_2 experiment, an average Global Warming in the atmosphere of more than 6°C was identified, and there was a change in the freshwater flow pattern in the North Atlantic. This change impacted the regions of deep convection and all dynamics associated with the Atlantic Meridional Overturning Circulation (AMOC). This work contributed to the knowledge about the mechanisms of AMOC and North Atlantic Deep Water dynamics in both the North and the South Atlantic Ocean.

Contents

List of Figures

List of Tables

List of Abbreviations

AABW	Antarctic Bottom Water, p. 29
AACC	Antarctic Circumpolar Current, p. 42
AAIW	Antarctic Intermediate Water, p. 81
AC	Agulhas Current, p. 123
AIM	Asia-Pacific Integrated Model, p. 18
AMIP	Atmospheric Model Intercomparison Project, p. 66
AMOC	Atlantic Meridional Overturning Circulation, p. 3
AOML	Atlantic Oceanographic and Meteorological Laboratory, p. 47
AR	Assessment Report, p. 15
AWG	Atmospheric Working Group, p. 56
BC	Brazil Current, p. 94
BMC	Brazil-Malvinas Confluence, p. 42
CAM	Community Atmosphere Model, p. 56
CCSM	Community Climate System Model, p. 28
CEDS	Community Emissions Data System, p. 72
CESM	Community Earth System Model, p. 28
CGD	Climate and Global Dynamics Laboratory, p. 55
CICE	Community Ice Code, p. 58
CISL	Computational and Information Systems Laboratory, p. 143
CISM	Community Ice Sheet Model, p. 67

CLM Community Land Model, p. 57

CMEMS Copernicus Marine Environment Monitoring Service, p. 76

CMIP5 5th Coupled Model Intercomparison Project, p. 16

CMIP6 6th Coupled Model Intercomparison Project, p. 62

CPL Coupler, p. 56

DAO Data Assimilation Office, p. 56

DECK Diagnostic, Evaluation, and Characterization of Klima, p. 66

DMSP Defense Meteorological Satellite Program, p. 73

DOE Department of Energy, p. 55

DWBC Deep Western Boundary Current, p. 41

ECMWF European Centre for Medium-Range Weather Forecasts, p. 76

ESM Earth System Model, p. 55

FAR First Assessment Report, p. 15

FireMIP Fire Model Intercomparison Project, p. 72

GAW Global Atmosphere Watch, p. 136

GCAM Global Change Assessment Model, p. 18

GCM General Circulation Model, p. 56

GHG Greenhouse Gases, p. 2

GWP Global Warming Potential, p. 27

GrIS Greenland Ice Sheet, p. 144

IMAGE Integrated Model to Assess the Global Environment, p. 18

IPCC Intergovernmental Panel on Climate Change, p. 6

ITCZ Intertropical Convergence Zone, p. 35

IWBC Intermediate Western Boundary Current, p. 118

JMA Japan Meteorological Agency, p. 136

LAMCE *Laboratório de Métodos Computacionais em Engenharia*, p. 66

LANL Los Alamos National Laboratory, p. 59

LENS Large Ensemble Numerical Simulation, p. 70

LMWG Land Model Working Group, p. 57

LSM Land Surface Model, p. 57

LUH Land Use Harmonization, p. 72

MARBL Marine Biogeochemistry Library, p. 67

MC Malvinas Current, p. 96

MESSAGE Model for Energy Supply Strategy Alternatives and their General Environmental Impact, p. 18

MOCHA Southern Overturning Circulation and Heatflux Array, p. 46

MOC Meridional Overturning Circulation, p. 37

MOM Modular Ocean Model, p. 64

MOSART Model for Scale Adaptative River Transport, p. 57

MOVE Meridional Overturning Variability Experiment, p. 44

MOZART Model for Ozone And Related Chemical Tracers, p. 56

NADW North Atlantic Deep Water, p. 3

NASA National Aeronautics and Space Administration, p. 56

NA North Atlantic Ocean, p. 34

NCAR National Center for Atmospheric Research, p. 55

NCEP National Centers for Environmental Prediction, p. 76

NERC Natural Environment Research Council, p. 46

NOAA National Oceanic and Atmospheric Administration, p. 46

NSF National Science Foundation, p. 55

NSIDC National Snow and Ice Data Center, p. 54

OSNAP Overturning in the Subpolar North Atlantic Program, p. 44

PFT Plant Functional Type, p. 57

PHC Polar Science Center Hydrographic Climatology, p. 70

POP Parallel Ocean Program, p. 59

RAPID Measuring interannual variability of the AMOC and meridional ocean heat transport at 26.5°N: The RAPID-MOCHA Array, p. 44

RCP Representative Concentration Pathway, p. 16

SACW South Atlantic Central Water, p. 121

SAMBA South Atlantic MOC Basin-wide Array, p. 44

SAR Second Assessment Report, p. 15

SLCF Short-Lived Climate Forcers, p. 20

SMMR Scanning Multichannel Microwave Radiometer, p. 73

SR1.5 Special Report on Global Warming of 1.5°C, p. 15

SRCCL Special Report Climate Change and Land, p. 16

SRES Special Report on Emission Scenarios, p. 16

SROCC Special Report The Ocean and Cryosphere in a Changing Climate, p. 16

SSM/I Special Sensor Microwave Imager, p. 73

SSMIS Special Sensor Microwave Imager/Sounder, p. 73

SST Sea Surface Temperature, p. 2

TAR Third Assessment Report, p. 15

TCRE Transient Climate Response Emissions, p. 72

TCR Transient Climate Response, p. 72

THC Thermohaline Circulation, p. 34

UNEP United Nations Environment Programme, p. 15

USP Universidade de São Paulo, p. 52

WACCM Whole Atmosphere Community Climate Model, p. 56

WBTS Western Boundary Time Series, p. 46

WDCGG World Data Centre for Greenhouse Gases, p. 136

WG Working Group, p. 15

WMO World Meteorological Organization, p. 15

List of Symbols

Bar	Bar (bar) is a unit of pressure and it is equal to 10^6 Pa., p. 51
Byte	A Byte (B), or a binary term is a unit of digital information., p. 66
Gigatonne	Gigatonne (Gt) is a measure of weight., p. 16
Joule	Joule (J) is a measure of energy., p. 93
Parts per billion	Parts per billion (ppb) is pseudo-unit, without unit of measurement to describe, in this case, mole fraction., p. 20
Parts per million	Parts per million (ppm), like ppb, is pseudo-unit also to describe mole fraction., p. 16
Pascal	Pascal (Pa) is a measure of pressure., p. 68
Sverdrup	Sverdrup (Sv) is a measure of flow., p. 35
Watt	Watt (W) is an unit of power., p. 38

Chapter 1

Introduction

"To a patient scientist, the unfolding greenhouse mystery is far more exciting than the plot of the best mystery novel. But it is slow reading, with new clues sometimes not appearing for several years. Impatience increases when one realizes that it is not the fate of some fictional character, but of our planet and species, which hangs in the balance as the great carbon mystery unfolds at a seemingly glacial pace."
SCHINDLER (1999)

The global climate has always aroused great interest in the scientific community. In 1824, Fourier demonstrated that without the atmosphere, the Earth would be much colder than it is, suggesting the importance of this component in climate and introducing the idea that climate change could occur towards a new level of equilibrium if it were to be forced to undergo such changes. Historically these changes have occurred and have been occurring, such as glacial and interglacial ages, for example (BROECKER, 1997; LENTON, 2013; MANABE and STOUFFER, 1999), forcing the Earth's climate system to adjust to a new pattern within each change.

Initially, the components of the climate system - hydrosphere, atmosphere, lithosphere, biosphere, and cryosphere - were not considered as a system itself, interacting with each other with energy and mass exchanges (GIORGI, 2005; GLEICK *et al.*, 2013; HOUGHTON, 2004; MCGUFFIE and HENDERSON-SELLERS, 2001; PEIXOTO and OORT, 1992; WMO, 1975), but as separate components. An example of this mode of thinking is in the work of WALKER (1923), which established the relationship of various atmospheric variables to changes in weather, without considering the other components. Subsequently, climate research began to study not only each component separately, but how their interaction occurs and how changes

in one component can impact the others. The work of BJERKNES (1966) was one of the pioneers in this change in mindset when he related, among other results, the change in intensity of trade winds with changes in local Sea Surface Temperature (SST).

The sun is the Earth's primary source of energy, which its surface receives as shortwave radiation (LUCARINI and RAGONE, 2011). However, once the Earth's surface absorbs this radiation, it re-emits it as longwave radiation. Then, a portion is absorbed by clouds, Greenhouse Gases (GHG), and particles into the atmosphere, warming the Earth in the called Greenhouse effect, an essential mechanism for Earth's life maintenance (COSTELLO *et al.*, 2009; MOSS *et al.*, 2000). Therefore, even if Earth's energy source comes from the sun, these atmosphere's constituents are the responsible ones for the radiation balance, in which the more radiation-absorbing constituents there are, the more radiation is trapped (REVELLE, 2013).

Among these constituents, the famous GHGs are the focus for the cause of Global Warming, anthropogenically emitted to the atmosphere as by-products of energy and food production (BROECKER, 1987; COSTELLO *et al.*, 2009). Their increase has been registered since the Industrial Revolution in the 18^{th} and 19^{th} centuries, along with an increase in average global air temperatures, together with other changes in climate (COSTELLO *et al.*, 2009; KEELING *et al.*, 2001; MASSON-DELMOTTE *et al.*, 2018). These changes are a significant concern and have been treated as such for the scientific community (SUNDQUIST, 2013).

The atmosphere is often interpreted as being primarily responsible for changing weather and climate in the various regions of the world. However, the interaction processes between the oceans and the atmosphere are essential for climate maintenance, since these two components are mainly responsible for the distribution of solar thermal energy over the planet (GRASSL, 2001; HARTMANN, 1994; LUCARINI and RAGONE, 2011). Understanding the mechanisms of interaction between ocean and atmosphere, as well as the mass and heat transports performed by each of these components on a global scale, is essential to understand climate dynamics (ASSAD, 2006; GARZOLI and BARINGER, 2007).

Net radiation incident on the atmosphere generates energy gain at low latitudes and energy loss at high latitudes. While the redistribution of this energy over continents is done exclusively by the atmosphere, over the oceans, it is carried out by the oceans along with the atmosphere, transporting heat to various regions of the Earth with the potential to change the global climate (ASSAD, 2006; PICKARD, 1974).

As stated earlier, the ongoing climate changes are a reason for concern by the scientific community. One of these concerns is related to the Atlantic Meridional

Overturning Circulation (AMOC) and the North Atlantic Deep Water (NADW) formation. They are considered the drivers of the stable current climate, as meridional heat transports in the ocean are the key to understand and evaluate climate, its variability, and potential future changes (ANSORGE *et al.*, 2014; DANABASOGLU *et al.*, 2020; TOMCZAK and GODFREY, 1994). In that way, evaluate changes in the deep circulation in the Atlantic ocean are of scientific interest and essential to understanding past and future climate changes (LUO *et al.*, 2018).

A shutdown in the NADW and the AMOC could lead to an Ice Age, which is a periodically natural event (ABE-OUCHI *et al.*, 2013; LENTON *et al.*, 2019). However, now it would be man-caused, or, at least, man-accelerated. In this context, evaluating the responses of AMOC and NADW patterns and the potential consequences to ocean circulation in a world with increased atmospheric GHG becomes imperative. That way, we can quantify how these changes will affect ecosystems, and eventually, if these ecosystems would be able to cope with them or if interventions must be made to diminish or slow down those changes.

This work addressed changes mainly in the Atlantic Ocean as a consequence of impacts on AMOC due to the continuous increase of the most prominent of GHG, the CO_2. To identify and evaluate these changes, coupled climate model results were used, which means that the components of the climate system used in this model exchanged information during the simulations. Since the climate system is not only complex but extremely chaotic, understand it poses an enormous challenge, as BROECKER (1987) also states. This work did not aim to exhaust this theme but to contribute to it, to be a new step towards this understanding.

1.1 Hypothesis

This thesis works on the hypothesis that an increase in the atmospheric CO_2 would enhance the greenhouse effect and Global Warming, forcing key tipping elements towards a tipping point. Global Warming can be understood as the long-term change in global surface temperature, tipping elements are features of the climate system (item 2.4.1), and tipping points are moments that mark a transition for a given climate feature (item 2.4).

Some of these tipping elements are the North Atlantic Deep Water formation and the Atlantic Meridional Overturning Circulation. Once they are essential to maintaining the current state of the climate system, alterations in the pattern, intensity, or both of these elements would have a profound impact on the Global Climate. This thesis contributes to the current knowledge about a tipping point in the features mentioned above and the dynamics that govern them.

1.2 Goals

The main goal of this thesis is to identify and quantify changes in the AMOC and the NADW patterns and their impacts mainly on the Atlantic Ocean through a constant increase of atmospheric CO_2 concentration.

1.2.1 Specific Goals

- Validate the control experiment against known climate features and evaluate its stabilization so it can be compared against a CO_2-forced experiment.
- Search for pieces of evidence of an AMOC and NADW tipping points in the CO_2-forced experiment.
- Analyze the impacts on AMOC and NADW from an increase in atmospheric CO_2.
- Analyze the impacts associated with AMOC, mainly in the South Atlantic Ocean, in the CO_2-forced experiment.
- Identify other effects on the planet that arose from an increase in atmospheric CO_2.

1.3 Structure of the thesis

This thesis was divided in the following manner; chapter 2 presents an overview of the phenomena considered for the development of the work. Chapter 3 exposes the methodology used, the Earth System Model, and its components, the descriptions of the experiments‘ results, the products used to validate the control experiment, and a description of the analyzes performed. Chapter 4 presents the results and discussions in which the validation of piControl and analysis of the altered experiment are exposed. Chapter 5 discloses a straightforward projection to apply the results. Chapter 6 summarizes the results, and chapter 7 presents the conclusions.

Chapter 2

Theoretical Foundation

In this chapter, a compendium of the considered phenomena for the development of the thesis will be made. A resume of what is climate will aid the understanding and importance of climate change and its prediction. In the theme of climate prediction, we present the Intergovernmental Panel on Climate Change, the importance of its regular reports, and a description of common GHGs. Still, on the matter of climate prediction, the subject of climate drift is addressed, and a relation with the numerical model used to perform the experiments in this work is constructed.

Tipping points and tipping elements are defined, as well as their characteristics and importance. The tipping elements chosen in this work are identified, and so are the needs they have to pass through a tipping point. Then, such tipping elements are characterized, which will build the base for the analysis performed in this thesis.

2.1 Climate

What is climate? According to the dictionary[3], the climate is "the composite or generally prevailing weather conditions of a region, as temperature, air pressure, humidity, precipitation, sunshine, cloudiness, and winds, throughout the year, averaged over a series of years.". On the other hand, PEIXOTO and OORT (1992) define it more directly as the average of given quantities that characterizes the structure of a climate component, such as atmosphere, hydrosphere, and others, over some time. Although climate has a less effect on day-to-day people's routine than the weather, it affects every aspect of our life like which food we eat, what diseases we are prone to catch and even how we do our shopping. DONOVAN (2014) comments that "...while you may think that the clothes you have hanging in your

[3]Definition according to www.dictionary.com

wardrobe simply reflect your fashion taste or lack of it, in reality, they reflect the climate in which you live and how it changes throughout the year.". That way, the climate is an essential aspect of life, so that study it and its potential changes are fundamental to the survival of humanity and other beings.

2.2 Climate Change

"We play Russian roulette with climate,
hoping that the future will hold no unpleasant surprises.
No one knows what lies in the active chamber of the gun..."
BROECKER (1987)

In this quote, Wallace Broecker was very concerned about the implications of human-made climate changes due to the release of greenhouse gases to the atmosphere, and he was not wrong to be concerned. It is well known that anthropic activities are partly influential in global climate change since the mid-nineteenth century, considerably altering the radiative balance of the atmosphere (BOLLMANN *et al.*, 2010; BROECKER, 1987; HOUGHTON, 2004, 2009; IPCC, 2013b; KIRTMAN *et al.*, 2013; LENTON *et al.*, 2009, 2008; MASSON-DELMOTTE *et al.*, 2018; MCGUFFIE and HENDERSON-SELLERS, 2001; RASCH, 2012; REVELLE, 2013; ROSENLOF *et al.*, 2013; STOCKER, 2011; TRENBERTH *et al.*, 2013; VECCHI *et al.*, 2006). Since the Intergovernmental Panel on Climate Change's (IPCC) first report, released in 1995, the anthropic influence on global climate and its cause on global warming has been discussed. While this statement causes disagreement among scientists, most of the scientific community does not doubt that warming is real (RASCH, 2012).

The worsening of the greenhouse effect caused by the increase in GHGs can trigger several effects on the planet, not only of an environmental nature but also with consequences for human life, since the climate system is interconnected and interacts continuously. Figure 1 illustrates only a few examples of the cause and effect chain caused by the increase in GHGs, but which already demonstrates the importance of this topic and the seriousness with which it should be treated. In the Special Report on Global Warming of 1.5°C, MASSON-DELMOTTE *et al.* (2018) cite evidence of climate and weather extremes in progress with the observed global warming and that they have the potential to worsen, and others are projected to occur.

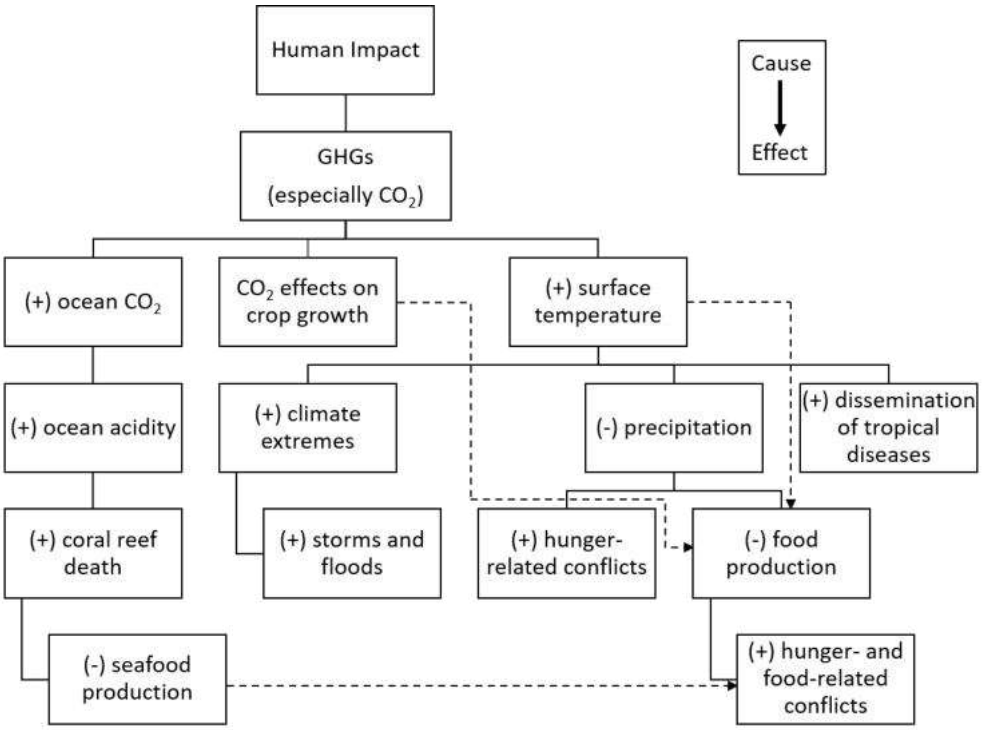

Figure 1: Schematics illustrating the cause-effect chain of some changes caused by the GHGs increase. Source: Modified from DIAMOND, 2019.

Figure 2 presents results comparing two coupled climate numerical model experiments for various regions of the world, considering the atmosphere, the cryosphere, and the ocean. The first set of results was obtained using only natural forcings, and another set was obtained using natural and anthropogenic forcings. Additionally, the observations regarding each case are presented. We can see that, in most cases, the differences between the experiments become more pronounced from 1960 on, and the observations follow the curves of the models that consider the human influence on the climate, indicating the interference of this component.

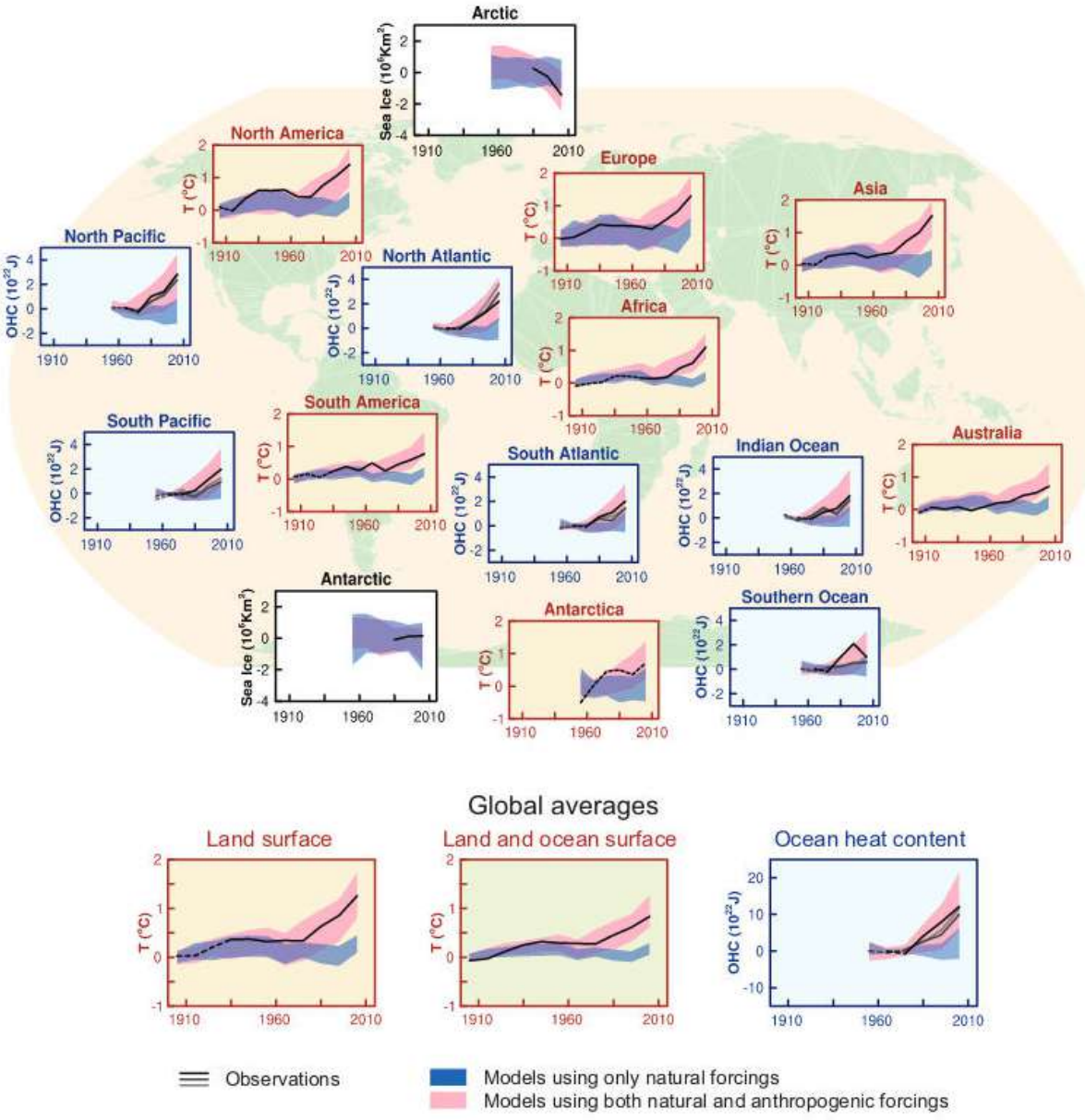

Figure 2: Comparison of observed and simulated climate change based on three large-scale indicators in the atmosphere, cryosphere and ocean: change in air temperature over continental surfaces (yellow panels, in °C), Arctic and Antarctic sea ice extent in September (white panels, in 10^6km^2) and heat stored on the surface of the largest ocean basins (light blue panels, in 10^{22}J)[4]. The air temperature changes are shown for North and South America, Europe, Africa, Asia, Australia, and Antarctic. The sea ice extent is shown for Arctic and Antarctic, and the ocean heat content is shown for the Atlantic, Pacific, Indian and Southern oceans. Source: IPCC, 2013a.

[4]Global averages are also shown. The anomalies are given in relation to 1880-1919 for surface

According to JOHANNESSEN *et al.* (2004), several climate-sensitive parameters are already experiencing changes. Among others, there are sea ice, snow cover, river runoff, glaciers, and permafrost. Some of these changes are, as of now, considered unprecedented over decades and even millennia (IPCC, 2013b). They could be identified and evaluated mainly from global-scale observations with remote sensing, especially for temperature, and paleoclimatic reconstructions, with which information from millions of years ago could be extracted (IPCC, 2013b; TRENBERTH *et al.*, 2013). It is essential to realize that remote sensing has been a valuable tool for observing the Earth's surface since its creation. Furthermore, although the sensors, retrieval algorithms, and accuracy improved over time, their importance and role in environmental monitoring can not be discarded MINNETT *et al.* (2019).

Some of these changes can be seen in Figure 3(a), which illustrates the observations of atmospheric concentrations of CO_2 at Mauna Loa Observatory since 1958. It can be seen a continuous increase in atmospheric CO_2 since the late 1950s, increasing its radiative forcing. The increase in the CO_2 ocean uptake from the atmosphere ends up increasing ocean H^+ (Figure 3(c)). This increase, as a consequence, has been decreasing ocean pH (Figure 3(b)) (LAUVSET *et al.*, 2020). The decrease in ocean pH promotes ocean acidification, which can be dangerous for ocean life (e.g., coral reefs) (ANTHONY *et al.*, 2008; JIANG *et al.*, 2019).

According to IPCC (2013b), atmospheric GHG concentrations have increased since 1750 due to human activity, exceeding pre-industrial levels by up to 150% for CH_4, for example. WALKER (2006) points out that the current level of GHGs guarantees that the world will continue to warm for decades to come, and the current structure of the world economy ensures that there will be further increases in the level of these gases over that time. The concern then revolves around what will be done to reverse this picture and how soon. How tolerable is this situation for humans?

MASSON-DELMOTTE *et al.* (2018) agree with WALKER (2006) and report that the warming between 2006-2015 was higher than 1850-1900, and it is increasing between 0.1°C and 0.3°C per decade. The authors also declare that this warming increase the climate-related risks for humans and systems, which depend on several factors such as geographic location and rate of warming, and others as levels of development vulnerability of the region.

temperatures, 1960-1980 for heat storage in the ocean and 1979-1999 for sea ice. All time series are decadal averages plotted at the center of each decade. For temperature panels, the observations are dashed lines if the spatial coverage of the examined areas is less than 50%. For heat storage panels and sea ice, the solid line indicates that data coverage is good and higher in quality, and the dashed line indicates that data coverage is only adequate, and uncertainty is higher. The model results come from the CMIP5 multi-model, whose shaded bands indicate 5 to 95% confidence intervals.

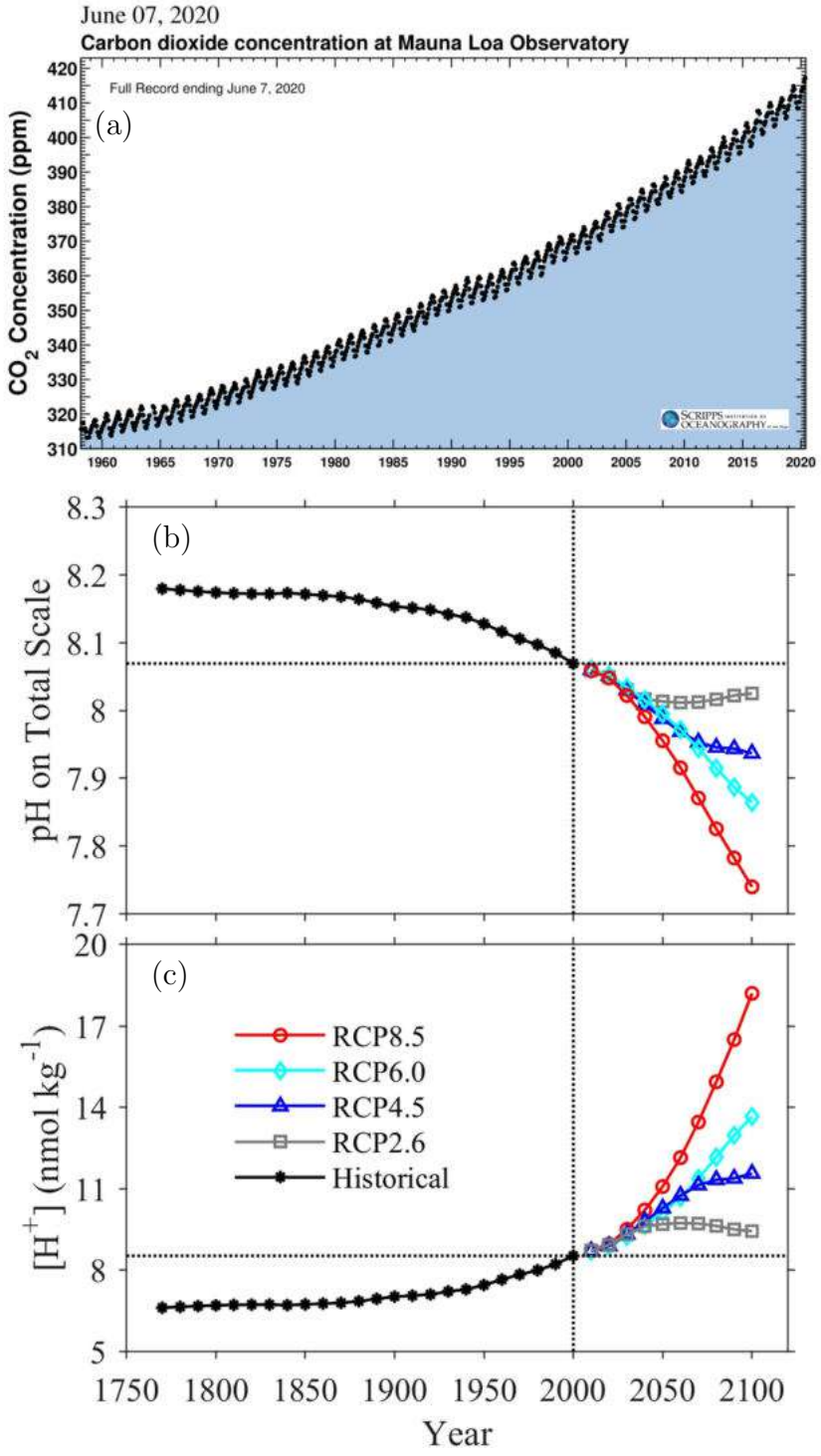

Figure 3: (a) Atmospheric concentrations of CO_2 since 1958 from Mauna Loa Observatory in Hawaii (19.5°N and 155.6°W) and time-series for (b) pH and (c) H^+ for historical and RCPs projections. Source for (a): Taken and modified from The Keeling curve website (https://scripps.ucsd.edu/programs/keelingcurve/). Dataset is available at KEELING and KEELING, 2017. Source for (b) and (c): Modified from JIANG *et al.*, 2019.

Another example that can be seen in Figure 4 is the annual (upper panel) and decadal (lower panel) averages of the global mean sea surface and the land temperature anomalies between 1850 and 2012. It can be seen a continuous increase in the temperature anomaly of these surfaces, indicating their heating. According to IPCC (2013b), more than half of this energy increase in the climate system is stored in the upper ocean (depths up to 700m). Observations in the period 1992-2005 of global ocean temperatures below 2000m indicate warming below 3000m depth for that period, with warming for the Southern ocean region (IPCC, 2013b).

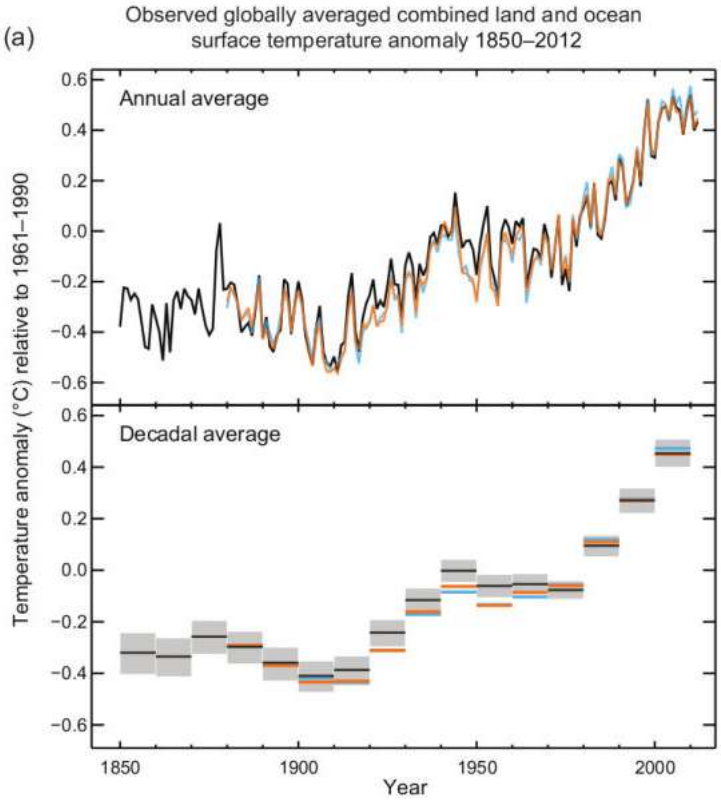

Figure 4: Observed global mean combined sea surface and land temperature anomalies from 1850 to 2012 from three datasets. The upper panel shows the annual averages, and the lower panel shows the decadal averages. Additionally, the lower panel shows the dispersion (uncertainty) associated with the black dataset. The anomalies are compared with the period averaged between 1961 and 1990. Source: IPCC, 2013b.

We currently have a large amount of measured data, thanks mainly to the advent of remote sensing, which aids in the spatial coverage of in situ observations (TRENBERTH *et al.*, 2013). Despite that, due to the consequences that climate change has on climate components, it becomes crucial that we not only identify them but also have the ability to predict them. Thus, the information generated with these predictions can be used so that competent authorities may establish miti-

gation plans to avoid or minimize the consequences for the environment and humans. Climate modeling then fills this gap that the measured data has. However, the observations are crucial because, among others, they can be used in the assimilation and calibration of numerical models (GRASSL, 2001; HURK *et al.*, 2013), which enhances the quality of the numerical prognostics.

2.3 Climate Prediction

"An open mind and a probabilistic approach
are required to deal with chaos in weather
and climate forecasts."
Gilbert Brunet through SCAIFE (2016)

Climate models have become an essential tool for scientific development for over 40 years (GNANADESIKAN *et al.*, 2006; MCGUFFIE and HENDERSON-SELLERS, 2001; PEIXOTO and OORT, 1992). They have been providing critical information for political and social decision making (STOCKER, 2011) and playing a key role in investigating the natural and anthropogenic variability of the climate system (GREGORY *et al.*, 2005; GUPTA *et al.*, 2013; HAGOS *et al.*, 2013; MANABE and STOUFFER, 1999). According to STOCKER (2011), a complete climate model considers the five components of the climate system and the coupling between them. Currently, humans are also considered a component since their influence on the planet has been causing significant alterations on it. The components mentioned above are:

- Atmosphere: a component formed by the portion of the air above the Earth's surface that contains gaseous, liquid, and solid substances. Some important processes include cloud formation and precipitation, heat transport, water vapor, dust and aerosols, and radiative balance.
- Hydrosphere: component formed by all the portion of water in the Earth in its liquid form. It includes all oceans and rivers and the portion of the water cycle after the precipitation phase. Some important processes include volume and heat transport, and various parameter changes at the air-sea interface.
- Cryosphere: a component formed by the entire portion of ice on Earth, including permafrost. Some processes include changes in the radiative balance of the Earth's surface and the influence of salinity in some regions of the globe.

- Lithosphere: component formed by the solid part of the Earth. The position of continents is a determining factor for climate zones and ocean currents. Some processes include surface reflectivity since different materials (sand, rock, and others) have different reflectivities.

- Biosphere: a component formed by the organic coverage of landmasses, such as vegetation and marine organisms. Some processes include the carbon exchange between different reservoirs and the atmospheric balance of various gases, including CO_2.

- Anthroposphere: component in which processes are caused or altered by human action. The most critical processes are those that emit substances that alter the radiative balance and the change in land use, such as deforestation, desertification, degradation, and transformation of soil in built-up areas. In most models, the anthroposphere is treated as an external force, such as the prescription of atmospheric emissions and concentrations of CO_2.

It is essential to define the set of components that is most appropriate to the scientific issue to be solved, also considering the spatial and temporal scales of the processes to be represented (STOCKER, 2011) so that robust results are produced. Table 1 presents the spatial-temporal characteristics of some Climate System component processes.

As stated earlier, human influence on climate has been a reality since the mid-nineteenth century. According to IPCC (2013b), human influence has grown over the years, impacting all components of the climate system with several consequences. Some consequences include atmosphere and oceans warming, changes in the global hydrological cycle, reduction of snow and ice in temperate and polar regions, changes on the global mean sea level, among others. Figure 5 depicts some interactions within the Earth System, including the human activities that modify and are modified by these interactions.

Table 1: Some examples of processes that determine climate, which component they refer to, and their characteristic time-space scales. Source: Modified from STOCKER, 2011.

Component	Process	Temporal Scale	Spatial Scale
Atmosphere	Droplet collision during cloud formation	10^{-6}-10^{-3}s (few μs-few ms)	10^{-6}m (few μm)
	Convective cell formation	10^{4}-10^{5}s (few hours-a day)	10^{2}-10^{4}m (dozens of m-dozens of km)
	Development of large scale weather systems	10^{4}-10^{5}s (few hours-a day)	10^{6}-10^{7}m (thousands-dozens of thousands of km)
	Persistence of pressure distributions	10^{6}s (few days)	10^{6}-10^{7}m (thousands-dozens of thousands of km)
	Southern Oscillation	10^{7}s (few months)	10^{7}m (dozens of thousands of km)
	Troposphere-stratosphere exchanges	10^{7}-10^{8}s (few months-few years)	Global
Hydrosphere	Ocean-atmosphere gas exchange	10^{-3}-10^{6}s (ms-few days)	10^{-6}-10^{3}m (μm-few km)
	Deepwater formation	10^{4}-10^{6}s (few hours-few days)	10^{4}-10^{5}m (dozens-hundreds of km)
	Mesoscale oceanic gyres	10^{6}-10^{7}s (few days-few months)	10^{4}-10^{5}m (dozens-hundreds of km)
	Rossby Wave Propagation	10^{7}s (few months)	10^{7}m (dozens of thousands of km)
	El Niño	10^{7}-10^{8}s (few months-few years)	10^{7}m (dozens of thousands of km)
	Deepwater convection	10^{9}-10^{10}s (dozens-hundreds of years)	Global
Cryosphere	Permafrost formation	10^{7}-10^{9}s (few months-dozens of years)	1-10^{6}m (a meter-thousands of km)
	Sea ice formation	10^{7}-10^{8}s (few months-few years)	1-10^{6}m (a meter-thousands of km)
	Land ice masses formation	10^{8}-10^{11}s (few-thousands of years)	10^{2}-10^{7}m (dozens of m-dozens of thousands of km)
Lithosphere	Reflectivity changes	10^{7}-10^{8}s (few months-few years)	10^{2}m-global (dozens of m-global)
	Isostatic balance of the Earth's crust by ice mass cover	10^{8}-10^{11}s (few-thousands of years)	10^{6}m-global (thousands of km-global)

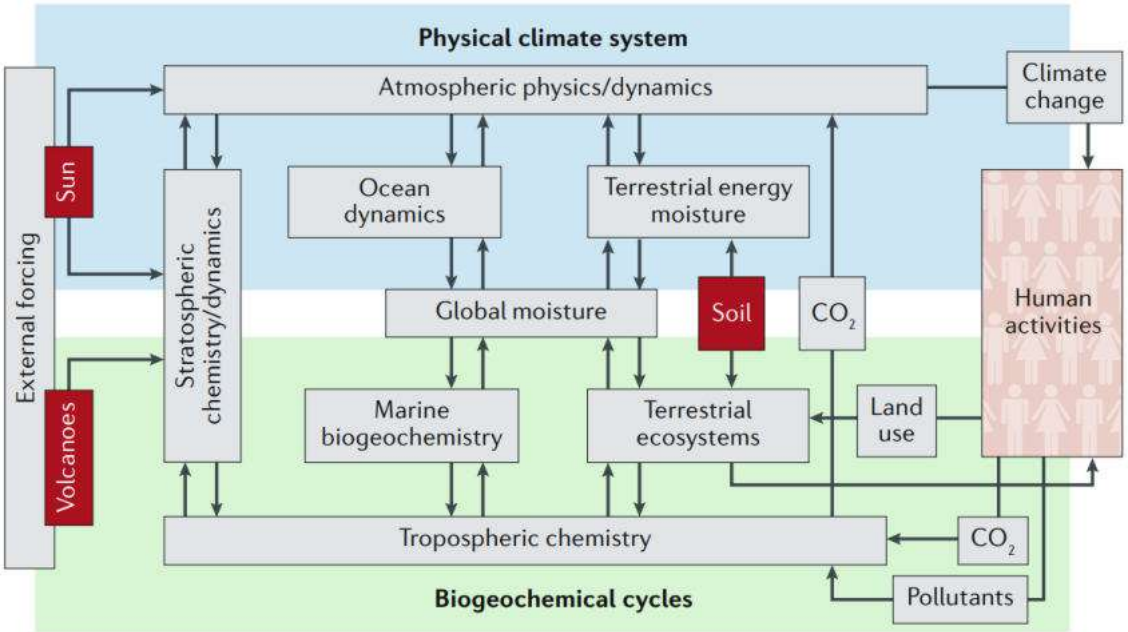

Figure 5: Scheme representing the Earth System and its interactios. Source: STEFFEN *et al.*, 2020.

Human influence on climate has been mainly assessed by IPCC reports (LENTON *et al.*, 2009; STEFFEN *et al.*, 2020), which are produced by research groups around the world and are published every six years on average (TRENBERTH *et al.*, 2013). The following section describes the IPCC, as well as the emission scenarios created for the last report, published in 2013.

2.3.1 IPCC

The IPCC was created in 1988 by the World Meteorological Organization (WMO) and the United Nations Environment Programme (UNEP) to provide decision-makers with regular assessments of the scientific basis of climate change, as well as to generate information on their impacts, future risks and to offer options for adaptation and mitigation (NAKICENOVIC *et al.*, 2000; TRENBERTH *et al.*, 2013). Thus, these assessments present projections of future climate change based on different scenarios, the risks these changes pose and discuss the implications of responsive action choices without determining what actions decision-makers should take (HOUGHTON, 2009; MOSS *et al.*, 2010). Also, historical experiments and experiments characterizing the current climate are generated as well.

The Assessment Reports (ARs) receive contributions by around 2500 researchers from various countries and fields of knowledge such as meteorology, biology, oceanography, and others who volunteer their time and knowledge to produce these documents. The authors of the reports are grouped into three Working Groups (WGs), who develop the report in three different strands. WGI produces the document entitled 'The Physical Scientific Basis', WGII produces the 'Impacts, Adaptation and Vulnerability' and WGIII produces the document entitled 'Climate Change Mitigation'.

Since it was created, the IPCC has published five ARs. The First Assessment Report (FAR) was published in 1990 (TRENBERTH *et al.*, 2013), the Second Assessment Report (SAR), was published in 1995, the Third Assessment Report (TAR), was published in 2001, the fourth report, AR4, was published in 2007 and the fifth and most recent, AR5, was published in 2013. By the end of the writing of this document, the 6^{th} AR had not yet been published. According to the IPCC's webpage, the three WGs contributions to the AR6 will be finalized in 2021, and the Synthesis Report will be finalized in 2022.

Besides the ARs, the IPCC also produces special reports on specific issues, and methodology reports, providing guidelines for GHG inventories (NAKICENOVIC *et al.*, 2000). These two kinds of reports are published between ARs, and after AR5, the following reports were published; the "Special Report on Global Warming of 1.5°C" (SR1.5) on October 2018, the "Methodology Report 2019 Re-

finement to the 2006 IPCC Guidelines for National Greenhouse Gas Inventories" on May 2019, the "Special Report Climate Change and Land" (SRCCL) on August 2019 and the "Special Report The Ocean and Cryosphere in a Changing Climate" (SROCC) on September 2019.

The models assessed on the reports simulate climate change based on a set of scenarios with anthropogenic forcing (IPCC, 2013b; MOSS *et al.*, 2008). These scenarios provide insights into how the future may develop in a variety of areas and help to assess uncertainty about the human contribution to climate change and system responses (MOSS *et al.*, 2010; NAKICENOVIC *et al.*, 2000). In the following section, the scenarios prepared for AR5, the Representative Concentration Pathways (RCPs), will be described.

2.3.1.1 RCPs

In AR5, new scenarios, called RCPs, were used to conduct the 5th Coupled Model Intercomparison Project (CMIP5) simulations under the responsibility of the WCRP (IPCC, 2013b). RCPs are scenarios that include a time series of emissions and concentrations of all GHGs, aerosols, chemically active gases, and land use, or land cover (MOSS *et al.*, 2008). Unlike Special Report on Emission Scenarios (SRES) (NAKICENOVIC *et al.*, 2000) used in AR3 and AR4 (IPCC, 2013b), RCPs provide scenarios that offer climate change mitigation approaches and are designed to complement and even replace scenarios previously used as SRES themselves, in some cases (MEINSHAUSEN *et al.*, 2011). Table 2 presents the concentrations of CO_2 achieved in each RCP scenario and the equivalent in the SRES. This proximity between the RCP and SRES scenarios can also be seen in Figure 6.

Table 2: AR5 scenarios, their average CO_2 concentrations in 2100, and equivalent SRES scenarios. Source: Modified from BÖCK, 2015.

RCP Scenario	**Atmospheric CO_2 in 2100 (ppm)**	**Atmospheric CO_2 in 2100 (Gt C)**[5]	**Equivalent SRES Scenario**
RCP 2.6	421	900	-
RCP 4.5	538	1150	B1
RCP 6.0	670	1430	A1B
RCP 8.5	936	1990	A1FI

Two main groups use the scenarios and their projections: the decision and policy-makers, called the ”end-users” and researches who adopt the scenarios for their use, called ”intermediate users” (MOSS *et al.*, 2008). According to MOSS *et al.* (2008, 2010), the letter ’R’ (Representative) means that each RCP is just one of many possible scenarios that would culminate in the assigned radiative forces.

[5] 1 Gt = 10^9 kg, 1ppm CO_2 = 2.13Gt C.

The letter 'P' (Pathway) shows that the target of interest is not only the long-term concentration level but also the trajectory built over time to achieve this result. RCPs are identified by the total radiative forcing in the year 2100 over the year 1750 as a result of the additional cumulative increase of CO_2 in the atmosphere during the 21st century. Table 3 presents the created RCPs, their radiative forcings, and other details.

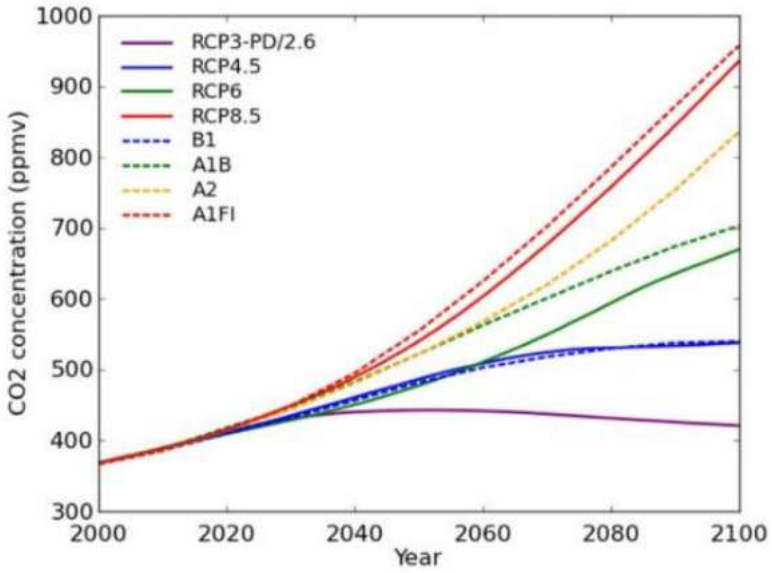

Figure 6: Time series of CO_2 concentration in parts per million by volume (ppmv) of the RCP (continuous lines) and SRES scenarios (dashed lines). Source: Modified from BÖCK, 2015.

The RCP scenarios are characterized as follows: RCP 2.6 represents a mitigation scenario, which results in a very low forcing, already showing a decline in the concentration of CO_2 by 2100 (Figure 6). RCPs 4.5 and 6.0 are scenarios that tend to achieve emission stabilization - RCP 4.5 is already stabilizing by 2100 - and high GHG emissions characterize scenario 8.5. For each scenario, changes in land use, atmospheric emission of pollutant gases, and GHG and annual anthropogenic emissions are defined until the year 2100 (IPCC, 2013b).

According to CMIP5 projections with RCPs, the average global surface temperature anomaly of 1850-1900 at the end of the 21st century (2081-2100) has the potential to exceed 1.5°C and to continue to warm after 2100 for all RCP scenarios except 2.6. The oceans are also predicted to continue to warm during the 21st century, and this heat will spread to the deep ocean, altering circulation. Arctic ice cover will continue to shrink and thin, and snow in the northern hemisphere will decrease due to rising temperatures. Figure 7 presents the time series from 1950 to

2100 of CMIP5 simulations for RCPs 2.6 and 8.5. Panel (a) shows the global average annual surface air temperature changes from the average of 1986-2005, panel (b) shows the extent of northern hemisphere sea ice in September (five-year average), and panel (c) shows the mean global ocean surface pH.

Table 3: Characteristics of RCPs. Fonte: Modified from MOSS *et al.*, 2010.

Name	**Radiative Forcing**	**Concentration (ppm)**	**Evolution**	**The model that created the RCP**
RCP 2.6	Peaks in ≈3W·m^{-2} before 2100 and then decreases	Peaks in ≈490 CO_2-equiv. before 2100 and then decreases	Peaks and decreases	IMAGE[6]
RCP 4.5	Stabilizes at ≈4.5W·m^{-2} after 2100	Stabilizes at 650 CO_2-equiv. after 2100	Stabilization without crossing the limit	GCAM[7]
RCP 6.0	Stabilizes at ≈6W·m^{-2} after 2100	Stabilizes at 850 CO_2-equiv. after 2100		AIM[8]
RCP 8.5	>8.5W·m^{-2} in 2100	>1370 CO_2-equiv. in 2100	Increase	MESSAGE[9]

[6]IMAGE - Integrated Model to Assess the Global Environment, Netherlands Environmental Assessment Agency, The Netherlands (STEHFEST *et al.*, 2014).

[7]GCAM - Global Change Assessment Model, Pacific Northwest National Laboratory, USA (EDMONDS *et al.*, 1994).

[8]AIM - Asia-Pacific Integrated Model, National Institute for Environmental Studies, Japan (MATSUOKA *et al.*, 1995).

[9]MESSAGE - Model for Energy Supply Strategy Alternatives and their General Environmental Impact, International Institute for Applied Systems Analysis, Austria (MESSNER and STRUBEGGER, 1995).

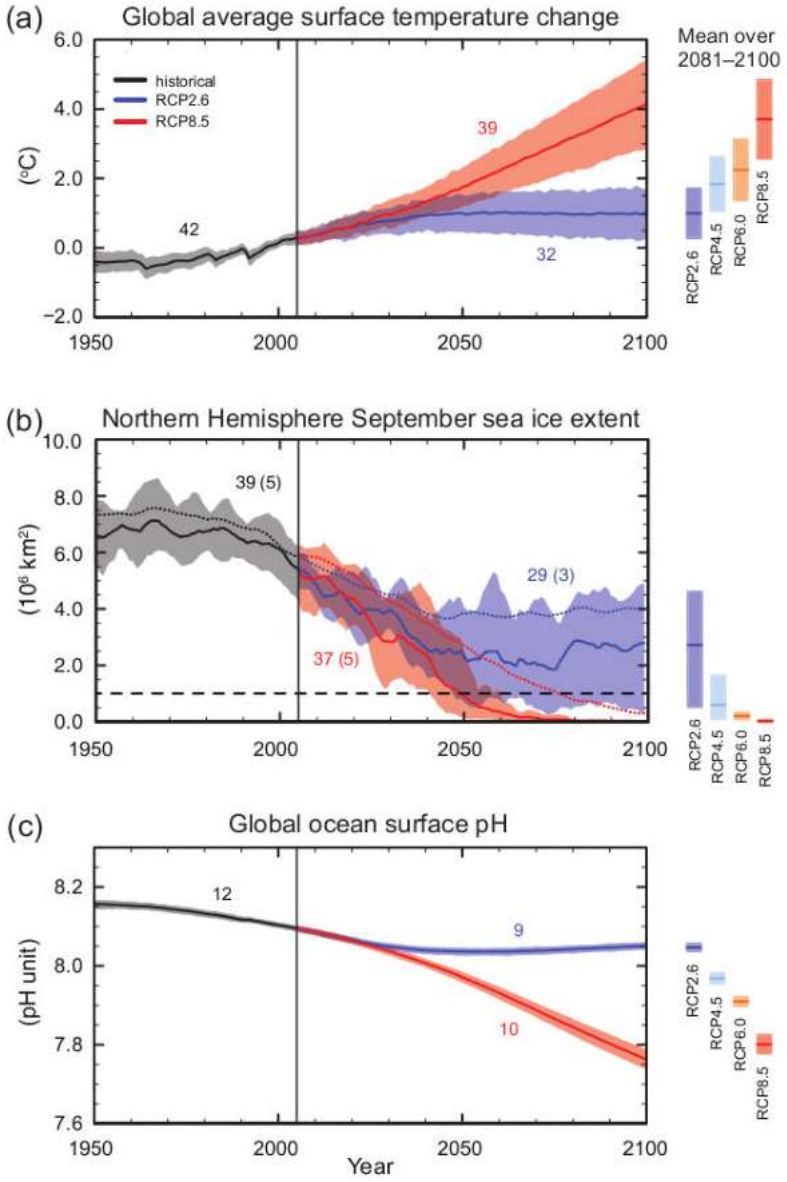

Figure 7: Time series from 1950 to 2100 of the CMIP5 multi-model simulations. (a) Change in global average annual surface air temperature compared with the average between 1986 and 2005, (b) Northern hemisphere sea ice extent in September (5-year average), and (c) Average global ocean surface pH. The lines represent the projections, and the shadows represent the uncertainty for the RCP 2.6 (blue) and RCP 8.5 (red) scenarios. The black lines and gray shadows represent the historical evolution modeled on reconstructed historical forcings. The average value and the uncertainties associated with it over the period 2081-2100 are given in vertical bars for all RCPs. The number of CMIP5 models used is indicated[10]. Source: Modified from IPCC, 2013b.

[10]For (b), the value in parentheses indicates a subset of models that most closely reproduce the mean climatic state in the 1979-2012 Arctic sea ice trend. The CMIP5 multi-model average is indicated in dotted lines. The black dashed line indicate conditions near ice-free regions - that is,

The recent IPCC Special Report entitled "Global Warming of 1.5°C" by MASSON-DELMOTTE *et al.* (2018) assesses some findings on the impacts of global warming and pathways of global GHG emissions. The authors report, among other resolutions, a good probability of global warming reaches 1.5°C in the next decades if the current rate continues. The estimated warming is increasing global SST at 0.1°-0.3°C per decade, resulting from current and past emissions. The report still cites, with medium confidence, the relation between extremes in climate and weather with global warming.

According to LENTON *et al.* (2008), human influence on climate has the potential to force the components of the climate system so that they cross a critical point and reach modes of operation different from the initial ones. This critical point or tipping point is the subject of this thesis and will be exposed in the item 2.4.

2.3.1.2 GHG

GHGs are those that absorb the thermal radiation emitted by the Earth's surface and act as a blanket for it (HOUGHTON, 2009). They are a subset of Short-Lived Climate Forcers (SLCF) species, which, in the case of GHGs, are gases that affect climate. Many of them are air pollutants and have lifetimes in the atmosphere that spans from a few days to a decade (BLAIN *et al.*, 2018). They are diverse, as are their concentrations in the atmosphere, as can be seen in Table 4.

The importance of these gases as GHGs depends as much on their concentration in the atmosphere as on the infrared radiation they absorb (HOUGHTON, 2009). Among GHGs that have increased their concentration in the atmosphere due to anthropogenic activities, CO_2 stands out and accounts for 72% of the increase in the greenhouse effect; methane then accounts for 21% and nitrous oxide for 7% (HOUGHTON, 2009).

Table 4: Greenhouse gas atmospheric concentrations.

Gas	**Value (ppb[11], fraction* or ppm[12])**	**Year of reference**	**Reference**
Water Vapor (H_2O)	Variable (0-0.02*)	2007	HOUGHTON, 2009
Carbon Dioxide (CO_2)	405.5ppm	2017	WMO, 2018
Methane (CH_4)	1859ppb		
Nitrous Oxide (N_2O)	329.9ppb		
Chlorofluorcarbons (CFCs)	0.001	2007	HOUGHTON, 2009
Ozone (O_3)	Variable (0-1000)		

the sea ice extent is less than 106km^2 for at least five years of consecutive numerical simulation.

It is important to understand why the change in GHG concentration impacts the global climate. For this, we need to define the concept of radiative forcing. According to HOUGHTON (2009) and MOSS *et al.* (2010), radiative forcing is the change in average net radiation at the top of the troposphere[13], which occurs due to a change in some elements of the climate system. If, for example, the concentration of carbon dioxide in the atmosphere doubled and everything else remained unchanged, there would be a net radiative imbalance at the top of the atmosphere of 3.7 $W \cdot m^{-2}$. This imbalance would act as a radiative forcing. Since the climate system always responds to restore the balance between incoming and outgoing radiation, this imbalance would cause the system to heat its surface to achieve equilibrium, increasing the global average temperature by 5-6°C (HOUGHTON, 2009; REVELLE, 2013). Similarly, a negative forcing would cause the system to cool its surface.

The following items define the GHGs and their processes:

- **Water Vapor**: Water vapor is a particular case within GHGs. According to MYHRE *et al.* (2013), while it can contribute to the natural greenhouse effect between two or three times more than CO_2, the number of anthropogenic emissions (mainly due to irrigated crops) are less than natural emissions[14]. Besides, it differentiates from other GHGs by its ability to condense and precipitate, which puts the water vapor typical residence time in the atmosphere of about ten days.

- **Carbon Dioxide and the Carbon Cycle**: carbon dioxide is the dominant form by which carbon is transferred in nature between natural carbon pools (EPA, 2020b), and it is the gas that most contributes to the anthropogenic radiative forcing (HOUGHTON, 2009; WMO, 2018). In our breathing process, we contribute as a natural source to this cycle; inhaling oxygen, we oxidize the carbon from our food and turn it into CO_2, which is exhaled. The decomposition of organic matter contributes in the same way. The photosynthesis process works oppositely, absorbing carbon dioxide and producing oxygen.

[11] ppb (parts per billion) is the number of molecules of the gas per billion (10^9) molecules of dry air.

[12] Fraction or ppm is the way molar fraction or mixing ratio is represented. They are the ratio between the number of moles of a constituent in a given volume and the total number of moles of all constituents in that volume. It differs from the volume mixing ratio (expressed as ppmv, for example) by non-ideality corrections of gases, which is significant concerning measurement accuracy for many GHGs.

[13] It is useful to define radiative forcing as the radiative imbalance at the top of the troposphere rather than at the top of the entire atmosphere. The formal definition of radiative forcing as stated in the IPCC reports is the change in net (*downward - upward*) irradiance (*solar + longwave* in $W \cdot m^{-2}$) in the tropopause due to a change in an external forcing after allowing the stratospheric temperatures to adjust to the radiative equilibrium, but with the surface and troposphere temperatures and state kept fixed at undisturbed values (HOUGHTON, 2009; IPCC, 2019).

[14] The anthropogenic emissions become important in the stratosphere. See FAQ 8.1 of MYHRE *et al.* (2013)

Taking into account the life span of humans, the anthropogenic CO_2 emitted into the atmosphere is not destroyed by chemical reactions but redistributed among the other carbon pools. Exchanges between these reservoirs occur over a wide range of time scales, and according to HOUGHTON (2009), around 50% of the increase in carbon dioxide in the atmosphere will be removed in 30 years, another 30% in some centuries and the remaining 20% may remain in the atmosphere for many thousands of years.

Compared to the atmosphere, the carbon reservoirs in the lithosphere and hydrosphere are much larger (PRENTICE *et al.*, 2001). That means that even small changes in these large reservoirs can have a significant effect on the atmospheric concentration of CO_2. For example, the release of 2% of the carbon stored in the oceans would double the concentration of carbon dioxide in the atmosphere (HOUGHTON, 2009). However, observations indicate that the increase of CO_2 in the atmosphere and the consequent rise in air temperature decreases the potential of the ocean and lithosphere to absorb the excess CO_2 from the atmosphere, altering the balance between these two components, also pointed out by EPA (2020b). Additionally, a warmer climate is likely to be associated with weaker ocean Meridional Overturning Circulation, further reducing carbon absorption by the oceans.

At a time when human activities were not considered a significant disturbance, and in short periods compared to geological scales, exchanges between reservoirs were considerably constant. As it is well known, the Industrial Revolution has moved this balance. Since then, more than 600 gigatons of carbon have been released into the atmosphere due to the burning of fossil fuels, increasing the carbon dioxide in the atmosphere by more than 145% from pre-industrial levels[15] by 2017 (HOUGHTON, 2009; PRENTICE *et al.*, 2001; WMO, 2018) (Figure 8). In addition to burning fossil fuels, human activities also contribute to the increase in carbon dioxide due to land-use change (HOUGHTON, 2009; WMO, 2018). Due to its amount in the atmosphere, carbon dioxide is the GHG that most contributes to radiative forcing on Earth (WMO, 2018).

[15] A pre-industrial mole fraction of 278 ppm is assumed (WMO, 2018).

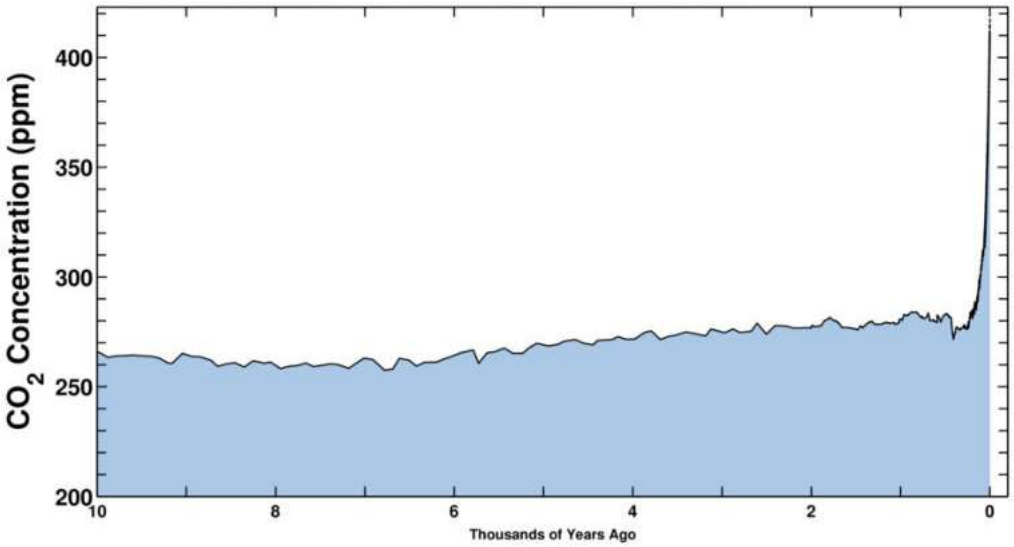

Figure 8: Historical time series of CO_2 concentration over the last 10,000 years from ice-core data, before 1958, and from Mauna Loa observations, post 1958. Source: Taken and modified from The Keeling curve website (https://scripps.ucsd.edu/programs/keelingcurve/).

- **Methane**: methane is the major component of natural gas, and it is mainly produced due to the decomposition of organic matter (SENUM and GAFFNEY, 1985). Ice core data indicate a stable concentration of this gas in the atmosphere for more than 2000 years before 1800, but since then, the concentrations have more than doubled (HOUGHTON, 2009; MYHRE *et al.*, 2013; PRATHER *et al.*, 2001). Studies also point to the close relationship between the CH_4 increase, the increase in the human population since the industrial revolution (HOUGHTON, 2009) and the consequent increase in food demand. Even though methane concentrations in the atmosphere are much lower than those of carbon dioxide, the effect of CH_4 as a greenhouse gas is 25-30 times higher than that of CO_2 (EPA, 2020b; LENTON *et al.*, 2019).

  Anthropogenic methane emission sources are numerous and varied, making it difficult to estimate the global production of this gas (PRATHER *et al.*, 2001). However, it is known that outside the wetland regions, the largest sources of CH_4 are related to human activities (HOUGHTON, 2009). According to the WMO (2018), approximately 40% of the methane in the atmosphere comes from natural sources, and the other 60% comes from the anthropogenic sources. The primary process of removing methane from the atmosphere is by reacting with the hydroxyl radicals OH present in the atmosphere due to reactions with sunlight, oxygen, ozone, and water vapor (HOUGHTON, 2009; PRATHER *et al.*, 2001; SENUM and GAFFNEY, 1985). Table 5 lists the natural and

anthropogenic sources of methane and also its sinks.

Table 5: Sources and sinks of methane (in millions of tons/year). Source: Modified from HOUGHTON, 2009.

	Best Estimate	**Uncertainty**
Natural Sources		
Wetlands	150	(90-240)
Termites	20	(10-50)
Ocean	15	(5-50)
Others (including hydrates)	15	(10-40)
Anthropogenic Sources		
Coal Mines, Natural Gas, and Oil Industry	100	(75-110)
Rice Fields	60	(30-90)
Enteric Fermentation	90	(70-115)
Waste Treatment	25	(15-70)
Landfills	40	(30-70)
Biomass burning	40	(20-60)
Sinks		
Atmospheric Removal	545	(450-550)
Soil Removal	30	(15-45)
Atmospheric Increase	22	(35-40)

- **Nitrous Oxide**: nitrous oxide is a gas commonly used as an anesthetic. Known as hilarious gas, it is a minor GHG. Its atmospheric concentration around 0.3ppm has grown by approximately 0.25% per year, and in 2011 it was almost 19% higher than in pre-industrial times (HOUGHTON, 2009; MYHRE *et al.*, 2013; PRATHER *et al.*, 2001). As for the CH_4, compared to the CO_2, nitrous oxide is around 300 times more effective as a GHG.

  The highest emissions are associated with natural sources and agriculture. Those related to human actions are probably due to the increased use of fertilizers in the soil. Another part is due to biomass burning and the chemical industry (synthetic fabrics with nylon, for example). The sink of N_2O is photodissociation in the stratosphere[16] (MYHRE *et al.*, 2013; PRATHER *et al.*, 2001; SEN-GUPTA, 1935), and the reaction with electronically excited oxygen atoms (GHORMLEY *et al.*, 1973; MYHRE *et al.*, 2013; PRATHER *et al.*, 2001), leading to an atmospheric lifetime of about 120 years, according to HOUGHTON (2009) and about 114 years, according to EPA (2020b).

- **Chlorofluorocarbons and ozone**: chlorofluorcarbons are human-made chemical compounds widely used in refrigerators, insulation materials, and

[16] Action of light in breaking the N_2O molecule, transforming it into $NO + N$ (SEN-GUPTA, 1935).

aerosol spray cans. They are considered chemically unreactive and, therefore, once released into the atmosphere, they can remain there for up to 100 or 200 years before being destroyed (HOUGHTON, 2009). Its use significantly increased during the 1980s, rising atmospheric concentrations since then and causing severe environmental problems.

One such problem is associated with the destruction of the ozone layer (HOUGHTON, 2009; MYHRE *et al.*, 2013). Ozone is an extremely reactive gas present in the stratosphere[17] and is formed by the action of ultraviolet radiation on oxygen molecules (HOUGHTON, 2009; PRATHER *et al.*, 2001). Likewise, ozone is destroyed as it absorbs ultraviolet radiation from the sun, which would be extremely harmful to all life forms on the Earth's surface (HOUGHTON, 2009). The amount of O_3 in the stratosphere depends on the balance of these two processes. CFC molecules that reach the stratosphere also react with ultraviolet radiation from the sun. That reaction releases chlorine atoms, which binds with ozone molecules, reducing them to oxygen molecules and preventing ozone from absorbing ultraviolet radiation from the sun (HOUGHTON, 2009; MYHRE *et al.*, 2013).

Another problem associated with CFCs and ozone is that both are GHGs. A CFC molecule has a greenhouse potential 5,000 to 10,000 times greater than a CO_2 molecule, and its radiative forcing effect is estimated to be about 12% of all greenhouse gases (or 0.3 $W \cdot m^{-2}$), despite the reduced concentration in the atmosphere compared to carbon dioxide (HOUGHTON, 2009). However, since CFCs deplete ozone molecules, the greenhouse effect of CFC is partially offset by the reduction of the ozone greenhouse effect (HOUGHTON, 2009).

In addition to being present in the stratosphere, ozone can also be found in the troposphere, either by transferring itself from the stratosphere or by local generation through chemical reactions, especially those involving the action of sunlight on nitrogen oxides (HOUGHTON, 2009; MYHRE *et al.*, 2013; PRATHER *et al.*, 2001). Unlike its action in the stratosphere, the ozone present in the troposphere, if in high concentrations, causes harm to the health of living beings. According to HOUGHTON (2009), observations and computer simulations suggest that the concentration of ozone in the troposphere has doubled since the industrial revolution, meaning a radiative forcing of about 0.35 $W \cdot m^{-2}$. Tropospheric ozone is also generated through reactions with nitrogen oxides emitted from aircraft. It is estimated that the radiative forcing of this ozone is similar to that of carbon dioxide emitted from aircraft, approximately 3% of current global fossil fuel consumption (HOUGHTON,

[17] Region of the atmosphere between 10 km and 50 km high.

2009).

There are also some compounds that, by indirect effects, contribute through chemical reactions with some previously mentioned gases, increasing or decreasing the greenhouse effect. Carbon monoxide (CO) and nitrogen oxides (NO and NO_2), for example, emitted by vehicle exhaust or aircraft, fit in this case. The CO, through chemical reactions, generates CO_2 (PRATHER *et al.*, 2001). This reaction also alters the concentrations of OH, which alter the concentration of CH_4. On the other hand, nitrogen oxides reduce atmospheric concentrations of methane, partially offsetting the increase in previously mentioned ozone due to aircraft (HOUGHTON, 2009). Besides that, nitrogen oxides can react with H_2O molecules, causing acid rain (EPA, 2020a).

Although not gaseous compounds, there are particles in the atmosphere that also alter the energy balance as they absorb radiation from the sun or spread it back into space. These particles are commonly called aerosols and have a diameter between 0.001 and 0.01mm (HOUGHTON, 2009). Aerosols have different origins, both natural and anthropogenic. The natural ones are related to particles originating from desert areas, forest burns, and marine spray. Less common but still relevant are aerosols produced by volcanic ash (HOUGHTON, 2009).

Among aerosols of anthropogenic origin, sulfate particles deserve attention. This aerosol is derived from sulfur dioxide, or sulfur anhydride (SO_2), a gas produced in large quantities by power stations and other industrial plants, where coal and oil are burned (HOUGHTON, 2009). As stated above, aerosols absorb solar radiation and therefore represent a global average negative radiative forcing between 0.2 to 0.4 $W \cdot m^{-2}$, attenuating the greenhouse effect (HOUGHTON, 2009). Although these particles have a short residence time in the atmosphere (about five days), their effects cannot be overlooked, as illustrated by Figure 9 (HOUGHTON, 2009).

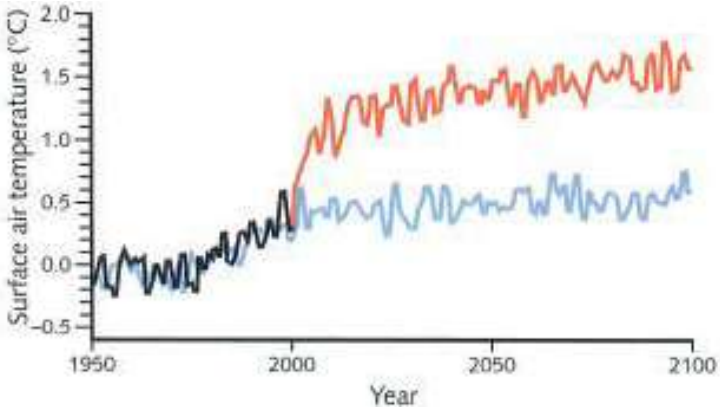

Figure 9: Time series, estimated by numerical modeling, comparing, since 2000, the evolution of global average air surface temperature by maintaining sulfur aerosols (blue line) and removing them (red line). Source: HOUGHTON, 2009.

An interesting term to define here is Global Warming Potential (GWP). It was created by the need to compare the radiative forcing of different gases, highly variable due to the different lifetime of each. GWP is always calculated relative to carbon dioxide. It represents the value of the time integration ratio of 1kg instant release of a given gas to 1kg instant release of CO_2 (HOUGHTON, 2009), that is, the value of the radiative forcing of a given gas relative to the radiative forcing of carbon dioxide. GWP depends on the integration time that is used. Thus, it is necessary to define a time horizon for this integration. Table 6 lists the greenhouse gas GWPs covered by the Kyoto Protocol.

Table 6: Kyoto Protocol GHGs and its GWPs for a 100-year time horizon.

Gas	**GWP**	**Reference**
Carbon Dioxide (CO_2)	1	EPA, 2017; HOUGHTON, 2009
Methane (CH_4)	28-36	EPA, 2017
Nitrous Oxide (N_2O)	265-298	EPA, 2017; HOUGHTON, 2009
Hidrofluorcarbons (HFCs)	12 to 12000[18]	HOUGHTON, 2009
Perfluorcarbons (PFCs)	5000 to 12000[18]	
Sulfur hexafluoride (SF_6)	22200	

2.3.2 Climate Drift

An important topic to address when dealing with climate modeling is whether or not climate drift is present in models. Drift can be conceptualized as spurious long-term changes unrelated to the internal variability of the system (GUPTA *et al.*, 2013). Drift in climate models can be a source of problems since a historical or control drift experiment used to start other forcing experiments will propagate the initial problems to them.

Climate drift may arise due to several factors, including:

- Simulation initialization may be in dynamic imbalance (GUPTA *et al.*, 2013).
- A coupling shock between model components can result in discontinuities in surface flows, as in the work of RAHMSTORF (1995).
- Numerical errors inherent in the model may be present, resulting in non-conservation of heat or humidity, as in the work of LUCARINI and RAGONE (2011).

According to GUPTA *et al.* (2013) and EYRING *et al.* (2016), climate models are usually simulated for only a few hundred years and not thousands as

[18] Values vary for different compounds.

would be desirable. As a consequence, experiments with external forcings (such as solar irradiance, for example) are performed from previous experiments that are not entirely balanced. This lack of balance can lead to changes not only associated with the forcings and the internal variability of the system but also changes linked to the process of model adjustment by masking the resulting climate change. Although simple, the solution of using long (thousands of years) integrations is not feasible due to the commonly available computational resources (EYRING *et al.*, 2016; GUPTA *et al.*, 2013; RAHMSTORF, 1995).

It is crucial to identify and quantify drift in the models to decide if it can be neglected or if it is significant to make corrections (GUPTA *et al.*, 2013; RAHMSTORF, 1995). GUPTA *et al.* (2013) evaluated the presence and importance of drift in climate models used in CMIP5 (see author's Table 1) compared mainly with the work of GUPTA *et al.* (2012), which evaluated the models used in CMIP3. Community Earth System Model version 2 (CESM2), the model which results were used (item 3.1), is not in the list of models evaluated by GUPTA *et al.* (2013). However, the Community Climate System Model version 4 (CCSM4), which represents a subset of a prior version of CESM2 (NCAR/UCAR, 2016), is part of the listing models in GUPTA *et al.* (2013). That way, we can use it as a representative of CESM2 since it has all the resources presented in CESM. According to the authors, the results of the global mean SST, temporal evolution drift analysis indicate percentual error values associated with drift close to 0% for CCSM4. Still, according to the authors, the total linear drift of precipitation and global mean SST are strongly correlated, suggesting that the drift associated with atmospheric parameters can be explained by changes in SST over time. Obeying this relationship, the authors also find low error values for precipitation and lower drift significance in terrestrial regions.

For the global mean steric sea level, CCSM4 has been shown to have a 20% error associated with drift. This higher value is already expected as this parameter is integrated through the water column, and, according to the authors, drift can represent a significant component in the deep ocean. Despite presenting higher percentages than the SST and the precipitation, the steric sea level presents low values of drift for the CCSM4, mainly compared to some other models evaluated. For the sea ice area, the authors observed errors in the Antarctic region of less than 10% and point out that the tendency associated with the internal decadal variability of sea ice is generally more significant than the drift trend, which decreases its significance. In summary, the authors argue that there has been a reduction in the drift from CMIP3 to CMIP5 models and that this improvement may be related to both more extended integralization periods, representation of physical parameterization, increase in horizontal or vertical resolution and the composition of one or more factors. Also, the close relationship between drift in SST, precipitation,

and sea ice may mean that changes in the ocean are manifested as drift in the atmosphere and cryosphere components.

The work of RAHMSTORF (1995) investigated the climate drift that arises from the coupling of the ocean and the atmospheric models. For this, the author used a global ocean climate model, and the interactions between the ocean and the atmosphere were applied through a one-layer idealized atmospheric model with horizontal heat diffusion and a linear parameterization of longwave radiation. The choice not to use a complete climate model of the atmosphere is based on the purpose of isolating the processes that occur in the ocean model due to coupling. According to the author, if a complete atmospheric model were to be used, these processes could be obscured by the atmosphere, and changes occurring after coupling could not be reliably attributed to a specific cause. That way, the model used in the study had no internal variability.

The results found by RAHMSTORF (1995) suggest that changes arising from coupling probably have as their leading cause changes in convection patterns, which are sensitive to disturbance and may generate different equilibrium states in an ocean model. These changes occurred more pronounced throughout the Southern Ocean, which explains the changes in the Antarctic Bottom Water (AABW) cell and the Indo-Pacific stream, and near the Arctic Ocean (see author's Figure 12), reducing the number of deep convection grid points by almost half. According to the author, decreased deep convection leads to decreased deep ocean ventilation, increasing heat flow at these points.

ZHANG (2011) also worked with climate drift from coupling shock in a coupled ocean-atmosphere simple model, due to the difficulties to address such problems in a coupled general circulation model. The author concludes that the use of coupled data assimilation to initialize coupled models, adjusting the model coherently by observations, reduces the coupling shock.

One way to eliminate drift generated by the coupling shock is to work with experiment anomalies, i.e., to subtract the altered round from the control round. However, this approach only applies if the coupling response is deterministic and similar in both experiments, a highly unlikely scenario as changes in convection patterns due to thermal feedback appear to be chaotic (RAHMSTORF, 1995). The author further suggests that one way to avoid these drift problems would be to spin the fully-coupled model for several thousand years until the coupling shock is no longer noticeable before performing any other experiments derivative from the first one. Although this might be difficult computationally, the initial conditions generated for the control experiment used here were derived from several centuries of integration, as described on item 3.2.1.1, which contributes to decrease drift from coupling shock.

2.4 Tipping Points

> *"One of the most concerning consequences of human-induced increases in atmospheric greenhouse gas concentrations is the potential for rapid regional transitions in the climate system."*
> *DRIJFHOUT* et al. *(2015)*

Tipping point is the critical point in the forcing or feature that marks the moment a transition is triggered, and the future state is changed (LENTON *et al.*, 2009; LENTON, 2013, 2020; LENTON *et al.*, 2008; LUCARINI and RAGONE, 2011; SCHEFFER *et al.*, 2001; WALKER, 2006). A simple way to understand this concept is to think about freezing water (SCHEFFER *et al.*, 2018). Even though the temperature drops gradually, after a threshold, the water will convert to ice. Tipping points happen when a perturbation triggers a change in the feature's dynamics, which in turn triggers a positive feedback, a self-amplifying modification, propelling the feature towards a new stable state (LENTON, 2013, 2020; LENTON *et al.*, 2008). Figure 10 outlines the process of a system traversing a tipping point. We can see that the shape of the well changes gradually so that the ball does not remain in equilibrium within it, but reaches a new equilibrium.

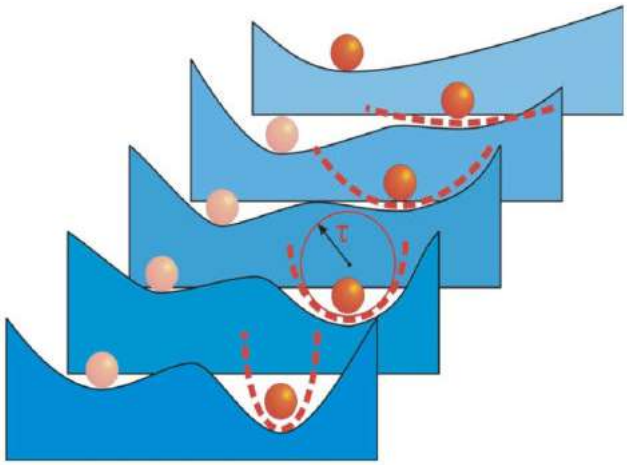

Figure 10: Scheme of passing through a tipping point: potential wells represent stable attractors, and the ball the state of the system. Under gradual forcing (from front to back), the potential right well becomes shallower and finally disappears (threshold), causing the ball to roll sharply to the left. The well bend is inversely proportional to the system response time τ for minor disturbances. Source: LENTON *et al.*, 2008.

Tipping points may occur in a wide range of systems, from social systems (GRODZINS, 1957; LENTON, 2013; SCHEFFER *et al.*, 2018; SCHELLING, 1971)

to environmental ones (LENTON, 2013; LENTON *et al.*, 2008; SCHEFFER *et al.*, 2001). Due to their extensive nature, tipping points can vary both in temporal and spatial scales, which in turn are related to the impact that such tipping causes on the overall system (LENTON, 2020) (Figure 11). When imposed on the climate system, the changed future state has the potential to cause large-scale impacts on human and ecological systems (LENTON *et al.*, 2008; RUSSIL and NYSSA, 2009). The idea of tipping points has been the subject of more and more scientific papers since the early 2000s, especially on the subject of 'climate change' (WALKER, 2006).

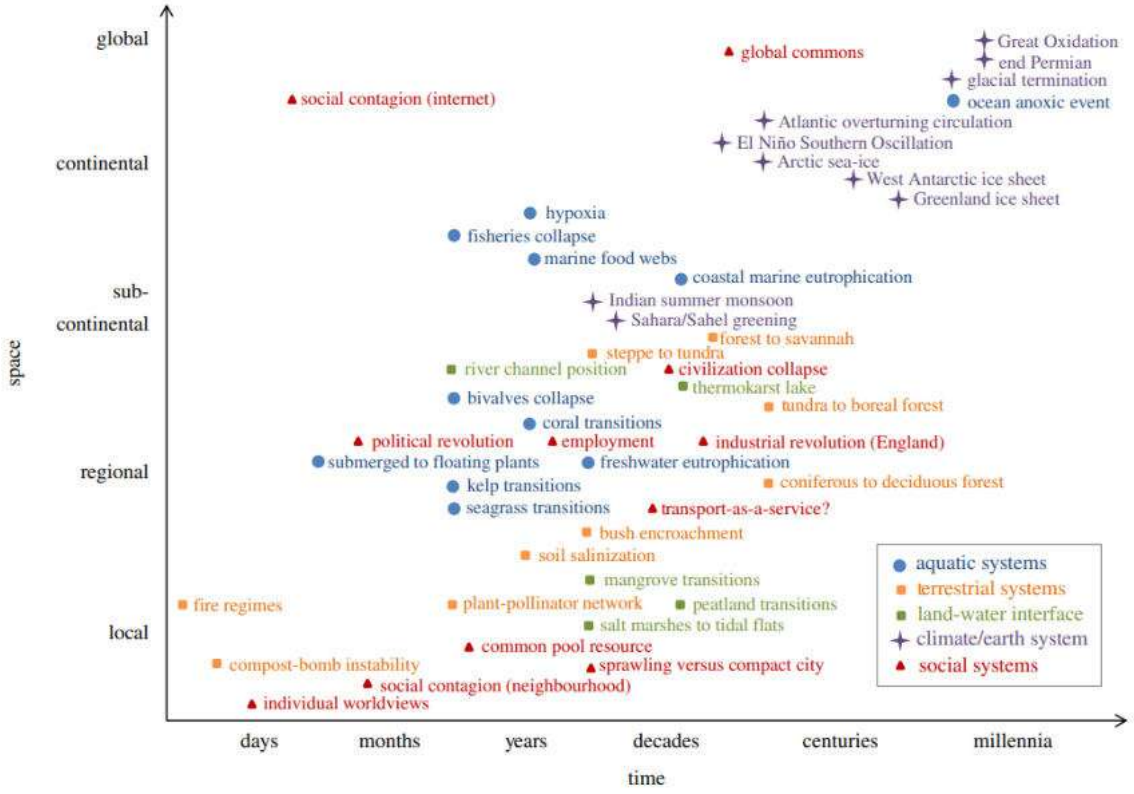

Figure 11: Examples of tipping points distributed by system types on different spatial and temporal scales. Source: LENTON, 2020.

The transition to a new equilibrium after passing a tipping point is not uniform in all cases. According to DRIJFHOUT *et al.* (2015) and LENTON *et al.* (2009), the transition may be faster than the forcing that causes it. In such cases, it is called abrupt climate change. Moreover, there are other cases where this change is slower (LENTON *et al.*, 2008). Still, according to the authors, there are reversible transitions, which the recovery, at the same point where the collapse happened, occurs when the forcing is reversed, and there are the irreversible transitions. LENTON *et al.* (2009) also mention transitions that occur immediately after the tipping point happens and transitions that happen sometime later. This latter type of transition is more challenging to detect (WALKER, 2006). According to (WALKER,

2006), tipping points that depend mainly on physics alone are more straightforward to predict than those involving a biological phenomenon or process. For these, the uncertainties associated with their triggers are even higher.

LENTON *et al.* (2009) also point out that there are cases where the passage through a tipping point is extremely discrete but still with the potential to impact the future. That type would be the case for an infinite order phase transition, where a slight change causes a slight divergence in the system, but the result becomes significantly different than if it did not exist (LENTON *et al.*, 2009, 2008).

As stated earlier, tipping points are moments that mark a transition. This transition occurs with features or processes, which in this case, apply to constituents of the Earth Climate System. In this context, these constituents are called tipping elements and will be described in the following item.

2.4.1 Tipping Elements

Tipping element is defined as the system element that is forced to go through a tipping point and which may be changed under certain circumstances by minor disturbances to a state other than the initial (LENTON *et al.*, 2009, 2008). According to LENTON (2013) and LENTON *et al.* (2008), for an Earth's system subsystem Σ to be considered a tipping element, it must meet some conditions:

1. The subsystem Σ must be associated with a specific region (or set of specific regions) of the globe with an approximate minimum scale of 1000 km.

2. Parameters affecting the system can be combined into a single control ρ. The control includes parameters that change continuously with the potential to modify the subsystem (Σ). This control would have a critical value ρ_{crit} so that a change $\hat{F}$ into a subsystem's feature F depends on whether ρ has exceeded ρ_{crit} with a small disturbance $\delta\rho$ for a period T. That is, forced trajectories, in which a slight deviation above a critical value that continues for some time, will inevitably lead to appreciable changes. The feature of the subsystem and the parameters that control it need not be climatic variables.

3. Influences on Σ are caused by human interference such that decisions made within a 'political time horizon' $T_P > 0$ can determine if ρ_{crit} is reached. This moment occurs at the critical time T_{crit}, usually within T_P.

4. The time to observe a qualitative change plus the trigger time is set in the 'ethical time horizon' T_E so that $T_{crit} + T \leq T_E$. The T_E definition implies that events in the far future may not have the power to influence present-day decisions.

5. The subsystem Σ contributes significantly to the overall mode of operation of the Earth's Climate System, to human well-being, or has great value as a unique biosphere feature.

Considering that transitions after crossing a tipping point have varying velocities, abrupt tipping is considered to be one whose observation time T is very short compared to T_P. Gradual tipping is thus classified when T has the same order of magnitude as T_P, and slow tipping occurs when $T \to T_P$ (LENTON *et al.*, 2008).

Under the conditions set for Σ to be considered a tipping element, LENTON *et al.* (2008) defined some potential tipping elements of political relevance in the climate system due to human influence (Figure 12). Additionally, Table 7 presents the subsystem features for a given element that would be changed, the control parameters and critical values, the time scale of change, and the key impacts after the occurrence of the tipping point. It is important to note that the authors chose these elements based on the consequences that could occur even in the present millennium, excluding those that would have consequences after 2100.

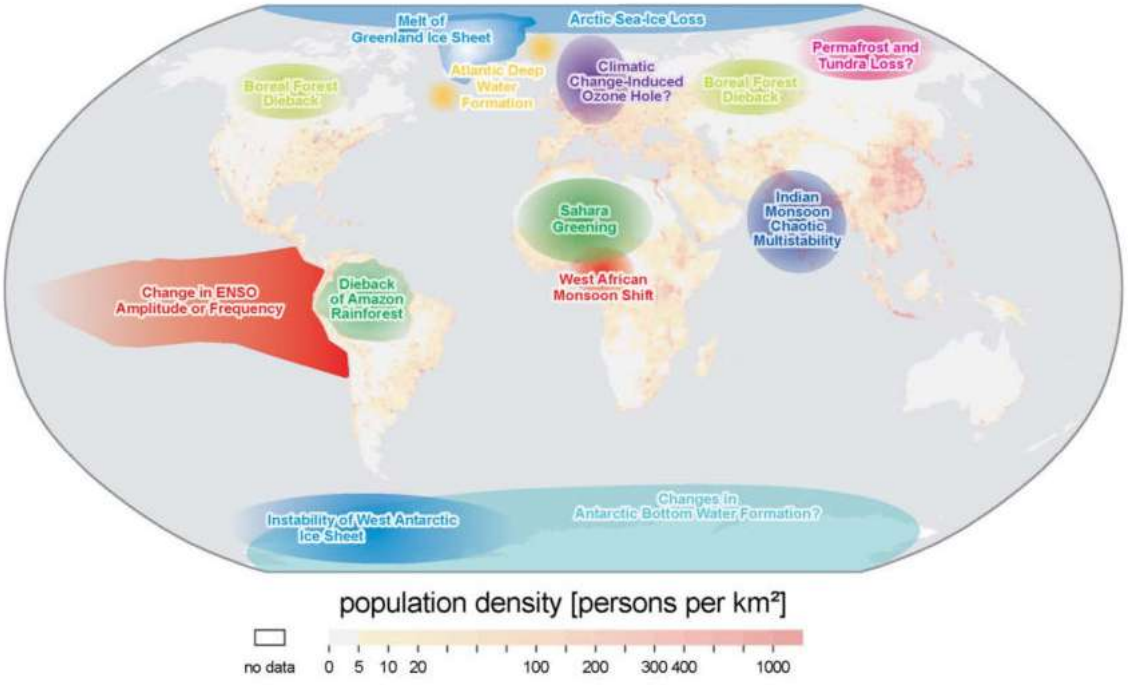

Figure 12: Map of potential future tipping elements of political relevance in the climate system superimposed on population density. The map shows only tipping elements that may pass through a tipping point due to anthropogenic forcing in this century. Question marks indicate the tipping elements whose condition is uncertain. Source: LENTON *et al.*, 2008.

As seen previously, several potential tipping elements are pointed to as of political relevance in the climate system due to anthropogenic forcing. Among them, the element composed by the change in NADW formation (Figure 12)) and the change in AMOC (Thermohaline Circulation - THC) (Table 7) was used as an object of study in this work. The consequences of climate change on AMOC are widely discussed and widespread in the scientific community as in the works of SCHMITTNER (2005); STEWART (2008); WUNSCH (2002), among others. According to STOCKER and WRIGHT (1991), a shutdown of the AMOC and NADW formation can occur if sufficient amounts of freshwater or heat enter the North Atlantic Ocean (NA) in a way that NADW formation is interrupted. LENTON (2013) and LENTON *et al.* (2008) add that with sufficient freshwater insertion into the NA, convection collapses in climate models.

Table 7: Potential future tipping elements of political relevance in the climate system, the features of each one and direction of change, their control parameters and critical values, the global warming necessary to achieve the tipping point, the timescales, and some impacts. 1 Sv = 10^6 $m^3 \cdot s^{-1}$ Source: Modified from LENTON *et al.* 2008.

Tipping Element	**Feature of the System, F (direction of change)**	**Control parameter (s), ρ**	**Critical Value (s), ρ_{crit}**[19]	**Global Warming**[19,20]	**Transition timescale**[19], T	**Key-impacts**
Arctic summer sea ice	Area extent (-)	Local ΔT_{ar}[21], ocean heat transport	Unidentified[22]	+0.5-2°C	≈10yr (rapid)	Amplified warmig, ecosystem change
Greenland ice sheet	Ice volume (-)	Local ΔT_{ar}[21]	+≈3°C	+1-2°C	>300yr (slow)	Sea-level +2-7m
West Antarctic Ice Sheet	Ice volume (-)	Local ΔT_{ar}[21] or less ΔT_{oceano}[23]	+≈5-8°C	+3-5°C	>300yr (slow)	Sea level +5m
Atlantic Thermohaline Circulation	Overturning (-)	Freshwater input to the NA	+0.1-0.5 Sv	+3-5°C	≈100yr (gradual)	Regional cooling, sea level, ITCZ[24]shift
El Niño Southern Oscillation	Amplitude (+)	Thermocline depth, sharpness in East Equatorial Pacific	Unidentified[22]	+3-6°C	≈100yr (gradual)	Drought in SE Asia and elsewhere
Indian summer monsoon	Rainfall (-)	Planetary albedo over India	0.5	N/A	≈1yr (rapid)	Drought, decrease in carrying capacity

Sahara/Sahel and West African monsoon	Vegetation fraction (+)	Precipitation	100mm·yr^{-1}	+3-5°C	≈10yr (rapid)	Increased carrying capacity
Amazon rainforest	Tree fraction (-)	Precipitation, dry season length	1,100mm·yr^{-1}	+3-4°C	≈50yr (gradual)	Biodiversity loss decreased rainfall
Boreal Forest	Tree fraction (-)	Local ΔT_{ar}[21]	+≈7°C	+3-5°C	≈50yr (gradual)	Biome switch
Antarctic Bottom Water	Formation (-)	Precipitation-Evaporation	+100mm·yr^{-1}	Unclear[25]	≈100yr (gradual)	Ocean circulation, carbon storage
Tundra	Tree fraction (-)	Growing degree days above zero	Missing[26]	-	≈100yr (gradual)	Amplified warming, biome switch
Permafrost	Volume (-)	$\Delta T_{permafrost}$	Missing[26]	-	<100yr (gradual)	CH_4 and CO_2 release
Marine Methane hydrates	Hydrate volume (-)	$\Delta T_{sediment}$	Unidentified[22]	Unclear[25]	10^3 to 10^5yr ($>T_E$)	Amplified global warming
Ocean anoxia	Ocean anoxia (+)	Phosphorus input to ocean	+≈20%	Unclear[25]	≈10^4yr ($>T_E$)	Marine mass extinction
Arctic ozone	Column depth (-)	Polar stratospheric cloud formation	195 K	Unclear[25]	<1yr (rapid)	Increased UV at surface

As stated earlier, the IPCC (2013b) points out that the continuous warming of the oceans in the 21st century will result in warming of the entire water column from the surface to the deep ocean, altering global ocean circulation. IPCC (2013b) still discusses the high probability of AMOC weakening over the 21st century and that this weakening would be highly correlated to the inhibition of deep convection, i.e., NADW formation, in high latitudes of the NA (LOZIER *et al.*, 2017; SCHMITTNER, 2005). Estimates based on RCP simulations indicate an average reduction of 11% (range 1-24%) for RCP 2.6 and an average reduction of 34% (range 12-54%) for RCP 8.5.

It is important to mention that, despite the anticipated decline, the IPCC points out that it is possible for an AMOC increase in a few decades due to the great natural variability. Additionally, although AMOC is unlikely to undergo an abrupt transition or collapse in the 21st century - for RCP scenarios - a collapse after this century cannot be disregarded. Deep circulation has the potential to influence climate over time scales of decades, centuries, and millennia, making the ocean the primary cause of climate variability (STEWART, 2008).

2.5 Atlantic Meridional Overturning Circulation

The AMOC is the Atlantic part of the Meridional Overturning Circulation (MOC), a meridional circulation that extends from the Southern Ocean to the NA in which a net northward flow of upper warm waters (thermocline and intermediate layers) are compensated by a net southward flow of deep cold waters – the southward flow of NADW (item 2.5.1) (BROECKER, 1987, 1997; FRAJKA-WILLIAMS *et al.*, 2019; GREGORY *et al.*, 2005; JOHNSON *et al.*, 2019; MANABE and STOUFFER, 1999; RAPID, 2019; SROKOSZ *et al.*, 2012; STAMMER *et al.*, 2002; STOUFFER *et al.*, 2006, 2007; TALLEY *et al.*, 2011; WALKER, 2006; WUNSCH, 2002). In the 1980s (COLLING, 1989), Wallace Broecker suggested the MOC diagram in which the author proposes the NADW formation as a trigger mechanism for this circulation (BROECKER, 1991; COLLING, 1989; STOCKER and WRIGHT, 1991). Coupled ocean-sea ice models show a link between AMOC intensification and an increase in

[19] Preliminary numbers and derivative from specialists evaluations.

[20] Global mean temperature change above present (1980 –1999).

[21] $\Delta T_{ar} \rightarrow$ air temperature difference.

[22] Theory, model results, or paleo-data suggest the existence of a critical threshold, but a numerical value is lacking in the literature.

[23] $\Delta T_{oceano} \rightarrow$ ocean's temperature difference.

[24] Intertropical Convergence Zone

[25] It can imply that either a global warming range is not established or it is not the only or the dominant forcing.

[26] Meaning no subcontinental scale critical threshold could be identified, even though a local geographical threshold may exist.

deep-water formation in high latitudes of the NA (DANABASOGLU *et al.*, 2016). Hence changes in the NADW formation patterns may have a direct influence on the AMOC.

AMOC is a fundamental component of the climate system. With its northward heat transport over the Atlantic Ocean, AMOC along with the westerlies in that region alleviates the harsh winter in Europe (ANTHOFF *et al.*, 2016; BROECKER, 1987, 1997; JOHNSON *et al.*, 2019; LOZIER *et al.*, 2017; MANABE and STOUFFER, 1999; RAPID, 2019; SROKOSZ *et al.*, 2012; VELLINGA and WOOD, 2002). Additionally, AMOC also plays an essential role in the uptake and distribution of important tracers such as carbon and oxygen (FRAJKA-WILLIAMS *et al.*, 2019; JOHNSON *et al.*, 2019; LOZIER *et al.*, 2017). The upper limb of AMOC hits maximum values of 1.3 PW[27] around 24.5°N, and it represents 25% of the global heat flux (SROKOSZ *et al.*, 2012). These upper waters that reach high latitudes in the North Atlantic are transformed in deeper ones by buoyancy loss due to strong cooling, altering the local ocean stratification (Figure 13) (ANTHOFF *et al.*, 2016; BROECKER, 1991; JOHNSON *et al.*, 2019; POND and PICKARD, 1983; SROKOSZ *et al.*, 2012; TALLEY *et al.*, 2011; WUNSCH, 2002).

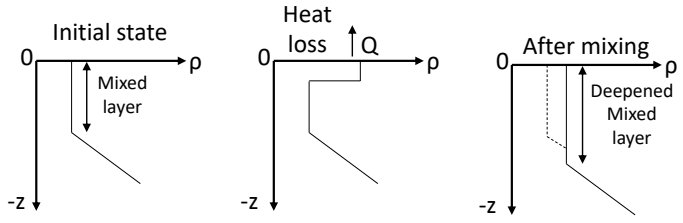

Figure 13: Scheme of the development of deeper mixed layer depth due to heat loss. x-axis represent the ocean density and the y-axis represent the ocean depth. The initial state (left panel) represents a density profile with a mixed layer. Heat loss (center panel) promotes an increase in density of the surface of the mixed layer; buoyancy is lost, which causes this layer to overturn (or convect) to a greater depth. Eventually, this convection mixes a deeper layer, which also gains density (right panel). The opposite can also happen if there is heat gain. Source: Inspired in TALLEY *et al.*, 2011.

Once the deep water masses are formed, and in isopycnal equilibrium, they become isolated from atmospheric ventilation and thus can store energy and chemical compounds for hundreds of years. This isolation gives the ocean the ability to influence climate on several timescales (FRAJKA-WILLIAMS *et al.*, 2019).

As this buoyancy forcing acts directly on the AMOC (JOHNSON *et al.*, 2019; RAHMSTORF, 1995; TALLEY *et al.*, 2011; WUNSCH, 2002), changes in the

[27] 1 W = 1 kg·m^{2}s^{-3} and 1 PW = 10^{15} W.

surface density in high latitudes of the North Atlantic may influence NADW formation and, by consequence, AMOC circulation (TALLEY *et al.*, 2011). STOCKER and WRIGHT (1991) estimate an amount of 0.35Sv of water vapor flowing to the Pacific ocean from high latitudes of NA due to evaporation (BROECKER, 1987). According to the authors, AMOC is not sensitive to this parameter unless it is reduced to values close to 0.03Sv, which would lead to a local lower density. On the other hand, LENTON *et al.* (2008), estimate the value of this evaporation reduction, or, in their case, freshwater input, between 0.1-0.5 Sv.

As a consequence of changes in local density, in the STOCKER and WRIGHT (1991) scenario, the authors identified changes in circulation. In the new equilibrium pattern, deep water is formed only on the Southern ocean. According to the authors, these conditions would be similar to the last glacial maximum. Besides freshwater, other components may alter this circulation, and RAHMSTORF (1995) comments that any sudden change on surface forcing may shut down or generate instabilities in the convection.

Similar to the work of STOCKER and WRIGHT (1991), in the work of MANABE and STOUFFER (1999), the authors, through coupled ocean-atmosphere modeling, add 0.1Sv of freshwater to the NA, between 50°N and 70°N. The fresher surface water prevented convective cooling and weakened the THC, which promoted a shallower upper AMOC cell. The consequences were multiple and not confined in the Atlantic ocean but on other regions, as the Pacific and the Southern oceans, for example.

VELLINGA and WOOD (2002), on the other hand, also performed a freshening experiment in the NA between 50°N and 90°N with a coupled ocean-atmosphere-sea ice-land model but with a salinity input of 2 in the first 800 m, which is equivalent to 16 Sv[28]. The perturbation provoked a shutdown in the THC in the first ten years, along with the northward heat transport and consequent heat release in the North Atlantic region. As in MANABE and STOUFFER (1999), the consequences were not localized in the Atlantic ocean, but they were spread worldwide.

Additionally, studies point out that just an AMOC weakening would have consequences in several climate features. An example would be the tropical rain belts (LOZIER *et al.*, 2017; WALKER, 2006). Any changes in AMOC influence the global climate, the ecosystems, and biogeochemical cycles once these changes alter the oceans' heat, nutrients, and carbon distribution (GANACHAUD and WUNSCH, 2000; SCHMITTNER, 2005). According to GREGORY *et al.* (2005), MANABE and STOUFFER (1999), and STOUFFER *et al.* (2006), a weakening in AMOC, which can be linked to anthropogenic factors, may be related to changes on the moist

[28]The conversion of salinity to freshwater is made considering a reference salinity of 35.

transport towards the poles. Additionally, the increase in high latitudes precipitations and increase in the river runoff, the changes on surface heat fluxes, and the increase of melted ice sheets may also play a role, which would stabilize the water column in deep convection zones.

The work of BAKKER *et al.* (2016) indicates that multiple factors may have a combined effect on AMOC strength. In their study, the authors found that the atmosphere warming and changes in the water cycle have a more significant effect on AMOC than merely the mass loss of the Greenland ice cap. However, this loss, combined with the other factors, significantly increases both the weakening of the AMOC and the likelihood of its collapse under continuous GHG emissions. Still, according to BAKKER *et al.* (2016), a collapse of AMOC means a 90% reduction in its intensity/strength/energy.

It is crucial to clarify that, although sometimes, MOC and THC may be used as synonyms, they are not. THC is the global ocean circulation driven by density differences caused by temperature and salinity. Although density differences trigger the THC, it interacts with wind-driven currents, and they can not be practically separated. MOC is what we determine in practice, the streamfunction on the depth-latitude plane. It includes the wind-driven circulation, and the modeling community widely uses it because it is easy to diagnose.

2.5.1 The North Atlantic Deep Water

The NADW is a water mass formed at high latitudes in the NA that occupies a large portion of the water column (STOCKER and WRIGHT, 1991; STOCKER *et al.*, 1992). Characterized by high salinities and oxygen concentration and low nutrient concentration (BROECKER, 1987, 1991; PICKARD, 1974; REID, 1989; TALLEY *et al.*, 2011), this water mass is the highest dissolved CO_2 reservoir in the ocean (GRUBER *et al.*, 2019; STEWART, 2008). According to BAILEY *et al.* (2005) and POND and PICKARD (1983), the NADW receives significant contributions to its formation from the Arctic ocean and the South Atlantic Ocean. According to COLLING (1989), in high latitudes of the NA, NADW is formed at the cyclonic subpolar gyres in the Labrador Sea and Norwegian and Greenland Seas (Figure 14). Areas also identified by LENTON *et al.* (2008).

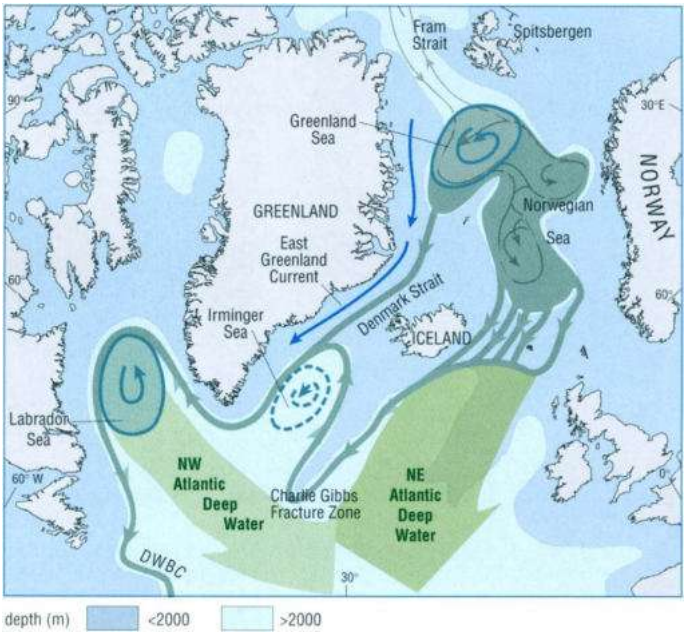

Figure 14: Scheme showing the cyclonic gyres in Labrador and Greenland Seas. The dashed cyclonic gyre is a less important region of deep-water formation in the Irminger Sea. Source: COLLING, 1989.

The NA imports warmer and saline waters from the SA (BAILEY *et al.*, 2005; MANABE and STOUFFER, 1995; PETERSON and STRAMMA, 1991; REID, 1994). On the other hand, the Arctic ocean contributes with cold water and ice to the Greenland Sea, which enters the region through the Fram Strait (grey arrows in Figure 14), and are carried southward in the East Greenland Current (blue arrows in Figure 14) (COLLING, 1989; LIQUE *et al.*, 2018; REID, 1994). This flow forms the western limb of the cyclonic circulation in this region. The eastern limb is formed by the northward Norwegian Current, carrying warm and saline surface waters into the mix (COLLING, 1989). Although negative E-P balance characterizes this region, the saline waters are as a result of sea ice formation (COLLING, 1989).

Once formed by deep convection[29] and reached buoyancy (GRASSL, 2001; TALLEY *et al.*, 2011), the NADW accumulated in the Labrador and Greenland Seas outflows to the NA through some locations. One of them is the Denmark Strait between Iceland and Greenland, and another one is between Iceland and the Faeroe Islands (Figure 14). These regions form the North-East Atlantic Deep Water, and it is the densest NADW formed. The Labrador Sea forms the less dense North-West Atlantic Deep Water (COLLING, 1989; LOZIER *et al.*, 2017; REID, 1994). Mixing these two locations gives rise to the NADW.

After reaching the NA, NADW continues to flow southward towards the SA as Deep Western Boundary Current (DWBC) (Figure 15) (BAILEY *et al.*, 2005;

[29] According to COLLING (1989), deep convection is associated with sea ice formation and cold, dry winds, which promotes evaporation.

COLLING, 1989; LOZIER *et al.*, 2017; STRAMMA and ENGLAND, 1999; TALLEY *et al.*, 2011). Once it flows to the NA, turbulent mixing and entrainment with overlying water ends up changing its characteristics from the origin. According to STRAMMA and ENGLAND (1999), near the Equator, NADW is found between 1200 m and 3900 m and near the Brazil-Malvinas Confluence (BMC) between 1700 m and 3000 m, indicating that it reduces its thickness when flowing southward due to mixing with CDW, which demonstrates these types of change. When NADW reaches latitudes near the Antarctic Circumpolar Current (AACC), it incorporates itself to this current, and it is exported to the Indian and South Pacific oceans (Figure 15) (CLARKE *et al.*, 2001; STRAMMA and ENGLAND, 1999) with an estimate of 15Sv (DONNERS *et al.*, 2005).

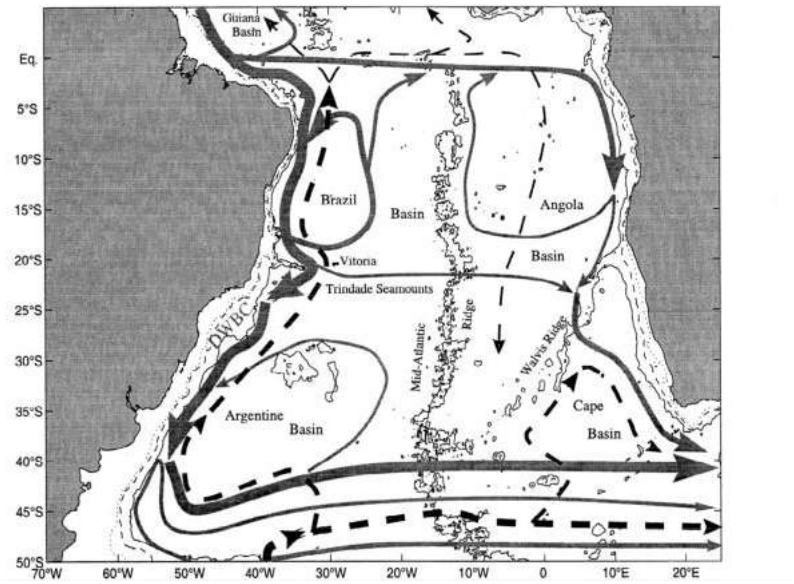

Figure 15: NADW flow diagram near the depth of 2000 meters as the thickest line in the figure. Additionally, AABW's trajectory is represented by the dashed line. Source: STRAMMA and ENGLAND, 1999.

2.5.2 Efforts for the AMOC Monitoring

Observe and measure AMOC is a challenge since these observations would have to cover an extensive area. In their work, MCCARTHY *et al.* (2015) review the AMOC measurement attempts. The overturning circulation presented variations over the years, using the precept that ice ages decrease this overturning, and ice core analysis indicates temperature variations of the order of 10°C at decadal to centennial scales. Based on that idea, the authors and FRAJKA-WILLIAMS *et al.* (2019) point out that this circulation must be measured continuously. Still, according to the authors and RAPID-AMOC (2019), monitoring would be essential both to quantify variability on sub-annual to annual scales and to assess the existence of

long term trends in the circulation and thus to try to identify tipping points on it.

That way, some programs were created to measure AMOC through its meridional volume transport - some also measure heat, freshwater, and carbon transport (FRAJKA-WILLIAMS *et al.*, 2019) - and represent an observing system of it along the Atlantic Ocean. As stated above, monitoring the AMOC is essential to understand its behavior in multiple temporal scales, once AMOC directly impacts the global climate. These programs have been diagnosing the origins and transport variability and investigating impacts of that variability on climate variables such as sea surface temperature and coastal sea level (FRAJKA-WILLIAMS *et al.*, 2019). The data from these programs are available, were used to enrich the discussions of this current work and will be described in the following items. Additionally, their geographical locations are shown in Figure 16.

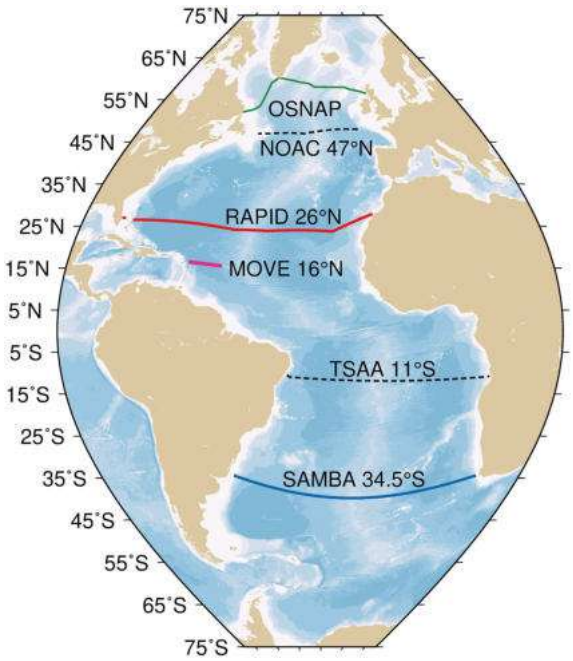

Figure 16: Scheme of the locations of arrays monitoring AMOC. Source: FRAJKA-WILLIAMS *et al.*, 2019.

As seen in Figure 16, there are a few programs that monitor AMOC on the Atlantic Ocean. It is relevant to notice that the arrays are not normalized between each other, meaning that they do not necessarily use the same equipment and sensors, or have the same length. Additionally, in each location, the ocean dynamic is different, and thus the methodology for estimating AMOC may vary substantially. On top of that, each program has its purpose, which can be different from each other. Table 8 displays the period of each program data and its corresponding mean and standard deviation values. The values were calculated through the time series of the data from each program.

Table 8: Some statistics for the AMOC measurements by each program. The bold letters next to the average transport values indicate the direction: N - northward or S - southward. STD stands for standard deviation.

	Time Period	Mean (Sv)	STD (Sv)
OSNAP[30]	Jul 2014-Apr 2016	8.03 **N**	2.65
RAPID[31]	Apr 2004-Sep 2018	6.44 **N**	2.87
MOVE[32]	Jan 2000-Jun 2018	17.49 **S**	5.08
SAMBA[33]	Mar 2009-Apr 2017	14.70 **N**	8.33

2.5.2.1 The OSNAP Program

The subpolar North Atlantic is characterized by an uneven cyclonic circulation that emits some "lobes" to fill out the gaps between landmasses located there (Figure 17). As a result, the complexities of this region require observations with high horizontal resolution. Circulation is usually full-depth since the transports are mostly barotropic (FRAJKA-WILLIAMS *et al.*, 2019). There is a significant overturning component in the horizontal circulation as the water masses gain density on their transformation path.

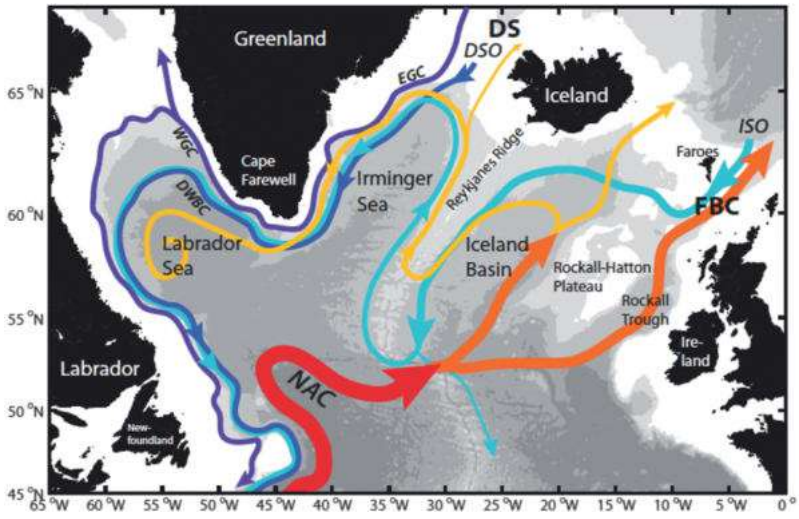

Figure 17: Scheme of the significant water pathways forming the North Atlantic Sub-polar Gyre. Warm waters are represented by red, orange, and yellow colors and cold ones by purple and shades of blue. DS: Denmark Strait, FBC: Faroe Bank Channel, EGC, and WGC: East and West Greenland Currents, respectively, NAC: North Atlantic Current, DSO: Denmark Strait Overflow and ISO: Iceland-Scotland Overflow. Source: LOZIER *et al.*, 2017.

[30] Overturning in the Subpolar North Atlantic Program

[31] Measuring interannual variability of the AMOC and meridional ocean heat transport at 26.5°N: The RAPID-MOCHA Array

[32] Meridional Overturning Variability Experiment

[33] South Atlantic MOC Basin-wide Array

The OSNAP Program consists of two sections, on the west and east of Greenland (Figures 16 and 18), and also includes floats and glider surveys. The west part crosses the Labrador Sea from 53°N to 60°N and the east one lengths from 60°N to the Scottish shelf at 57°N passing through Reykjanes Ridge (connecting the south of Iceland to the Mid-Atlantic Ridge) and the Rockall Plateau (west of Ireland) (FRAJKA-WILLIAMS *et al.*, 2019). The full array is active since 2014, and the first recovery was made 21 months later in 2016 (FRAJKA-WILLIAMS *et al.*, 2019).

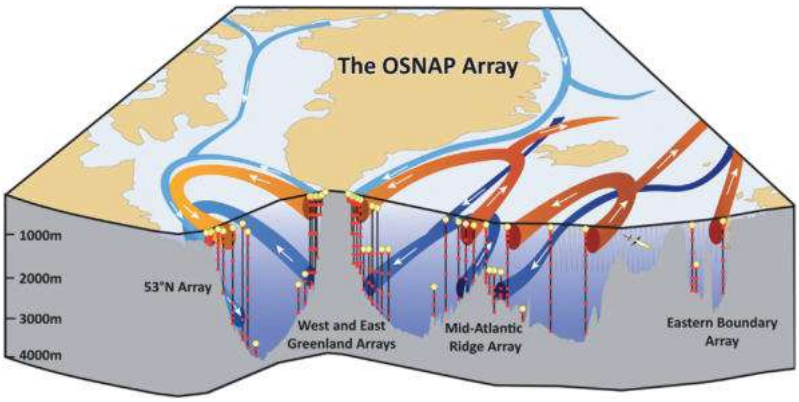

Figure 18: Scheme of OSNAP array. The thin vertical grey lines represent the glider survey path. The red paths represent warm saline waters from the subtropics, the light blue ones represent fresh cold surface waters from the pole, and dark blue paths are deep waters originated in high-latitude North Atlantic and the Arctic. Source: LOZIER *et al.*, 2017.

Figure 19 represents the AMOC time series integrated on the water column from OSNAP (LOZIER *et al.*, 2019). The AMOC displays positive values throughout the series, and its mean and standard deviation values are exposed in Table 8. Although exhibiting mean values around 8Sv, we observe higher values between April and August 2015. These occasional higher values may be related to some event that caused this variability, but the time series is too short (less than two years) to be sure.

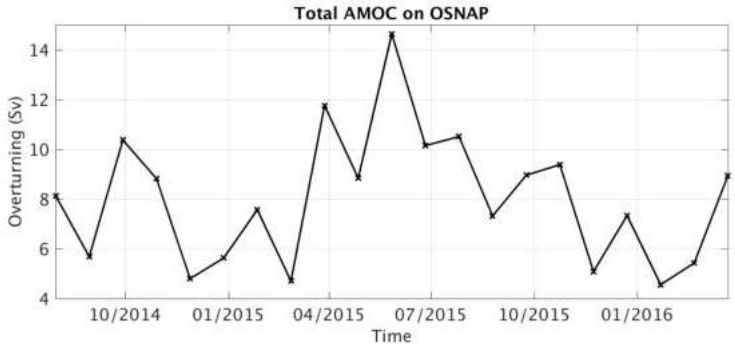

Figure 19: Zonally and vertically averaged time series of the total AMOC values on OSNAP moorings.

2.5.2.2 The RAPID Program

Sparse observations and the potential impacts that a change in the AMOC could have were the beginning of a process that culminated in the RAPID program. The program, in which the National Oceanic and Atmospheric Administration (NOAA) and the Western Boundary Time Series (WBTS) also participate as the RAPID/NOAA/WBTS program, consists of the family of RAPID programs. It is funded by the Natural Environment Research Council (NERC), by the National Science Foundation-funded Southern Overturning Circulation Heat-flux Array project and by NOAA, which funded the WBTS project (MCCARTHY *et al.*, 2015).

The main objective of RAPID is to develop and maintain a system that continually observes the strength and structure of AMOC (RAPID, 2019). It comprises a series of moorings on the 26.5°N parallel extending from Morocco to Florida (Figures 16 and 20), measuring temperature, salinity, and velocity of currents from near the surface to the bottom (LOZIER *et al.*, 2017; RAPID-AMOC, 2019). The program consists of three interconnected projects:

- In March 2004, 19 moorings were installed across the Atlantic at the latitude of 26.5°N to measure the southern branch of MOC (CUNNINGHAM *et al.*, 2007; FRAJKA-WILLIAMS *et al.*, 2019; MCCARTHY *et al.*, 2015; RAPID, 2019).

- Through the Southern Overturning Circulation and Heatflux Array (MOCHA) project, additional moorings were placed on the western contour, also along the 26.5°N parallel in order to solve the DWBC transport (JOHNS *et al.*, 2008; RAPID, 2019), formed by NADW. With additional moorings, density profiles could be monitored over the entire basin, from the western boundary through the Mid-Atlantic Ridge to the eastern boundary, allowing continuous measurement of the transatlantic pressure gradient (RAPID, 2019).

- Dr. Molly Baringer of Atlantic Oceanographic and Meteorological Laboratory (NOAA/AOML) leads the monitoring of the northward MOC branch through submarine telephone cables in the Florida Strait (BARINGER and LARSEN, 2001; FRAJKA-WILLIAMS *et al.*, 2019; RAPID, 2019).

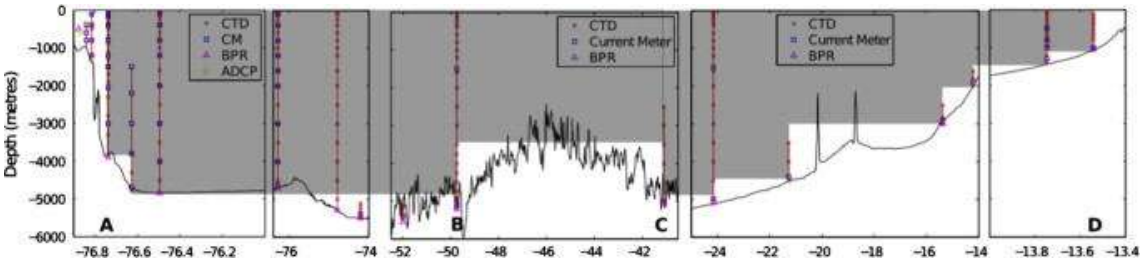

Figure 20: Scheme of the moorings deployed in October 2012. A, B, C, and D refer respectively to the western, the Mid-Atlantic Ridge west, the Mid-Atlantic Ridge east, and eastern boundary arrays. Source: MCCARTHY *et al.*, 2015.

On that region of RAPID, the ocean circulation is dominated by an anticyclonic gyre, a 1000m-deep western boundary current confined between Florida and Bahamas, and the southward flow of NADW between 1000 m and 5000 m of depth (FRAJKA-WILLIAMS *et al.*, 2019). Below the NADW and west of the Mid-Atlantic Ridge, there is a northward flow of 1-3 Sv of AABW (FRAJKA-WILLIAMS *et al.*, 2011). Although the array of moorings is quite extensive, some regions are not sampled; e.g., the waters above 1000m on the eastern boundary, deep waters east of EB1 mooring - located at 24°W meridian - and either side of the Mid-Atlantic Ridge. Also, the waters shallower than 100m are often unsampled (FRAJKA-WILLIAMS *et al.*, 2019).

Since its beginning until 2012, the mooring's array was reclaimed and redeployed annually. Since 2012, this maintenance is done every 18 months (FRAJKA-WILLIAMS *et al.*, 2019; RAPID, 2019). Already in the first year of registration, it was noted that there is great MOC variability even on sub-annual scales (CUNNINGHAM *et al.*, 2007). Following the first phase from 2004 to 2008, RAPID was funded until 2014 under RAPID-WATCH to provide a long and unique MOC (RAPID-WATCH, 2012) time series. The program is currently funded under RAPID-AMOC until 2020 (FRAJKA-WILLIAMS *et al.*, 2019; RAPID, 2019; RAPID-AMOC, 2019). According to LOZIER *et al.* (2017), the RAPID program was a landmark for the science community. However, some model studies suggest that AMOC fluctuations over interannual time scales showed coherence only over limited distances.

2.5.2.2.1 Methodology for AMOC Estimation

According to the descriptions on the RAPID (2019) website, the methodology for estimating MOC flow over 26.5°N can be obtained by decomposing it into three components (more details in MCCARTHY *et al.* (2015)):

- The transport across the Florida Strait.
- The flow induced by the interaction between the wind and the ocean surface (Ekman Transport).
- The transport related to the difference in the density of seawater between the American and African continents.

Transport across the Florida Strait

Figure 21 outlines how currents in the Florida Strait are monitored via submarine telephone cables. The northward flow of the Florida Current (T) conducts electricity because of the salinity in the water. As charged particles in the water pass through the Earth's magnetic field (B), an electric field is generated, which induces voltage (U) in the telephone cables that cross the region. By performing a calibration, this induced voltage can be used as a continuous indicator of ocean current intensity across the strait.

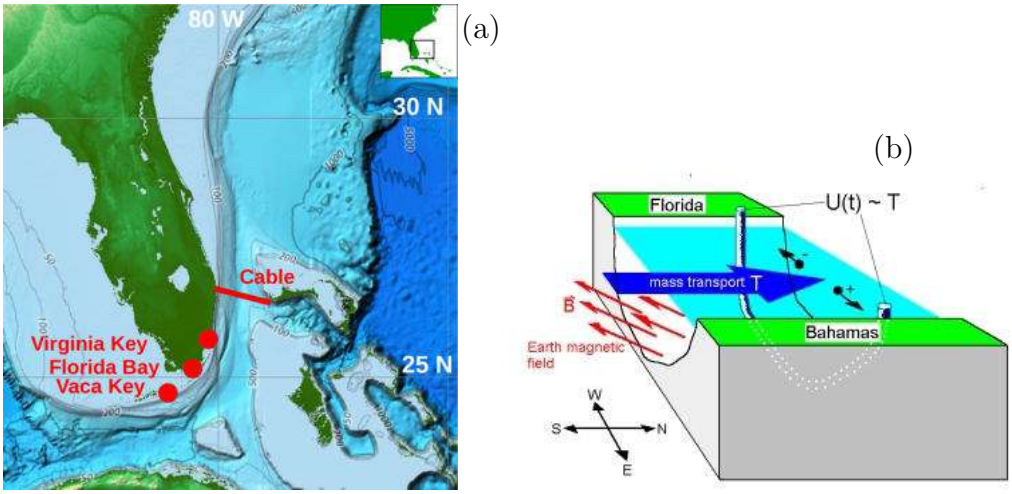

Figure 21: (a) Florida Strait's location and (b) Scheme of the Florida Strait currents monitored using submarine telephone cables. Source: Composed and modified from PARK and SWEET, 2015; NOAA-AOML, 2019 and RAPID, 2019.

Ekman transport

Wind stress acting on the ocean surface generates a southern (north-south) Ekman transport (Figure 22) typically confined to the first 50 m of the ocean. In the 26°N parallel, the contribution of Ekman transport to MOC is relatively small, representing about 2-4 Sv on average; however, it is responsible for the more

significant variability of the short time in the sub-annual scale. In RAPID, winds are estimated using satellite and ship measurements.

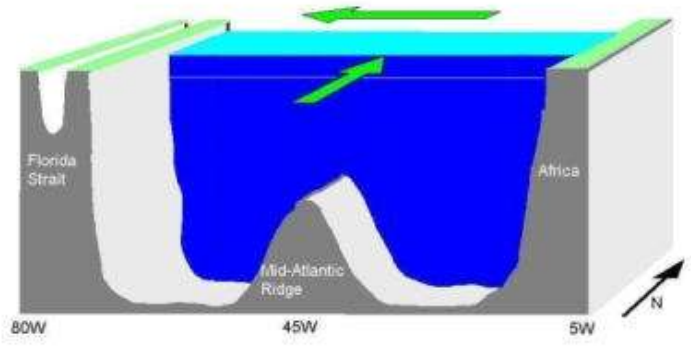

Figure 22: Scheme of wind stress acting on the ocean surface and Ekman transport. Source: RAPID, 2019.

Density transport

Assuming we know the vertical density profile at two distinct points, then the vertical change in the meridional flow between these two points can be estimated (Figure 23). As stated earlier, one of the aims of RAPID moorings array is to measure vertical density profiles at different longitudes between the Bahamas and the African continent. Differences in these profiles allow estimating the velocity of currents in parallel 26.5°N.

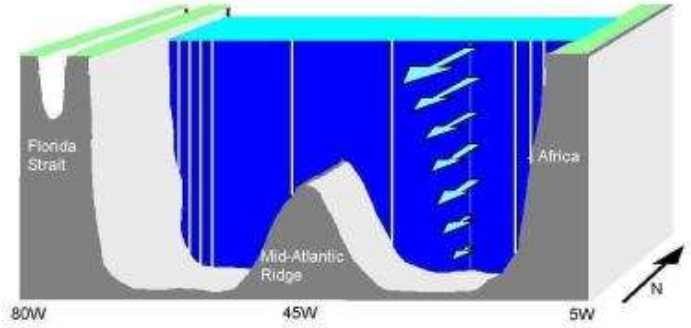

Figure 23: Scheme of the meridional flow change profile at 26.5°N. Source: RAPID, 2019.

AMOC calculation

Finally, a combination of the above items (density, Ekman, and cross-Florida Strait transports) (Figure 24) gives us a rough estimate of the meridional

velocity across the 26.5°N parallel. Often, the meridional mass transport calculated is not zero, and, in order to obtain a MOC estimate, a spatial (but not temporal) constant correction is applied to the velocity field.

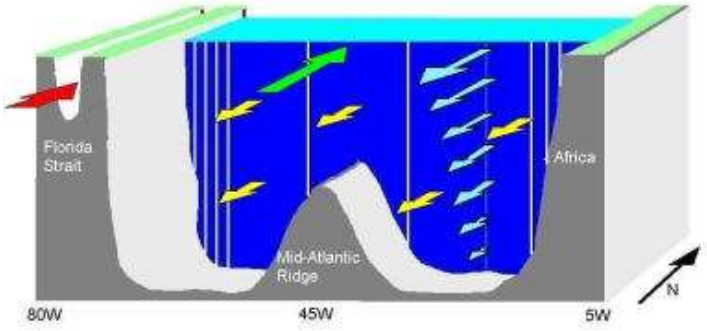

Figure 24: Scheme of MOC transport through the 26.5°N parallel. The red arrow represents the Florida Strait transport, the green one the Ekman transport, the blue arrows are related to the induced density transport, and the yellow arrows represent the correction made to the velocity. Source: RAPID, 2019.

Figure 25 represents the AMOC time series (a) integrated on the water column and (b) a depth profile from RAPID (SMEE *et al.*, 2019). It can be seen that the AMOC integrated on the water column is positive and has mean and standard deviation values as exposed in Table 8. For the profile (Figure 25(b)), we generally see positive values associated with northward transports from the surface until deep depths and negative values associated with southward transports below them. Occasionally southward transports are captured from the surface to the bottom, and it can be associated with events of AMOC variability over time.

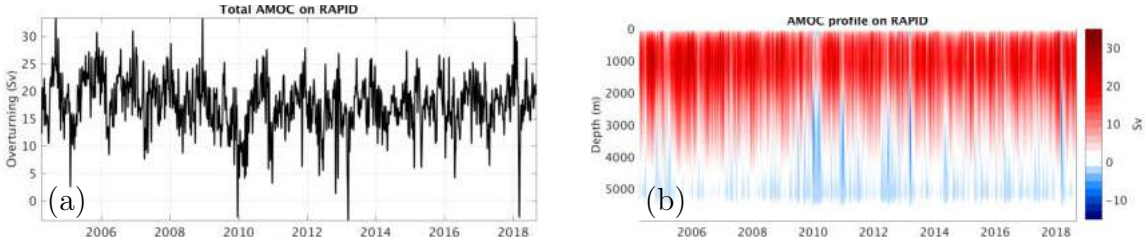

Figure 25: Zonally averaged time series of the (a) total and (b) profile AMOC values on RAPID moorings.

2.5.2.3 The MOVE Program

One observation system that is not full basin covered but was created to sample time-varying AMOC is the MOVE Program. It extends on the 16°N

parallel from east of Guadaloupe (60.5°W) to the west of the Mid-Atlantic ridge (51.5°W) (FRAJKA-WILLIAMS *et al.*, 2019). That region is where most of the overturning circulation flow takes place, and it is dynamically characterized by the DWBC flowing southward, northward flowing of AABW - mainly on the west of the Mid-Atlantic Ridge and episodic northward eddies from the Antilles islands (FRAJKA-WILLIAMS *et al.*, 2019).

The first MOVE deployments were in the early 2000s, and it has been in operation since then, with its funding been renewing annually. The earlier moorings measured only below 1000m, but the recently deployed moorings are full height, extending until 100m of the surface (FRAJKA-WILLIAMS *et al.*, 2019). It is important to mention that the MOVE array was designed to measure the overturning variability instead of its absolute value.

Figure 26 represents the total ocean volume transport across the MOVE line in the depth layer defined by pressures between 1200 and 4950 dbar[34], which would represent the NADW flow. The transport is southward, and the values are in agreement with the literature (DONNERS *et al.*, 2005; STRAMMA and ENGLAND, 1999). There are some gaps throughout the series that probably represent temporary interruptions of data acquisition.

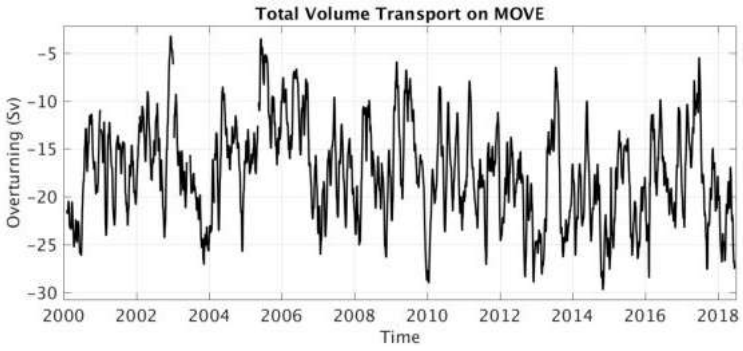

Figure 26: Zonally averaged time series of the total ocean volume transport across the MOVE section between 1200 and 4950 dbar.

2.5.2.4 The SAMBA Program

The South Atlantic ocean is home to several important features, and some of them rely on the passages between ocean basins, as the Africa-Antarctic passage, for example. Through this passage, the AACC provides an enormous mass exchange between the South Atlantic and the Indian basins (CLARKE *et al.*, 2001; FRAJKA-WILLIAMS *et al.*, 2019; STRAMMA and ENGLAND, 1999). In turn, the Indian Ocean exports warm and saline waters to the South Atlantic through the Agulhas Leakage and these waters are exported to the NA and have the potential

[34] 1 dbar = 10^{-1} bar.

to impact AMOC (ANSORGE *et al.*, 2014; BEAL *et al.*, 2011; BIASTOCH *et al.*, 2009; GORDON, 2003; PETERSON and STRAMMA, 1991; REID, 1989; TALLEY *et al.*, 2011). That way, the need to monitor AMOC in the South Atlantic as well is related to understand its variability in this region and its sources (MEINEN *et al.*, 2018).

With that in mind, SAMBA was thought to monitor the western and eastern boundary regions of the South Atlantic at the 34.5°S parallel (ANSORGE *et al.*, 2014; MEINEN *et al.*, 2013) (Figure 27). West SAMBA was first moored offshore of South America (ANSORGE *et al.*, 2014; FRAJKA-WILLIAMS *et al.*, 2019; MEINEN *et al.*, 2013). In 2012, more instruments were set in order to improve horizontal resolution, and in 2013, the array was extended until the Brazilian upper continental slope (ANSORGE *et al.*, 2014; FRAJKA-WILLIAMS *et al.*, 2019). Several entities represent the project; the one in Brazil is Prof. Dr. Edmo Campos from Universidade de São Paulo (USP). On the eastern side of the South Atlantic basin, offshore of Africa, a set of arrays was installed from 2008 until 2010 (FRAJKA-WILLIAMS *et al.*, 2019). These moorings were extended in 2013 from the Walvis Ridge to the South African coast (ANSORGE *et al.*, 2014; FRAJKA-WILLIAMS *et al.*, 2019).

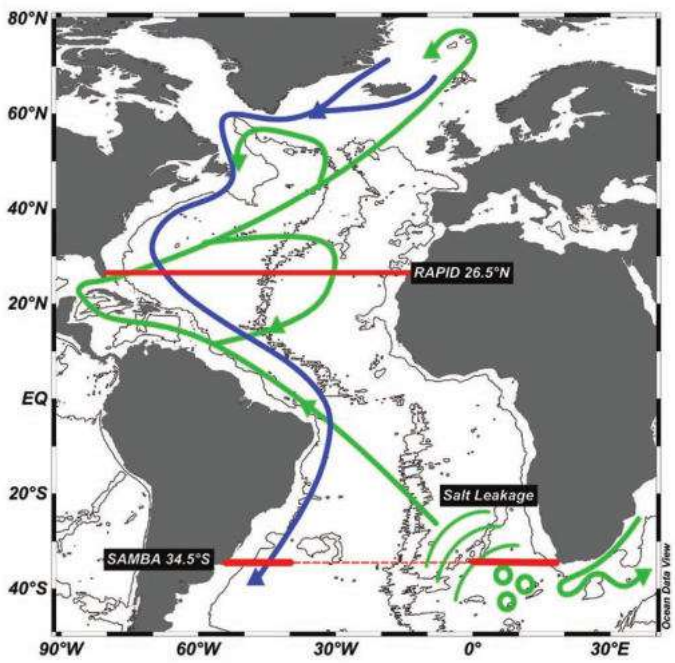

Figure 27: A simplified scheme of the AMOC with the RAPID and SAMBA arrays represented by the red lines. The green and blue lines represent the AMOC. Source: ANSORGE *et al.*, 2014.

The methodology for the AMOC estimation (see details on (FRAJKA-WILLIAMS *et al.*, 2019)) provides only the time-variability of it instead of the

observational mean. Additionally, the parallel where the array is set is a highly variable region, with western and eastern boundary currents and a diverse of timescales (MEINEN *et al.*, 2018). Figure 28 represents the total MOC volume transport for the SAMBA Program located on either side of the basin close to the 1,350 dbar isobath (MEINEN *et al.*, 2018). The transport is northward for most of the series due to the components acting from the surface until the level pressure mentioned. There is a large gap between 2011 and late 2013 that probably represents an interruption of data acquisition.

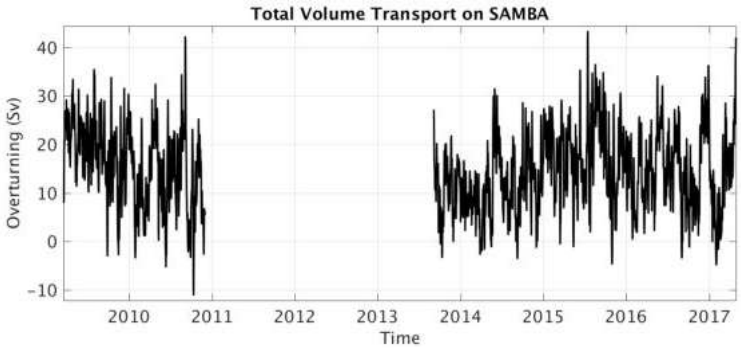

Figure 28: Zonally averaged time series of the MOC volume transport across 34.5°S for the SAMBA Program.

2.6 Sea ice

Ice found in the sea can be originated from two sources: blocks from the glaciers and freezing seawater (PICKARD, 1974). This latter source represents most of the ice found in the sea, and it is called sea ice (HARTMANN, 1994). The first stage of freezing seawater is characterized by forming a mixture of water with already formed ice crystals, called frazil (DELWORTH *et al.*, 2006; PICKARD, 1974). As the crystals grow, they retain salt-saturated portions of water, with salinity ranging from 5 to 15. These portions are called brine (DELWORTH *et al.*, 2006; LIQUE *et al.*, 2018; PICKARD, 1974).

For the formation of sea ice, the freezing point of seawater goes from 0°C to -1.91°C with a salinity of 35, and the sea ice has a higher density than pure ice, reaching 924 kg·m^{-3} (PICKARD, 1974). The amount of salt in sea ice is directly proportional to its formation rate. This velocity is favored under conditions of low salinity, poor mixing due to currents and wind, shallow depths, and previous ice presence, which alleviates ocean turbulence (PICKARD, 1974).

2.6.1 Sea Ice Terminology

According to the National Snow and Ice Data Center (NSIDC), sea ice is described by its area of coverage, thickness, age, and movement according to weather patterns, wind, and current. The study of sea ice by remote sensing is accomplished, employing pixels or grid cells. The same approach is used in numerical model studies since space is discretized in cells of a given resolution. The sea ice concentration parameter, a prognostic variable of the CESM sea ice model CICE (item 3.1.4), will be conceptualized below based on the NSIDC.

Sea ice concentration is a unitless term, but typically described as a percentage and can be defined as the amount of area covered by ice compared to a given area, which in numerical modeling refers to grid resolution. Regions with a value of 0 represent areas without ice, and regions with a value of 100% represent areas entirely covered by ice. Values between 0 and 100% indicate, in the case of numerical modeling, the percentage of the grid covered by ice. Figure 29 presents, in a simplified manner, how the calculation of sea ice concentration is performed. If the cell is divided into a given amount of equal parts, the concentration of sea ice will be equal to the number of parts with ice divided by the total number of cells.

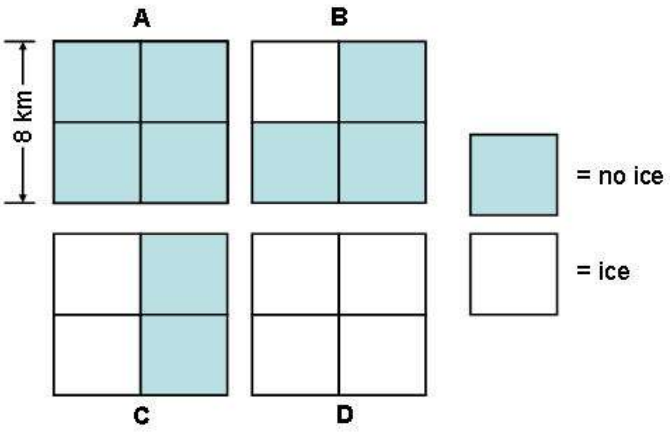

Figure 29: Schematic representation of how the calculation of sea ice concentration is performed. At 'A', the concentration would be 0%, at 'B' would be 25%, at 'C' would be 50%, and at 'D' would be 100%. Source: NSIDC, 2018.

Chapter 3

Methodology

This work made use of results from a coupled earth system numerical model as a method to evaluate the potential of a rupture of AMOC and NADW patterns in the Earth Climate System from the CO_2 increase as a forcing. The model is one of the state-of-the-art Earth System models and has been used recurrently in the IPCC reports. The following sections will present the model description and its components, the experiments chosen to be used, the observed data and reanalysis products that aid the analysis, and the methodology applied in the results, which followed the works of LENTON *et al.* (2008) and BAKKER *et al.* (2016).

3.1 The CESM

CESM (HURRELL *et al.*, 2013) results were used in this study, once this model is one of the best Earth System models that exist nowadays (KNUTTI *et al.*, 2013). CESM was developed as part of a project sponsored by the National Science Foundation (NSF) and the Department of Energy (DOE), and it is administered by the Climate and Global Dynamics Laboratory (CGD) and the National Center for Atmospheric Research (NCAR). This project aimed to develop a climate model that can be used to understand climate and climate change. The design of the model aims to identify and model the physical, chemical, and human components that govern the climate system and the intrinsic feedback system on time scales of hundreds of years or more. According to IPCC (2013b) and KIRTMAN *et al.* (2013), Earth System Models (ESMs) are climate models that include the carbon cycle and simulate the global pattern of CO_2 flows between the ocean and the atmosphere, releasing gases in the tropics and absorbing them at medium and high latitudes (EYRING *et al.*, 2016).

The experiments performed with CESM used five components that represent the elements of the climate system (BOGENSCHUTZ *et al.*, 2018; CRAIG *et al.*, 2012; HURRELL *et al.*, 2013). They are the atmosphere, land, sea ice, ocean,

and river transport. Interactions between components, i.e., exchanges of geophysical flows through each component, are performed through a central coupler (BOGENSCHUTZ *et al.*, 2018; CRAIG *et al.*, 2012; HURRELL *et al.*, 2013; RANGEL, 2019), called CPL7 (CRAIG *et al.*, 2012). According to (CRAIG *et al.*, 2012), the coupler aims to establish communication between the components of the model, interpolating data from different grids, merging fields, and producing diagnostics. Components can be coupled in various configurations, depending on the desired purpose. The results obtained here were simulated with all of five components, which will be described in the following items with an emphasis on the oceanic component, on which the results were focused.

3.1.1 CAM

The Community Atmosphere Model (CAM) is the model component that simulates the atmosphere on a global and climate scale. It was developed by scientists participating in the Atmospheric Working Group (AWG) (NEALE *et al.*, 2010). This working group is formed by NCAR's scientists and technicians, members of the academic community in general, and government laboratories (RANGEL, 2019). CAM6 is the seventh generation of the NCAR atmospheric General Circulation Model (GCM). This version is the first to be able to simulate the process of cloud droplet formation activated by aerosols and precipitation processes due to the size of the condensation nuclei and the interaction between cloud particles in an explicit way (RANGEL, 2019).

The model is discretized horizontally in a finite volume scheme (DANABASOGLU *et al.*, 2020; NEALE *et al.*, 2010; RANGEL, 2019). This scheme was initially developed and used at the National Aeronautics and Space Administration (NASA) Data Assimilation Office (DAO) for a variety of types of simulations (DANABASOGLU *et al.*, 2020; NEALE *et al.*, 2010). Vertically, CAM6 is discretized with a Lagrangian mapping that works as the *eta* coordinate (DANABASOGLU *et al.*, 2020; NEALE *et al.*, 2010). The workhorse resolution of CAM is the nominal 1°[35] with 32 vertical levels.

CAM has three more configurations; the CAM-CHEM, with the addition of the Model for Ozone And Related Chemical Tracers (MOZART) mechanism. The other two configurations are high top models - CAM has its top at 3.6 hPa -; the Whole Atmosphere Community Climate Model (WACCM), which is CAM with 70 vertical levels with a top model at $6{\cdot}10^{-6}$hPa, and the WACCM-X, which is WACCM with thermosphere and ionosphere extensions (DANABASOGLU *et al.*, 2020).

[35] More details in section 3.2.

3.1.2 CLM

The Community Land Model (CLM) is the land model of CESM (LAWRENCE *et al.*, 2020, 2019; OLESON *et al.*, 2004, 2010) that evaluates the physical, chemical, and biological processes in which the land ecosystems interact with climate. It was developed as an effort by the NCAR's Land Model Working Group (LMWG) to expand NCAR's Land Surface Model (NCAR LSM) (LAWRENCE *et al.*, 2020, 2019; OLESON *et al.*, 2010). It includes a prognostic Carbon-Nitrogen model, and several land uses, including anthropogenic land use (DANABASOGLU *et al.*, 2020; LAWRENCE *et al.*, 2020, 2019; OLESON *et al.*, 2010).

In CLM, spatial land surface heterogeneity is represented in a hierarchy where grid cells are composed of multiple land units, snow or soil columns and plant functional types (PFTs) (HURRELL *et al.*, 2013; LAWRENCE *et al.*, 2020, 2019; OLESON *et al.*, 2010). According to the authors, the land unit is designed to represent large spatial patterns as a glacier, lake, wetland, urban, or vegetated. Still, each land unit can be further characterized; the vegetated land unit may be described as natural or managed (e.g., crops). On the other way, the urban land unit may be categorized into classes such as city core, industrial or commercial, and suburban. At the second hierarchical level, the columns are intended to identify variabilities in the soil and snow states within a land unit. The columns in a vegetated land unit, for example, could exhibit independently vertical profiles of temperature, or the managed vegetation land unit could have two different columns; irrigated and non-irrigated. Finally, 16 PFTs are designed to differentiate broad categories of plants by their biogeophysical and biogeochemical functional characteristics.

When in coupled simulations, CLM uses the same horizontal discretization and resolution used in CAM, and it has 25 vertical levels. The current state of the atmosphere is used to force the land model that calculates the surface energy, radiative fluxes, and others (LAWRENCE *et al.*, 2020; OLESON *et al.*, 2010). Then, parameters as the soil and snow hydrologic states and the albedo are passed to the atmospheric model through the coupler (LAWRENCE *et al.*, 2020; OLESON *et al.*, 2010).

3.1.3 MOSART

The Model for Scale Adaptative River Transport (MOSART) is the river transport model in CESM, and its main objective is to provide freshwater input data for the ocean model in coupled simulations (LAWRENCE *et al.*, 2020, 2019). It is adaptative because it was developed to be used for local, regional e even global scales (LI *et al.*, 2013). In CESM workhorse, MOSART is used with a $^1/_2^\circ$ of horizontal

resolution (DANABASOGLU *et al.*, 2020; LAWRENCE *et al.*, 2020). MOSART receives surface and subsurface runoff from CLM (LAWRENCE *et al.*, 2019). It is capable of simulating flooding, and it represents wetlands, capturing these land units from CLM through a prognostic surface water storage (LAWRENCE *et al.*, 2019).

The model divides each grid or watershed into three categories of hydrologic units, the hillslopes, that convert surface or subsurface into tributaries, the tributaries that discharge into a single main channel, and the main channel that connects the local spatial unit with the upstream/downstream units through the river network (LAWRENCE *et al.*, 2020, 2019; LI *et al.*, 2013). For spatial units that are sufficiently large, i.e., the river network consists of more than one reach, the major reach of the network can be treated as the main channel (LI *et al.*, 2013). MOSART assumes that all the tributaries within a spatial unit, which can be a lat/lon grid or a watershed, can be treated as a single hypothetical sub-network channel with a transport capacity equivalent to all the tributaries combined (LAWRENCE *et al.*, 2020, 2019; LI *et al.*, 2013). According to the authors, three runoff routing processes across a spatial unit are represented in MOSART.

1. Hillslope to the tributaries: in each spatial unit, surface runoff is routed as overland flow into the sub-network channel (tributaries), while subsurface runoff generated in the spatial unit directly enters the sub-network channel;

2. Sub-network channel to the main channel: the sub-network channel (tributaries) receives water from the hillslopes, routes water through the channel and discharges it into the main channel;

3. Main channel: the main channel receives water from the sub-network (tributaries) channel within the spatial unit or water routed, if any, from the upstream spatial units, and discharges the water to its downstream spatial unit or the ocean.

3.1.4 CICE

The Community Ice Code (CICE) is the sea ice component in CESM, and it is a result of an effort to build a sea ice model to be used in fully coupled climate simulations (HUNKE and LIPSCOMB, 2010; ROBERTS *et al.*, 2018). The sea ice, although a smaller component if compared to the atmosphere and oceans and, for the most part, seasonal, is critical for the Earth Climate System, once it governs the atmosphere-ocean exchanges of heat, moisture, and momentum and high-latitude surface radiation balance (ROBERTS *et al.*, 2018). CICE simulates the ocean-sea ice and atmosphere-sea ice interactions, and it is compatible with POP, both using

the same horizontal resolution in coupled simulations, but CICE has eight vertical layers (DANABASOGLU *et al.*, 2020).

3.1.5 POP

The ocean component of CESM is the Parallel Ocean Program (POP) model in version 2, developed by Los Alamos National Laboratory (LANL) (HURRELL *et al.*, 2013; SMITH *et al.*, 2010). POP is a general global ocean circulation model that uses, as vertical discretization, a level coordinate scheme and solves the primitive equations of ocean dynamics (HURRELL *et al.*, 2013; SMITH *et al.*, 2010). The model was written in the 1990s, but it was only included as an oceanic component of the CCSM (predecessor model to the CESM) in 2001. The release of the second and current version of POP occurred in January 2004 (SMITH *et al.*, 2010). Ocean dynamics in the model are described by primitive equations in three dimensions using hydrostatic and Boussinesq approximations (SMITH *et al.*, 2010). The following sub-items will describe its horizontal, vertical, and temporal discretizations.

3.1.5.1 Horizontal Discretization

POP is horizontally discretized in a finite difference method in the Arakawa staggered B grid, fixed in time and space (GRIFFIES *et al.*, 2008), where the velocities are evaluated at the vertices, and the tracers are evaluated at the center of the grid. (Figure 30) (SMITH *et al.*, 2010). This type of grid allows accurate representation of geostrophic currents and inertial gravity waves (ASSAD, 2006; GRIFFIES *et al.*, 2000, 2008). In simulations with resolutions coarser than $^1/_2^\circ$, the meridional grid spacing near the equator decreases, approaching a resolution of $^1/_2^\circ$ to improve wave representation and equatorial currents (SMITH *et al.*, 2010).

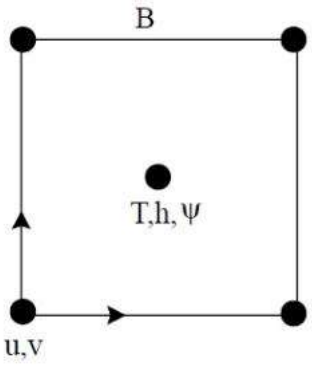

Figure 30: Scheme of the location of horizontal variables in the Arakawa B grid, where T represents tracers, h represents the layer thickness, Ψ represents the horizontal streamfunction or free surface height, and u and v refer to the horizontal velocity components. Source: Modified from GRIFFIES *et al.*, 2000.

Another way to visualize the staggered grid is to idealize it as two grid cells, one associated with tracer variables (T cell) and the other associated with velocity variables (U cell), as shown in Figure 31. According to the figure, the polygon formed by the solid line represents the T cell, where the tracer variables are arranged, more specifically at the circles, and the polygon formed by the dashed line represents the U cell, where the velocity variables are arranged, more specifically at the diamonds. i and j are distributed in the grid so that i increases in the x-direction, or eastward in polar coordinates and j increases in the y-direction, or northward in polar coordinates (SMITH *et al.*, 2010).

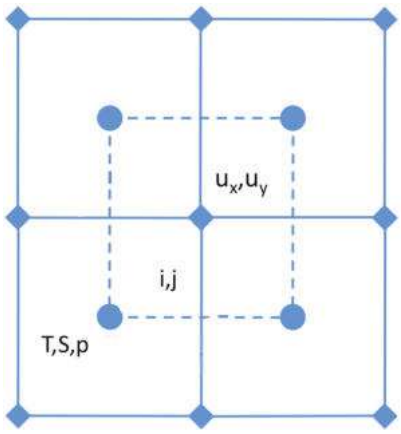

Figure 31: 2-grid visualization of the staggered horizontal B grid. Solid lines represent the T cell where tracer variables are arranged in the circles, and dashed lines represent the U cell where velocity variables are arranged in the diamonds. Source: Modified from SMITH *et al.*, 2010.

POP allows the construction of global numerical grids with the numerical poles away from geographic poles (SMITH *et al.*, 2010). This method is employed to

minimize the numerical problems associated with meridian convergence at the north pole (GRIFFIES *et al.*, 2000, 2005; MADEC and IMBARD, 1996; SMITH *et al.*, 2010). Unlike the south pole, the north pole is dominated by the Arctic ocean, and grid strangulation due to meridian convergence leads to numerical problems. Thus, the model allows the construction of semi-analytical grids with two poles, called dipolar or with three poles, called tripolar. This method is essential for the proposed objectives since the correct simulation of features in high latitudes of the northern hemisphere is necessary for an accurate representation of NADW and AMOC, the tipping elements that were investigated.

In these schemes, the southern hemisphere is a usual grid with the south pole grid located at the geographic one. In the northern hemisphere, there is one singularity in the case of dipolar grids or two singularities in the case of tripolar grids. In those cases, the method is to displace the numerical north pole to land masses, typically North America, Asia, or Greenland (MADEC and IMBARD, 1996; SMITH *et al.*, 2010). The tripolar grids were developed by MURRAY (1996), and due to the two northern hemisphere, singularities require additional communication along the northern grid boundary to connect this grid along the line between the two north poles (SMITH *et al.*, 2010).

Three processes can construct the dipole grids available for use by POP, according to SMITH *et al.* (2010), and all methods produce equivalent orthogonal grids, i.e., the areas remain proportional to those of the Earth. However, the shapes are deformed, compared to reality. An example of a dipolar grid is represented in Figure 32. In this grid, the north pole is located in North America, and the south pole is a Mercator grid with the pole at the geographic South Pole. In both hemispheres, the grid ends in a hollow circle surrounding the pole, meaning that the area within the circle is excluded from the simulation (SMITH *et al.*, 2010).

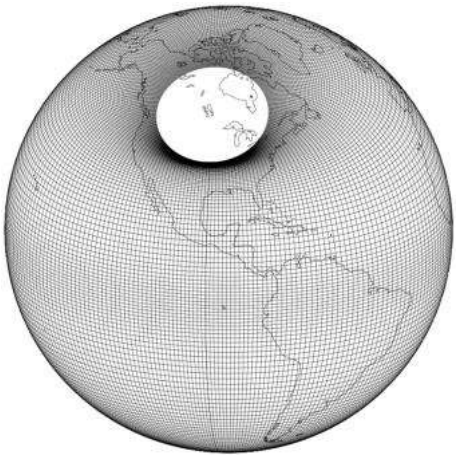

Figure 32: Example of a dipolar grid focusing on the northern displaced pole. Source: SMITH *et al.*, 2010.

Tripolar grids can also be constructed using the same construction methods of dipolar grids; the difference is that, as stated earlier, the north pole will have two singularities instead of one. Of the various grids discussed in MURRAY (1996), one of the variations is particularly useful for ocean models (SMITH *et al.*, 2010) and has two singularities in the northern hemisphere; one in North America and one in Eurasia. Such a grid, shown in Figure 33, was built for the French OPA model (MADEC *et al.*, 1998) and was made available for testing in the POP. In this type of grid, the spacing in the Arctic is much more uniform than in the dipolar grid.

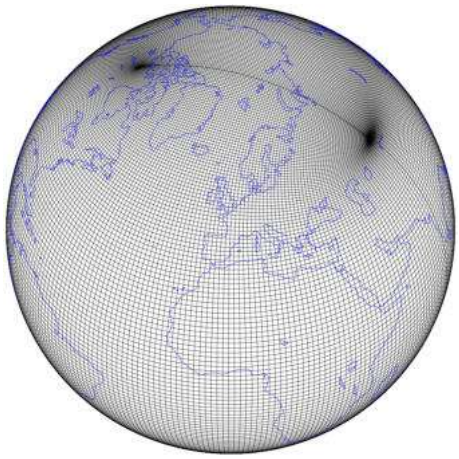

Figure 33: Example of a tripolar grid focusing on the two northern displaced poles. Source: SMITH *et al.*, 2010.

For NCAR simulations, the tripolar grid is only used for higher horizontal resolutions grid, like the 0.1° resolution, and so, for more restricted simulations. The 6$^{\text{th}}$ Coupled Model Intercomparison Project (CMIP6) simulations analyzed here used a version 7 dipolar grid with the displaced pole over Greenland with 1° resolution (called f09_g17). For this grid, the cells around Greenland have higher resolution than the surroundings, which is interesting for the goals of this work related to high latitude overturning and NADW formation. However, this grid resolution is taken from the Pacific, so features like the Kuroshio Current might not be well represented.

3.1.5.2 Vertical Discretization

POP is a model discretized in vertical levels in a fixed Eulerian grid with z-coordinates. The vertical discretization scheme is shown in Figure 34. The index k indicates the vertical direction and increases from the surface ($k = 1$) to the bottom ($k = km$), and the thickness of each layer given a level k is represented by $dz(k)$. The T grid variables (Figure 31) are located at the midpoint of each level. However, since the vertical grid may not be uniform, i.e., it may have different thicknesses for different levels ($dz(k) \neq dz(k+1)$), the interfaces with the vertical velocities w may

not be exactly half of the distances between the points of T grid variables (SMITH *et al.*, 2010).

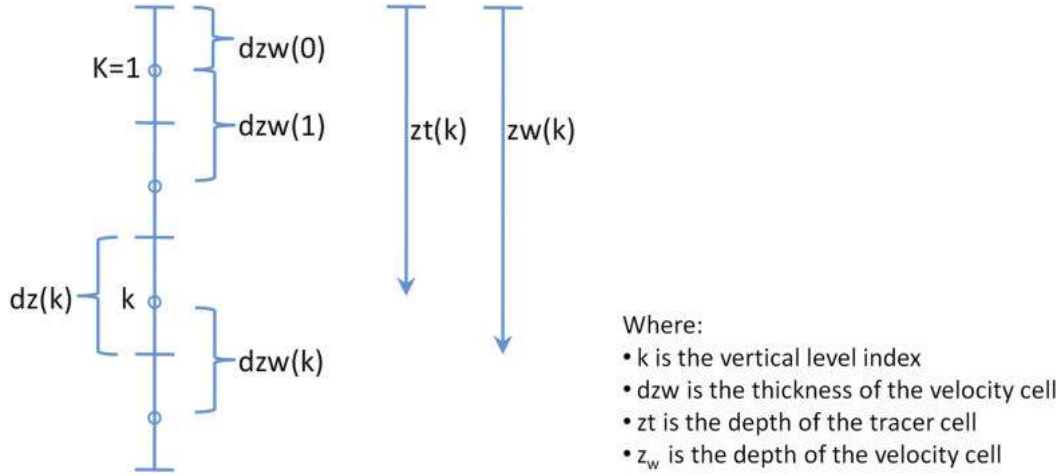

Figure 34: Scheme of POP vertical discretization. Source: Modified from SMITH *et al.*, 2010.

The z-coordinate is negative towards the bottom, but the depths are positive towards it. Usually, $dz(k)$ is smaller at lower depths and gradually increases towards greater depths. Figure 35 represents a three-dimensional T cell with the location of the vertical velocities w, which advects tracers, and w^u, which advects momentum. Note that the vertical velocities w are located at the midpoint of the top and bottom faces of the cell. In contrast, the horizontal velocities are located at the midpoints of the vertical edges, which, in a two-dimensional view, these velocities would be located at the vertices. (Figure 30). In z-level discretization, the depth of each point (i,j,k) is independent of its horizontal location unless partial bottom cells are being used. Similarly, the topography is defined in T cells, which are filled with land or ocean, except when partial bottom cells are used.

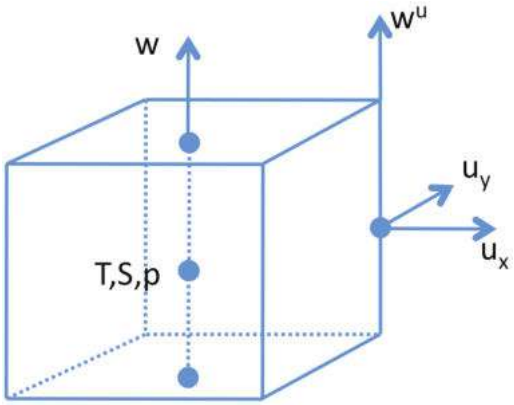

Figure 35: 3D T cell with the location of the horizontal and vertical variables. T, S, and p represent horizontal tracers, u_x and u_y represent horizontal velocities, and w and w^u represent vertical velocities that advect tracers and momentum, respectively. Source: SMITH *et al.*, 2010.

The advantages of the z-coordinate include the easy representation of the horizontal pressure gradient, the accuracy of the representation of the seawater equation, it solves the heat transport satisfactorily, ensures a better representation of the ocean surface layers, and represents well the diabatic processes. As for disadvantages, the method has difficulty in representing the topography and bottom boundary layer (GRIFFIES *et al.*, 2000). Another disadvantage is the complexity of advective marker representation and diffusion along tilted density surfaces in the ocean interior (GRIFFIES *et al.*, 2000).

Despite the disadvantages, the method satisfactorily solves heat transports as it maintains the same resolution throughout the domain in the upper layers. In addition to this fact, this type of discretization ensures a better representation of the ocean surface layers, which guarantees a better representation of the heat, mass, and energy exchange processes between the oceans and the atmosphere.

To mitigate some of these problems, POP provides two options that can be incorporated into the vertical grid. One is to allow the surface layer to have a variable thickness, which would improve the representation of changes in sea surface height and surface tracer fluxes. The other one is to use partial bottom cells. This method, first introduced by ADCROFT *et al.* (1997) and later developed for the Modular Ocean Model (MOM) model by PACANOWSKI and GNANADESIKAN (1998), is employed to represent bottom topography better, allowing vertical bottom cell thickness to vary in space (GRIFFIES *et al.*, 2005; SMITH *et al.*, 2010; WITTENBERG *et al.*, 2006). Figure 36 represents the bottom topography along the equator represented with full cells (top panel) and partial cells (bottom panel). We can see that the representation of partial bottom cell topography has smaller gradients than the full one. However, this method does not increase the model's

ability to solve highly dense flows near the bottom (GRIFFIES *et al.*, 2005).

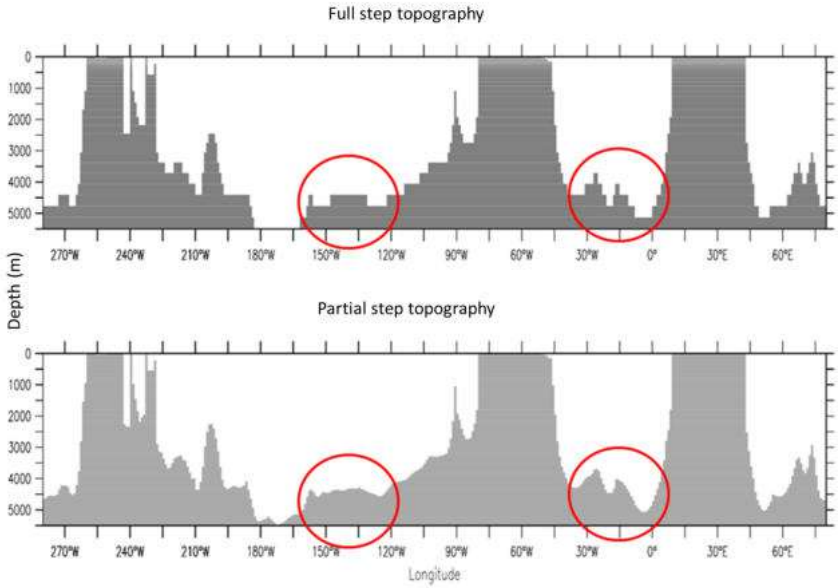

Figure 36: Bottom topography along the equator showing the difference in background representation with intact cells (above) and partial cells (below). The red circles emphasize two regions where the method produced much more smoothed gradients. Source: Modified from GRIFFIES *et al.*, 2005.

3.1.5.3 Temporal Discretization

POP is time-discretized with a modified leapfrog scheme with an independent time step for barotropic and baroclinic processes. The modification is related to the fact that some terms are evaluated semi-implicitly and, among those that are treated explicitly, only the advection operators are evaluated as a leapfrog scheme, at the central time level. On the other hand, the diffusive terms are evaluated using a forward step. This difference is because forward steps are unstable for advection schemes, and leapfrog is unstable for diffusive schemes (SMITH *et al.*, 2010).

Baroclinic and barotropic processes in the ocean have different time scales (GRIFFIES *et al.*, 2000). These differences motivated the creation of independent time step algorithms for these two processes, increasing the computational efficiency of numerical models (GRIFFIES *et al.*, 2000; RINGLER *et al.*, 2013). Barotropic equations are vertically integrated equations of momentum and continuity. In POP, the speed of the barotropic mode is limited by fast surface gravity waves (GRIFFIES *et al.*, 2000; RINGLER *et al.*, 2000), of approximately gH=200m·s^{-1} (SMITH *et al.*, 2010). The speed of the baroclinic mode is limited by gravity wave speed of the first internal mode, on the order of 10^0m·s^{-1} (GRIFFIES *et al.*, 2000; SMITH *et al.*, 2010). According to HALTINER and WILLIAMS (1980), truncation errors associ-

ated with horizontal discretization are generally much more significant than those associated with temporal discretization. This particularity means that as long as the numerical scheme is stable, the increase in time step does not result in simulation degradation (RINGLER *et al.*, 2000).

3.2 Experiments Description

A good way to establish relationships of cause and effect is to have a control experiment and an altered one (EYRING *et al.*, 2016). The experiments used in this thesis were performed for the CMIP6 (EYRING *et al.*, 2016) by NCAR scientists (DANABASOGLU *et al.*, 2020). According to EYRING *et al.* (2016), one of the CMIP's aims with the multi-model output is to make it publicly available for the community in a standardized way. The experiments used here are part of the CMIP6's Diagnostic, Evaluation, and Characterization of Klima (DECK) experiments. The DECK experiments comprise a historical Atmospheric Model Intercomparison Project (AMIP), a pre-industrial control simulation, and two CO_2 forced simulations (DANABASOGLU *et al.*, 2020; EYRING *et al.*, 2016). Still, according to EYRING *et al.* (2016), the DECK experiments are appropriate for quantifying and understanding climate change response characteristics.

That way, two DECK experiments from the CMIP6 were chosen to evaluate how the AMOC reacts to a CO_2 forced climate. One was chosen to be used as a control experiment, and the other one as the altered experiment. Both experiments were also part of earlier CMIP phases (EYRING *et al.*, 2016). The piControl experiment was performed to simulate the pre-industrial control. It will be described in item 3.2.1 and generated 48TB[36] of results. The 1pctCO_2 simulated a 1% increase per year in the atmospheric CO_2 concentration, it will be described on item 3.2.2 and generated 5TB of results. The GHG atmospheric concentrations for both experiments followed MEINSHAUSEN *et al.* (2017).

It is important to mention that the large number of results and size of files, associated with the irregular horizontal model grids made the post-processing of these experiments highly time-consuming and computationally costly. Additionally, the experiments' choice was made in consonance with CGD scientists, notably Dr. Gokhan Danabasoglu, when the author of this thesis traveled to NCAR to attend the 2019 CESM Tutorial between 5^{th} to 9^{th} August 2019. The venue took place at Mesa Lab, Boulder, CO, USA. This tutorial's attendance was possible through the financing by PEC-20480 Project between Royal Dutch Shell (Shell) and the *Laboratório de Métodos Computacionais em Engenharia* (LAMCE).

Table 9 sums up some characteristics of each experiment. As stated

[36] 1 TB = 10^{12} B

earlier, for both experiments, the following models were active: the atmospheric model CAM6, the land model CLM5, the sea ice model CICE5.1.2, the ocean model POP2 with active Marine Biogeochemistry Library (MARBL), and the river model MOSART. The land ice model, the Community Ice Sheet Model in its version 2.1 (CISM2.1), was implemented in a non-evolving configuration once the model was coupled in a one-way mode, which means that the simulations assumed fixed ice-sheets (DANABASOGLU *et al.*, 2020; MUNTJEWERF *et al.*, 2020b; RANGEL, 2019). Although CISM can be run in a two-way coupling between Greenland and land and atmosphere models, DANABASOGLU *et al.* (2020) do not mention Greenland-ocean coupling. MUNTJEWERF *et al.* (2020a,b), on the other hand, performed simulations in CESM2 with an interactive CISM. The authors highlight that since Greenland and the adjacent ocean have little interaction, the ice sheet-ocean coupling was implemented in a one-way configuration also, which the ocean model receives freshwater flux from CISM via MOSART. For the piControl experiment, the atmospheric forcings were all used as cyclically climatological fields (DANABASOGLU *et al.*, 2020).

According to EYRING *et al.* (2016), there are some recommendations for the CMIP6's control simulations, which are:

- The conditions must be invariant over time, except for those important for the mean climate as the diurnal insolation cycles.
- Conditions like GHG and ozone concentrations and surface land conditions should be representative of the year 1850.
- Orbital parameters should be fixed at 1850 values.
- Land use should not change and must reflect the agricultural maps from 1850.
- The solar constant must be fixed at a mean value - without an 11-year solar cycle.
- Volcanic aerosols should be as close as possible to the 1850-2014 mean.
- For models without interactive ozone chemistry, they should specify pre-industrial ozone fields.
- For models with interactive chemistry or aerosols, the CMIP6 pre-industrial emissions dataset should be used or a monthly climatological dataset of aerosol and optics properties if the models do not calculate aerosols concentrations internally.

Table 9: Configurations of the experiments. Source: Modified from EYRING *et al.*, 2016

Experiment	Forcing	Integration	Purposes
piControl	n/a	1200 years	Evaluate unforced variability
1pctCO$_2$	1% yr^{-1} CO$_2$ increase	150 years	Climate sensitivity and feedback

The grid used in the simulations is the f09_g17 grid, known as the 'workhorse' grid used by NCAR scientists, with 1° of horizontal resolution, on average. Table 10 displays, in more detail, the horizontal and vertical resolution for each model component used for piControl and 1pctCO$_2$ simulations. In POP, 0.64°is the coarsest resolution since it varies significantly. It spans from 0.27° at the equator, decreases until 0.53° at 32° S, and is kept constant southwards. In high latitudes of the northern hemisphere, it varies between 0.38°, at the northwestern Atlantic until 0.64° at the northwestern Pacific.

Table 10: Horizontal resolutions and horizontal and vertical grid points for each model component.

Component	**Meridional**		**Zonal**		**Vertical**
	Resolution	Points	Resolution	Points	
CAM	0.900° (≈100km)	192	1.250° (≈139km)	288	32 levels
CLM					25 levels
POP	0.640° (≈71km)	320	1.125° (≈125km)	384	60 levels
CICE					8 layers
MOSART	0.500 (≈56km)	360	0.500 (≈56km)	720	-

Additionally, Table 11 displays the coupling frequency configured for both experiments. Each model's coupling frequency determines at what interval a particular model sends the prognostic fields to the coupler that are going to be used by other models. After the coupler's regriding is performed, the prognostic fields from model A are sent to the other models B, C, or D. These models use those fields as forcings to calculate their prognostic fields.

Figure 37 represents the (a) ocean and (b) atmospheric vertical levels profiles used on the simulations - 60 layers for the ocean and 32 for the atmosphere. The profiles show the vertical coordinate on the y-axis, depth in meters for the ocean, and hPa[37] for the atmosphere. The x-axis shows the thickness of the layers. For both profiles, there are regions where the thickness between layers is smaller than other regions - shown in more detail inside each panel. The ocean has the surface

[37] 1 Pa = 1 N·m^{-2} and 1 hPa = 100 Pa.

more vertically resoluted with a 10 m-thickness in the first 160 m and a maximum thickness of 250 m at 3500 m (DANABASOGLU *et al.*, 2020). For the atmosphere, besides having the surface with more levels, it has its top layers more resoluted as well. The top is at 3.6 hPa, which is about 40 km high (DANABASOGLU *et al.*, 2020).

Table 11: The coupling frequency used between the coupler and each model component in seconds.

Model	Coupling frequency
CAM	1800
CLM	
POP	3600
CICE	1800
MOSART	10800

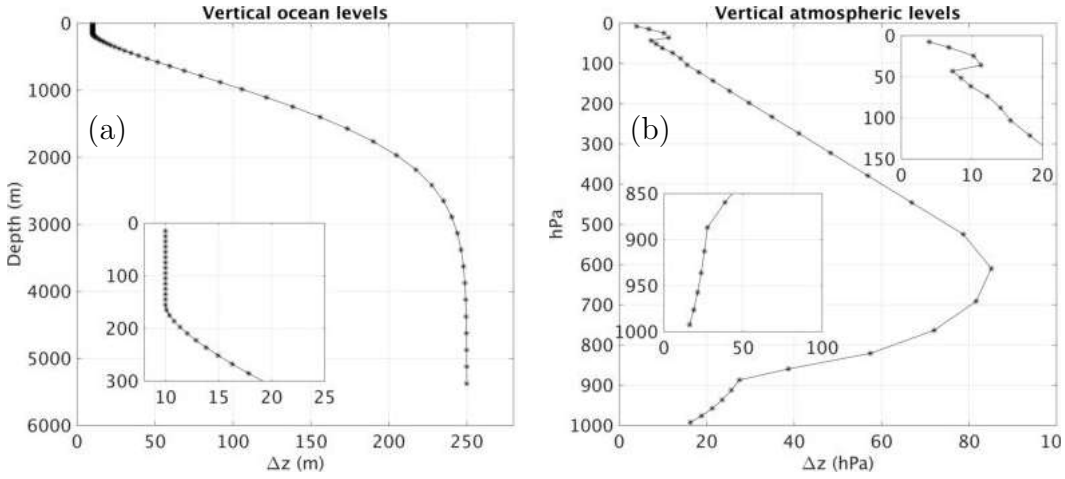

Figure 37: Vertical levels distribution on (a) POP and (b) CAM.

Both experiments are considered scientifically validated. Such experiments are composed of a multidecadal simulation, followed by a scientific review of the results generated (NCAR/UCAR, 2019).

3.2.1 piControl

According to EYRING *et al.* (2016), a control experiment is a simulation with all conditions held constant and with best estimates from the historical period forcing. The piControl was created to represent the pre-industrial period with non-evolving conditions. These conditions were chosen to represent the period preceding the beginning of the large-scale industrialization, and it has the year of 1850 as its reference year (EYRING *et al.*, 2016; NCAR/UCAR, 2019). The non-evolving conditions were set up so one can evaluate the coupled system and study the unforced

variability of the climate system. So this experiment serves as a baseline for other experiments branching from it (EYRING *et al.*, 2016; NCAR/UCAR, 2019).

Although it is known that the climate in 1850 was not stable, i.e., there was already a carbon radiative forcing increase due to anthropogenic GHG and pre-1850 secular changes in land use (see HOUGHTON (2010), HURTT *et al.* (2011) and IPCC (2013b) for more details), the assumptions made for the piControl are the following. There are no secular changes in forcing (concentrations of atmospheric constituents and land use are fixed), and the Earth's orbital characteristics are constant. That way, since there are no changes in forcing, natural or anthropogenic, the piControl is suited to study the internal variability of the climate system (EYRING *et al.*, 2016).

For the model to come into balance with the forcing, the piControl starts after a climate spin-up (EYRING *et al.*, 2016; NCAR/UCAR, 2019), and it was run for 1200 years. According to DANABASOGLU *et al.* (2020), in these long control simulations, it is crucial to keep top-of-the-atmosphere global- and time-mean heat fluxes $<|0.1|\mathrm{W{\cdot}m^{-2}}$ in order to avoid unrealistic warm or cold climate states. To achieve that, some tunning was necessary during the simulations, which resulted in an average imbalance of $+0.05\mathrm{W{\cdot}m^{-2}}$ (DANABASOGLU *et al.*, 2020). These adjustments remained fixed for the subsequent simulations that arose from this experiment, such as the 1pctCO_2 experiment.

3.2.1.1 Initial Conditions

The ocean and sea ice initial conditions were obtained from a compendium of integrations. First, the results in year 402 of one member of the CESM1 Large Ensemble Numerical Simulation (LENS) PI Control integration (DANABASOGLU *et al.*, 2020) was chosen among three. The other two members considered ended up simulating unrealistic sea ice cover and were discarded (DANABASOGLU *et al.*, 2020; KAY *et al.*, 2015). The LENS member was initialized from the Polar Science Center Hydrographic Climatology in its version2 (PHC2) January-mean potential temperature and salinity fields (STEELE *et al.*, 2001). Then a series of simulations were performed to achieve the initial conditions. From the PI Control LENS, the results from year 161 were taken, which initialized simulation 293. Then, the results from year 130 were taken to initialize simulation 297. From that, the results from year 249 were used to initialize simulation 299. Finally, the ocean and sea ice initial conditions were taken from year 134 of simulation 299 (DANABASOGLU *et al.*, 2020). To sum up, these conditions represent fields integrated for more than 1000 years after initialization from PHC2. Figure 38 presents a diagram of the strategy used to obtain the initial conditions.

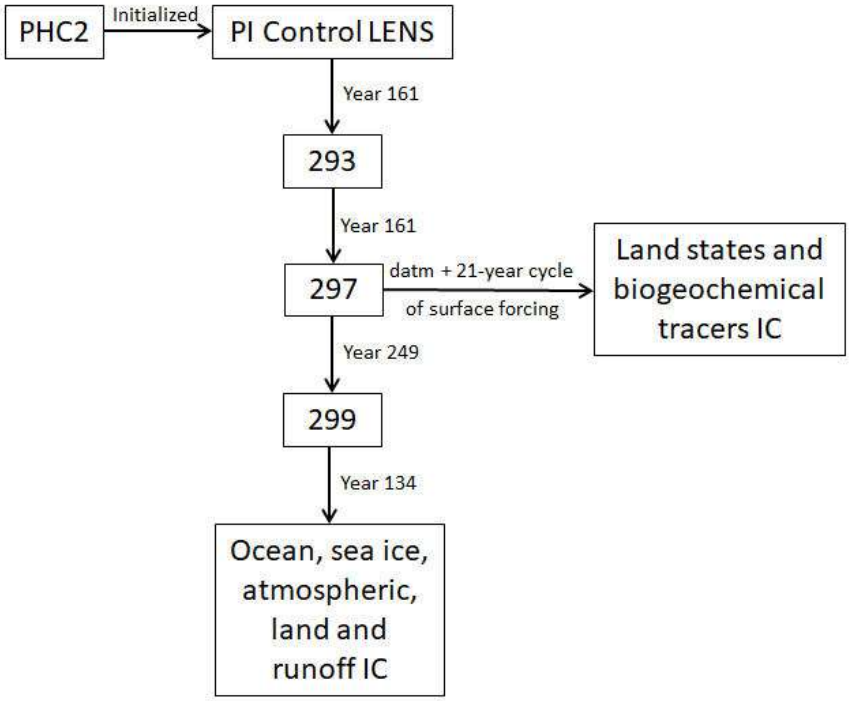

Figure 38: Diagram that shows how the model components' initial conditions were obtained. PHC2 means Polar Science Center Hydrographic Climatology 2, PI means Pre-industrial, LENS means Large Ensemble Numerical Simulation, IC means initial conditions, and datm means the atmospheric component in data configuration.

The simulations described above were also used to initialize the atmospheric, land, and runoff components of CESM2. The land states and biogeochemical tracers were taken from long spin-up runs from land and ocean model components, respectively, in the following manner. The active atmospheric component was replaced by the data one, repeating the twenty-one year-cycling of the surface forcing extracted from simulation 297 (Figure 38). The land model was initialized from bare ground and then normally spun-up for several hundred years. Concerning the biogeochemical tracers of the ocean model, to avoid drift, the physical ocean state was configured to reset to its initial condition at the beginning of each 21-year cycle, which kept it synchronized with the atmospheric surface forcing (DANABASOGLU *et al.*, 2020).

3.2.1.2 Forcing Datasets

The atmospheric model (CAM6) obtained several forcings generated by WACCM6[38]. WACCM calculates chemical and aerosol constituents from emissions based on inventories specified by CMIP6 that considered anthropogenic and biomass

[38]WACCM6 is also discretized in finite volume, and it was used in the same configuration as CAM6. However, WACCM6 uses 70 vertical levels, instead of 32, with the top one at $6{\cdot}10^{-6}$ hPa, which is located about 140 km high from the ground (DANABASOGLU *et al.*, 2020).

burning but also uses CMIP6 forcings when needed (DANABASOGLU *et al.*, 2020; EYRING *et al.*, 2016). The forcings provided from WACCM6 are stratospheric ozone and aerosols for radiative effects, tropospheric oxidants for chemistry, H_2O production rates due to CH_4 oxidation in the stratosphere and N deposition to the land and ocean components (DANABASOGLU *et al.*, 2020).

The simulation strategy was the following: WACCM6 simulation 295 generated the prescribed forcings for CAM6 simulation 299 (Figure 38). Then WACCM6 was conducted with initial conditions for the other model components (ocean, sea ice, and land) from simulation 299, and the chemical and aerosols constituents of the average of years 21-50 generated were used in the CAM6 piControl simulation (DANABASOGLU *et al.*, 2020).

The CMIP6 providing forcing includes anthropogenic emissions from 1850 to 2014, obtained from the Community Emissions Data System (CEDS) (DANABASOGLU *et al.*, 2020; HOESLY *et al.*, 2018). They consist of reactive gases like CO, CH_4, NH_3, NO_x, SO_2, and carbonaceous aerosols (black and organic carbon), besides CO_2 (HOESLY *et al.*, 2018). Biomass burning emissions were taken from VAN MARLE *et al.* (2017). They were estimated through satellite records, existing proxies, and the average of six Fire Model Intercomparison Project (FireMIP) model results to cover gaps in proxies (DANABASOGLU *et al.*, 2020). Although the emissions data sets were used since 1850, both of them are available since 1750 (HOESLY *et al.*, 2018; VAN MARLE *et al.*, 2017).

Regarding land cover and land use for CLM5, the dataset combines present-day satellite cover descriptions with land use time series from the Land Use Harmonization in its version 2 (LUH2). Also, CLM5 and ocean biogeochemistry use N-deposition from WACCM6 simulations (DANABASOGLU *et al.*, 2020).

3.2.2 1pctCO_2

The 1pctCO_2 is a climate change idealized experiment that was branched from year 501 of the piControl, and for that reason, only the first 500 years of the piControl were considered on the analysis. 1pctCO_2 differs from piControl by the increase of 1% of atmospheric CO_2 concentration per year (Figure 39) from the global annual mean 1850 value of 284.3ppm (EYRING *et al.*, 2016; MEINSHAUSEN *et al.*, 2017; NCAR/UCAR, 2019). According to EYRING *et al.* (2016), the 1pctCO_2 experiment can be used to analyze model Transient Climate Response (TCR) and Transient Climate Response Emissions (TCRE) to cumulative carbon, which would be the change on the transient global average surface air temperature per unit of accumulated CO_2 emissions (IPCC, 2013b).

Figure 39 shows the CO_2 forcing in the 1pctCO_2 experiment over time

in (a) a latitude distribution and (b) an average distribution. It can be seen that the distribution over latitude is uniform (the CO_2 isolines are not tilted), and the increase in the CO_2 is exponential (Figure 39(b)). Figure 39(b) also indicates when the CO_2 concentration in the atmosphere doubles and quadruples related to its initial value. Still, according to EYRING *et al.* (2016), the logarithmic increase in CO_2 is proportional to the radiative forcing, so, in the 1pctCO_2 experiment, the radiative forcing increases linearly.

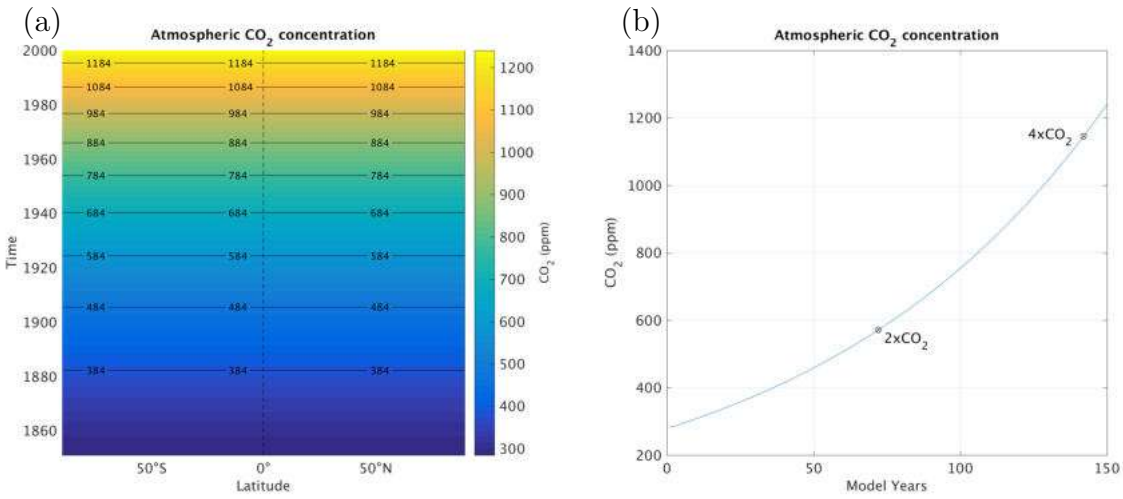

Figure 39: Atmospheric CO_2 concentration forcing (a) over latitude and (b) on average. The two points on the curve in (b) identify where the CO_2 concentration doubles and quadruples.

3.3 Observed Data

Observed data from various sources and types were acquired in order to compare them with the experiments analyzed and will be described in the following items.

3.3.1 NSIDC

Sea ice information is derived from the compilation of two passive microwave satellite data sets provided by NSIDC (FETTERER *et al.*, 2017). The following data description is based on the user guide available on the website *http://nsidc.org/data/G02135*.

The two satellites are the Nimbus-7 Scanning Multichannel Microwave Radiometer (SMMR), with acquisitions since October 1978 and the Special Sensor Microwave Imager (SSM/I) and Special Sensor Microwave Imager/Sounder (SSMIS) from the Defense Meteorological Satellite Program (DMSP) satellite group with

acquisitions since August 1987. The concentration of sea ice can be estimated by the brightness temperature of the data obtained by the sensors, made possible by the difference in brightness temperature signatures between sea ice and water. The Sea Ice Index product was created by NASA Goddard Space Flight Center, which converts brightness temperatures to ice concentration estimates.

Data were acquired on monthly averages and are produced from daily gridded sea ice concentration fields. Two types of data are available; the 'extent' and 'area' of sea ice. According to the NSIDC, the 'extent' of sea ice defines a region covered or not by ice, according to the cutoff value of 15%[39]. Above this value, the cell is considered covered by ice, and below it, the cell is considered free of ice. 'Area' considers the sea ice percentage in the cells above the 15% cutoff to determine how much of the region is covered by ice.

Taking as an example, three cells of 25 km x 25 km covered by 16%, 2%, and 90% of sea ice, two of these cells are considered covered by ice. To determine the 'extent', these two cells are considered as 100% ice. Thus, multiplying the grid cell by 100% yields an extension of 1250 km^2 of sea ice (25 km$\times$25 km$\times$2cells). For the 'area' calculation, the grid cells' area above the 15% cutoff is multiplied by the percentage of ice in these cells and then summed. So the total area of these grids would be 662 km^2 ([25 km$\times$25 km$\times$16%]+[25 km$\times$25 km$\times$90%]).

To obtain the monthly mean 'extent', first, the daily extent for each day of the month is calculated from the daily grid data using the cutoff concentration of 15% and the size of each grid cell[40]. After this process, daily extension averages are made to obtain the monthly average[41]. Values need to be assigned to the region near the North Pole - called the North Pole hole, as the sensor does not image this area. Thus it is assumed that the region is entirely covered by sea ice and considered in the calculation of ice extent.

The average monthly 'area' is obtained in the same way as the 'extent'; however, the sea ice concentration in each cell is taken into account, as explained above. It is important to note that the 'extent' value is always higher than the 'area', since 'area' takes into account the sea ice concentration in each cell and does not compute the North Pole hole region as the 'extent' does. This region has an

[39]The boundary region where sea ice ends, and water begins is demarcated where the estimate of grid cell concentration is less than 15% since values less than 15% in passive microwave sensors contain considerable uncertainty. Thus, values of less than 15% are considered equal to 0%.

[40]Each grid is nominally 625 km^2 (25 km x 25 km). However, it is important to note that each cell area may differ due to the Earth's curvature and the stereographic projection of the data. The 'area' is obtained by multiplying the grid cell size (625 km^2) by the map scale square in the center of the cell grid. Thus the areas range from 382 km^2 to 664 km^2 in the northern hemisphere and 443 km^2 to 664 km^2 in the southern hemisphere.

[41]Each cell in the grid counts as 0 km^2 or the value itself if it passes the 15% cut. The values of all cells are then summed to produce a single daily 'extension' value across the hemisphere in km^2. Only then these values are averaged to acquire the monthly value.

area of 1.19 million km^2 for SSMR from the beginning of the series until August 20, 1987, 0.31 million km^2 for SSM/I between August 21, 1987, until December 2007 and 0.029 million km^2 between the August/September 1987 limit and December 2007/January 2008. Due to this discontinuity, the August 1987's value was removed from the time series due to this significant disparity. Also, when there is not enough satellite data to process the data, it is not computed and is replaced by a flag value. Table 12 indicates the months and years in which data were missing or excluded in each variable, and Figure 40 presents the time series of the data obtained.

Table 12: Dates of missing values in sea ice data.

Year	Month	Extent	Area
1987	August		x
	December	x	x
1988	January	x	x

The acquired data begins in November 1978 and ends in June 2018. Discontinuities are observed in the series (Figure 40), where there are no 'extension' or 'area' values at times indicated in Table 12. It is important to note that for some years, there is no data in all months. Nonetheless, the evaluation of piControl was made through a climatological analysis, and these few lacking months did not impact the results. More extended time series (G10010 data from WALSH *et al.* (2019)) were not available because the data administrators reported some issues with it and suggested not to use them until corrections were made.

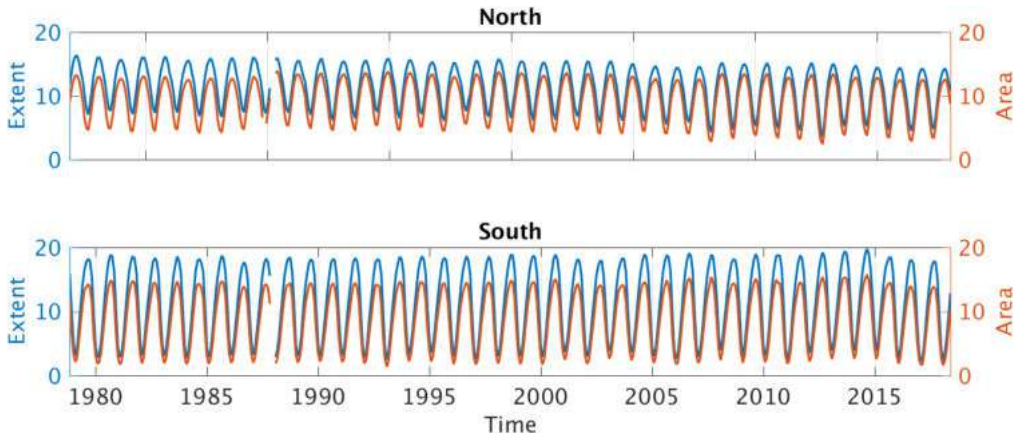

Figure 40: Time series of NSIDC sea ice data for the northern (upper panel) and southern (lower panel) hemispheres. The left y-axis concerns the 'extent' series, and it is related to the blue lines, and the right one concerns the 'area' , and it is related to the orange lines, for both panels.

3.3.2 AMOC

Item 2.5.2 described several AMOC monitoring programs: the OSNAP Program, the RAPID Program, the MOVE Program, and the SAMBA Program. The OSNAP, RAPID, and SAMBA programs are localized in strategic regions for the results evaluations in this work. Nevertheless, the OSNAP time series was considered too short to be used, totaling less than two years of measured data. Additionally, despite having more than eight years of data, the SAMBA program exhibited a large gap between the years 2011 and 2013, leaving the longer record with less than four whole years. Thus SAMBA data was also unconsidered to be used. RAPID data, on the other hand, were successfully used to aid the analysis evaluation, exhibiting more than 14 years of continuously monitoring. RAPID data were employed as climatology data, which used a 12-year average, from January 1st, 2005, and December 31th, 2017.

3.4 Reanalysis Products

Reanalysis products were used to make comparisons against piControl as a way to validate it (HODGES *et al.*, 2011). These products are the combination of numerical forecast models assimilated with observational data, producing robust spatially-covered atmospheric and oceanic information (HODGES *et al.*, 2011; JONES *et al.*, 2016). Currently, some reanalysis products are available. Among them, the ERA-Interim (BERRISFORD *et al.*, 2011) and National Centers for Environmental Prediction (NCEP) Reanalysis 2 were chosen for the atmosphere, and the Copernicus Marine Environment Monitoring Service (CMEMS) product was chosen for the ocean. The products will be described in the following sections.

3.4.1 ERA-Interim

ERA-Interim is a reanalysis product from European Centre for Medium-Range Weather Forecasts (ECMWF) with global coverage from 1979 until now and a monthly updated archive (BERRISFORD *et al.*, 2011; DEE *et al.*, 2011). The ERA-Interim project started in 2006, aiming to connect the existing ERA-40 product with the next generation of ECMWF reanalysis and upgrade it not only by improving the model representation but also improving the data treatment before the 4DVAR data assimilation (BERRISFORD *et al.*, 2011).

ERA-Interim makes use of a spherical-harmonic T255 spectral discretization, which gives a horizontal resolution of approximately 0.7°or 79 km. Sixty levels represent the vertical atmosphere from surface until 0.1 hPa, and sub-daily 3-hourly and 6-hourly results adequately describe the atmosphere (BERRISFORD *et al.*,

2011; DEE *et al.*, 2011). The reanalysis product was acquired in monthly means of the daily mean from jan/2000 to dez/2009.

3.4.2 Reanalysis-2

Reanalysis-2 (R-2) is a project from NCEP and an improvement from the R-1 project (KALNAY *et al.*, 1996; KANAMITSU *et al.*, 2002). The improvements include physical parametrizations and the quality control of the data to be assimilated (KANAMITSU *et al.*, 2002). The project consists of the use of a unique analysis/forecast system and performs data assimilation from 1957 until the present (KALNAY *et al.*, 1996). The grid is spectrally discretized and truncated at T61, which means a horizontal resolution of approximately 2.5°or 277 km. The results were obtained in monthly means from January 1979 to October 2019.

3.4.3 CMEMS Product

The results of the CMEMS, more specifically, the product GLOBAL-REANALYSIS-PHY-001-025 - whose abbreviation is GLORYS2V4 - were used. Details of these results are described below, based on CMEMS (2017a) and CMEMS (2017b).

The purpose of the CMEMS product is to provide recent ocean simulations with a resolution of 1/4°, which integrates the period in which satellite altimetry data is available and in situ observations are possible for use in data assimilation. Thus, the product provides thermodynamic and dynamic variables in three dimensions and sea surface height in addition to sea ice variables. The results were acquired monthly and cover the period from 1993 to 2015. Table 13 summarizes the main characteristics of the results used.

Table 13: Characteristics of GLORYS2V4 product. Source: Modified from CMEMS, 2017a.

	GLORYS2V4
Geographic Limits	180°W-180°E / 77°S-90°N
Variables Available	Temperature Salinity Zonal Velocity Meridional Velocity
Period	1993-2015
Frequency	Monthly
Horizontal Resolution	1/4°
Vertical Levels	75
Assimilated Observations	Altimetric sea level anomaly In situ temperature and salinity profiles Sea surface temperature observations Sea Ice concentration

3.5 Analysis Methodology

The analysis methodology of the results from the 1pctCO_2 experiment was proposed to evaluate, in the best way, the questions investigated here. That way, this methodology was based on three segments, which were:

1. Evaluation of an AMOC tipping point following the methodology mainly proposed by LENTON *et al.* (2008) and BAKKER *et al.* (2016). The thresholds indicated by the authors for a THC tipping point were analyzed as well as changes in NADW formation regions and on the AMOC cell. The analysis, covered on item 4.2, included: surface air temperature and atmospheric CO_2 time series, horizontal distribution and time series of the freshwater flux, as well as the parameters that calculate it, horizontal distribution and time series of the mixed layer depth, and vertical profiles and time series of the meridional transport streamfunction.

2. The dynamics of vertical profiles and time series of the volume and heat transports across some meridional and zonal sections in the South Atlantic and the Indian Ocean, related to the AMOC, were analyzed, and their changes identified on item 4.3.

3. Changes on some features of the Earth Climate System were identified and discussed relating the importance of AMOC on climate on item 4.4. The features evaluated in the atmosphere were the horizontal distribution of surface air temperature and the sea level pressure latitudinal distribution. On the sea

ice, changes in the annual distribution of sea ice concentration were analyzed, as well as the time series and horizontal distributions of this parameter for the months of minimal sea ice in the Arctic and the Antarctic. Furthermore, on the ocean, analyzes of the sea surface temperature, the surface ocean heat flux, the global meridional heat transport, and ocean heat content were performed.

3.5.1 Analysis Performed

Two sets of analysis were conducted:

- Validation of the piControl experiment through the ocean, atmospheric and sea ice model analysis.
- Evaluations of changes in AMOC and ocean circulation due to CO_2 forcing and identification of some changes in the climate system.

Additionally, item 5 proposes a simple projection of the changes observed in the 1pctCO_2 experiment into the future, based on *in situ* CO_2 measurements. Besides the prognostic variables available in each model, some other parameters and statistical quantities were estimated. The kinetic energy (E_c) was one of them, and it was calculated through Equation (3.1).

$$E_c = \frac{mv^2}{2} \tag{3.1}$$

Where:

- m is the mass.
- v is the velocity of the current.

The advected heat (Ht - Equation (3.2)) and volume transports (Vt - Equation (3.3)), and other variables were evaluated across zonal and meridional sections illustrated in Figure 41 with its limits in Table 14. Additionally, the Heat (Equation (3.4)) was also calculated.

$$Ht = \rho \cdot c_p \int_0^L \int_{-h(z)}^0 v\theta dz dx \tag{3.2}$$

$$Vt = \int_0^L \int_{-h(z)}^0 v(x,z,t) dz dx \tag{3.3}$$

$$Heat = \rho \cdot c_p \cdot \theta \tag{3.4}$$

Where:

- v is the velocity component normal to the section.
- L is the limit of the lateral dimension.
- $-h(z)$ is the limit of the vertical dimension.
- z is the vertical dimension.
- x is the lateral dimension.
- t is the temporal dimension.
- ρ is seawater density.
- θ is the potential temperature.
- c_p is the seawater specific heat.

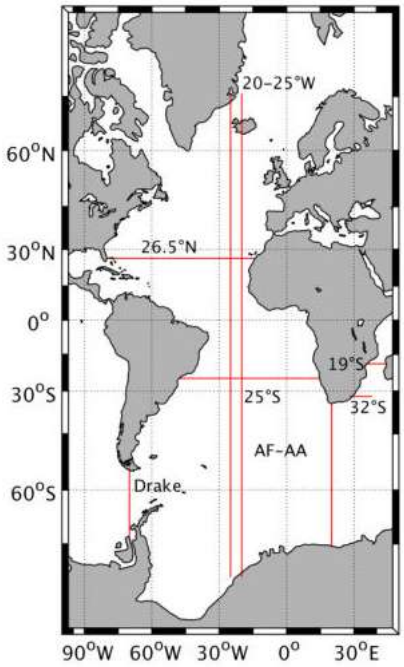

Figure 41: Sections evaluated.

Table 14: Geographic limits of the sections evaluated.

Section	**Latitude**	**Longitude**
Drake	50°S-70°S	70°W
AF-AA	35°S-70°S	20°E
20°-25°W	75°S-71°N	20°W-25°W
26.5°N	26.5°N	80°W-14°W
19°S	19°S	35°E-44°E
25°S	25°S	50°W-15°E
32°S	32°S	28°E-38°E

Table 15 displays the thermohaline index intervals of the water masses usually found in the Atlantic Ocean. These parameters were used to examine the distribution of the top of the water masses on the water column. The thermohaline intervals are a composition of the works of SANCHO (2012), SANCHO (2014), SANCHO *et al.* (2015) and some are also found in FRAJKA-WILLIAMS *et al.* (2019), TALLEY *et al.* (2011) and TOMCZAK and GODFREY (1994).

Table 15: Intervals for the potential temperatures, salinities, and the top potential sigma of the common water masses found in the Atlantic Ocean. Source: composition of the works of SANCHO, 2012, SANCHO (2014), SANCHO *et al.*, 2015, FRAJKA-WILLIAMS *et al.*, 2019, TALLEY *et al.*, 2011 and TOMCZAK and GODFREY, 1994

Water Mass	**Temperature (°C)**	**Salinity**	**Sigma ($kg \cdot m^{-3}$)**
AAIW[42]	3°<T<6°	34.2<S<34.6	27.2465
NADW	3°<T<4°	34.6<S<35	27.7575
AABW	T<2°	S<34.8	27.81

To isolate one or more oceans of interest, a file applying different values for each ocean was used, as Figure 42 shows.

[42] Antarctic Intermediate Water

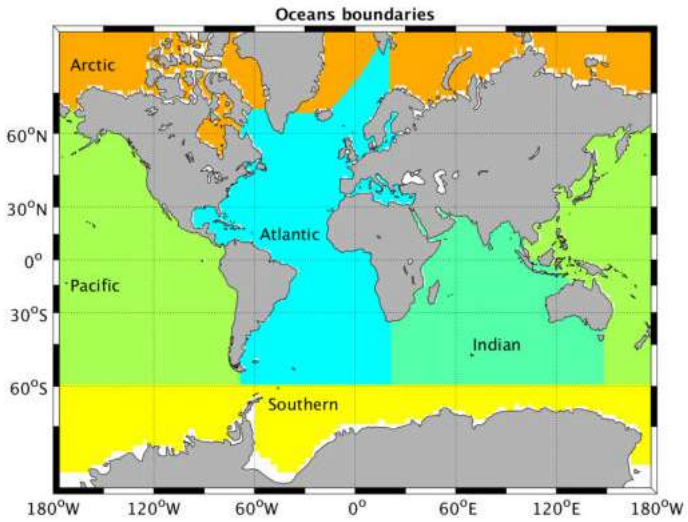

Figure 42: Oceans with marked boundaries.

The total surface freshwater flux ($sfw f_{total}$) into the ocean was calculated through Equation (3.5), following Gokhan Danabasoglu (personal communication, January 14th, 2020).

$$sfw f_{total} = (P - E + R + M_{ice} + S) - Q/L \tag{3.5}$$

Where:

- P is the precipitation flux
- E is the evaporation flux
- R is the river runoff flux (liquid + frozen)
- M_{ice} is the melting of sea ice
- S is the salt flux due to ice melt
- Q is the heat flux due to ice formation (contribution from the frazil ice formation)
- L is the latent heat of fusion

The analysis of freshwater flux was performed in the NA between the latitudes of 50°N and 70°N (Figure 43) following the work of MANABE and STOUFFER (1999).

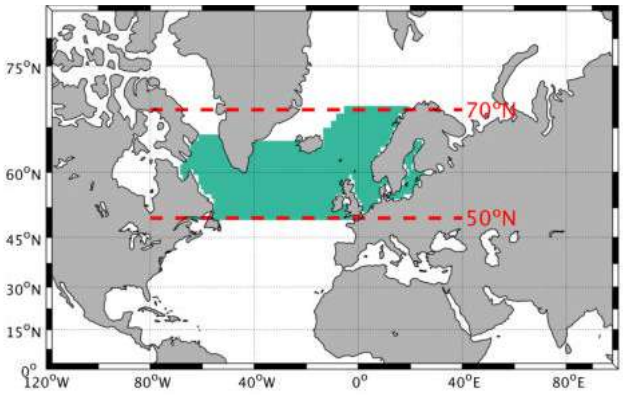

Figure 43: Area where the freshwater flux was evaluated. The Atlantic Ocean was isolated through the file that divides the ocean basins (Figure 42). Then the region between 50°N and 70°N was isolated.

According to SMITH *et al.* (2010), the mixed layer depth is defined in the POP code after LARGE *et al.* (1997) as the deepest penetration of the turbulent mixing. The buoyancy profile (b_k) at depth z_k is scanned to find the maximum value $(b_k - b_1)z_k^{-1}$, where the first buoyancy level b_1 is equal to the surface buoyancy. This value is the maximum buoyancy gradient between any depth in the water column and the surface. The mixed layer depth is the shallowest depth where the local, interpolated buoyancy gradient is equal to this maximum value.

The time series of the mixed layer depth was evaluated in four areas in the NA, chosen due to negative anomalies in this region (item 4.2), besides being locations where NADW is formed. Additionally, Table 16 displays the geographical limits of each Area.

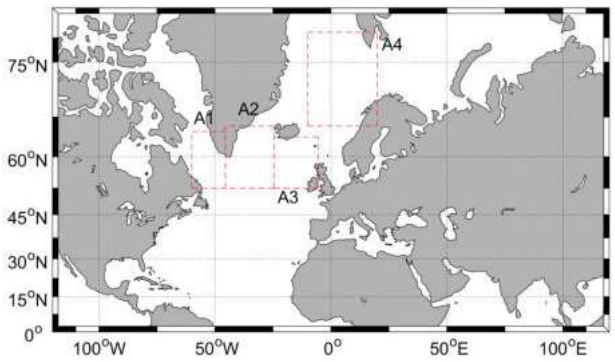

Figure 44: Locations of the four areas chosen to monitor the mixed layer depth time series.

The AMOC is calculated as a streamfunction (ψ) of the zonally-integrated and vertically-accumulated meridional volume transport in depth coordinates (Equation (3.6)) (FRAJKA-WILLIAMS *et al.*, 2019). One can also calculate AMOC for each depth.

Table 16: Geographic limits of the four areas of Figure 44.

Area	**Latitude**	**Longitude**
Area 1	52.5°N-65°N	60°W-45.5°W
Area 2	52.5°N-66°N	45.5°W-24.5°W
Area 3	52.5°N-64°N	24.5°W-5.5°W
Area 4	66°N-78°N	10°W-20°E

$$\psi(z) = \int_{z}^{0} \int_{x_w}^{x_e} v(x, z')dxdz' \tag{3.6}$$

Where:

- z is the limit of the vertical dimension
- v is the meridional velocity across the section
- x_w is the west limit of zonal section
- x_e is the east limit of zonal section

The months for the seasonal analysis were separated as summer being the average of December, January, and February and winter being the average of June, July, and August as defined by PEIXOTO and OORT (1992). Statistical quantities, such as variance (σ^2 - Equation (3.7)), standard deviation (σ - Equation (3.8)), the root mean square error (RMSE - Equation (3.9)) and the Correlation (Cor - Equation (3.10)) were also calculated to assist on the analysis.

$$\sigma^2 = \frac{1}{(N-1)} \sum_{i=1}^{N} (x_i - \bar{x})^2 \tag{3.7}$$

$$\sigma = \sqrt{\frac{\Sigma(x_i - \bar{x})^2}{N}} \tag{3.8}$$

Where:

- N is the data sample.
- x_i is the data at i point.
- $\bar{x}$ is the sample mean.

$$RMSE = \sqrt{\frac{\Sigma_{i=1}^{N}(x_{obs,i} - x_{model,i})^2}{N}} \tag{3.9}$$

Where:

- N is the data sample.

- $x_{obs,i}$ is the observed data at i point.
- $x_{model,i}$ is the estimated data by the model at i point.

$$Cor = \frac{Cov(x,y)}{\sigma_x \cdot \sigma_y}, Cov(x,y) = \frac{1}{N}\sum_{i-1}^{N}(x_i - \bar{x})(y_i - \bar{y}) \tag{3.10}$$

Where:

- σ is the standard deviation of each data sample x and y.
- N is the data sample.
- x_i and y_i are the data at i point.
- $\bar{x}$ and $\bar{y}$ are the sample mean.

The anomaly between any parameter was calculated through Equation (3.11)

$$anomaly = \phi_{1pctCO_2} - \phi_{average(piControl)} \tag{3.11}$$

Where:

- ϕ is the variable of interest.

Chapter 4

Results and Discussions

"Climate models reproduce many features of
our current climate and they all
predict a warmer world for the future."
Jeff Knight through SCAIFE (2016)

In this chapter, the results of two CMIP6 experiments are analyzed as a method to achieve the aims proposed in this work. In section 4.1, the piControl is validated through the analysis of known features against descriptions in the literature, observed data, and reanalysis products, the last two described in sections 3.3 and 3.4. The validation of piControl is an essential step in order to certify that it can be used as a comparison parameter for changes identified in the 1pctCO_2 experiment.

Once validated, tipping points in the THC and NADW formation were investigated in section 4.2. Then, in section 4.3, other changes related to AMOC were identified. Finally, section 4.4 identified changes in some of the components of the Earth Climate System due to the increased CO_2 forcing.

4.1 piControl Experiment: validation

The control experiment used in the present work (item 3.2.1) was heated through a spin-up, and the first 500 years of the simulation were used for the analyzes. From that point, the altered experiment (item 3.2.2) was initialized. This integration length is the recommended minimum period for simulating piControl (EYRING *et al.*, 2016; NCAR/UCAR, 2019). However, EYRING *et al.* (2016) warn that more extended piControl simulation periods for the CMIP6 participating models are recommended to eliminate any residual drift. Nonetheless, based on CMIP5's piControl's 500-year analysis (GUPTA *et al.*, 2013), we understand that

CESM is a model that inherently produces little climate drift and thus any residual drift from the assessed piControl period did not influence the results and discussions obtained here.

As stated earlier, the piControl started after a climate spin-up, and so the model was already in balance when the experiment began. This behavior can be confirmed by the total ocean monthly kinetic energy time series (Figure 45). It can be observed by the kinetic energy and the growth rate[43], that both are stable, and there are no increases or decreases that outlier the pattern of the time series. This pattern was expected as it is described in EYRING *et al.* (2016). The total increase in the kinetic energy is $9.7{\cdot}10^{-3}$ $m^2{\cdot}s^{-2}$, one order of magnitude lower than its average, or 14.5% at the end of the 500 model years.

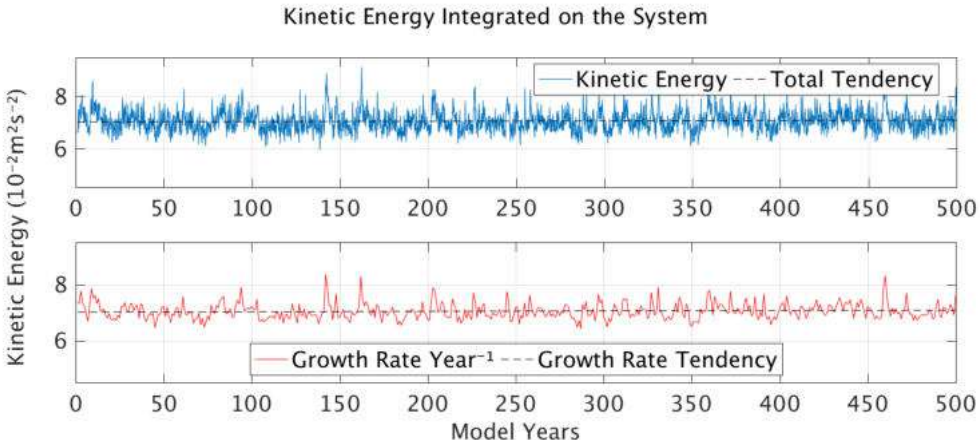

Figure 45: Annual average series of the ocean kinetic energy integrated on the volume and its tendency (upper panel), and the time series of the growth rate of the kinetic energy per year and its tendency (lower panel). The growth rate is calculated as the 12-month tendency for each model year.

The kinetic energy time series above represents all the water column, integrated over the 60 vertical ocean levels. Analyzing some layers separately (Figure 46), we can see that the top layer is the one with higher energy, once it is under the influence of the energy coming from the atmosphere. The second layer is already ∼35% less energetic than the first one, and it is as energetic as the bottom layer, on average. However, the bottom layer is not as variable as the second one. The third layer (2000-3000 m) is ∼55% less energetic than the first one, and it is as energetic as the 4^{th} layer (3000-4000 m).

[43]The growth rate was calculated as the 12-month tendency for each year individually.

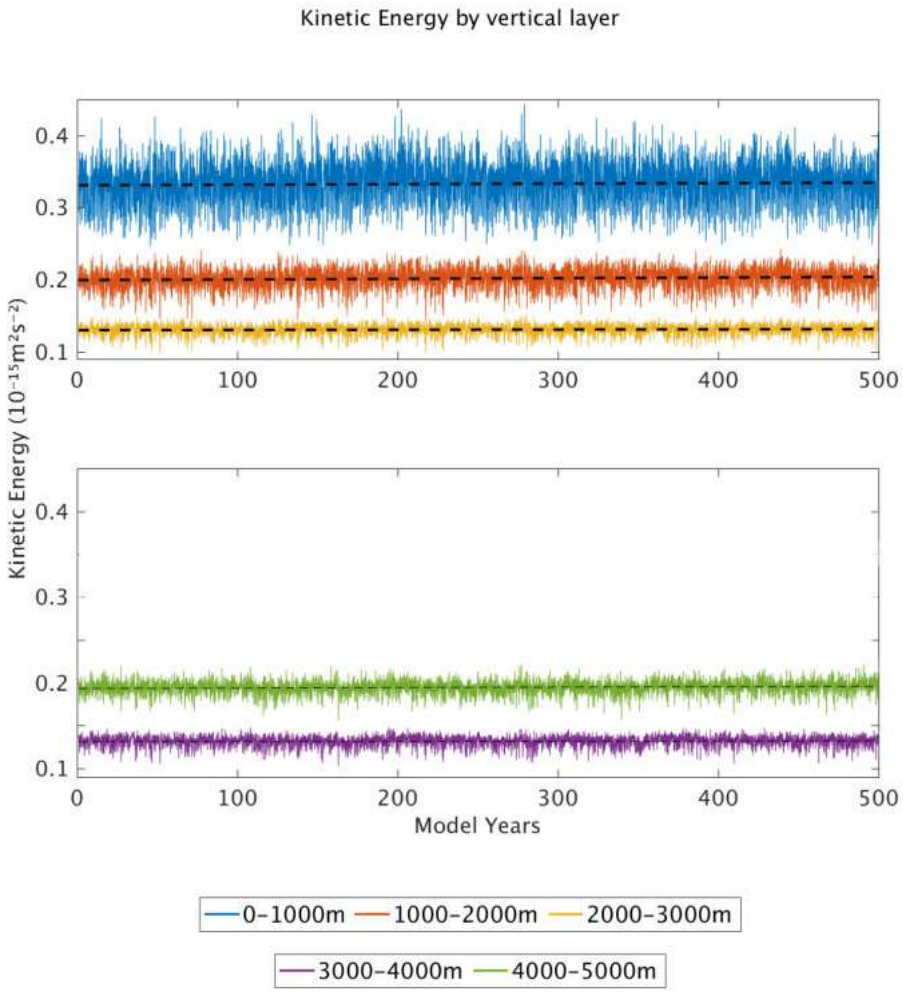

Figure 46: Annual average series of the kinetic energy on the ocean, integrated by layers of 1000 m thick each. Dashed lines represent the tendency for each layer. The upper panel depicts layers of the first 3000 m, and the lower panel depicts layers from 3000 m to 5000 m. The time series were divided into two panels to avoid overlap of different layers with similar kinetic energy.

Despite the differences between the layers, we observe that they do not exhibit significant increases or decreases, as we can see in Table 17, and that the whole time series show cyclic behavior since the beginning. Table 17 shows, for each layer of Figure 46, the vertical levels used to represent each one and the absolute and percentual increase of the kinetic energy per layer for the 500 years. One can see that the most significant increase is about ∼2% for the layer 1000-2000 m, which represents only $0.03{\cdot}10^{-15}$ $m^2{\cdot}s^{-2}$ of the average value for this layer. Additionally, the first layer has 40 vertical levels, once the surface layers have more vertical resolution than the deep ones (see Figure 37(a)).

Table 17: Absolute and percentage of increase in kinetic energy by layer of Figure 46 at the end of the series compared to the beginning.

Layer	**Vertical levels**	**Abs increase (10^{-15} m^2s^{-2})**	**% increase**
0-1000 m	1-40	0.0035	1.044%
1000-2000 m	41-46	0.0043	2.176%
2000-3000 m	47-50	0.0013	0.975%
3000-4000 m	51-54	$7.7526 \cdot 10^{-4}$	0.590%
4000-5000 m	55-60	0.0024	1.240%

Figure 47 shows the surface heat flux averaged over time and longitude for the first 400 years of the piControl against an observational product[44] (Keith Lindsay, personal communication, October 16th, 2019) with the same average between 1984 and 2006. We can see that the curves agree reasonably, with some differences, but the pattern and the values are comparable. NCAR performed this analysis as a part of the diagnostics package and evaluation of the simulation.

We can still associate the surface heat flux patterns in Figure 47 with characteristics of the general atmospheric circulation. It is possible to identify negative peaks around 60°, in both hemispheres, associated with low atmospheric pressure and moist winds. To the north and south of those low-pressure regions, dry climate is dominant. A different pattern is found around the equator. Although it is a region of moist winds, it is the one with high surface temperature values, favoring evaporation.

[44]According to Keith, the observational product was based on experiment a.b27.03, obtained from a CESM run with all data models. After the run, the computed fluxes from coupler output were extracted for these comparisons.

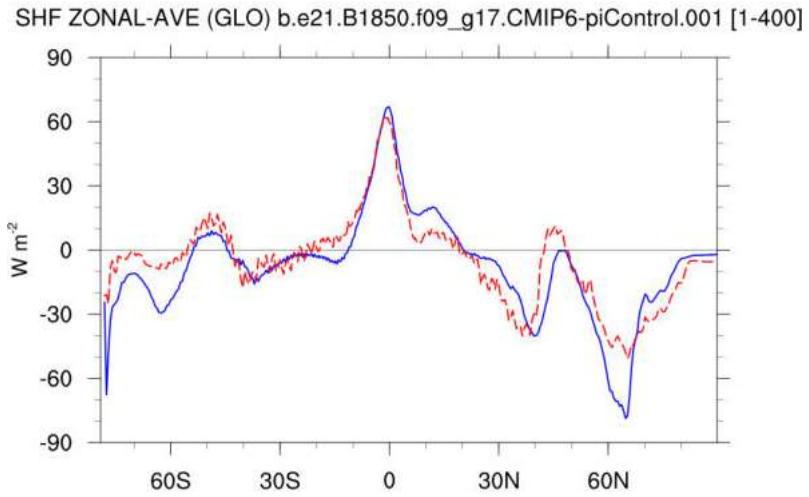

Figure 47: Latitudinal distribution of the surface heat flux for the first 400 years of the piControl (blue line) compared to observations (red line). Source: NCAR's piControl diagnostics package available at http://webext.cgd.ucar.edu/B1850/b.e21.B1850.f09_g17.CMIP6-piControl.001/ocn.

Since the analysis above is in good agreement with the observational product, and so, validated, Figure 48 shows the annual cycle of the surface heat flux globally and for both hemispheres. The heat flux presents positive values for the summer in each hemisphere, indicating heat gain, and negative ones for the winter, indicating heat loss. Additionally, we can see that the global cycle follows the south hemisphere's cycle. It is well known that the oceans work as a vast heat reservoir for the climate. Specifically, the southern hemisphere plays a significant role in this in comparison with the northern hemisphere, once the ocean/continent ratio in the south (4:1) is higher than in the north (1.5:1) (ASSAD, 2006). That is the reason the global cycle tends to follow the southern one. This result is in agreement with the ones on ASSAD (2006) and SANCHO (2014).

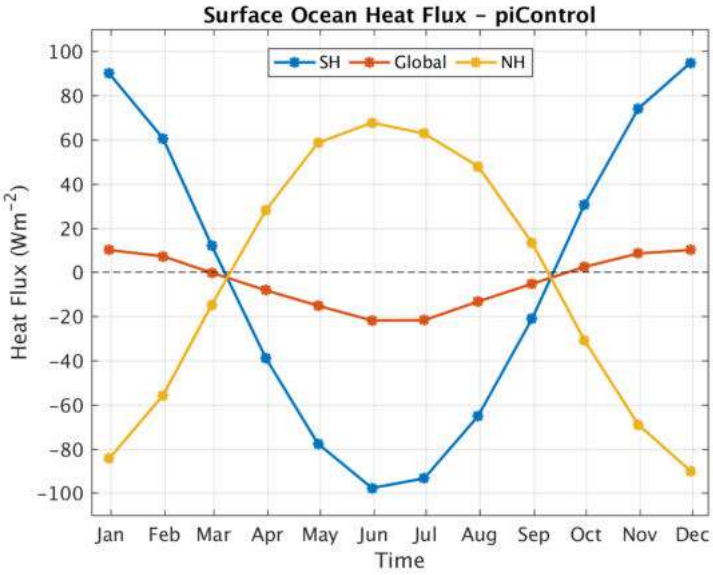

Figure 48: Average annual cycle of the surface heat flux for the entire globe, and separated by hemisphere. SH denotes Southern Hemisphere, and NH denotes Northern Hemisphere. The black dashed line marks the zero.

Climatological features were evaluated in the sections illustrated in Figure 41. Some of them regard the average advective heat (Equation (3.2)) and volume transports (Equation (3.3)) across Drake, AF-AA, and 25°S for the average of the whole period of the piControl. Figure 49 displays the volume transport profile on (a) Drake and (b) AF-AA. For the Drake Passage, practically the whole region presents positive volume transports, which translates as the seawater moving eastward. The same behavior occurs with the advective heat transport in this region (not shown here). This eastward flow is expected once the region is dominated by the eastward AACC, forced by the westerlies (CLARKE *et al.*, 2001; KAMPEL and SILVA JR, 1996; PICKARD, 1974; RUSSEL, 2006; TOMCZAK and GODFREY, 1994). Also, the value of this Vt integrated in the water column compares favorably with previous works (Table 18).

The AF-AA passage (Figure 49(b)) exhibits a less homogeneous transport profile. Still, its integrated Vt also agrees with the literature, and it flows eastward, as its advective heat transport, which can be seen in Table 18. There is a region in the south part of the section with westward transports, also found on SANCHO (2014). Another westward flow region is on the north part of the section, confined in shallower waters. This flow is consistent with the Agulhas retroflection and is an important source of warm and saline waters to the South Atlantic ocean (ANSORGE *et al.*, 2014; BEAL *et al.*, 2011; BIASTOCH *et al.*, 2009; GORDON, 2003; PETERSON and STRAMMA, 1991; REID, 1989; TALLEY *et al.*, 2011) and to the MOC (ANSORGE *et al.*, 2014; BIASTOCH *et al.*, 2009; GORDON, 2003; LUTJE-

HARMS and VAN BALLEGOOYEN, 1988; LUTJEHARMS, 2006). Although there are westward flows in this section, the eastward one prevails, and it is more intense on the north-central part of the section, where the water column is shallower.

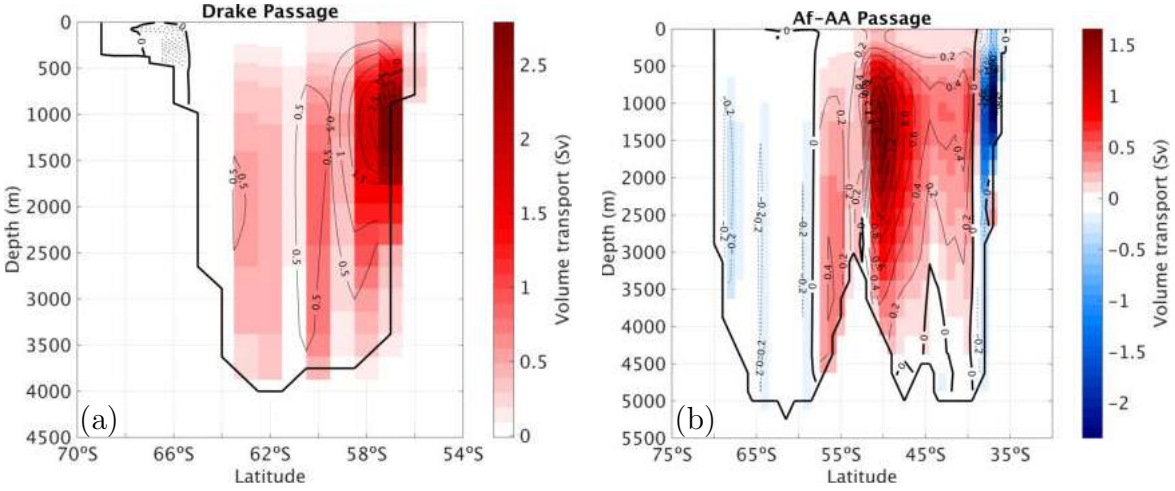

Figure 49: Volume transport profile for the average of piControl across (a) the Drake Passage and (b) Africa-Antarctic Passage. The colors depict the intensity and direction of the flow; red means eastward flow, and blue means westward flow. Additionally, contours show the transport values in Sv; continuous lines for eastward flows and dashed ones for westward flows.

The 25°S parallel is a different case from the Drake and AF-AA passages because, although its integrated Vt (Figure 50(a)) is negative, hence southward, its Ht (Figure 50(b)) is positive, hence northward, as can be seen on Table 18. This behavior is well known and makes the South Atlantic a unique ocean once it is the only one that carries heat from higher to lower latitudes (ASSAD *et al.*, 2009; BOLLMANN *et al.*, 2010; CAMPOS *et al.*, 1999; GANACHAUD and WUNSCH, 2000; GARZOLI and BARINGER, 2007; RINTOUL, 1991; SANCHO, 2014; SANCHO *et al.*, 2015; SROKOSZ *et al.*, 2012; STAMMER *et al.*, 2003; TALLEY *et al.*, 2011; ZHENG and GIESE, 2009; ZHU *et al.*, 2014). This behavior is counterintuitive because typically heat is carried from low to high latitudes, i.e., from the Equator to the poles (ASSAD, 2006; GRASSL, 2001; TALLEY *et al.*, 2011; TOMCZAK and GODFREY, 1994).

Table 18: Compendium of the Volume (Vt) and Heat transports (Ht) across known sections in the literature and their standard deviations when available. The bold letters next to the transport values indicate the direction: N - northward, S - southward, and E - eastward. Variations in the transport values may arise from slightly different positioning of the section, and different sources for each estimation. Source: Modified from SANCHO *et al.*, 2015.

Author	Section	Vt (Sv)	Ht (PW)
RINTOUL (1991)	**Drake**	130.00 ± 13.00 **E**	-
GANACHAUD and WUNSCH (2000)	**Drake**	140.00 ± 6.00 **E**	1.30 **E**
CUNNINGHAM *et al.* (2003)	**Drake**	136.70 ± 7.80 **E**	-
STAMMER *et al.* (2003)	**Drake**	124.00 ± 5.00 **E**	1.14 ± 0.06 **E**
	AF-AA	124.00 ± 6.00 **E**	1.01 ± 0.15 **E**
	32°S	0 ± 1.90	0.27 ± 0.25 **N**
	20°S	0 ± 1.60	0.27 ± 0.25 **N**
GARZOLI and BARINGER (2007)	**35°S**	-	0.60 ± 0.18 **N**
	34°20'S	-	0.49 ± 0.18 **N**
ASSAD *et al.* (2009)	**Drake**	141.30 ± 11.10 **E**	$1.52 \pm 0.80 \cdot 10^{-3}$ **E**
	AF-AA	143.90 ± 10.80 **E**	$0.98 \pm 0.40 \cdot 10^{-2}$ **E**
	32°S	-	0.60 ± 0.02 **N**
ZHENG and GIESE (2009)	**Drake**	-	1.65 ± 0.07 **E**
	AF-AA	-	0.94 ± 0.12 **E**
	30°S	-	0.59 ± 0.07 **N**
	20°S	-	0.69 ± 0.08 **N**
SANCHO (2014)	**Drake**	136.70 ± 11.19 **E**	$1.58 \pm 8.53 \cdot 10^{-4}$ **E**
	AF-AA	137.30 ± 10.52 **E**	$0.86 \pm 4.23 \cdot 10^{-3}$ **E**
	25°S	0.45 ± 0.30 **S**	$0.88 \pm 6.87 \cdot 10^{-3}$ **N**
ZHU *et al.* (2014)	**Drake**	177.00 **E**	1.77 **E**
	AF-AA	177.70 **E**	1.60 **E**
	30°S	0.46 **S**	0.01 **N**
	0°latitude	0.98 **S**	0.26 **N**
SANCHO *et al.* (2015)	**Drake**	132.73 **E**	1.77 **E**
	AF-AA	131.79 **E**	1.42 **E**
	25°S	0.38 **S**	0.72 **N**
KOENIG *et al.* (2016)	**Drake**	140.00 ± 10.00 **E**	-
This work	**Drake**	156.22 ± 0.44 **E**	1.58 ± 0.01 **E**
	AF-AA	153.02 ± 0.35 **E**	1.02 ± 0.01 **E**
	25°S	0.84 ± 0.06 **S**	$0.50 \pm 0.14 \cdot 10^{-2}$ **N**

According to TALLEY *et al.* (2011), the northward Ht in the South Atlantic happens to compensate for the vast amount of heat lost in subpolar NA and Nordic Seas with a northward flow of upper water. In contrast, this flow is returned southward through deep cold water, which is another form to define the AMOC. When we look at the contour lines of the stored heat in MJ[45] over the Ht in the 25°S parallel section (Figure 50(c)), we can see that most of the heat is concentrated in the upper 1000 m, a layer that has most of the Ht moving northward. The stored heat in the upper 1000 m is one order of magnitude higher than the rest of the

[45] 1 J = 1 kg·m^{2}s^{-2} and 1 MJ = 10^6 J.

section (135.73 GJ[46] from the surface to 1000 m and 12.60 GJ from 1000 m to the bottom).

Still, in Figure 50, we can identify several known features close to the Brazilian coast (west limit of the section). From the surface to the bottom, there is the southward flowing Brazil Current (BC), the northward-flowing AAIW (CLARKE *et al.*, 2001; RINTOUL, 1991), the southward flowing NADW in deep layers and the northward-flowing AABW close to the bottom (LIMEBURNER *et al.*, 2005; SPEER and ZENK, 1993).

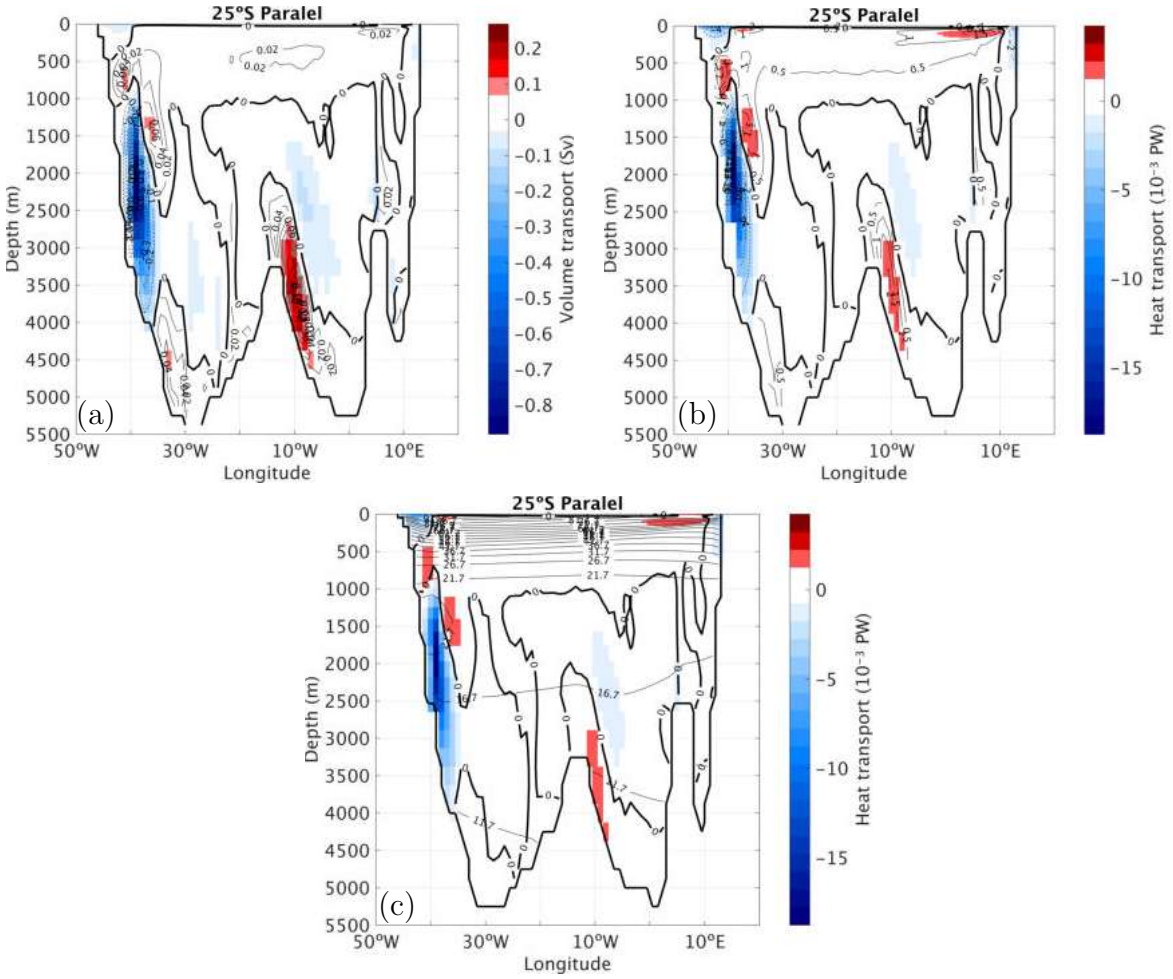

Figure 50: (a) Volume and (b) advective heat transport profiles, and (c) advective heat transport (color) with stored heat contour lines for the average of piControl across 25°S parallel. The colors depict the intensity and direction of the flow; red means northward flow, and blue means southward flow. Additionally, in (a) and (b), contours show the transport values in Sv; continuous lines for northward transport and dashed ones for southward transport.

Figure 51 represents the potential temperature (upper panel), salinity (central panel) and potential sigma (lower panel) distributions on the water col-

[46] 1 GJ = 10^9 J

umn for the zonal average of a meridional set of sections in the Atlantic Ocean between 20°W and 25°W (Figure 41 in section 3.5.1). This set of sections was chosen after the work of TALLEY *et al.* (2011) and span from the South to the North Atlantic. The isolines in each panel represent the top of water masses using the values in Table 15 in section 3.5.1.

The profiles show distributions that are in agreement with the literature. The temperature profiles represent NADW with cold temperatures and deep depths, and its rise in the southern hemisphere as seen by TALLEY *et al.* (2011). The AABW is shown exiting the South Atlantic towards the bottom of the ocean, also seen by TALLEY *et al.* (2011). AAIW appears with less cold temperatures, but can be seen more clearly on the salinity profile (central panel), which appears leaving the South Atlantic as a salinity minimum, also represented in FRAJKA-WILLIAMS *et al.* (2019), TALLEY *et al.* (2011) and TOMCZAK and GODFREY (1994). The sigma profile displays the correct order of each water mass along the water column according to its thermohaline index (Table 15).

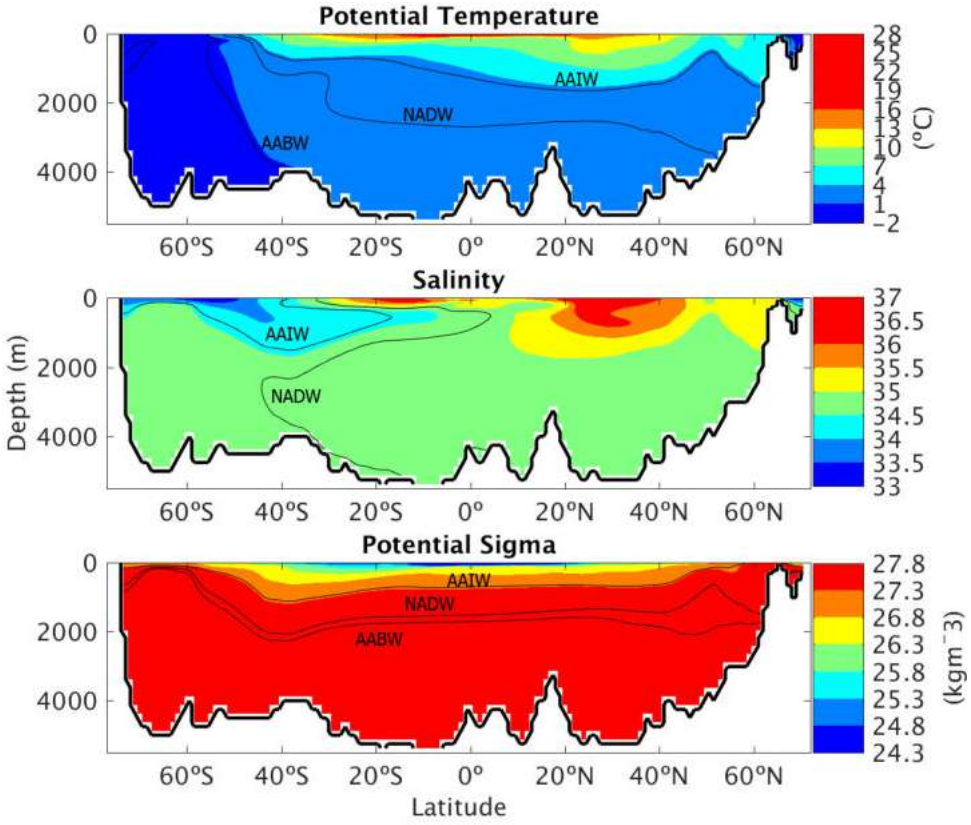

Figure 51: Potential temperature (upper panel), salinity (central panel), and potential density (lower panel) profiles in a cross-ocean average of sections between 20°W to 25°W. Additionally, the contours depict the water masses' identifications.

Another important climatological feature is the seasonality of the BMC displayed in Figure 52 and obtained through the average of the whole period of (a)

piControl and (b) the CMEMS product (item 3.4.3). This confluence is formed on the encounter of the warm, southward flowing BC and the cold northward-flowing Malvinas Current (MC) (CARLSON *et al.*, 2008; CATALDI, 2008; TALLEY *et al.*, 2011). It is an important feature not only because of the BMC and the SST distribution but the MC is formed as a branch of AACC after it passes the Drake Passage (CATALDI, 2008; FETTER and MATANO, 2008). Additionally, the seasonality of the BMC reflects the influence of the South Atlantic Subtropical High and the South Atlantic Subtropical Gyre.

The BMC is seasonal, as said earlier, and it is shifted southward in the summer, due to the strengthed BC and northward in the winter, due to the strengthed MC (CAMPOS *et al.*, 1999; PICKARD and EMERY, 1990). The strengthening of BC in summer is associated both with intensified trade winds (RODRIGUES *et al.*, 2007) and the shift of the bifurcation northwards (CARLSON *et al.*, 2008; TOSTE, 2017). We can see in Figure 52(a) and (b) that the SST distribution is similar, although generally higher in CMEMS than in piControl. Nonetheless, the confluence, identified mainly by the 18°C contour line, presents seasonality, and it is located near 42°S in summer and near 36°S in winter for both products. The RMSE Figure 52(c) displays higher values where the two currents interact dynamically and may be associated with the higher horizontal resolution used in CMEMS, which provides finer representations that are not possible in piControl. Despite that, piControl was able to represent both currents and the seasonality of the BMC.

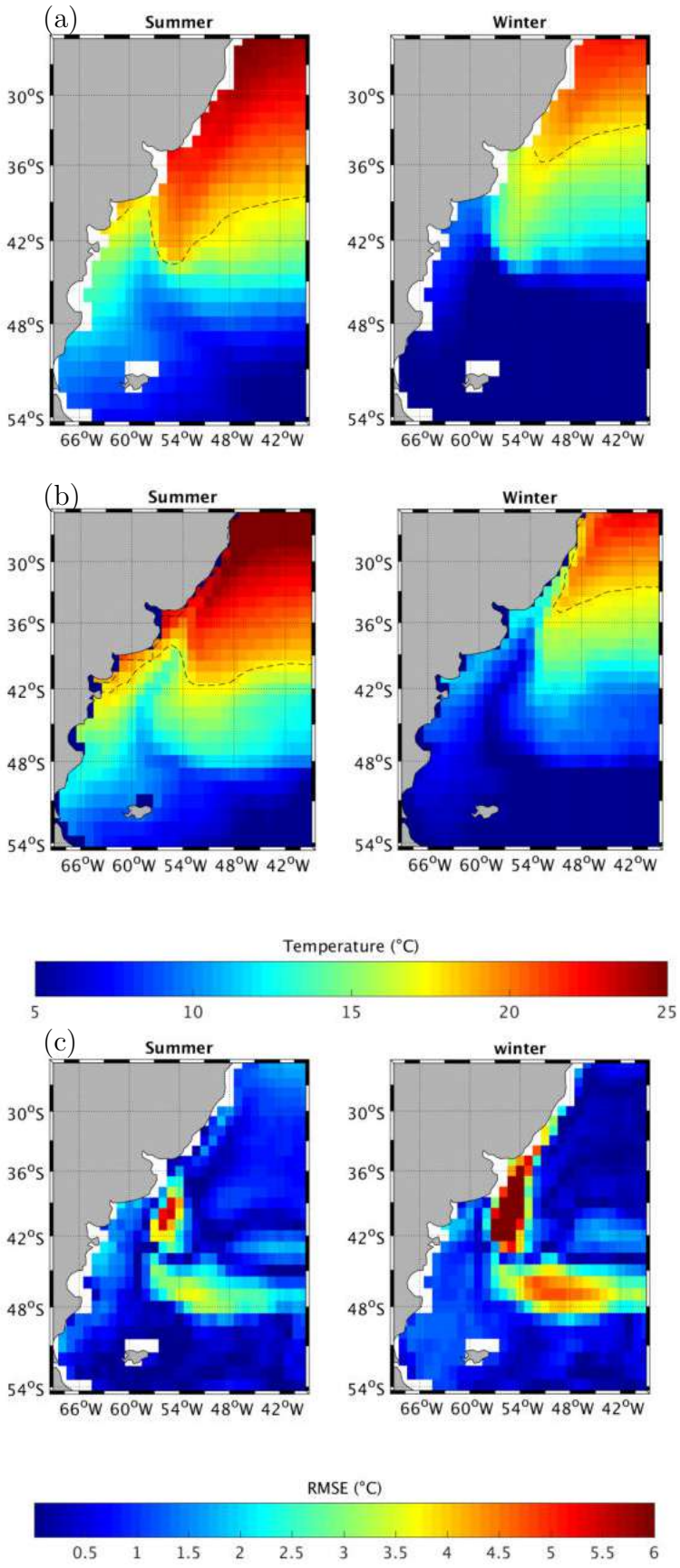

Figure 52: Seasonality of the Brazil-Malvinas Confluence in summer and winter for the (a) average of piControl and (b) average of CMEMS product. The black dashed line represents the 18°C isoline delimitation. Additionally, (c) depicts the RMSE between them.

Figure 53 illustrates the zonal mean distributions of sea level pressure and surface temperature from the atmosphere model of the piControl experiment in comparison with ERA-Interim (item 3.4.1), also used in the work of STAMMER *et al.* (2018) and Reanalysis 2 (item 3.4.2). For all panels, the piControl agrees in pattern as in values with the reanalysis products in mid and low latitudes, diverging a little towards the poles. That divergence is not particular of the piControl once even the reanalysis presents differences between them. The difficulty to properly represent high latitudes is related to some reasons. One of them being the lack of observations for model data assimilation (LAZZARA *et al.*, 2014; SMITH *et al.*, 2019). Another one is the meridian convergence in grid models, which poses a difficulty for the numerical model to resolve quantities in a single point (STANIFORTH and THUBURN, 2012). Besides that, in low latitudes, the fast and easier-to-calculate barotropic modes are dominant. On the other hand, in high latitudes, the baroclinic modes are dominant, which poses another challenge for numerical models.

For the sea level pressure, there is good agreement in the high-pressure belts positions for summer and winter, with differences less than four hPa between them. From summer to winter, there is a northward shift of these high-pressure belts, described in PEIXOTO and OORT (1992); the southern hemisphere shift from near 30°S in summer to near 20°S in winter due to the northward shift of the ITCZ in winter, and the northern hemisphere shift from near 30°N in summer to near 40°N in winter. For both periods, the low-pressure belts also exhibit northward shifts according to the literature (PEIXOTO and OORT, 1992).

The surface temperature latitudinal distributions follow the expected patterns. They agree with the literature (PEIXOTO and OORT, 1992) with lower (higher) temperatures in mid and high latitudes for winter (summer) in each hemisphere. Near the Equator, there is not much change in temperature between summer and winter. Towards the poles, the results diverge a little, mainly for Reanalysis 2 near Antarctica. It is also interesting to notice that the temperature difference between summer and winter is more significant in the northern hemisphere, which can be associated with the higher continent-ocean ratio in that region. That would favor higher temperature changes in comparison with the lower continent-ocean ratio region.

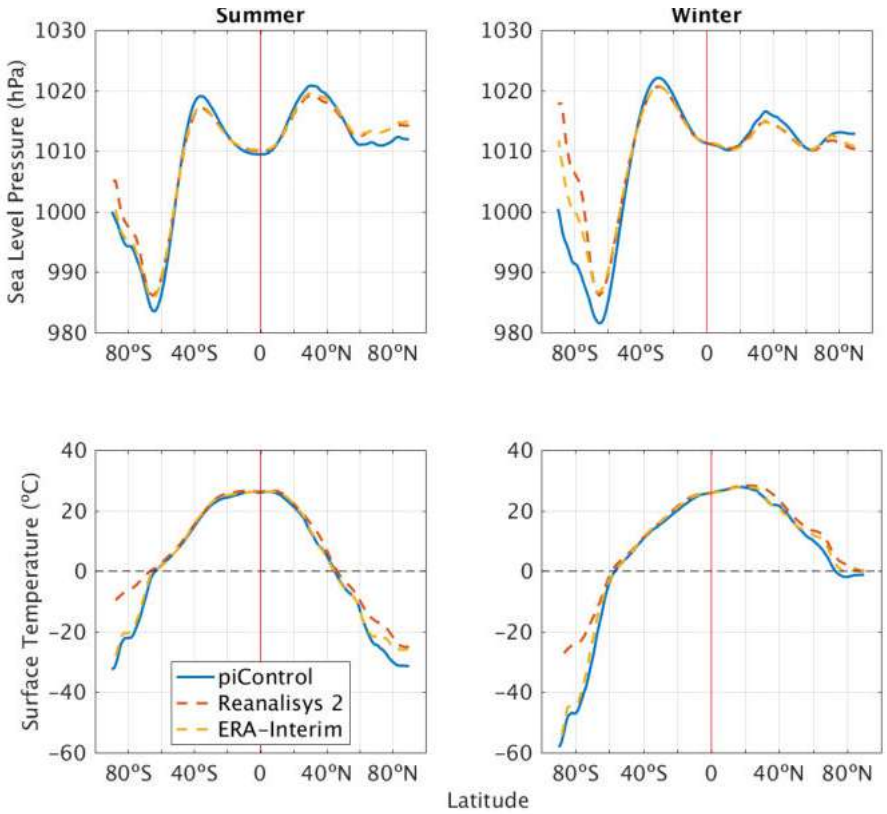

Figure 53: Zonal mean distributions of sea level pressure (upper panels) and surface temperature (lower panels) in summer (left panels) and winter (right panels) for the average of piControl experiment against Reanalysis 2 and ERA-Interim. Additionally, the red line marks the equator, and the zero is marked as the black dashed line on the surface temperature.

The sea ice concentration on piControl was validated through its annual climatology in comparison with NSIDC data (see item 3.3.1) for both north and south hemispheres (Figure 54). For the NSIDC data, only whole years were used, so the first two months and the last six were discarded, and the average was made from January 1979 to December 2017 (39 years). For the piControl, the 500 years of the simulation were averaged.

For the southern hemisphere, we observe that the piControl is in good agreement with the NSIDC, both in pattern and values and presents low RMSE values (Figure 55), higher than zero mainly where the piControl simulation has more ice than the NSIDC data in the summer and less in the winter. Despite that, the average RMSE is around 1% (Table 19), and the correlation between the piControl and the NSIDC data is 98.52%. These slight differences may be related to the model's capacity to represent the velocity of the sea ice formation/melting or to a modification in this velocity because of the emissions of GHGs, which increased since the Industrial Revolution. That modification of the climatological pattern of sea ice formation is represented in the observed data and not in the simulation.

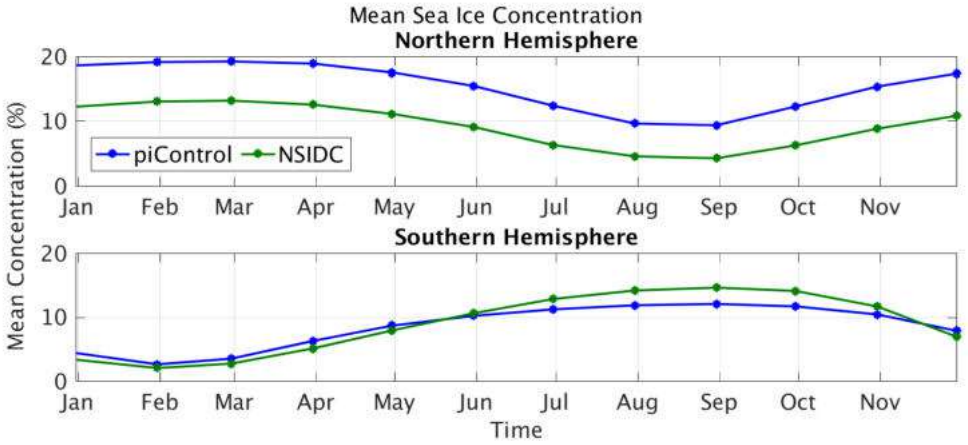

Figure 54: Time series of sea ice concentration for the northern (upper panel) and the southern (lower panel) hemispheres for the average of piControl and NSIDC data.

The pattern of the northern hemisphere climatology for the piControl is in good agreement with the NSIDC data throughout the year. It exhibits a correlation of 99.54%, with differences in the mean concentration values (Figure 55 (upper panel) and Table 19). Although the differences are appreciable, they may be associated, again, with the period in which the NSIDC averages were taken; after the Industrial Revolution and under higher emissions of GHG than before it. That way, the lower sea ice concentration values may be simply due to less sea ice in this period, in consequence of higher GHG emissions.

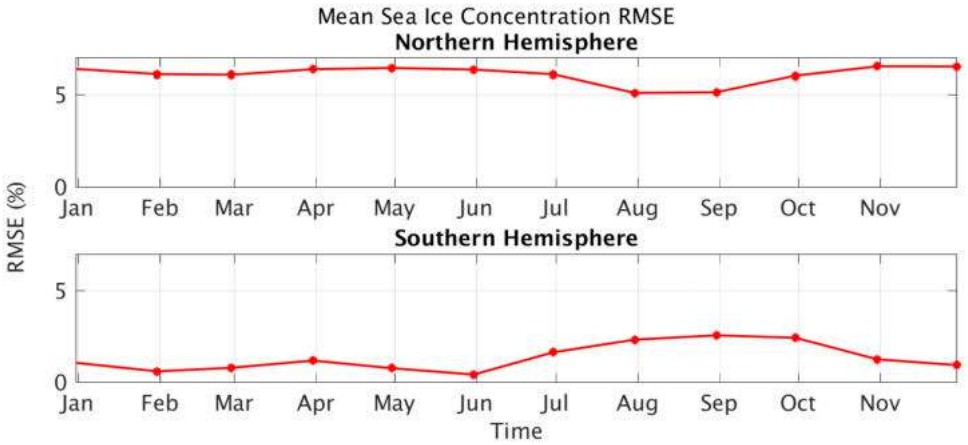

Figure 55: RMSE time series for sea ice concentration of Figure 54 for the northern hemisphere (upper panel) and the southern hemisphere (lower panel).

For both hemispheres, the sea ice concentration follows the climatology, with minimum values in September (February) for the northern (southern) hemi-

sphere (HOLLAND *et al.*, 2006; LIQUE *et al.*, 2018; SANCHO, 2014). Additionally, according to the NSIDC User's Guide regarding the data used, ice concentration values are sensitive to the algorithm used to calculate them, and the 15% cutoff for assessing the presence or absence of ice also influences, once a larger or smaller cuts produce different results.

Table 19: Average, minimum, and maximum RMSE values in % of the RMSE time series of Figure 55.

	Northern Hemisphere	**Southern Hemisphere**
Average	6.0776	1.3140
Minimum	5.0703	0.4035
Maximum	6.5104	2.5508

According to the above analysis, piControl is considered validated as it was able to exhibit several climatological characteristics not only of the ocean but also of the atmosphere and sea ice. Thus, piControl is suitable to be used to make comparisons with the 1pctCO_2 experiment, which will be covered in the next items. Additionally, more validations of piControl can be found in DANABASOGLU *et al.* (2020) and in the NCAR's piControl diagnostics package.

4.2 AMOC Tipping Point

To investigate the occurrence of a tipping point on the AMOC, the methodologies of LENTON *et al.* (2008), presented on item 2.4.1 and BAKKER *et al.* (2016), exposed on item 2.5 were used. Figure 56 illustrates the global mean surface air temperature of piControl and 1pctCO_2 experiments along with CO_2 forcing used on both experiments. We can see that the global surface air temperature on piControl is reasonably stable, oscillating between 13 and 14°C, with an average of ∼13.88°C. This temperature is comparable to the 1951-1980 average value of 14°C from HANSEN *et al.* (2010). The authors estimated this value through observations and filled the gaps with global climate model results where those observations were not available. Although HANSEN *et al.* (2010) relate that this estimation has significant uncertainty, they state that it is consistent with previous results.

As the CO_2 increases in the 1pctCO_2 experiment, so does the surface temperature, which exhibits a fast and continuous increase. The average increase temperature rate is ∼0.04°C·year^{-1}, or ∼3.3°C·century^{-1}, similar to the results of MANABE and STOUFFER (1999) of ∼3.5°C·century^{-1} that also simulated a 1% CO_2 increase with a climate model. The surface air temperature increase in the 1pctCO_2 experiment is highly correlated (∼99%), with the CO_2 forcing increase. In the end, the average global surface air temperature is ∼19.85°C, almost 6°C more

than the average in piControl and exceeding in almost 4°C the 2°C climate threshold (COSTELLO *et al.*, 2009; DRIJFHOUT *et al.*, 2015; MANN, 2009; MASSON-DELMOTTE *et al.*, 2018; NORDHAUS, 1975; RANDALLS, 2010; VUUREN *et al.*, 2011).

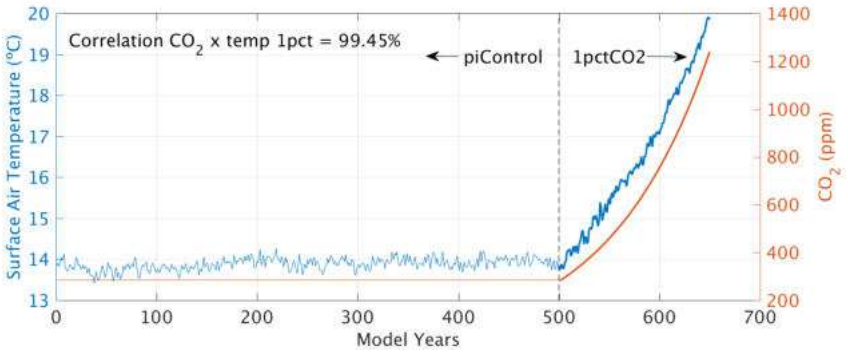

Figure 56: Annual global mean series of surface air temperature and CO_2 forcing used in piControl and 1pctCO_2. The thin lines regard the piControl and the bold ones the 1pctCO_2 experiment. The left y-axis shows the surface air temperature for the blue lines, and the right y-axis shows the CO_2 concentration for the orange lines. Additionally, it is shown the correlation coefficient between the series of surface air temperature and the atmospheric CO_2 forcing in 1pctCO_2.

LENTON *et al.* (2008) propose a methodology to identify tipping points, as described in item 2.4. Their work stipulates some control parameters and critical values for each tipping element (Table 7). According to the authors, the global warming necessary for the THC to pass through a tipping point would be an increase of 3-5°C of the global air temperature above 14.05°C, which would be the average of 1980-1999 stipulated by IPCC (2007).

Considering the average increase rate of ∼0.04°C·year^{-1} plus the difference between the piControl and the 1980-1999 averages, the necessary warming would be achieved after year 80 of the 1pctCO_2[47]. In fact, in year 101, the air temperature is 3°C higher (17.16°C) than the 1980-1999 average (∼14.05°C), and in year 137, it is 5°C higher (19.14°C).

This increase in global air temperature would have to be associated with a freshwater input to the NA of 0.1-0.5 Sv. Several works relate the importance of the freshwater flux on AMOC and how changes in this parameter could affect this circulation (JOHNSON *et al.*, 2019; RAHMSTORF, 1995; STOCKER and WRIGHT, 1991; TALLEY *et al.*, 2011; WUNSCH, 2002). The work of MANABE and STOUFFER (1999), among other results, discuss the implications of an abrupt climate change on the THC, as stated earlier. To achieve that purpose, the authors perform

[47] Which would correspond to year 580 if we consider a continuous-time series.

a hosing experiment, adding 0.1 Sv of freshwater into high latitudes of NA, specifically between 50°N and 70°N. In the present work, the freshwater input analysis was evaluated in the same region, represented in Figure 43 of section 3.5.1. The region is very similar to the one used in MANABE and STOUFFER (1999) (see Fig. 2 of the authors). For this analysis, we reference the results as the freshwater flux into the NA, but they are restricted to the region of Figure 43.

Figure 57 presents the time-average of the total surface freshwater flux to the NA in the piControl in mSv. The upper panel displays the negative values of freshwater input, and the lower one displays the positive values of the freshwater input. The freshwater distribution was divided into two panels to facilitate visualization of both since negative fluxes are two orders of magnitude lower than the positive ones.

The distribution of freshwater flux signal in piControl is in agreement with the works of FORRYAN *et al.* (2019) and MCDONAGH *et al.* (2015). Although there are a few regions of negative freshwater flux, mainly near Ireland and between Sweden and Finland, on most NA, the freshwater flux is positive, indicating a gain of freshwater by the ocean, which reduces surface salinity and, hence, buoyancy. Still, on the positive distributions, most of the region has low freshwater input values, with higher values near both sides on the south of Greenland and the east coast of North America.

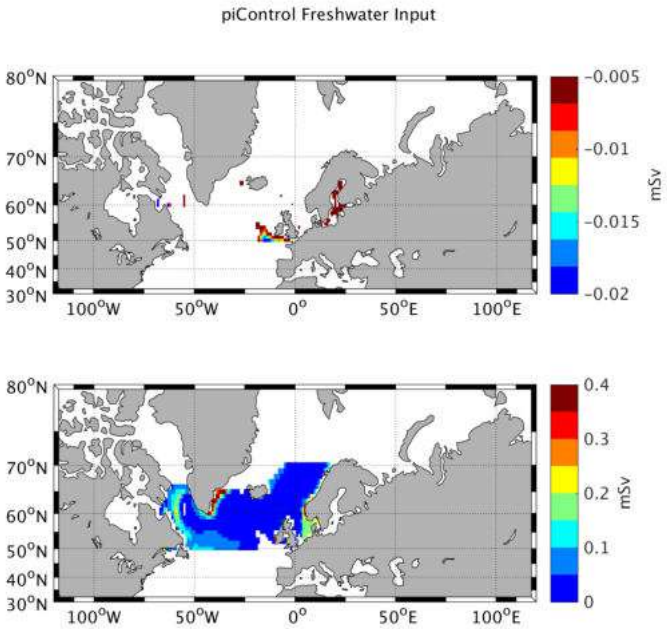

Figure 57: Average freshwater flux on the NA, between 50°N and 70°N, for piControl. The upper panel displays negative input, and the lower panel displays positive input. The results were divided into two panels to facilitate visualization due to the different orders of magnitude between positive and negative values.

Figure 58 presents the freshwater flux anomaly for the last decade of the 1pctCO$_2$ experiment (average of years 141-150). The anomaly is mainly positive, meaning an increase in the freshwater flux in the last decade of 1pctCO$_2$ experiment compared to the piControl; behavior also occurring at present-day climate (LENTON *et al.*, 2019). Negative values were found in the north of Iceland and the regions of the highest positive freshwater fluxes in Figure 57. The negative anomalies are located in critical regions for the NADW formation. Hence, these changes may trigger modifications in this mechanism like the weakening identified in this work and showed in later analyzes.

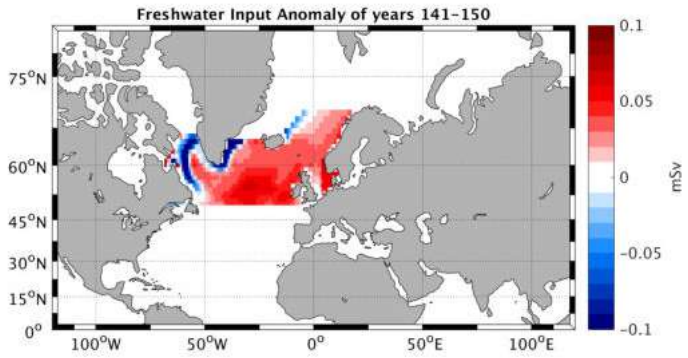

Figure 58: Last decade (141-150-mean) anomaly of the 1pctCO$_2$, compared to the 500 year-mean piControl for the freshwater flux. Positive (negative) values mean more (less) freshwater flux in the last decade of 1pctCO$_2$ compared to the average period of piControl.

To complement the analysis above and evaluate the contributions from the parameters of the freshwater calculation (Equation (3.5)), Figure 59 presents the average time series for the variables used to calculate it. The salt flux is not shown here because it is directly related to the sea ice melting flux time series with a correlation between them of 99.72% and a similar reduction in the last decade of the 1pctCO$_2$ experiment of 92.52%.

The sea ice parameters show a decrease throughout the series and similar reduction percentages, but they are not highly correlated, indicating different forcings acting on each one. On the other hand, runoff flux displays increase throughout the series, and the evaporation flux exhibits a decrease throughout the series. The precipitation flux presents some increases and decreases along the 150 years of the 1pctCO$_2$ experiment. However, the last decade average presents a value similar (18.10 mg$\cdot$m$^{-2}\cdot$s^{-1}) to the piControl mean (18.00 mg$\cdot$m$^{-2}\cdot$s^{-1}).

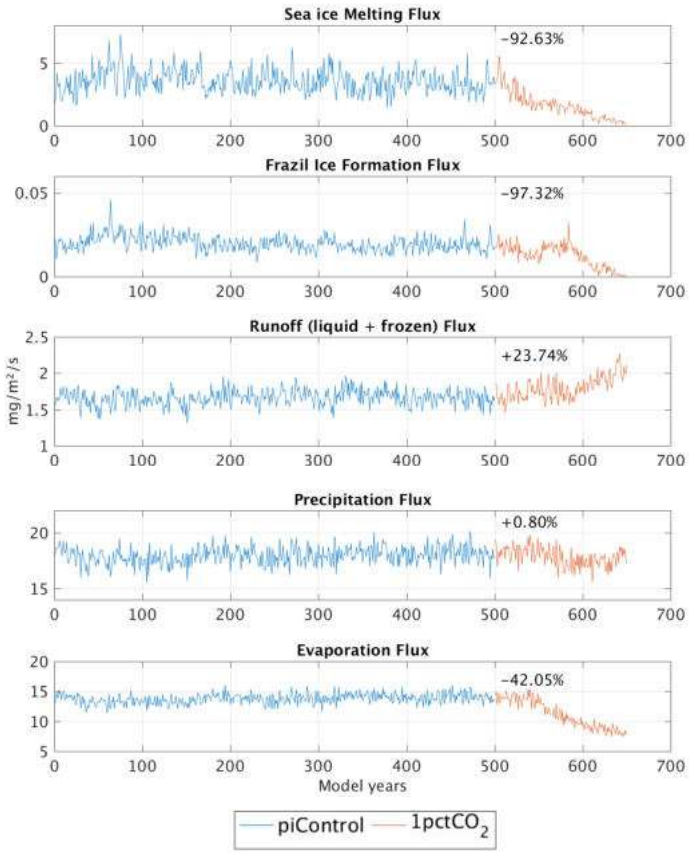

Figure 59: Annual mean series of the parameters used to calculate freshwater. Additionally, in each time series box, there is the percentage of increase (+) or decrease (-) in the last decade of the 1pctCO$_2$ experiment compared to the average of piControl. The evaporation flux is a parameter intrinsically negative, once is the amount of freshwater being lost by the ocean. Nonetheless, it has been represented as a positive flux only to facilitate analysis and visualization.

It is important to notice that despite the absolute values of each flux and their changes, the variables related to sea ice presented reductions near 100%. This percentage of reduction can be problematic once the sea ice is essential for climate (BITZ *et al.*, 2005) because, among others, it participates in the albedo feedback, and it has the potential to increase Global Warming (SCHNEIDER and DICKINSON, 1974).

Figure 60 (upper panel) presents the time series of the mean freshwater input in piControl (blue line), and it can be seen that the time series is reasonably stable. To determine whether the 1pctCO$_2$ experiment increased the freshwater input, we need to compare it to the mean value of piControl, and so all the values higher or lower than $3 \cdot \pm\sigma$ were excluded to avoid unrealistic high or low average values. That way, the mean piControl freshwater input value is 0.024 Sv. Figure 60 (upper panel) additionally displays the time series of the mean freshwater input in 1pctCO$_2$ (orange line), and its behavior is not as stable as the piControl's. There is

a decrease in the first 50 years and then an increase. There is a period of apparent stabilization after year 600 and then another increase. Since the 1pctCO$_2$ freshwater time series is variable, to evaluate its increase over time and avoid an isolated positive, the 1pctCO$_2$ anomaly was divided in decades, and it is shown in the lower panel of Figure 60.

It can be seen that the threshold of 0.1-0.5 Sv is not achieved by the end of the 1pctCO$_2$ experiment. The last decade's anomaly is ∼0.009 m·Sv, which is much lower than the increase needed to satisfy LENTON *et al.* (2008)'s threshold. Nonetheless, this freshwater input amount caused significant changes in the AMOC cell and its dynamics, which will be presented and discussed in the following analysis.

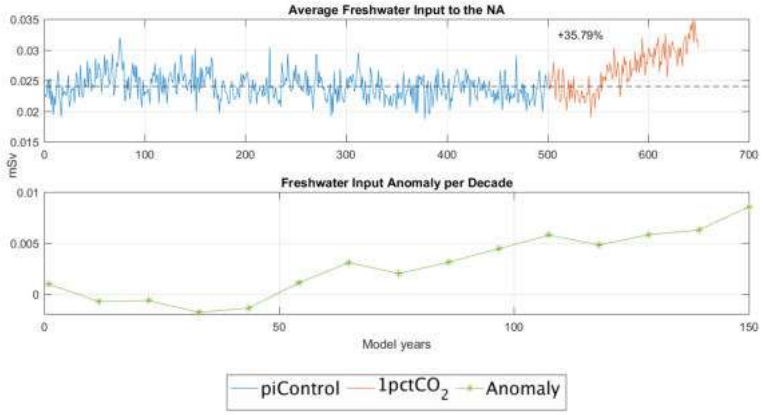

Figure 60: Freshwater input time series for piControl and 1pctCO$_2$ (upper panel) and decadal freshwater input anomaly (lower panel). The dashed black line in the upper panel represents the mean value of the freshwater input in piControl. To evaluate the changes in freshwater input in the 1pctCO$_2$ experiment, decadal anomalies were calculated, excluding values higher and lower than $3 \cdot \pm\sigma$. Additionally, the percentage of increase in the last decade of the 1pctCO$_2$ experiment is displayed.

As we have seen, the freshwater input is a balance of several parameters (Figure 59), which changes can act increasing or decreasing the freshwater flux. A decrease in sea ice melting acts to decrease the freshwater flux to the ocean. On the other hand, a decrease in frazil ice formation and the evaporation flux and an increase in the runoff flux contributes to increasing the freshwater flux to the ocean. However, as each parameter exhibits different ranges, the percentage of change is not helpful to evaluate which parameter or set of parameters most contributed to changes in freshwater input. That way, Table 20 displays the absolute values of each contribution to the freshwater flux in the last decade of the 1pctCO$_2$ experiment.

Table 20: Contributions of each parameter to the freshwater flux in the last decade of the 1pctCO_2 experiment. The (+) sign means contributions to increase freshwater, and the (-) sign means contributions to decrease it.

Parameter	**Contribution in mg·m^{-2}·s^{-1}**
Sea Ice Melting	-3.30
Salt	-0.01
Frazil Ice Formation	+0.02
Runoff	+0.39
Precipitation	+0.14
Evaporation	+5.80

We notice that the decrease in the evaporation flux was the main factor in the increase in freshwater flux despite the contribution of sea ice melting flux to decrease it. Moreover, although the contributions of these two variables are of opposite sign, they may be physically related. The decrease in evaporation may have responded to the colder SST distribution at the end of the 1pctCO_2 experiment (Figure 61), which is similar to the distribution of the positive anomaly of freshwater flux in the last decade of this same experiment. Also, colder SSTs probably led to the reduction in sea ice melting near Greenland, thus explaining its decrease. This region of colder SSTs may be related to the advection of cold surface Arctic waters due to the intensification and southward extension of east Greenland current, as shown in the work of MANABE and STOUFFER (1999).

Evaporation flux and sea ice melting flux showed a correlation of 81.86%, which indicates some relation between them. It is interesting to notice that these two variables work in opposite directions to change freshwater, and thus the AMOC, and the same feature (SST) triggered changes in both of them. Thus, the fact that one feature may trigger changes that work to weaken and strengthen the AMOC cell could be one of the reasons to explain its stability through climate change forcings.

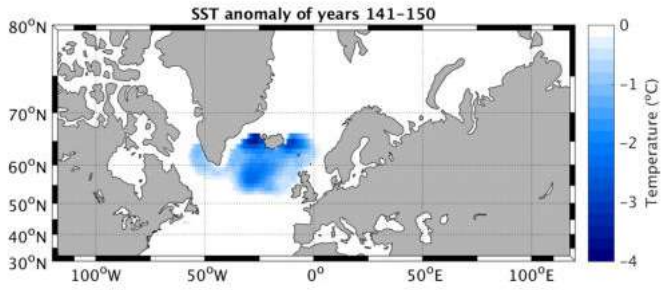

Figure 61: Last decade (141-150-average) negative anomaly of the 1pctCO_2, compared to the 500 year-average piControl for the sea surface temperature. Negative values mean colder surface temperature in the last decade of 1pctCO_2 compared to the average period of piControl.

Regarding the methodology proposed by LENTON *et al.* (2008), the Global Warming necessary for the THC to pass through a tipping point was achieved, but the freshwater input was not. Despite this behavior of the freshwater, lower than the expected for a tipping point in the THC, there were some significant changes in AMOC, as stated earlier, and such changes are going to be analyzed next.

According to LENTON *et al.* (2008), the feature of the THC tipping point would be a decrease in the overturning. Evaluating some parameters that characterize this overturning, Figure 62 presents fields of the mixed layer depth anomaly at March on the North Atlantic for three different averaged decades: the first one (years 1 to 10), the middle one (years 71-80) and the last one (years 141-150).

Positive values indicate an increase in mixed layer depth, and negative values indicate a decrease. March was chosen for being climatologically the month when the mixed layer at the North Atlantic is deeper (CARTON *et al.*, 2008; LARGE *et al.*, 1997; LIQUE *et al.*, 2018), and it is widely used in the literature (e.g., LIQUE *et al.* (2018); LOHMANN *et al.* (2009); MAURITZEN and HÄKKINEN (1997), and others). We can notice, in the first decade, a signal of increase in the Labrador Sea, west of Greenland and the Norwegian Sea, and no significant signal on the rest of the ocean. Advancing in time shows the shallowing of the mixed layer, mainly around the Labrador and Norwegian Seas - essential regions for the NADW formation and, hence, the AMOC (COLLING, 1989; TALLEY *et al.*, 2011) - and southeast of Greenland.

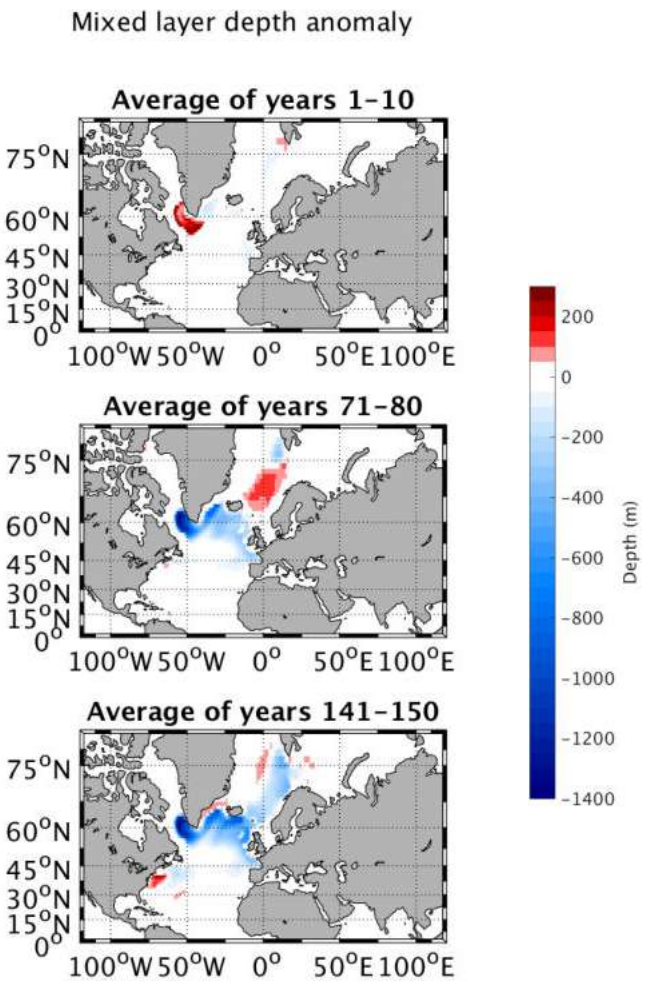

Figure 62: Mixed layer depth anomaly in March for average years 1-10, 71-80, and 141-150 compared to the average of the piControl experiment. Positive (negative) values indicate an increase (decrease) in the mixed layer depth.

Isolating the main areas identified by strong negative anomalies in Figure 62, four areas were chosen to be monitored and are depicted in Figure 44 of section 3.5.1. Besides being the locations with negative anomalies in Figure 62, these areas are also the main areas where the NADW is formed (COLLING, 1989). Additionally, Area 1 is also monitored in YEAGER and DANABASOGLU (2014).

Taking the maximum value from each area at each time for both experiments gives us the time series of the maximum mixed layer depth for March at each area (Figure 63). We can see for the piControl that all four areas are relatively stable. Area 1 exhibits high variability and depths greater than 1000 m for most of the series - which agrees with GRASSL (2001) and TALLEY *et al.* (2011) about deep convection regions having mixed layer depths of up to 2000 m. The high variability in Area 1 may be related to its location for being a region between continental masses. Areas 2, 3, and 4 are shallower than Area 1 (Table 21), and Area 3 is the least variable of them all.

For the 1pctCO$_2$ time series, all areas exhibit a strong shallowing at some point, different for each one, and they lose most of its variability, as can be seen in Figure 64. Table 21 shows the percentage of reduction in the mixed layer depth in the last decade in each area. It can be seen that Area 1 is the first one to present this strong shallowing, and the others follow it, as also seen by MUNTJEWERF *et al.* (2020b). Also, Area 1 is 82.55% correlated with Area 2, and this one is 85.41% correlated with Area 3. Lastly, Area 4 is correlated with 78.48% with Area 3.

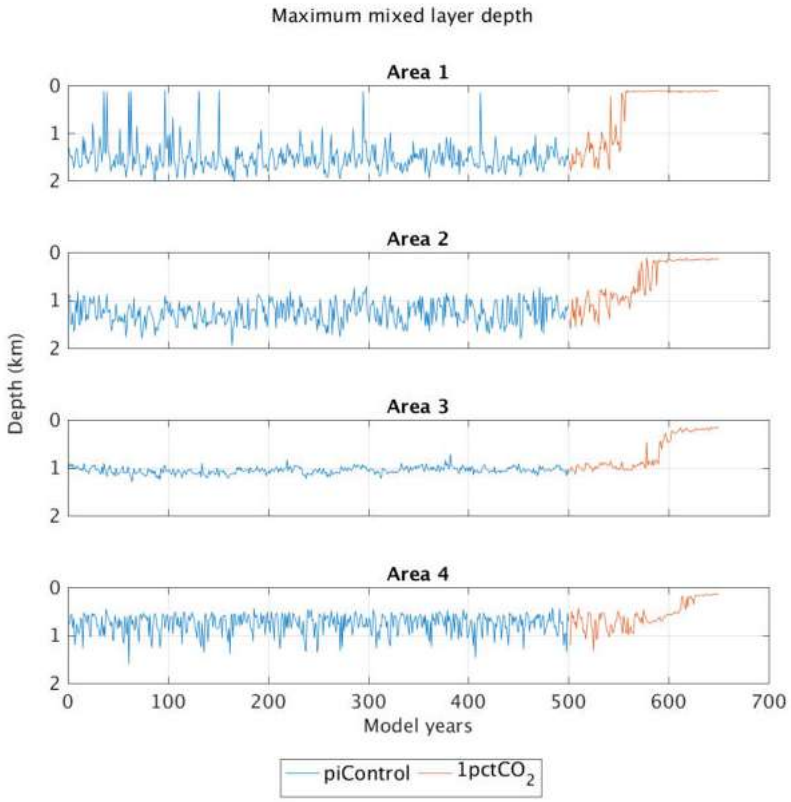

Figure 63: Maximum mixed layer depth time series in March for each area in piControl and 1pctCO$_2$.

The pattern of mixed layer depth change and the correlations may indicate that Area 1 influences on Area 2, which influences Area 3, and this last one influences Area 4. We can also see in Table 21 that the percentage of reduction in depth decreases from Area 1 to Area 2, 3, and 4. So, from Area 1 through Area 4, the abrupt shallowing of the mixed layer depth happens latter, smoother, and less critically. Additionally, Figure 64 presents the percentage of variability loss at the end of the 1pctCO$_2$, and we can see that in all Areas, the variability is practically reduced to zero, which means the deep convection is shut down. Similar behavior of a shut down in Labrador Sea convection was also observed by DRIJFHOUT *et al.* (2015) and MUNTJEWERF *et al.* (2020b). DRIJFHOUT *et al.* (2015) report that the shutdown was provoked by the warming and freshening and associated surface

density decrease in NA convective areas. The mixed layer depth and convection behavior in these areas are expected in a GHG forcing climate (BAKKER *et al.*, 2016; DRIJFHOUT *et al.*, 2015; GREGORY *et al.*, 2005; ZHANG and WU, 2012).

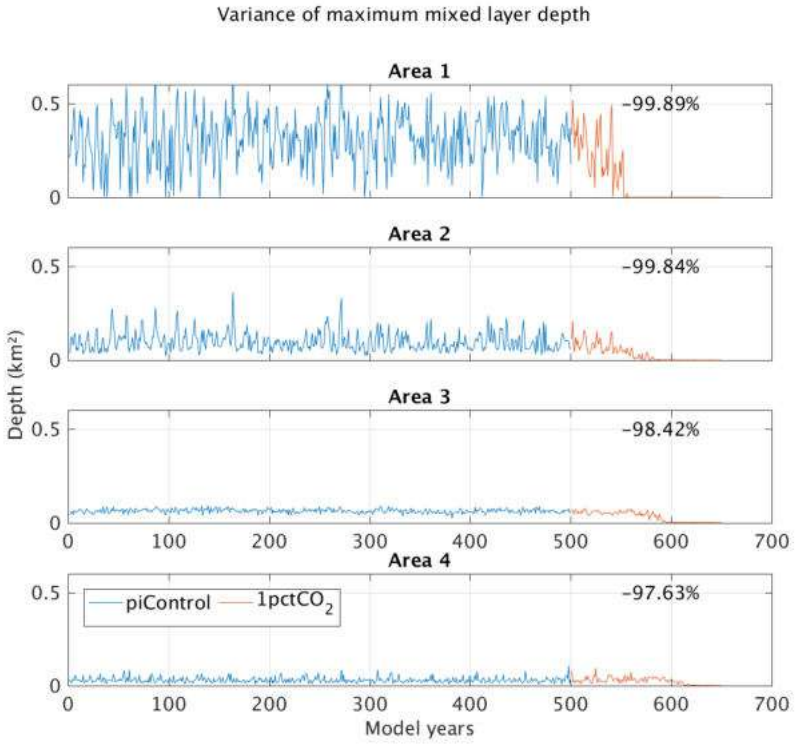

Figure 64: Variance time series (in km^2) for the mixed layer depth of Figure 63. The texts inside the time series represent the reduction in the variability in the last decade of the 1pctCO$_2$ experiment.

Table 21: Mixed layer depth changes in the last decade in 1pctCO$_2$. The % of reduction refers to the piControl depth mean.

Area	**piControl mean (m)**	**1pctCO$_2$ last decade (m)**	**% reduction**
A1	1518.28	116.17	92.35%
A2	1268.41	142.21	88.79%
A3	1055.24	169.26	83.96%
A4	758.00	148.51	80.41%

If we analyze the Atlantic basin meridional transport streamfunction for the last decade in each experiment, following BRYAN *et al.* (2007), it can be seen, in Figure 65 (upper panel), that the piControl profile is similar not only to the work of BRYAN *et al.* (2007) but to the works of LUO *et al.* (2018), MANABE and STOUFFER (1999), STAMMER *et al.* (2018) and YEAGER and DANABASOGLU (2014) as well. We notice that the northward upper branch of AMOC extends

from the surface until 3000 m, but it is stronger around 1000 m. Additionally, the maximum values are found near 30°N in that depth, approximately. The lower branch is weaker than the upper one and moves in the opposite direction.

With CO_2 forcing, we observe weakening and shallowing of the upper branch, also seen by MANABE and STOUFFER (1999) and MUNTJEWERF *et al.* (2020b), and strengthening of the lower one, which also became broader. MANABE and STOUFFER (1999) related the lower branch strengthening with the strengthening of the AABW flow, also seen in SANCHO (2014). The core of the maximum overturning of the upper branch moved southward and shallowed, confining itself near-surface and between 10°N and 20°N. The weakening in the AMOC upper branch results in less heat reaching high latitudes in the NA. This behavior may be a consequence of positive feedback induced by the changes in the mixed layer depth (Figure 63) and shut down of deep convection, a similar behavior also observed by DRIJFHOUT *et al.* (2015).

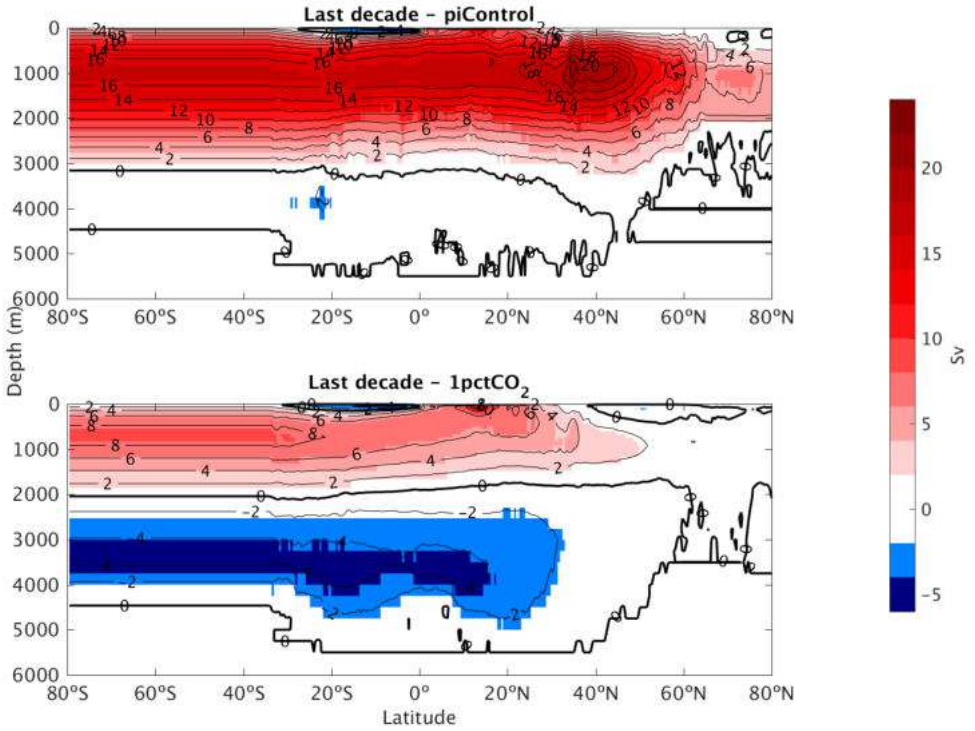

Figure 65: Last decade latitude average profiles for each experiment of the stream function in Sv. The contours are in a 2 Sv interval. Red-shaded areas indicate northward transport, and blue-shaded areas indicate southward transport.

Another way to observe the upper and lower branches of AMOC is through a zonally integrated profile in a specific latitude. Figure 66 displays the zonally integrated meridional transport profile at the 26.5°N parallel in the Atlantic for the RAPID (description in item 2.5.2.2), averaged from January 1st, 2005, and December

31^{th}, 2017, and piControl and 1pctCO$_2$ experiments, averaged for the whole period of each. For the piControl, the upper limb of the AMOC cell agrees well with RAPID data in pattern and value. The lower one is less intense and approximately 1500 m shallower than what is observed from RAPID (Table 22), which will be taken under consideration when analyzing the 1pctCO$_2$ experiment.

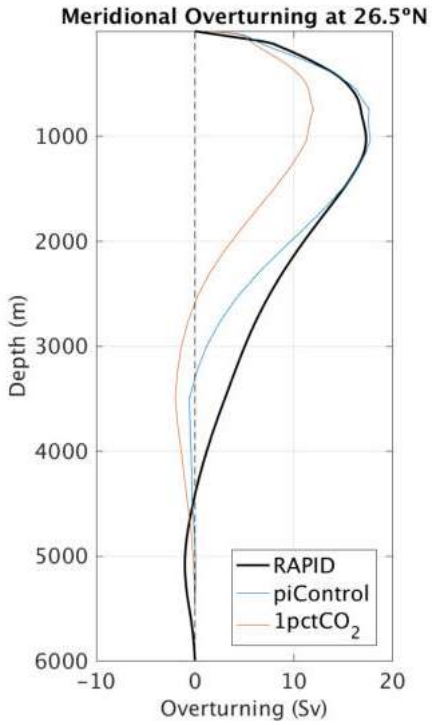

Figure 66: Zonally integrated and time-averaged meridional transport profile in the Atlantic at 26.5°N for RAPID, piControl, and 1pctCO$_2$.

In the 1pctCO$_2$ experiment, there is a reduction of 28.52% and a shallowing of almost 300 m in the upper AMOC in comparison with piControl (Figure 66). In the lower part, the depth of the maximum value is the same in piControl, but there was a strengthening of 255.36% in the 1pctCO$_2$. Since piControl misrepresented RAPID by 45.00%, the strengthening in 1pctCO$_2$ would be of approximately 97% of the RAPID climatology. Although RAPID is a well-established program and cannot be discarded, the RAPID results reflect a 13-year period in comparison with much more extended periods from the numerical experiments.

Table 22: MOC upper and lower branches maximum values and corresponding depths for time-averaged RAPID, piControl, and 1pctCO$_2$.

Source	Upper branch		Lower branch	
	Depth	**Value**	**Depth**	**Value**
RAPID	1030.66 m	17.34 Sv	5084.78 m	-1.01 Sv
piControl	1041.37 m	17.77 Sv	3503.45 m	-0.56 Sv
1pctCO$_2$	744.40 m	11.99 Sv		-1.99 Sv

As seen previously, the changes in mixed layer depth did not begin before year 50 of 1pctCO$_2$, and the resulting feature at the end of the experiment was remarkably different from that at the beginning of it. With that in mind, Figure 67 displays profiles similar to that of Figure 66, but the 1pctCO$_2$ profiles are a product of an average of years 1-10 (left panel) and years 141-150 (right panel). In the first decade (Figure 67-left), there is no change in the upper branch of AMOC, and the maximum value is very similar to piControl. However, it is located in shallower waters (Table 23). The lower branch already shows a strengthening in the first ten years of simulation, but the depth of the maximum stays the same in piControl and the average for the whole period of 1pctCO$_2$.

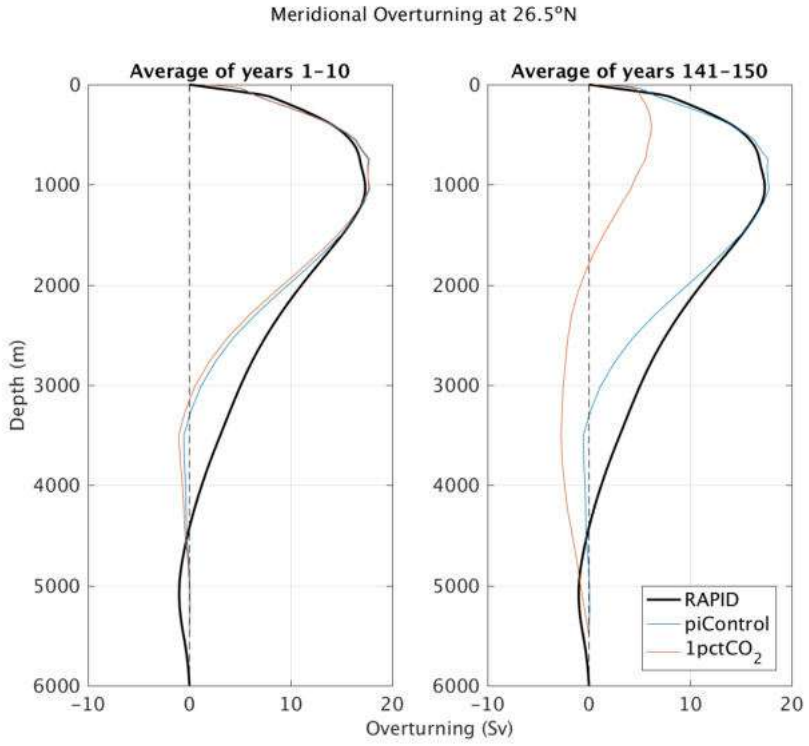

Figure 67: Zonally integrated and time-averaged meridional transport profile in the Atlantic at 26.5°N for RAPID and piControl. For 1pctCO$_2$, the left panel shows the average of the first decade, and the right panel shows the average of the last decade.

In the last decade (Figure 67 - right panel), the upper branch shallows almost 60% related to piControl and weakens approximately 65%. The lower branch, despite exhibiting the maximum value at the same depth in piControl, becomes broader, occupying almost 3000 m of the water column, which confines the upper branch in shallower waters. This feature is also noticeable in Figure 65. The lower part of the AMOC cell becomes more than 380% stronger than in piControl. Considering the strength difference between RAPID and piControl, the strengthening in the last decade of the 1pctCO$_2$ experiment would be of more than 170% from the RAPID climatology.

Table 23: MOC upper and lower branches maximum values and corresponding depths for the first and last decades and time-averaged 1pctCO$_2$, additionally to the piControl.

1pctCO$_2$	**Upper branch**		**Lower branch**	
	Depth	**Value**	**Depth**	**Value**
piControl	1041.37 m	17.77 Sv	3503.45 m	-0.56 Sv
1-10	744.40 m	17.75 Sv		-1.06 Sv
141-150	424.99 m	6.15 Sv		-2.73 Sv
Time-average	744.40 m	11.99 Sv		-1.99Sv

The behavior of the meridional transport profile in the last decade of 1pctCO$_2$ is probably related to less formation of NADW and more formation of AABW. MANABE and STOUFFER (1999) and STOCKER *et al.* (1992) related that changes in the gradient of sea surface salinity between the Southern Ocean and the North Atlantic might cause an increase in the AABW formation. Figure 68 displays the sea surface salinity anomaly for the last decade of 1pctCO$_2$, and we can notice that, although there is a slight decrease in surface salinity in the Southern Ocean, the freshening in the North Atlantic is more appreciable. Since the AABW spreading is modulated by the NADW (STOCKER *et al.*, 1992), the strengthening in the AABW formation (which will be discussed later) and the decrease in NADW formation probably led AABW to spread through the deep Atlantic further north.

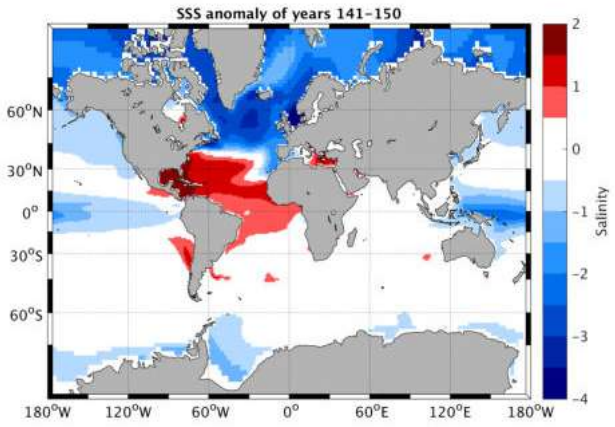

Figure 68: Last decade (141-150-mean) anomaly of the 1pctCO$_2$, compared to the 500 year-mean piControl for the sea surface salinity. Positive (negative) values indicate an increase (decrease) in surface salinity in the last decade of 1pctCO$_2$ compared to the average period of piControl.

Figure 69 exhibits the time series of the maximum overturning below 500 m, following BRYAN *et al.* (2007), for piControl and 1pctCO$_2$. We observe that piControl varies between 20 and 25 Sv, which agrees with the numerical model results in GREGORY *et al.* (2005) and MUNTJEWERF *et al.* (2020a). There is a low-frequency variability, but in overall, the overturning in piControl does not show any trends.

In 1pctCO$_2$, the overturning weakens continuously, and related to the average of piControl, excluding the values higher or lower than $3 \cdot \pm\sigma$, it decreases $\sim$61% in the last decade. By that moment, the overturning reaches 8.87 Sv, similar to the value of 8.6 Sv between 2081-2100, simulated by MUNTJEWERF *et al.* (2020a). It can not be said for sure because the 1pctCO$_2$ experiment does not integrate further after year 150. However, its behavior at the end of this experiment leads us to believe that AMOC finds a new equilibrium level.

According to BAKKER *et al.* (2016), a reduction of at least 90% would have to be necessary for considering a collapse in the AMOC. Although in the 1pctCO$_2$ experiment, the CO$_2$ quadruples compared to its initial value, according to the literature, it was not sufficient to cause a collapse in the AMOC nor to achieve the tipping point freshwater threshold. It is possible that the increase in the CO$_2$ forcing and the freshwater input being gradual, allowed the Climate System to adjust and absorb these forcings, which probably would not be the case if the CO$_2$ was suddenly quadrupled (MANABE and STOUFFER, 1999; MASSON-DELMOTTE *et al.*, 2018).

Although a sudden increase in the atmospheric CO$_2$, instead of a gradual one, would probably cause more damage or, at least, more initial abrupt damage

than the ones identified here, this type of increase is not as realistic as the one in the 1pctCO$_2$ experiment (WALKER and KASTING, 1992). On the other hand, DRIJFHOUT *et al.* (2015) observed a more consistent collapse in AMOC with simulations with RCP 2.6 than with RCP 4.5 and RCP 8.5, i.e., a lower-emission scenario than RCPs 4.5 and 8.5. According to the authors, the NA cooling that would be observed in a collapsed AMOC weakens with stronger forcing. Since the 1pctCO$_2$ experiment is a gradual but intensive CO_2 emission experiment, its nature may have contributed to preventing AMOC to collapse.

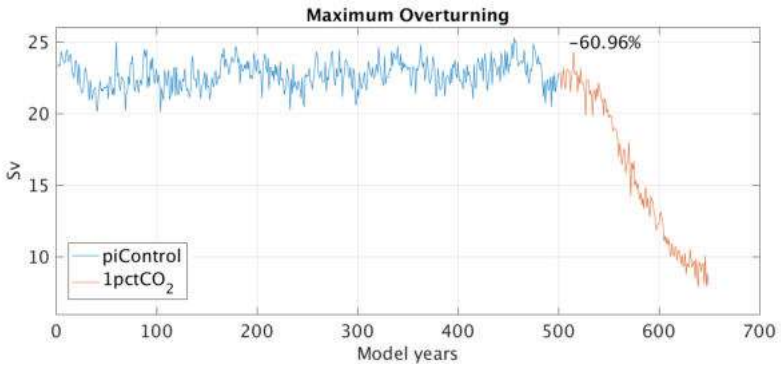

Figure 69: Annual average series of the maximum overturning in the Atlantic basin deeper than 500 m. Additionally, it is shown the percentage of reduction in the last decade of the 1pctCO$_2$ experiment.

4.3 Changes on AMOC-related Dynamics

In section 4.2, we have evaluated changes in AMOC cell and NADW formation dynamics, searching for a tipping point in them. Although the thresholds for the tipping point were not achieved according to the literature used, we have shown several appreciable changes that occurred due to the increase in atmospheric CO_2. This section will analyze other changes in some features in the Atlantic Ocean that modify or are modified by the AMOC.

Figure 70 displays the volume transport profiles at 25°S for the time-average piControl, the average of the last decade of 1pctCO$_2$, and the anomaly between them. Regarding the western boundary current system, we identify an intensification of the southward flow of BC, also present in the downscaling of RCP 4.5 projection of TOSTE *et al.* (2018). Additionally, CARLSON *et al.* (2008) discuss that in slow AMOC periods, the BC may have acted storing and redirecting part of the excess heat and salt left behind by AMOC. Below the BC, we can see that the positive core that characterizes the northward flow of the AAIW disappears in the last decade of the 1pctCO$_2$ experiment. TOSTE *et al.* (2018), in their work, also identified a northward shift in the BC bifurcation and formation. It is possible that

the Intermediate Western Boundary Current (IWBC), constituted by the AAIW, may have also shifted its bifurcation northwards. This change would result in a southward, instead of an expected northward flow in a climatological representation, as shown in Figure 71.

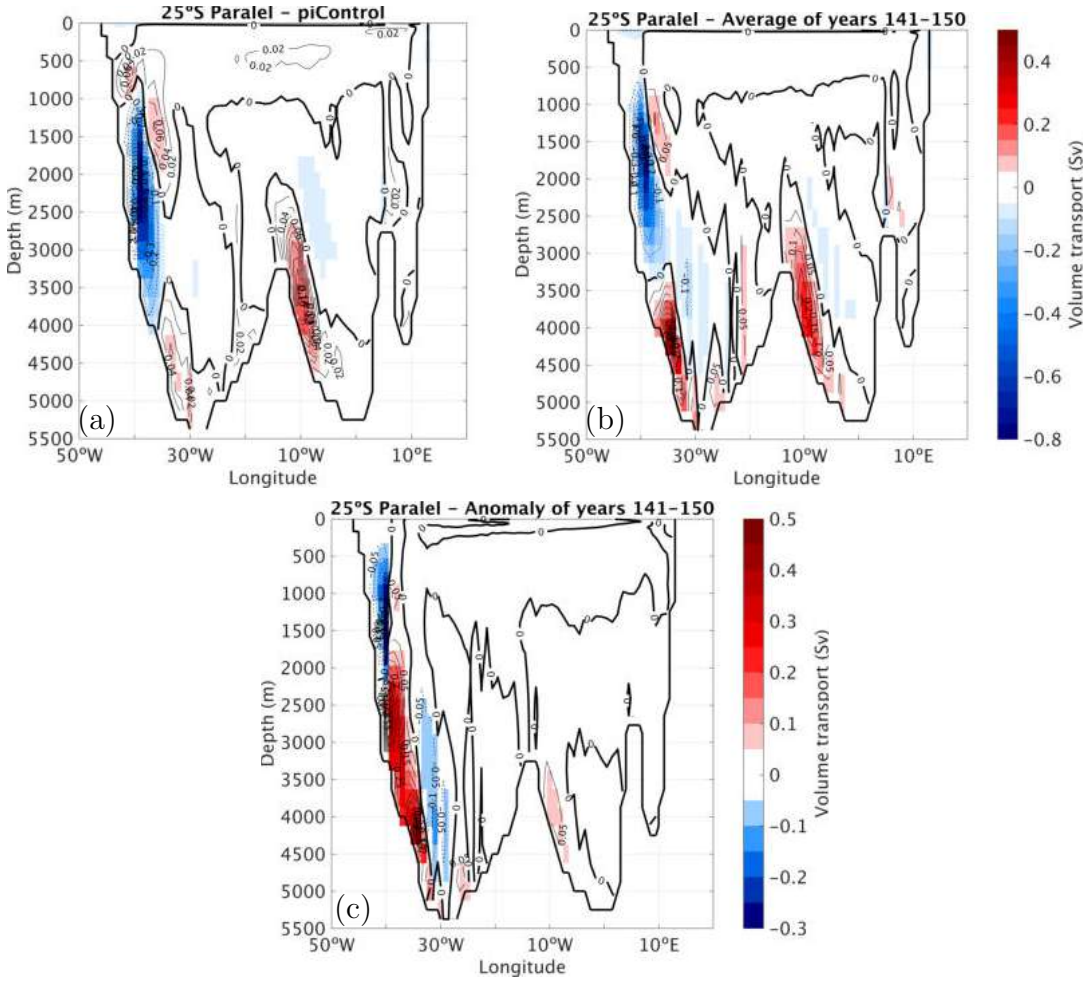

Figure 70: Volume transport profile in the 25°S parallel for (a) the time-average piControl, (b) average of the last decade of 1pctCO_2, and (c) the anomaly between them. The colors depict the intensity and direction of the flow in (a) and (b). Red means northward flow, and blue means southward flow. In (c), for northward (southward) flow, red colors mean strengthening (weakening), and blue colors mean weakening (strengthening). Additionally, contours show the transport values in Sv in (a) and (b) and anomaly values in (c).

The NADW becomes more confined to the coast between 1000 m and 2000 m, but stronger between those depths, intensifying its southward flow. This water mass also becomes ∼500 m shallower, and the flow from 2000 m until near its base becomes weaker than in piControl. If we split the NADW into an upper part, spanning from 1000 m to 2000 m, and a lower one, spanning from 2000 m to 4000 m, in the last decade of 1pctCO_2, the upper part becomes narrower, which can explain

its intensification southwards. On the other hand, the shallowing of the lower part reflects the shut down of deep convection in the NA's high latitudes.

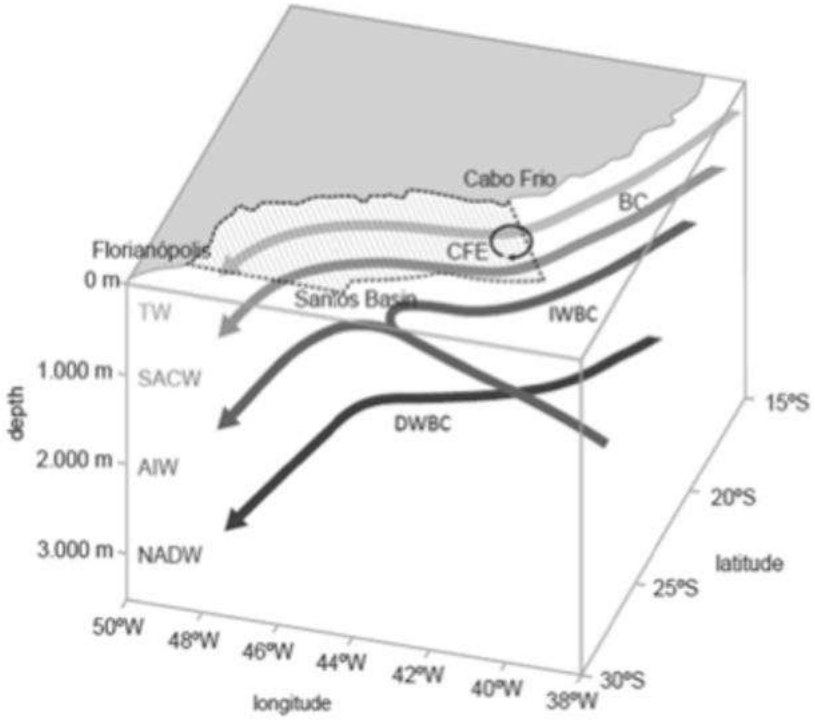

Figure 71: Schematic representation of the western boundary current system in the water column between 15°S and 30°S on the Brazilian coast. Source: ALVES DOS SANTOS *et al.*, 2015.

Below the NADW, the AABW occupies the additional 500 m above 4000 m, filling the NADW gap, and it also gets stronger in the 1pctCO_2 experiment. This strengthening of the AABW was also found in the work of MANABE and STOUFFER (1999), which the authors identified this water mass extending more northward, which intensified the reverse overturning cell, also observed in this work. On the east side of the basin, close to the Mid Atlantic Ridge, the deep northward flow intensifies. Despite the northward strengthening in the section, the 25°S parallel integrated Vt intensifies its flow southwards by 6.62% compared to the piControl (Table 24).

In Figure 70, we have pointed out some changes in the western southward flow in the 25°S parallel, characteristics of the NADW flow. If we take the southward transport values westward of 35°S and deeper than 1000 m, we obtain the flow characteristic of the NADW. Figure 72 displays the time series of the integrated volume (upper panel) and heat (lower panel) transports of this flow. Although the upper part of NADW intensifies, as seen in the 25°S Vt profiles, the lower part's decrease dominates the integrated transport, which decreases continuously from the

beginning to the end of the 1pctCO$_2$ experiment. That also agrees with the analyzes on item 4.2. Vt's behavior also means that the southward Vt strengthening was not due to the upper NADW intensification.

Table 24: Integrated Vt and Ht values for the time-average piControl and the average of the last decade for 1pctCO$_2$ for the sections located on the South Atlantic Ocean. The bold letters next to the transport values indicate the direction: N - northward, S - southward, and E - eastward.

Section	**piControl**		**1pctCO$_2$**	
	Vt	**Ht**	**Vt**	**Ht**
Drake	156.22±0.44 Sv **E**	1.58±0.01 PW **E**	176.30±0.48 Sv **E**	2.87±0.01 PW **E**
AF-AA	153.02±0.35 Sv **E**	1.02±0.01 PW **E**	174.22±0.35 Sv **E**	2.60±0.01 PW **E**
25°S	0.84±0.06 Sv **S**	$0.50\pm0.14\cdot10^{-2}$ PW **N**	0.89±0.05 Sv **S**	$0.15\pm0.20\cdot10^{-2}$ PW **N**

The Ht (lower panel) displays a different path, and a clear tendency is not seen, although it increases at the end of the 1pctCO$_2$ experiment. Estimating the decadal averages of the Ht of the 1pctCO$_2$ (not shown here), a more evident behavior is identified. The Ht starts - the first decade, an average of years 1-10 - with values close to 0.32 PW, and it oscillates around that value until decade 10. After that, in decade 11, it increases to 0.33 PW and 0.34 PW in decade 13, stabilizing at that value. Although the 1pctCO$_2$ experiment does not integrate further in the future, it appears that the NADW Ht finds a new equilibrium in a level higher than in the piControl.

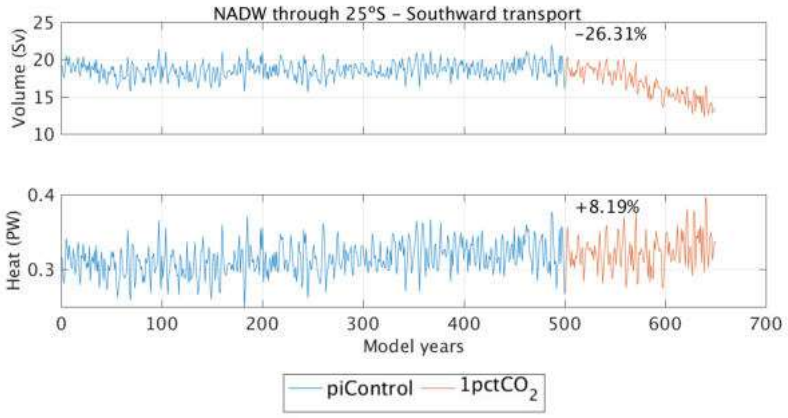

Figure 72: Annual average series of southward integrated volume (upper panel) and heat (lower panel) transports of the NADW for piControl and 1pctCO$_2$ experiments. The NADW transport in this region is southward, hence it is characterized by negative values. Nonetheless, it has been represented as a positive flux to facilitate the visualization. Additionally, the text in each panel shows the percentage of increase (+) or decrease (-) in the last decade in 1pctCO$_2$.

On the Drake and AF-AA passages, the eastward integrated Vt increases (Table 24) due to an increase in the westerlies (HODGSON and SIME, 2010), also

seen in the work of MANABE and STOUFFER (1999). The atmospheric heating, caused by the increase in CO_2 forcing, modified the atmospheric pressure gradient, behavior also seen in the works of MITCHELL (1983), RIVIÈRE (2011), SAUNDERS *et al.* (2018), and others. This surface heating induced an increase in the air rise in the low-pressure belts, which dynamically intensified the high-pressure ones. The strengthening of both Polar and Ferrell cells intensified the pressure gradient, increasing the westerlies that flow between them.

Observations show that in warming climates, there is a reduction in the potential of the ocean to absorb the excess of atmospheric CO_2 (HOUGHTON, 2009). In this context, SAUNDERS *et al.* (2018) and others comment about the relationship between the strengthening of the westerlies with a weakening of the Southern Ocean carbon sink system. According to the authors, these winds influence the upwelling of carbon-rich deep waters, thus altering the sinking/releasing balance of CO_2 (HODGSON and SIME, 2010; TOGGWEILER *et al.*, 2006).

In addition to changes in atmospheric temperature gradients, modifications on the westerlies can also be caused by changes in sea surface temperatures and sea ice (SIME *et al.*, 2013). Alterations in the temperature gradients, such as we obtained in the 1pctCO_2 experiment, ended up increasing the flow of the westerlies and the carbon-rich deep waters upwelling. At the same time, retraction of sea ice, also observed in this experiment (which will be shown in further analysis), promotes more available surface area for atmosphere-ocean exchanges (SAUNDERS *et al.*, 2018). If the increase in atmospheric CO_2 led to a release of more CO_2 from the deep Southern Ocean, that would establish positive feedback of CO_2 release, and if that is true, when and how does it stop?

Still, regarding the Drake Passage's Vt, its increase may influence the dynamics related to the BMC location, for example, once the MC is formed by the AACC, as stated earlier (CATALDI, 2008; FETTER and MATANO, 2008). Similarly, the BC intensification, identified on the 25°S section, may also regulate the BMC positioning. Additionally, this intensification may affect the spread of the water masses composing the BC in the South Atlantic Ocean, like the South Atlantic Central Water (SACW) (PASSOS, 2012).

As stated earlier, although the 25°S parallel exhibits an increase in its southward integrated volume transport, its northward heat transport decreases, which could mean a decrease in the role of South Atlantic Ocean transporting heat northwards. However, if we observe in Table 24, we notice an increase in Drake's Ht of 81.65%, while in 25°S, it decreases 70.00%, which is counterintuitive, once the Drake Passage transport feeds some of the 25°S transport (SANCHO *et al.*, 2015).

If we integrate not the whole water column at 25°S but the positive and negative values separately, we would be able to calculate the changes of the north-

ward and southward flows in this region. By doing that, we understand that the northward Ht did not weaken, but the southward one strengthened more than the northward one, as shown in Table 25. This southward Ht increase is related to Vt changes, especially the increase in the southward BC and the decrease in the northward AAIW. Nonetheless, the weakened integrated Ht in this region helps explain the weakening of the upper branch of the AMOC cell.

Table 25: Integrated northward and southward Ht across the 25°S parallel for the time-average piControl and the average of the last decade for 1pctCO_2.

	piControl	**1pctCO_2**	**Increase**
Northward	1.55 PW	1.70 PW	9.68%
Southward	1.04 PW	1.55 PW	49.04%

The Ht profiles in the 25°S section (not shown here) follow the changing pattern of the Vt profiles (Figure 70), and they exhibit northward strengthening of the AABW. The AAIW core, an important source for the northward transport and the upper branch of the AMOC cell (SCHMITZ, 1996; SCHMITZ JR. and MCCARTNEY, 1993; TOMCZAK and GODFREY, 1994), disappears, which it was also seen in the Vt profiles.

In general, Vt in the Drake Passage increases in the whole water column (not shown here). For the AF-AA Passage (Figure 73), in the northern part of the section, there is a weakening below 1500 m of the eastward transport. On the other hand, in the south part there is also a weakening but for westward transport. However, the feature that deserves more attention is the apparent weakening of the westward Agulhas Leakage (Figure 73).

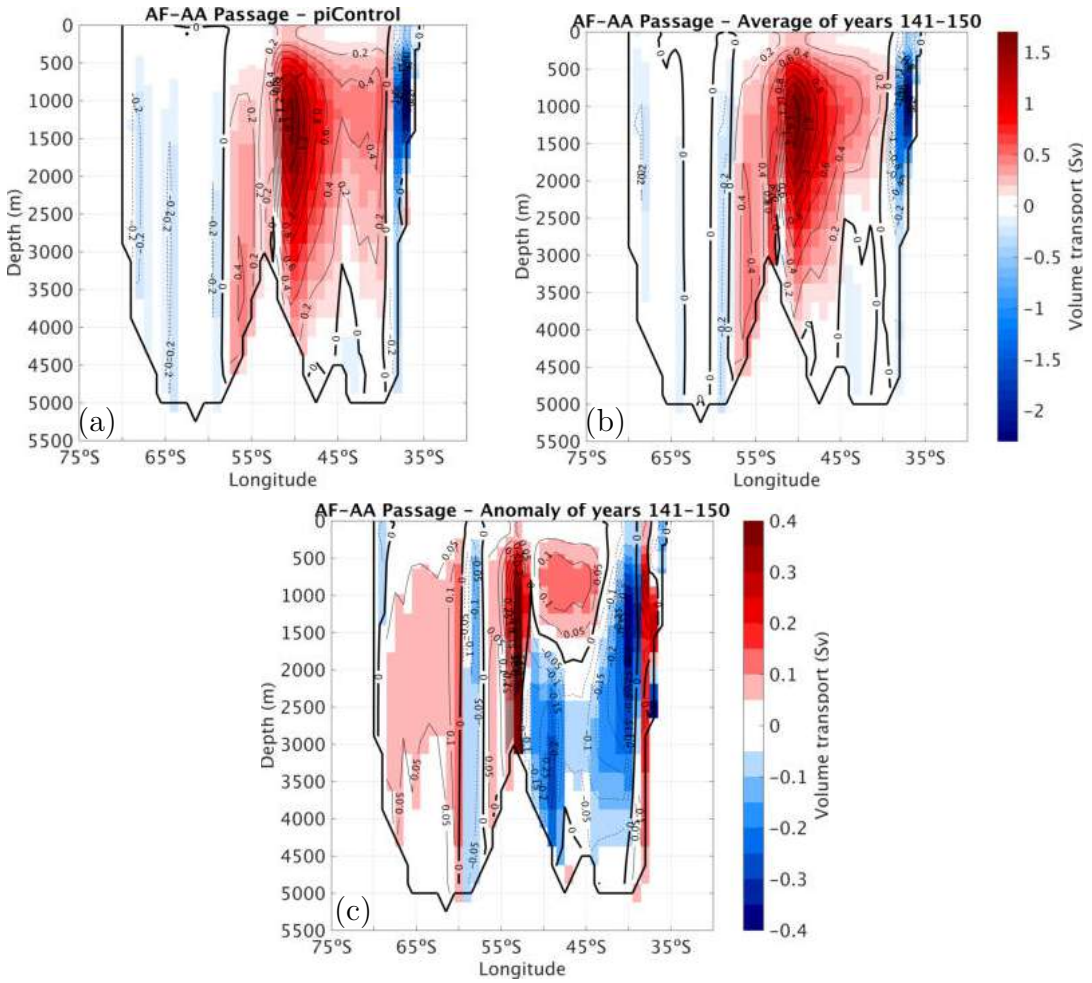

Figure 73: Volume transport profiles in AF-AA Passage for (a) the time-average piControl, (b) average of the last decade of 1pctCO_2, and (c) the anomaly between them. The colors depict the intensity and direction of the flow in (a) and (b). Red means eastward flow, and blue means westward flow. In (c), for eastward (westward) flow, red colors mean strengthening (weakening), and blue colors mean weakening (strengthening). Additionally, contours show the transport values in Sv in (a) and (b) and anomaly values in (c).

Figure 74 displays the time series of the westward volume and heat transports that correspond to the Agulhas Leakage, obtained through the negative values north of 40°S from the AF-AA Passage section. We can see that the depth-integrated Vt of this feature exhibits decrease practically throughout the series. However, in the anomaly profile in Figure 73(c), there is a small region of increase near the coast of Africa in shallower waters. On the other hand, Ht presents an increase throughout the series. Since the Agulhas Current (AC) has its origin in the Indian Ocean, and it is fed mainly by the Mozambique Current (LUTJEHARMS, 2006), the Vt and Ht from surface until 1000 m in two sections (Figure 41 in section 3.5.1) in the Indian Ocean were evaluated to monitor this transport before its retroflection. The

section in the 19°S parallel between the coast of Africa and Madagascar will capture the Mozambique Current, and the section at 32°S, between the coast of Africa and 38°E, will capture the AC before it retroflects (Table 14).

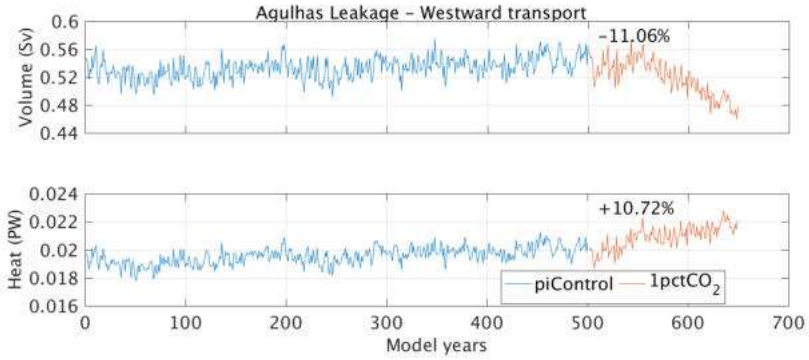

Figure 74: Annual average series of westward volume (upper panel) and heat (lower panel) transport of the Agulhas Leakage for piControl and 1pctCO$_2$ experiments. The Agulhas flow in this region is westward, hence it is characterized by negative values. Nonetheless, it has been represented as a positive flux to facilitate the visualization. Additionally, the text in each panel shows the percentage of increase (+) or decrease (-) in the last decade in 1pctCO$_2$.

Figure 75 represents the integrated Vt and Ht in the 32°S parallel in the Indian Ocean (Figure 41) from the surface until 1000 m. The transports in the 19°S will not be shown here because they exhibit very similar behaviors with the ones in the 32°S, but any differences will be described. First, we can see that the AC Vt in the piControl experiment has lower values in this section than the ones obtained on the AF-AA section, once its volume increases as this current flows downstream (LUTJEHARMS, 2006). The transports in the 19°S section also depict lower values than both of them. Nonetheless, the behavior of the transports in the three regions is similar and does not exhibit tendencies throughout the series in piControl.

In the 1pctCO$_2$, there is a decrease in Vt of almost 24% in the 32°S section, and the Ht practically maintains its average piControl value, showing a decrease of less than 1.40%. The weakening in Vt decreases from 19°S, through the 32°S to the Agulhas Leakage in AF-AA Passage, as shown in Table 26. The fact that the flow increases monotonically downstream, but the weakening decreases, in the same way, leads us to think that the forcing acting on the Agulhas weakening has a remote source, rather than forcing this current along its path. A remote source of the forcing ended up causing lower changes as the flow gains volume. The high correlation (91.82%) between the percentages of decrease in the last decade of 1pctCO$_2$ and average Vt in piControl for each region reinforces that hypothesis, i.e., the reduction in the weakening is related with the volume gained by the current.

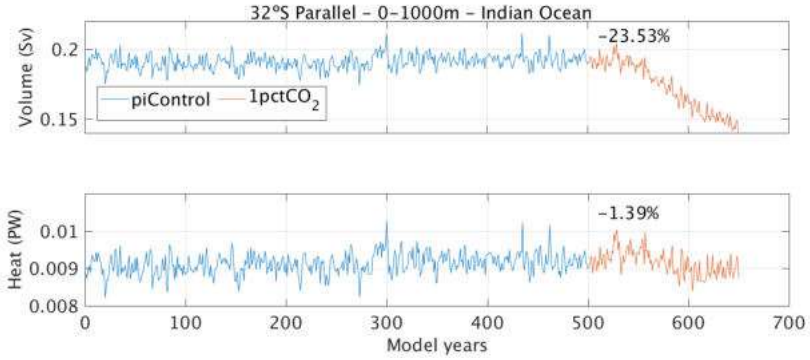

Figure 75: 32°S section time series of southward volume (upper panel) and heat (lower panel) transports of the Agulhas Current for piControl and 1pctCO$_2$ experiments. The Agulhas Current in this region flows southward, hence it is characterized by negative values. Nonetheless, it has been represented as a positive flux to facilitate the visualization. Additionally, the text in each panel shows the percentage of decrease in the last decade in 1pctCO$_2$.

The behavior showed with Vt along the three regions is amplified for the Ht. The Ht in 1pctCO$_2$ begins with a weakening of more than 14% in the 19°S and decreases to a weakening of 1,39% at 32°S. In the AF-AA Passage, there is an increase in the heat transported by this current of 10.72% compared to the average piControl (Table 26). This heat gain in this region may be related to the AACC itself in a way that, when in retroflection, the AC interacts dynamically with the AACC, draining some of its heat, thus strengthening the westward Ht even though Vt is weakened. Analyzing the correlation between the Vt and Ht series for the 1pctCO$_2$ experiment, there is a decrease in the influence of Vt in the Ht from 90.97% in 19°S, through 74.18% in 32°S to 22.54% in AF-AA, which may indicate the influence of the AACC in the Agulhas retroflection and even some influence in the 32°S section.

Table 26: Changes on the Vt and Ht of the Agulhas Current in the last decade of 1pctCO$_2$ compared to the average of piControl for the three sections where this current was monitored. The (+) sign means an increase in the parameter, and the (-) sign means decrease.

Section	Vt	Ht
19°S	-41.52%	-14.32%
32°S	-23.97%	-1.39%
AF-AA Passage	-11.59%	+10.72%

4.4 Consequences for the Earth Climate System

In section 4.2, while searching for a tipping point in the THC, we have identified several changes related to the AMOC system, mainly in the NA, which were a product of the global atmospheric increase of CO_2. Section 4.3 also identified changes related to AMOC due to the CO_2 forcing but focusing more on the South Atlantic Ocean. These features were analyzed compared to the piControl, which was validated to be used for such purpose in section 4.1. This section will identify and analyze changes in the Earth Climate System that are not necessarily related to the AMOC. The following analyzes will draw a general view of modifications in different features and components of the climate system at the same time as we will establish and hypothesize relations between them and AMOC.

Figure 76 displays fields of surface air temperature for (a) the average of piControl and (b) the average of the last decade of the 1pctCO_2 experiment. Additionally, the positive and negative anomalies are also shown in (c) and (d), respectively. The anomalies were separated due to the different order of magnitude between them, which would difficult the proper visualization of both behaviors. The expected air temperature distribution in piControl is presented, displaying higher temperatures over the equator and lower ones towards the poles, and that this pattern is maintained in the last decade of 1pctCO_2 (Figure 76(b)) but with lower gradients between the poles and the equator, explained by the positive anomalies.

In Figure 76(c), for almost the entire globe, there is an increase in the air temperature with a maximum value of $\sim$16.14°C in Canada (green mark) near 74°N. More significant anomalies are found in higher latitudes, which promoted the lower temperature gradients in the last decade of 1pctCO_2. There is only a region where the temperatures were colder in the last decade of the 1pctCO_2 experiment (Figure 76(d)), and this region is similar to the colder SST anomaly in Figure 61, which decreased the evaporation flux and promoted an increase of freshwater flux. This increase in freshwater flux ended up inhibiting the deep convection in the NADW formation sites.

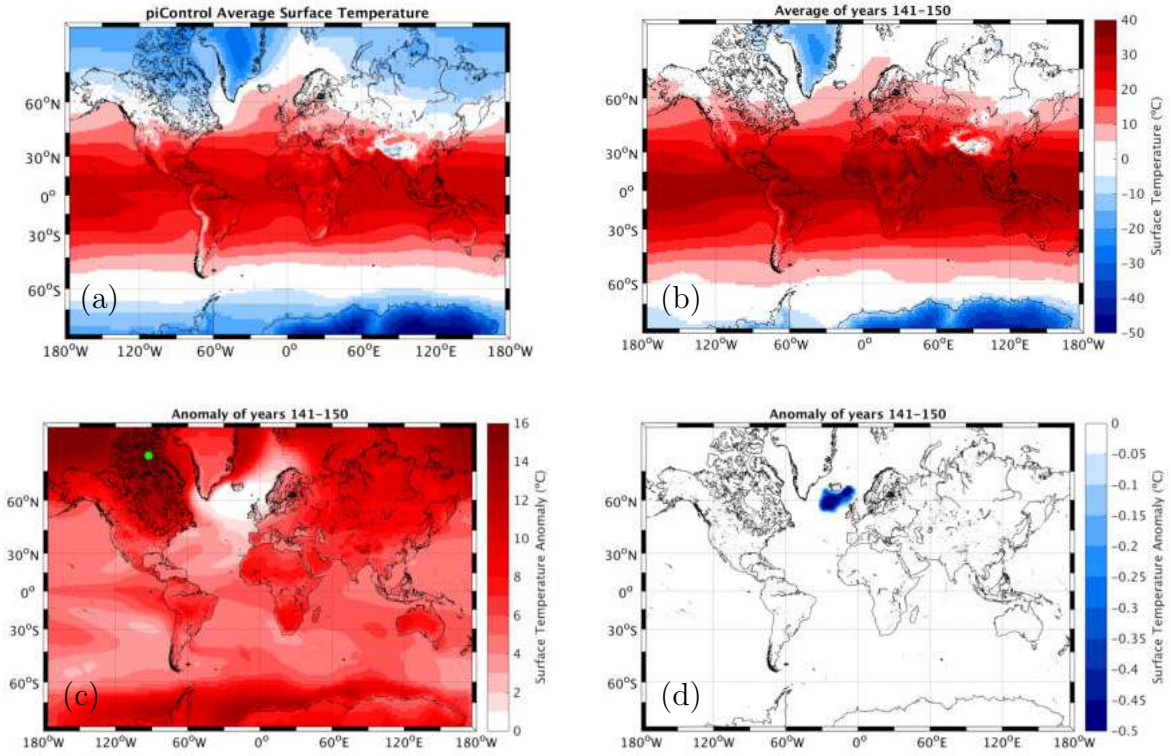

Figure 76: Fields of surface air temperature for (a) average of piControl, (b) average of the last decade of 1pctCO$_2$, (c) positive, and (d) negative anomaly of the last decade of 1pctCO$_2$ compared to the average of piControl. The green spot on (c) marks the location of the maximum positive anomaly.

Figure 77 shows the zonally averaged distribution of sea level pressure in summer (left panel) and winter (right panel) for the average of piControl and the average of the last decade of 1pctCO$_2$ experiment. The text inside the panels shows the most prominent differences between piControl and 1pctCO$_2$. The pressure distribution in the last decade of 1pctCO$_2$ follows the pattern of piControl's and in overall show intensification both on high-pressure belts and low-pressure belts. This intensification was responsible for the strengthening of the Southern Ocean westerlies and, along with increased air temperature (Figure 76), increased Vt and Ht in Drake and AF-AA Passages.

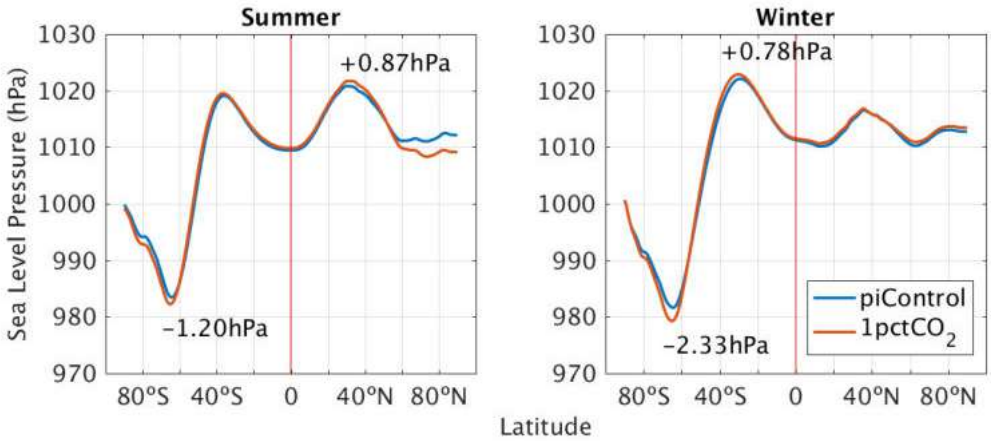

Figure 77: Zonal mean distributions of sea level pressure in summer and winter for the piControl and the last decade of the 1pctCO$_2$ experiment. The red line marks the equator. Additionally, the text in each panel shows the pressure increase (+) or decrease (-) in the last decade in 1pctCO$_2$ compared to the average of piControl.

If we analyze the annual and not the seasonal sea level pressure average for the piControl and the last decade of the 1pctCO$_2$ experiment, the intensification of 0.70 hPa for both high-pressure belts become more apparent. On the other hand, there is not a clear difference in the northern hemisphere's low-pressure belt between the two experiments. However, in the southern hemisphere, there is an intensification of 1.69 hPa in the low-pressure belt. As said earlier, the intensification of the southern hemisphere's pressure belts led to westerlies strengthening between them, increasing AACC flow, and possibly intensifying carbon-rich deep waters upwelling.

Figure 78 displays the annual zonal and meridional mean series of sea ice concentration in the Arctic (blue lines) and Antarctic (green lines) for the average of piControl (continuous lines), like in Figure 54, and the average of the last decade of 1pctCO$_2$ experiment (dashed lines). The sea ice seasonality is maintained, but it can be seen a clear reduction in sea ice concentration for both regions at the end of the 1pctCO$_2$ experiment. Mainly, in late summer and during autumn for the Arctic (July to November) and in middle summer and the beginning of autumn in the Antarctic (January to March), the sea ice concentration retracts almost 100%, leaving the regions almost ice-free. If maintained, this retraction in the Arctic could promote the emergence of new deep convection sites as identified in the work of LIQUE *et al.* (2018). Although the authors did not discuss the implications of these new sites' appearance on the AMOC, due mainly to the lack of more extended integrations, they admit the possibility of local ventilation through deep mixing. On the other hand, ice-free regions in Antarctica can lead to modifications in air-sea exchanges of several elements, including carbon due to the more available surface

ice-free area (SAUNDERS *et al.*, 2018).

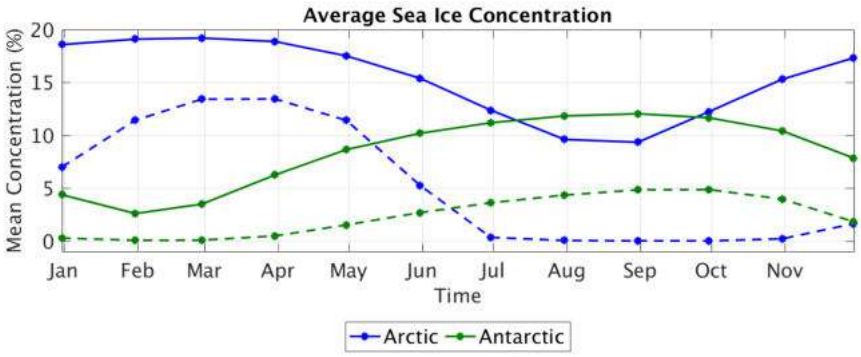

Figure 78: Annual mean series of sea ice concentration in the Arctic (blue lines) and Antarctic (green lines) for the average of piControl (continuous lines) and the average of the last decade of 1pctCO$_2$ experiment (dashed lines).

Figure 78 gives us the distribution of the average sea ice through a year and how it changed in the last decade of the 1pctCO$_2$ experiment. In Figure 79, we can see how the sea ice in the climatological months of minimum concentration behaves. The months of climatological minimum concentration were identified in Figure 54; September for the Arctic and February for the Antarctic. On the left panel of Figure 79, the sea ice edge for (a) September in the Arctic and (b) February in the Antarctic is displayed. The sea ice edge is the boundary between sea ice and open water, and it is a metric to evaluate its spatial distribution. In the Arctic, we can see that, in piControl, the sea ice extends through the entire Arctic circle (located at ~66°33‘N) and further. In the 1pctCO$_2$ experiment, The extension of sea ice is drastically reduced, as seen in Figure 78, almost confining the sea ice to the 80°N parallel. In (c), we observe this reduction of almost 100% in the last decade of the 1pctCO$_2$ experiment.

In February for the Antarctic, the reduction also approaches 100% (Figure 79(d)). The sea ice edge distribution is different than in the Arctic, and the reductions, in absolute values, are lower, as can be seen in Figure 78. Nonetheless, near the Drake Passage, and at the east Antarctic sector, near longitudes 15°W and 50°E, the sea ice vanishes (Figure 79(b)), and we can only see the piControl edge (blue lines only). These reductions in sea ice alter the albedo in these regions and contribute to magnify Global Warming (BITZ *et al.*, 2005; SCHNEIDER and DICKINSON, 1974) and the effects it caused in NADW and AMOC weakening.

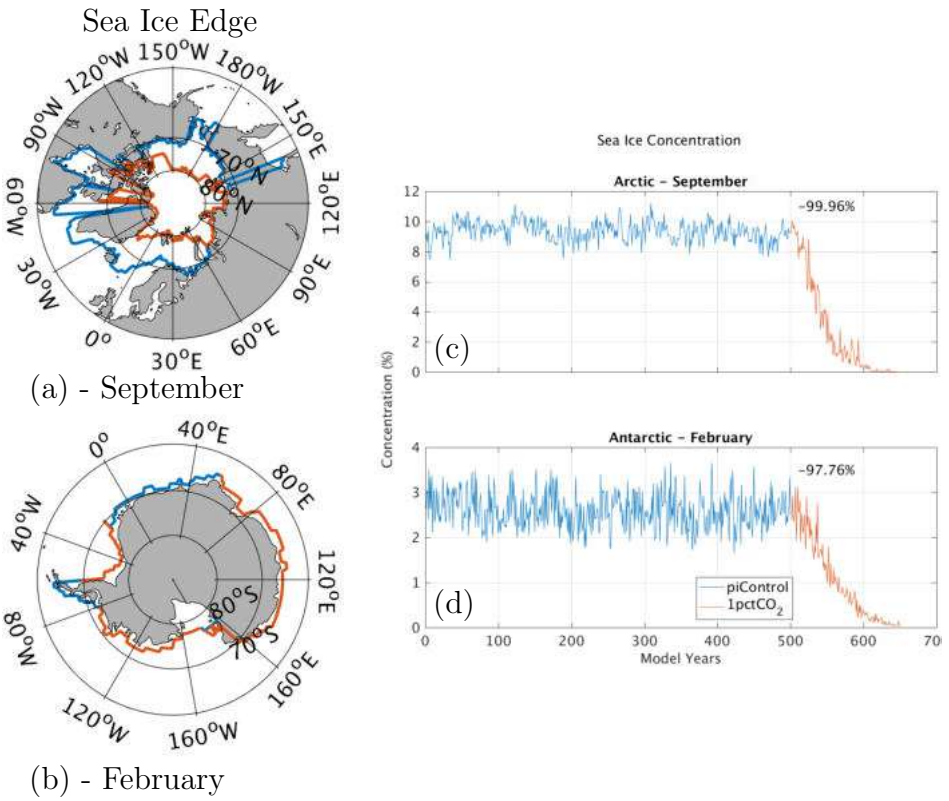

Figure 79: The left panel displays the geographic location of the sea ice edge for the average of piControl (blue lines) and the average of the last decade of the 1pctCO$_2$ experiment (orange lines) for (a) September in the Arctic and (b) February in the Antarctic. In (b), the regions where there is only the edge of the 1pctCO$_2$ experiment (orange lines) means that it overlapped the control. Regions where there is only the edge of piControl (blue lines) means the 1pctCO$_2$ sea ice was reduced to zero. Also, on the right panels, the time series of the sea ice concentration for (c) September in the Arctic and (d) February in the Antarctic are depicted along with the percentages of reduction for each one in the last decade of 1pctCO$_2$ experiment.

The analysis presented in Figure 76 for the surface air temperature was performed for the SST (Figure 80). We also observe the expected SST distribution in piControl and 1pctCO$_2$ experiments, with higher temperatures over lower latitudes and decreasing temperatures towards higher latitudes. However, differently than the surface air temperature, the more significant SST increase happened between 30°S and 30°N, with higher positive anomalies in that region in the last decade of 1pctCO$_2$ (Figure 80(c)). Furthermore, the only region with negative SST anomalies coincides with that in the surface air temperature.

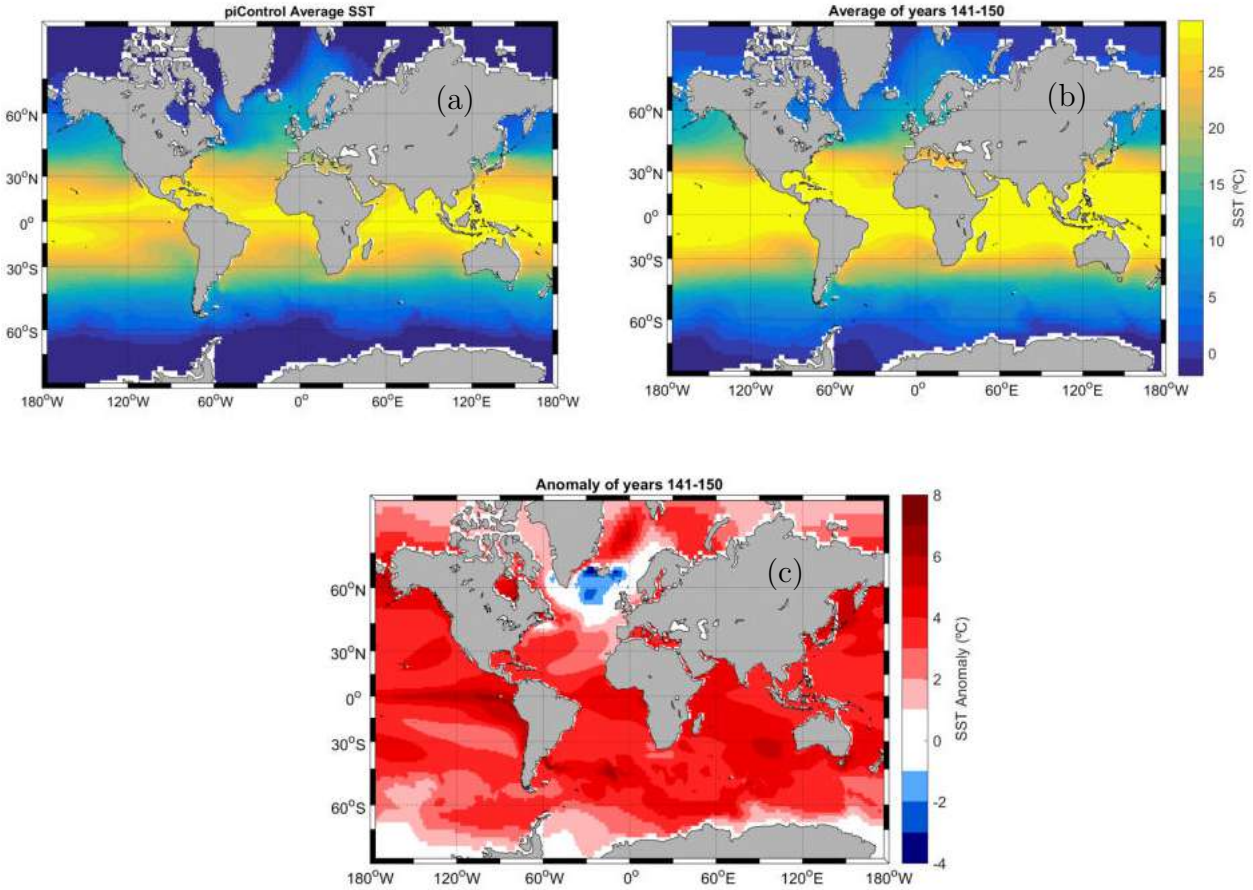

Figure 80: Fields of sea surface temperature for (a) average of piControl, (b) average of the last decade of 1pctCO$_2$, and (c) anomaly of the last decade of 1pctCO$_2$ compared to the average of piControl.

Figure 81 shows the annual average cycle of the surface heat flux globally and for each hemisphere. The continuous lines refer to the piControl experiment, as shown in Figure 48, in item 4.1, and the dashed lines refer to the last decade of the 1pctCO$_2$ experiment. For the southern hemisphere, there is little change throughout the year, with more significant differences between November and February, which higher positive values, compared to the piControl, indicate heat gain by the ocean, behavior that can be expected due to the air temperature increase. In the northern hemisphere, there is an intensification of the negative surface flux between November and January of a similar magnitude of the southern hemisphere, indicating more ocean heat loss. The similar, although of opposite sigh, behavior in the northern and southern hemisphere may be related to some compensation mechanism between both hemispheres in a way that more heat gain in on side is compensated by more heat loss on another side.

In late boreal spring, between May and September, on the other hand, are the moments when the most noticeable changes occur. The more significant increase

happened in July of almost ∼40 W·m^{-2}, which corresponds to an increase of 63.62% in the ocean heat gain. The higher heat gain by the ocean caused a change in the global curve, making its design closer to a zero straight line than it was before. This change in the pattern means that, although the northern hemisphere has a low ocean/continent ratio, the amount of heat that it is absorbing, increases its importance. This behavior may be related to the decrease in the NA evaporation and retraction of sea ice.

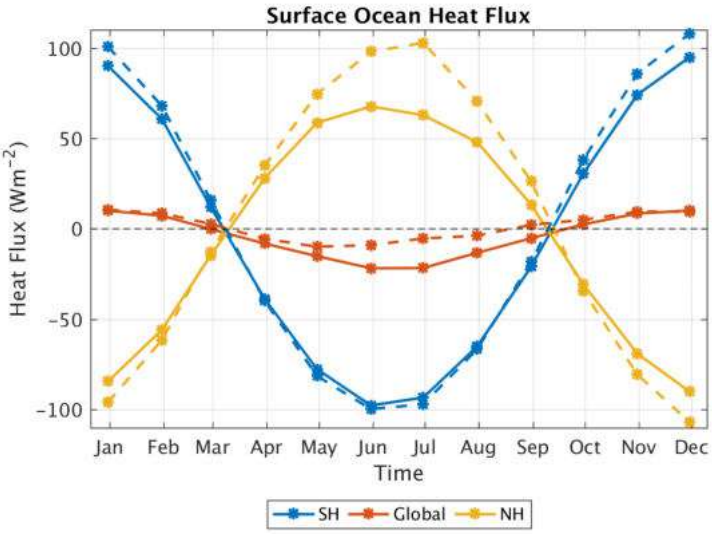

Figure 81: Average annual cycle of the ocean surface heat flux for the entire globe and separately by hemisphere for the piControl (continuous lines) and the last decade of 1pctCO$_2$ (dashed colored lines). SH denotes Southern Hemisphere, and NH denotes Northern Hemisphere. The black dashed lines mark the zero.

Figure 82 presents the zonally averaged distribution of the global meridional heat transport integrated on the entire water column. Positive values indicate transport northward, and negative ones indicate transport southward. We can see that the meridional heat transport follows its expected behavior, transporting heat from the equator to the poles in both hemispheres, and it is similar to the work of STAMMER *et al.* (2018). For the piControl, in the northern hemisphere, the heat transport peaks in ∼1.54 Pw near 20°N while in the southern hemisphere, it peaks in ∼1.16 PW near 11°S. This difference, both in value and in the location of the maximum heat transport is related with the South Atlantic Ocean that, different from others, transports heat northward and not poleward (ASSAD *et al.*, 2009; BOLLMANN *et al.*, 2010; CAMPOS *et al.*, 1999; GANACHAUD and WUNSCH, 2000; GARZOLI and BARINGER, 2007; RINTOUL, 1991; SANCHO, 2014; SANCHO *et al.*, 2015; SROKOSZ *et al.*, 2012; STAMMER *et al.*, 2003; TALLEY *et al.*, 2011; ZHENG and GIESE, 2009; ZHU *et al.*, 2014). Additionally, the maximum

value of 1.54 PW near 20°N is close to the value the upper limb of AMOC reaches of 1.30 PW around 24.5°N, according to SROKOSZ *et al.* (2012), which reinforces the AMOC influence on this flow.

The last decade of the 1pctCO$_2$ experiment shows a decrease of 32.61% in the northward heat transport, and it is related to a similar weakening (32.53%) on the upper branch of AMOC cell and its capacity to transport heat northwards. On the other hand, southward transport shows an increase and may also be related to the strengthening of the lower AMOC cell. Nonetheless, the 1pctCO$_2$ experiment conserves the pattern of heat transport in piControl; what corroborates the earlier discussions about not achieving a tipping point in AMOC but still observe several changes on AMOC and global climate related to the increase in atmospheric CO$_2$.

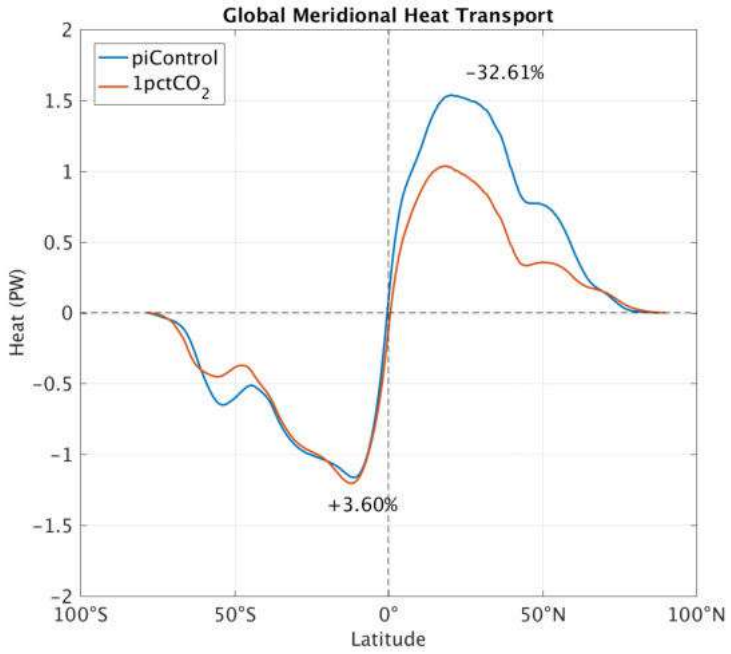

Figure 82: Latitudinal distribution of the zonally averaged and depth-integrated heat transport for the average of piControl and the average of the last decade of the 1pctCO$_2$ experiment. Additionally, the texts show the percentage of increase (+) or decrease (-) in the last decade of 1pctCO$_2$ compared to the average of piControl. The black dashed lines mark the zero transport and 0° latitude.

The ocean heat content or, the heat absorbed by the ocean, is highly correlated with Global Warming (IPCC, 2013a) and the increase in the ocean heat is related to several consequences like sea-level rise, ice melt and coral bleaching (BROWN, 1997; IPCC, 2013b; JENKINS *et al.*, 2016). Analyses of ocean heat content zonally and meridionally averaged were performed for each ocean individually, according to Figure 42 in section 3.5.1, and by hemisphere. So, the oceans were divided into North and South Atlantic, North and South Pacific, Indian, Arctic,

and Southern oceans.

Analysis of the heat content integrated on the water column and in the first 1000 m (not shown here) show very similar behaviors for all oceans. piControl presents a relatively stable time series, and 1pctCO_2 shows a continuous increase in all oceans. Table 27 displays the percentages of increase in each case. We observe that the Arctic and the Southern oceans absorb much more heat than the others. This warming favors not only ice melting, which decreases surface salinity, altering buoyancy but may also decrease the ocean potential to absorb CO_2, as said in section 4.3.

Table 27: Changes in the heat content in the last decade of 1pctCO_2 compared to the average of piControl for each ocean. The (+) sign means an increase in the parameter compared to the average of piControl.

Ocean	Whole water column	0-1000 m
North Atlantic	+23.64%	+25.80%
South Atlantic	+28.51%	+31.50%
North Pacific	+21.04%	+21.84%
South Pacific	+22.32%	+22.87%
Indian	+28.56%	+29.73%
Arctic	+654.59%	+5038.13%
Southern	+138.08%	+233.06%

Different than what happened when we integrated the ocean heat content on the whole water column and the first 1000 m, Figure 83 presents the heat content time series between 2000 m-4000 m depth for each ocean. This depth interval was chosen for being the layer where the NADW is inserted in (TOMCZAK and GODFREY, 1994). We observe that piControl is not stable in this depth interval and shows an increase throughout the series for all oceans.

Although the kinetic energy in the deep ocean remains stable in piControl, as seen in Figure 46, it seems that the thermodynamics in deep layers may need more extended integrations to stabilize as in the work of LI *et al.* (2012) which deep ocean stabilized after 5,000 years. Regardless, this apparent non-stability does not exclude the analyses presented here, as in the work of VELLINGA and WOOD (2002), which states that although their 100-year control integration experiment was not in equilibrium, their assessment of the impacts of a NA freshening in the THC was still valuable. However, the consequences of some slowest climate parameters like deep ocean heat content may have been underestimated.

In the 1pctCO_2 experiment, not all oceans show an increase in the heat content in deep layers. Among those that do, the Arctic and Southern oceans remain with higher increases, which may affect deep and bottom water formation rates or patterns. The Atlantic ocean is the only one that shows a decreasing behavior in

ocean heat content in the 1pctCO$_2$ experiment. There is a lag of approximately 30 years at the start of the decrease between North and South Atlantic as the decrease started first in the NA, about 50 years after 1pctCO$_2$ began, and then moved to South Atlantic. This behavior may be related to the changes in the AMOC cell that started in the NA first. Since the 2000 m-4000 m layer would be the one where the NADW would be represented, this decrease in the ocean heat content may be related to less formation of NADW in the NA, which, after some years, impacted the South Atlantic Ocean.

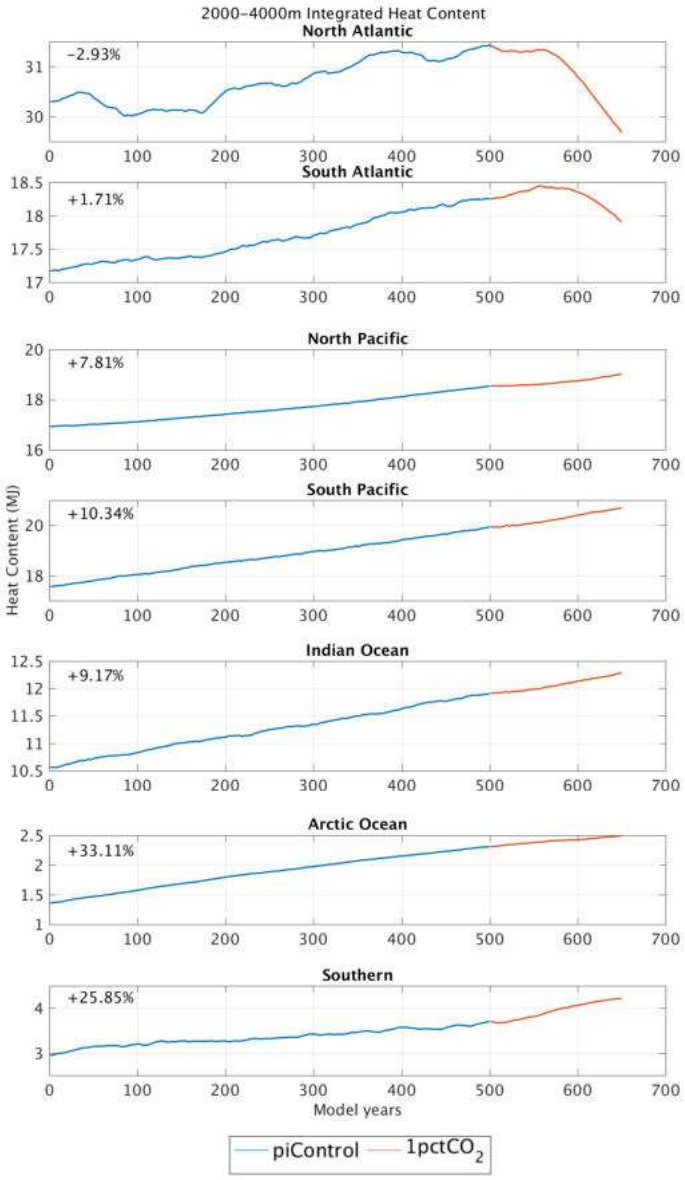

Figure 83: Annual mean series of the heat content in each ocean between 2000 m and 4000 m. Additionally, in each time series box, there is the percentage of increase (+) or decrease (-) in the last decade of the 1pctCO$_2$ experiment compared to the average of piControl.

Chapter 5

Final Discussions

As said before in section 3.2.2, the 1pctCO_2 is a climate change idealized experiment, meaning that it is neither a real CO_2 emission experiment nor a climate projection. Different than the IPCC's climate projections that, based on a range of future outcomes that take into account socioeconomic parameters, these projections describe possible developments of anthropogenic drivers of climate (O'NEILL *et al.*, 2016). Furthermore, although the 1pctCO_2 experiment is suitable to identify climate responses, its impossibility to project the changes identified in this work into the future or even relate them to past events may lead readers possibly to reduce its importance. However, if we could relate 1pctCO_2 atmospheric concentration time series with measured atmospheric CO_2, then we could bring it into a situation closer to reality.

Nowadays, there are numerous measurements of GHGs concentrations around the world. The World Data Centre for Greenhouse Gases (WDCGG) is a data center operated by the Japan Meteorological Agency (JMA) under the Global Atmosphere Watch (GAW) program of WMO. The WDCGG collects and archives GHGs data and data from some related gases like CO, making it available publicly to society. Figure 84 exhibit a map with the locations where WDCGG has stations for measurements of GHGs, which data comes from a variety of sources.

Figure 84: Map with the locations of GHG data acquisition stations around the world. Source: WDCGG, 2018.

Mauna Loa is one of the sites, the oldest one, to collect GHG data (COSTELLO *et al.*, 2009) and the one that is referenced in IPCC's reports and other scientific works, like Figure 3(a) in this thesis. It is located in Hawaii, and it was used to make comparisons with 1pctCO_2 experiment CO_2 forcing data.

If we take the atmospheric CO_2 measured in Mauna Loa since 1959 (Figure 85 - upper panel), we observe that CO_2 concentration began at 315.97 ppm and reached 411.44 ppm in 2019, an increase of 95.47 ppm in 60 years, or an average of 1.59 ppm per year. On the other hand, the atmospheric CO_2 emissions in 1pctCO_2 began in 284.32 ppm in year 1 (Figure 85 - lower panel) and reached 1239.84 ppm in year 150, an increase of 955.52 ppm in 149 years, or an average of 7.05 ppm per year.

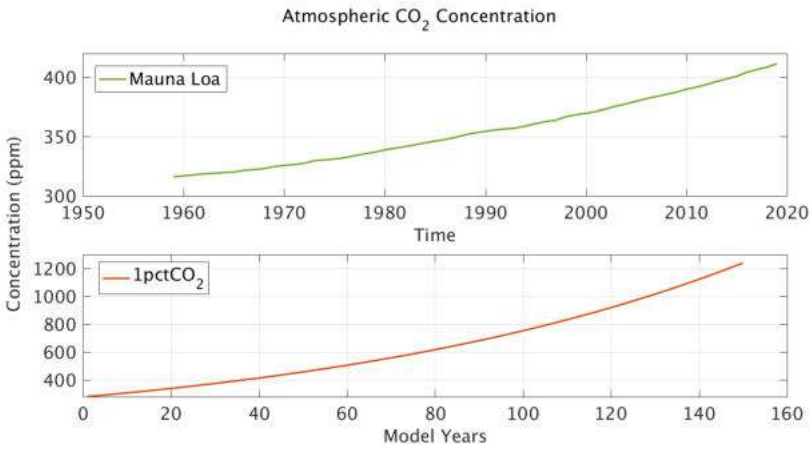

Figure 85: Time series of atmospheric CO_2 concentration measured in Mauna Loa (upper panel) and used as atmospheric forcing in 1pctCO_2 experiment (lower panel). Mauna Loa CO_2 data was acquired on the NOAA website, the institution responsible for the acquisition. The scientist responsible is Dr. Pieter Tans, NOAA/ESRL (www.esrl.noaa.gov/gmd/ccgg/trends/), and Dr. Ralph Keeling, Scripps Institution of Oceanography (scrippsco2.ucsd.edu/).

Even though the increase in 1pctCO_2's CO_2 is more than four times higher than the observations, it is possible to design a parallel between them, in an attempt to project when in the future the changes on the Climate Earth System, presented in this thesis, could occur. We have seen that the minimum surface air temperature threshold, proposed by LENTON *et al.* (2008), was achieved after year 100 in 1pctCO_2. Although the freshwater did not meet the same criteria, through its decadal anomaly (Figure 60 in item 4.2), we have identified a marked increase after decade eight and a change of pattern after decade 10. Also, the maximum mixed layer depth in the four Areas in NA (Figure 63 in item 4.2) exhibited marked different behaviors at the end of the 1pctCO_2 experiment that began around year 50 in Area 1.

That way, the projections were made for the model years 50, 100, and 150. Years 50 and 100 were chosen based on the features just presented, and the last year was included because 1pctCO_2 is an intensive CO_2-forcing experiment, and it would be interesting to project how far in the future are we away from it. That way, based on the average increase per year of Mauna Loa, the 50, 100, and 150 atmospheric CO_2 concentrations in the 1pctCO_2 experiment - 458.38 ppm, 753.87 ppm, and 1239.84 ppm, respectively - would be achieved after years 2048, 2234 and 2540.

Although years 2234 and 2540 seem a little bit too far in the future, the year 2048 lies within a reasonable range, only 28 years ahead and much less than the IPCC's long-term projections for 2100, lying more on a near-term projection (MOSS

et al., 2008). The atmospheric CO_2 concentration projected for the year 2048 would increase the average global surface air temperature by 1.61°C above pre-industrial levels, as MASSON-DELMOTTE *et al.* (2018) also obtained in the IPCC Special Report, and by 1.44°C above the average of 1980-1999, estimated by IPCC (2007). An associated average input of freshwater to the NA of 2.88 $m^3 \cdot s^{-1}$ would cause reductions in the mixed layer depth, and hence in deep convection in the NA of more than 22% in the Labrador Sea area and more than 33% in the Norwegian Sea area, reducing NADW formation and weakening the AMOC by 13.39%.

Besides these, other changes in the Earth Climate System may occur due to the increase in atmospheric CO_2 concentration, as we have seen throughout this work. Although no tipping point in the THC was identified, as stated earlier, the changes observed are significant, with the potential to impact several living beings, humans included.

It is imperative to state that the projection made here did not take into account the future profile with its economic, social, environmental, and political characteristics. The projection elaborated here was built considering the average atmospheric CO_2 emissions recorded in Mauna Loa, and it was meant to provide an exercise of what future may hold to us (MASSON-DELMOTTE *et al.*, 2018). The consequences of CO_2 in the atmosphere for the Earth Climate System may develop more os less severely depending on our environmental politics concerning climate change and GHG emissions.

Chapter 6

Final Considerations

This work investigated, through CO_2 forcing model results, a tipping point in the Thermohaline Circulation and evaluated the climate change that has arisen from it. Two CMIP6 simulations ran with NCAR's CESM were evaluated. An unforced control experiment was used to evaluate changes in the CO_2 forced experiment. piControl was run for 500 model years when the 1pctCO_2 experiment started with a 1% increment of CO_2 per year, which was run for 150 model years. NCAR scientifically validated both experiments. Nonetheless, a validation of piControl was performed against observed and reanalysis data and descriptions on the literature of known climatic features. This step was taken to assure that piControl was suited to be used as a control experiment and to be compared with 1pctCO_2.

Analysis of the kinetic energy from piControl showed that this experiment was already in dynamical balance since its beginning. The kinetic energy time series for several layers also confirmed that behavior and despite exhibiting different variabilities and levels of energy, all layers depicted small growth rates. On the other hand, the heat content in deep layers exhibited continuous growth throughout the piControl, which indicates that the thermodynamics in the deeper ocean did not stabilize and need more extended integrations. The heat fluxes on the ocean surface were also evaluated and showed a known pattern for both northern and southern hemispheres, which lose heat for the atmosphere in winter and absorb it in the summer. It was also noticed that the global average tends to follow the classic southern hemisphere distribution due to the difference in ocean/continent ratio between northern and southern hemispheres.

Still, on the validation of piControl, volume and heat transports across known sections were evaluated in the South Atlantic Ocean. These parameters were calculated across the Drake and Africa-Antarctic sections and also for the 25°S parallel. Their integrated values agreed with several works for the same locations, and essential features were identified throughout these sections like the Agulhas leakage in the Africa-Antarctic section and the western boundary current system in

the 25°S parallel. This last section also depicted a unique characteristic of the South Atlantic Ocean of exporting heat northward. The upper branch of AMOC returns to the NA through mainly the first 1000 m in the 25°S parallel, carrying an amount of heat that is one order of magnitude higher than the rest of the water column.

The thermohaline distribution on the Atlantic Ocean was evaluated through a cross-ocean set of sections zonally averaged. AAIW, NADW, and AABW thermohaline index were identified in the water column according to previous works in the literature. Additionally, the Brazil-Malvinas Confluence seasonality was evaluated through SST distribution against the CMEMS product, and the 18°C isotherm shift between summer and winter was identified. The analysis of the BMC evaluates not only this Confluence but both the dynamic of Brazil and Malvinas Current. The first one is inserted in the South Atlantic Subtropical Gyre, forced by the South Atlantic Subtropical High, and the second one is formed by instabilities in the AACC after it passes through the Drake Passage.

Other model components were also validated. The zonal mean distributions of sea level pressure and surface air temperature from the atmospheric model were compared against two reanalysis data. In mid and low latitudes, piControl agreed well with ERA-Interim and Reanalysis 2. Towards the poles, divergences were observed, which is not a problem particular to the piControl. Little observations in high latitudes and the difficulty of numerical models to represent parameters in converging meridian grid cells were some reasons pointed out to justify the differences between the three numerical products.

The annual climatology of sea ice concentration from the sea ice model component was also evaluated and compared with satellite observed sea ice from the NSIDC. The pattern for the northern and southern hemispheres agreed with NSIDC data and followed the known climatology. Quantities were correctly represented for the southern hemisphere. In the northern hemisphere, mean errors of more than 5% were identified and are related to the periods considered for the analysis. NSIDC observations originated from a higher GHG forcing period compared to the piControl, and so these differences are due to less sea ice registered by NSIDC.

Changes in the 1pctCO_2 experiment were diverse, and so were the consequences of them. As expected, the increase in the mean surface air temperature was highly correlated with CO_2 forcing, increasing the air temperature by almost 20°C at the end of the experiment. Despite the high temperatures, a region of colder SSTs in the North Atlantic inhibited evaporation and the surface heat loss, which led to an increase of freshwater input to the NA, and a decrease near the NADW formation regions, decreasing sea surface salinity. Surface density was not increased, and hence the deep convection ended up being shut down. This behavior was also seen in the work of MANABE and STOUFFER (1999). It appears that changes

began in the Labrador Sea and were advancing to the east and north of the NA, towards the Norwegian Sea.

The profile of the AMOC cell with its upper and lower branches exhibits appreciable changes in the 1pctCO_2 experiment. The loss of mixed layer depth variability, leading to a shut down of deep convection in the NA, weakened and shallowed the upper branch of the AMOC cell, mainly in high latitudes of the NA. Additionally, the increase in freshwater input and decrease in sea surface salinity decreased the salinity gradient between the NA and the Southern Ocean, strengthening AABW and the lower branch of the AMOC cell. This change on the AMOC cell caused a reduction of more than 60% in the maximum overturning in the last decade of the 1pctCO_2.

In the South Atlantic Ocean, several changes regarding the features found in the sections in this region were identified. In the 25°S, the strengthened AABW occupied the gap of a shallower NADW in the deep ocean. Although less intense, the NADW carries more heat at the end of the 1pctCO_2 experiment compared to the piControl, decreasing the northward heat transport by the South Atlantic Ocean. The AACC between Drake and AF-AA Passages is strengthened, forced by stronger westerlies due to the increased pressure gradient in the atmosphere. At AF-AA Passage, the AC Leakage is weakened due to forcing in the Indian Ocean, which also contributed to impact the northward heat transport to the NA. Although less intense, like the NADW, it carries more heat westward, draining it dynamically from the AACC.

Other changes in the Earth Climate System were evaluated. Positive air surface temperature anomalies in almost the entire globe were identified, with a maximum over high latitudes in North America. More significant positive anomalies were positioned in high latitudes, decreasing the equator-to-pole temperature gradient. Negative temperature anomalies were found only in the NA, south of Iceland, between Greenland and Europe. This region of colder air temperatures is similar to the negative SST anomaly identified that promoted a decrease in the evaporation flux in the NA. The zonally averaged sea level pressure distributions showed an intensification in the high- and low-pressure belts, which promoted the strengthening of the westerlies in the Southern Ocean. The sea ice concentration in both hemispheres retracts drastically, exposing much more ocean areas in both hemispheres, compared to the piContol, altering the albedo in these regions and with the potential to create new deep convection sites and change air-sea fluxes.

The average surface heat flux in the last decade of the 1pctCO_2 experiment shows a significant increase in the positive values of heat flux for the northern hemisphere, indicating more ocean heat gain compared to the piControl, almost equivalent to the values of the southern hemisphere. The change in the latitudinal

distribution of heat transport reflects changes in the AMOC cell with a decrease in the northward heat transport and an increase in the southward one. Overall, the ocean heat content indicates that the oceans are warming substantially, with particular attention to the Arctic and Southern Oceans. The deep layers for the North and South Atlantic, on the other hand, show a decrease in the ocean heat content in the 1pctCO_2 experiment, which can be related to changes in the AMOC cell and NADW formations.

Despite being an idealized experiment, a straightforward projection into the future made based on measured atmospheric CO_2 concentrations showed some relevant consequences for the Earth Climate System in less than 30 years from now. This exercise demonstrated not only the relevance of the results identified here as well as a potential future for us if nothing is done to reduce GHGs atmospheric emissions.

Through CO_2-forced experiment results, this work made contributions to the knowledge about the mechanisms that govern and may influence AMOC dynamics and NADW formation, both in the North and in the South Atlantic Oceans. Besides, without achieving a THC tipping point, it has identified several consequences for the Earth Climate System that arouse from the continuous increase in CO_2 forcing. Furthermore, it was shown that concerning climate changes may occur not far in the future, and their reality is related to environmental policies humankind is employing. In addition to the environmental consequences due to Global Warming showed here, other studies reveal its consequences for human life like shorter gestational lengths (BARRECA and SCHALLER, 2020), leading to lower birth weights, for example.

It is important to clear out that the analysis performed in this study did not assess changes due to the internal variability of the experiments. As said previously in the Introduction (item 1), the topics explored here still can be deeper evaluated, and, as always, these gaps will be filled in future works.

Some acknowledgments to the sources that provided the observed and numerical products are essential. The Natural Environment Research Council funds the RAPID-WATCH MOC monitoring project, and the data are freely available from "www.rapid.ac.uk/rapidmoc". OSNAP data were collected and also made freely available by the OSNAP project and all the national programs that contribute to it. The NOAA Climate Program Office funds the MOVE project. Initial funding came from the German Bundesministerium fuer Bildung und Forschung. OSNAP data are also freely available. Computational and Information Systems Laboratory (CISL) provided computational and data resources, including the Cheyenne supercomputer (doi 10.5065/D6RX99HX) at NCAR, which is sponsored by the NSF.

Chapter 7

Conclusions

This work made use of an Earth System model to investigate and evaluate the tipping point mechanisms for the Atlantic Meridional Overturning Circulation. Based on the proposed methodology and the scientific literature, it was found that the CO_2 increase simulated by the 1pctCO_2 experiment was not sufficient to cause a tipping point in the monitored features, indicating that the radiative forcing and the energy input into the system must be more intense.

CESM is a powerful and complex earth system model that simulates major features in our Earth System and has been used to assess climate change for several years. Nonetheless, it is vital to have in mind that, as every numerical model, CESM is incapable of simulating all aspects and phenomena of the climate system, especially those sub-grid processes. One example of such a process is the one happening inside clouds, for example, which can increase warming to up to 8°C due to the abrupt dissolution of stratocumulus clouds (LENTON *et al.*, 2019).

It should be noted that although the CISM was not simulated in a two-way mode, this choice of configuration did not impact on the assessments of AMOC weakening in the 1pctCO_2 experiment. This assumption was made based on the work of MUNTJEWERF *et al.* (2020b) that performed a simulation with a CESM2.1 1pctCO_2 experiment with a dynamic Greenland Ice Sheet (GrIS). The authors found a substantial decline in AMOC, but such decline started before the increase in GrIS runoff. MUNTJEWERF *et al.* (2020a) also found similar behaviors of AMOC performing the same experiment with CESM2.1 with and without dynamic GrIS.

Despite not achieving a tipping point, several changes were identified, resulting from the increase in atmospheric CO_2, altering the dynamics and thermodynamics of oceans and atmosphere. Additionally, the sea ice concentration changes in both hemispheres contributed to the amplification of the albedo feedback (SCHNEIDER and DICKINSON, 1974). LENTON *et al.* (2019) state that changes in a feature, as the AMOC slow-down, for example, even without achieving a tipping point, can trigger changes in other climate system tipping elements as a

drought in Africa's Sahel region or the Amazon. On the other hand, theses droughts can trigger other types of changes, beginning a domino effect and causing a global tipping point (Figure 86). Although LENTON (2020) points out the existence of this domino effect or "tipping cascade", the author emphasizes that tipping cascades are not the rule.

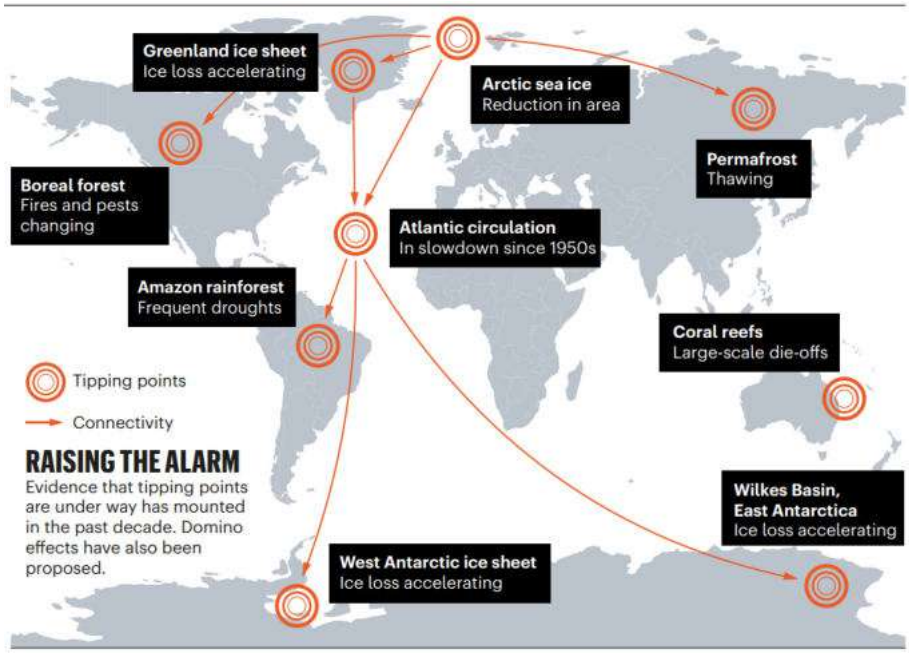

Figure 86: Domino effect occurring in different tipping elements worldwide. Source: LENTON *et al.*, 2019.

Despite this, it is undeniable that we are on the way to a moment of change of pattern. Although we did not seem to have achieved a major tipping point in the climate system yet, the increase in the intensity and frequency of extreme events shows the climatic variability amplification due to the addition of energy into the system (COSTELLO *et al.*, 2009; IPCC, 2013a; SANCHO, 2014). This moment of climatic disruption is not in the near future. However, the probability of this process accelerating is closely related to the social model we live in regarding unrestrained consumption, unclean energy production, and planned obsolescence.

Never in the history of science has there been more technology and knowledge about climate and future climate change scenarios. It is time for public policies to take action with climate mitigation measures and changes in the population's social life with conducts of awareness about the production of waste, conscious and sustainable consumption, reduction of the production of raw materials in search of reuse of inputs already produced, and environmental education about each one's role in preserving the environment and the consequences of climate change for society itself, to name a few examples.

7.1 Future Work

As said before, the results output from the two numerical experiments used here are extensive; a whole thesis could have been written evaluating the internal variability of the climate system from the piControl, so imagine how numerous would be the works with all these results. That is the reason why the analyses presented here were not exhausted. How could they? The beauty of science resides in creating more questions from one already existing. That does the job of electing some future themes to work with very hard, but here are some attempts.

One of the analyses that caught the attention regards the feedback mechanisms controlling the CO_2 sink/source balance between the Southern Ocean and the atmosphere. Investigate how this mechanism works, how it could be affected, enhanced, or shut down is an exciting path to follow. Another one concerns the sources to the upper limb of the AMOC cell, what is the contribution from each one, and how they could be impacted in a warming climate. Would they suffer the same fate or some compensation mechanisms could enter the equation?

Once these results are a product of coupled Earth System model experiments, one can wonder how the other climate components and climatic features responded to the increase in the atmospheric CO_2. An example would be the land model and how the PFTs dynamic behaved through the 1pctCO_2 experiment; were there changes in vegetation types at the end of the forced experiment? How would the climate be affected if, along with the increase in the atmospheric CO_2, would urban and managed vegetated land units expand?

As we can see, the options are numerous, a real scientific playground where the imagination can wander around indefinitely. If used wisely, these types of Earth System models can improve our knowledge about climate feedback mechanisms, which in turn could help us manage and control the anthropogenic impact on climate.

Bibliography

ABE-OUCHI, A., SAITO, F., KAWAMURA, K., et al., 2013, "Insolation-driven 100,000-year glacial cycles and hysteresis of ice-sheet volume", *Nature*, v. 500 (08), pp. 190–193. doi: <10.1038/nature12374>.

ADCROFT, A., HILL, C., MARSHALL, J., 1997, "Representation of topography by shaved cells in a height coordinate ocean model", *Monthly Weather Review*, v. 125, pp. 2293–2315. doi: <10.1175/1520-0493(1997)125<2293:ROTBSC>2.0.CO;2>.

ALVES DOS SANTOS, F., SANTI COIMBRA DE OLIVEIRA, A. L., MENDES SOARES, F. L., et al., 2015, "Chapter 7 - Projeto Azul: Operational Oceanography in an Active Oil and Gas Area Southeastern Brazil". In: Liu, Y., Kerkering, H., Weisberg, R. H. (Eds.), *Coastal Ocean Observing Systems*, Academic Press, pp. 99–118, Boston. ISBN: 978-0-12-802022-7. Availability: <http://www.sciencedirect.com/science/article/pii/B9780128020227000079>.

ANSORGE, I. J., BARINGER, M. O., CAMPOS, E. J. D., et al., 2014, "Basin-Wide Oceanographic Array Bridges the South Atlantic", *Eos, Transactions American Geophysical Union*, v. 95, n. 6, pp. 53–54. doi: <10.1002/2014EO060001>. Availability: <https://agupubs.onlinelibrary.wiley.com/doi/abs/10.1002/2014EO060001>.

ANTHOFF, D., ESTRADA, F., TOL, R. S. J., 2016, "Shutting Down the Thermohaline Circulation", *American Economic Review*, v. 106, n. 5 (May), pp. 602–06. doi: <10.1257/aer.p20161102>. Availability: <http://www.aeaweb.org/articles?id=10.1257/aer.p20161102reater .

ANTHONY, K. R. N., KLINE, D. I., DIAZ-PULIDO, G., et al., 2008, "Ocean acidification causes bleaching and productivity loss in coral reef builders", *Proceedings of the National Academy of Sciences*, v. 105, n. 45, pp. 17442–17446. doi: <10.1073/pnas.0804478105>. Availability: <https://www.pnas.org/content/105/45/17442>.

ASSAD, L. P. F., 2006, *Influência do Campo de Vento Anômalo Tipo Enso na Dinâmica do Atlântico Sul*. Ph.D. Thesis, Programa de Engenharia Civil, COPPE, Universidade Federal do Rio de Janeiro, Rio de Janeiro.

ASSAD, L. P. F., TORRES JR, A. R., ARRUDA, W. Z., et al., 2009, "Volume and Heat Transports in the World Oceans from an Ocean General Circulation Model", *Revista Brasileira de Geofísica*, v. 27, pp. 181–194. doi: <10.1590/S0102-261X2009000200003>.

BAILEY, D., RHINES, P., HÄKKINEN, S., 2005, "Formation and pathways of North Atlantic Deep Water in a coupled ice–ocean model of the Arctic–North Atlantic Oceans", *Climate Dynamics*, v. 25 (10), pp. 497–516. doi: <10.1007/s00382-005-0050-3>.

BAKKER, P., SCHMITTNER, A., LENAERTS, J. T. M., et al., 2016, "Fate of the Atlantic Meridional Overturning Circulation: Strong decline under continued warming and Greenland melting", *Geophysical Research Letters*, v. 43, n. 23, pp. 12,252–12,260. doi: <10.1002/2016GL070457>. Availability: <https://agupubs.onlinelibrary.wiley.com/doi/abs/10.1002/2016GL070457>.

BARINGER, M. O., LARSEN, J. C., 2001, "Sixteen years of Florida Current Transport at 27° N", *Geophysical Research Letters*, v. 28, n. 16, pp. 3179–3182. doi: <10.1029/2001GL013246>. Availability: <https://agupubs.onlinelibrary.wiley.com/doi/abs/10.1029/2001GL013246>.

BARRECA, A., SCHALLER, J., 2020, "The impact of high ambient temperatures on delivery timing and gestational lengths", *Nature Climate Change*, v. 10 (01). doi: <10.1038/s41558-019-0632-4>.

BEAL, L., DE RUIJTER, W. M., BIASTOCH, A., et al., 2011, "On the role of the Agulhas system in ocean circulation and climate", *Nature*, v. 472, pp. 429–436. doi: <10.1038/nature09983>.

BERRISFORD, P., DEE, D., POLI, P., et al., 2011, *The ERA-Interim archive Version 2.0*. Relatório Técnico 1, European Centre for Medium-Range Weather Forecasts - ECMWF, 11. Availability: <https://www.ecmwf.int/node/8174>. Place of publication: Shinfield Park, Reading.

BIASTOCH, A., BÖNING, C., SCHWARZKOPF, F., et al., 2009, "Increase in Agulhas leakage due to poleward shift of Southern Hemisphere westerlies", *Nature*, v. 462, pp. 495–499. doi: <10.1038/nature08519>.

BITZ, C. M., HOLLAND, M. M., HUNKE, E. C., et al., 2005, "Maintenance of the Sea-Ice Edge", *Journal of Climate*, v. 18, n. 15, pp. 2903–2921. doi: <10.1175/JCLI3428.1>. Availability: <https://doi.org/10.1175/JCLI3428.1>.

BJERKNES, J., 1966, "A possible response of the atmospheric Hadley circulation to equatorial anomalies of ocean temperature", *Tellus*, v. 18, n. 4, pp. 820–829. doi: <10.1111/j.2153-3490.1966.tb00303.x>.

BLAIN, D., E., C. B., FUGLESTVEDT, J., et al., 2018, *Expert Meeting on Short-Lived Climate Forcers (SLCF)*. Relatório técnico, WMO and UNEP. Report of the Expert Meeting on Short-Lived Climate Forcers, Pub. IGES, Japan.

BOGENSCHUTZ, P., GETTELMAN, A., HANNAY, C., et al., 2018, "The path to CAM6: coupled simulations with CAM5.4 and CAM5.5", *Geoscientific Model Development*, v. 11 (01), pp. 235–255. doi: <10.5194/gmd-11-235-2018>.

BOLLMANN, M., BOSCH, T., COLIJN, F., et al., 2010, *World ocean review, 2010: living with the oceans*. ISBN 978-3-86648-012-4. Rio de Janeiro, Maribus.

BROECKER, W. S., 1987, "Unpleasant surprises in the greenhouse?" *Nature*, v. 328, pp. 123–126. doi: <10.1038/328123a0>. Availability: <https://doi.org/10.1038/328123a0>.

BROECKER, W. S., 1997, "Thermohaline Circulation, the Achilles Heel of Our Climate System: Will Man-Made CO2 Upset the Current Balance?" *Science*, v. 278, n. 5343, pp. 1582–1588. doi: <10.1126/science.278.5343.1582>. Availability: <https://science.sciencemag.org/content/278/5343/1582ter .

BROECKER, W., 1991, "The Great Ocean Conveyor", *Oceanography*, v. 4, n. 2, pp. 79–89. doi: <10.5670/oceanog.1991.07>.

BROWN, B., 1997, "Coral bleaching: causes and consequences. Coral Reefs 16 (Suppl): S129-S138", *Coral Reefs*, v. 16 (12), pp. S129–S138. doi: <10.1007/s003380050249>.

BRYAN, F., NAKASHIKI, N., YOSHIDA, Y., et al., 2007, "Response of the Meridional Overturning Circulation During Differing Pathways Toward Greenhouse Gas Stabilization", *Washington DC American Geophysical Union Geophysical Monograph Series*, (01), pp. 351–363. doi: <10.1029/173GM22>.

BÖCK, C., 2015, *Variabilidade dos Transportes Oceânicos da Corrente do Brasil em um Cenário de Emissões do IPCC*. Ph.D. Thesis, Programa de Engenharia Civil, COPPE, Universidade Federal do Rio de Janeiro, Rio de Janeiro.

CAMPOS, E., BUSALACCHIA, A., GARZOLI, S., et al., 1999, "The South Atlantic and Climate". In: Comission, I. O. (Ed.), *The Ocean Observing System for Climate (OceanObs99)*, St. Raphael, France.

CARLSON, A. E., OPPO, D. W., CAME, R. E., et al., 2008, "Subtropical Atlantic salinity variability and Atlantic meridional circulation during the last deglaciation", *Geology*, v. 36, n. 12 (12), pp. 991–994. doi: <10.1130/G25080A.1>. Availability: <https://doi.org/10.1130/G25080A.1>.

CARTON, J. A., GRODSKY, S. A., LIU, H., 2008, "Variability of the Oceanic Mixed Layer, 1960–2004", *Journal of Climate*, v. 21, n. 5, pp. 1029–1047. doi: <10.1175/2007JCLI1798.1>. Availability: <https://doi.org/10.1175/2007JCLI1798.1>.

CATALDI, M., 2008, *Estudo Numérico da Influência das Anomalias da TSM do Atlântico Sul Extratropical e do Pacífico Equatorial no Regime Hidrometeorológico das Regiões Sul e Sudeste do Brasil*. Ph.D. Thesis, Programa de Engenharia Civil, COPPE, Universidade Federal do Rio de Janeiro, Rio de Janeiro.

CLARKE, A., CHURCH, J., GOULD, J., 2001, "The Ocean and Climate: Ocean Processes and Climate Phenomena". In: Siedler, G., Church, J., Gould, J. (Eds.), *Ocean Circulation and Climate: Observing and Modelling the Global Ocean*, ISBN 0-12-641351-7, Academic Press, London, San Diego, pp. 11–30.

CMEMS, 2017a, *Product User Manual for Global Ocean Reanalysis Products GLOBAL-REANALYSIS-PHY-001-025*. Relatório técnico, COPERNICUS Marine Environment Monitoring Service, a.

CMEMS, 2017b, *Quality Information Document for Global Ocean Reanalysis Products GLOBAL-REANALYSIS-PHY-001-025*. Relatório técnico, COPERNICUS Marine Environment Monitoring Service, b.

COLLING, A., 1989, *Ocean Circulation*. ISBN 978-0750652780. Oxford, Elsevier.

COSTELLO, A., ABBAS, M., ALLEN, A., et al., 2009, "Managing the Health Effects of Climate Change", *Lancet (London, England)*, v. 373, n. 9676 (05),

pp. 1693–1733. doi: <10.1016/S0140-6736(09)60935-1>. Availability: <https://doi.org/10.1016/S0140-6736(09)60935-1>.

CRAIG, A., VERTENSTEIN, M., JACOB, R., 2012, "A new flexible coupler for earth system modeling developed for CCSM4 and CESM1", *The International Journal of High Performance Computing Applications*, v. 26, pp. 31–42. doi: <10.1177/1094342011428141>.

CUNNINGHAM, S. A., ALDERSON, S. G., KING, B. A., et al., 2003, "Transport and variability of the Antarctic Circumpolar Current in Drake Passage", *Journal of Geophysical Research: Oceans*, v. 108, n. C5. doi: <10.1029/2001JC001147>. Availability: <https://agupubs.onlinelibrary.wiley.com/doi/abs/10.1029/2001JC001147>.

CUNNINGHAM, S. A., KANZOW, T., RAYNER, D., et al., 2007, "Temporal Variability of the Atlantic Meridional Overturning Circulation at 26.5°N", *Science*, v. 317, n. 5840, pp. 935–938. doi: <10.1126/science.1141304>. Availability: <https://science.sciencemag.org/content/317/5840/935er .

DANABASOGLU, G., LAMARQUE, J.-F., BACMEISTER, J., et al., 2020, "The Community Earth System Model Version 2 (CESM2)", *Journal of Advances in Modeling Earth Systems*, v. 12, n. 2, pp. 35p. doi: <10.1029/2019MS001916>. Availability: <https://agupubs.onlinelibrary.wiley.com/doi/abs/10.1029/2019MS001916>.

DANABASOGLU, G., YEAGER, S. G., KIM, W. M., et al., 2016, "North Atlantic simulations in Coordinated Ocean-ice Reference Experiments phase II (CORE-II). Part II: Inter-annual to decadal variability", *Ocean Modelling*, v. 97, pp. 65–90. doi: <https://doi.org/10.1016/j.ocemod.2015.11.007>. Availability: <http://www.sciencedirect.com/science/article/pii/S1463500315002231>.

DEE, D. P., UPPALA, S. M., SIMMONS, A. J., et al., 2011, "The ERA-Interim reanalysis: configuration and performance of the data assimilation system", *Quarterly Journal of the Royal Meteorological Society*, v. 137 (apr), pp. 553–597. doi: <10.1002/qj.828>.

DELWORTH, T. L., BROCCOLI, A. J., ROSATI, A., et al., 2006, "GFDL's CM2 Global Coupled Climate Models. Part I: Formulation and Simulation Characteristics", *Journal of Climate*, v. 19, n. 5, pp. 643–674. doi: <10.1175/JCLI3629.1>.

DIAMOND, J., 2019, *Reviravolta: Como indivíduos e nações bem-sucedidas se recuperam das crises*. Record. ISBN: 9788501117731. Availability: <https://books.google.com.br/books?id=HumjDwAAQBAJ>.

DONNERS, J., DRIJFHOUT, S., HAZELEGER, W., 2005, "Water mass transformation and subduction in the South Atlantic", *Journal of Physical Oceanography. American Meteorological Society*, v. 35, pp. 1841–1860. doi: <10.1175/JPO2782.1>.

DONOVAN, S. K., 2014, "Climate: a very short introduction by Mark Maslin. Oxford University Press, Oxford, 2013. No. of pages: xii+159. Price: UK£7.99. ISBN 978-0-19-964113-0 (paperback)." *Geological Journal*, v. 49, n. 6, pp. 651–651. doi: <10.1002/gj.2538>. Availability: <https://onlinelibrary.wiley.com/doi/abs/10.1002/gj.2538reater .

DRIJFHOUT, S., BATHIANY, S., BEAULIEU, C., et al., 2015, "Catalogue of abrupt shifts in Intergovernmental Panel on Climate Change climate models", *Proceedings of the National Academy of Sciences*, v. 112, n. 43, pp. E5777–E5786. doi: <10.1073/pnas.1511451112>. Availability: <https://www.pnas.org/content/112/43/E5777>.

EDMONDS, J. A., WISE, M. A., MACCRACKEN, C. N., 1994, *ADVANCED ENERGY TECHNOLOGIES AND CLIMATE CHANGE: AN ANALYSIS USING THE GLOBAL CHANGE ASSESSMENT MODEL (GCAM)*. Technical Report PNL-9798, Pacific Northwest National Lab. (PNNL), Richland, WA (United States), United States, May.

EPA, 2017, *Understanding Global Warming Potentials*. Availability: <https://www.epa.gov/ghgemissions/understanding-global-warming-potentials>. EPA - United States Environmental Protection Agency. Accessed in July, 3rd 2020.

EPA, 2020a, *Acid Rain*, a. Availability: <https://www.epa.gov/acidrain/what-acid-rain>. EPA - United States Environmental Protection Agency. Accessed in July, 3rd 2020.

EPA, 2020b, *Overview of Greenhouse Gases*, b. Availability: <https://www.epa.gov/ghgemissions/overview-greenhouse-gasesxtgreater . EPA - United States Environmental Protection Agency. Accessed in July, 3rd 2020.

EYRING, V., BONY, S., MEEHL, G. A., et al., 2016, "Overview of the Coupled Model Intercomparison Project Phase 6 (CMIP6) experimental design and

organization", *Geoscientific Model Development*, v. 9, n. 5, pp. 1937–1958. doi: <10.5194/gmd-9-1937-2016>. Availability: <https://www.geosci-model-dev.net/9/1937/2016/>.

FETTER, A. F. H., MATANO, R. P., 2008, "On the origins of the variability of the Malvinas Current in a global, eddy-permitting numerical simulation", *Journal of Geophysical Research: Oceans*, v. 113, n. C11. doi: <10.1029/2008JC004875>. Availability: <https://agupubs.onlinelibrary.wiley.com/doi/abs/10.1029/2008JC004875>.

FETTERER, F., KNOWLES, K., MEIER, W., et al., 2017, *Sea Ice Index, Version 3. GO2135*. Relatório técnico, NSIDC: National Snow and Ice Data Center, Boulder, Colorado USA. Availability: <http://nsidc.org/data/G02135>. Updated daily. Accessed June, 8th 2018.

FORRYAN, A., BACON, S., TSUBOUCHI, T., et al., 2019, "Arctic freshwater fluxes: sources, tracer budgets and inconsistencies", *The Cryosphere*, v. 13, n. 8, pp. 2111–2131. doi: <10.5194/tc-13-2111-2019>. Availability: <https://www.the-cryosphere.net/13/2111/2019/>.

FRAJKA-WILLIAMS, E., CUNNINGHAM, S. A., BRYDEN, H., et al., 2011, "Variability of Antarctic Bottom Water at 24.5°N in the Atlantic", *Journal of Geophysical Research: Oceans*, v. 116, n. C11. doi: <10.1029/2011JC007168>. Availability: <https://agupubs.onlinelibrary.wiley.com/doi/abs/10.1029/2011JC007168>.

FRAJKA-WILLIAMS, E., ANSORGE, I. J., BAEHR, J., et al., 2019, "Atlantic Meridional Overturning Circulation: Observed Transport and Variability", *Frontiers in Marine Science*, v. 6, pp. 260. doi: <10.3389/fmars.2019.00260>. Availability: <https://www.frontiersin.org/article/10.3389/fmars.2019.00260% textgreater .

GANACHAUD, A., WUNSCH, C., 2000, "Improved Estimates Of Global Ocean Circulation,Heat Transport and mixing From Hydrographic Data", *Nature*, v. 408, pp. 453–457. doi: <10.1038/35044048>.

GARZOLI, S., BARINGER, M., 2007, "Meridional heat transport determined with expandable bathythermographs—Part II: South Atlantic transport", *Deep Sea Research Part I: Oceanographic Research Papers*, v. 54 (08), pp. 1402–1420. doi: <10.1016/j.dsr.2007.04.013>.

GHORMLEY, J. A., ELLSWORTH, R. L., HOCHANADEL, C. J., 1973, "Reaction of excited oxygen atoms with nitrous oxide. Rate constants for

reaction of ozone with nitric oxide and with nitrogen dioxide", *The Journal of Physical Chemistry*, v. 77, n. 11, pp. 1341–1345. doi: <10.1021/j100630a005>. Availability: <https://doi.org/10.1021/j100630a005>.

GIORGI, F., 2005, "Climate Change Prediction", *Climatic Change*, v. 73, pp. 239–265. doi: <10.1007/s10584-005-6857-4>.

GLEICK, P., COOLEY, H., FAMIGLIETTI, J., et al., 2013, "Improving Understanding of the Global Hydrological Cycle: Observation and Analysis of the Climate System: The Global Water Cycle". In: Asrar, G., Hurrel, J. (Eds.), *Climate Science for Serving Society: Research, Modelling and prediction Priorities*, ISBN 978-94-007-6691-4, Springer, pp. 151–184, Dordecht.

GNANADESIKAN, A., DIXON, K., GRIFFIES, S., et al., 2006, "GFDL's CM2 Global Coupled Climate Models. Part II: The Baseline Ocean Simulation", *Journal of Climate - Special Section*, v. 19, pp. 675–697. doi: <10.1175/JCLI3630.1>.

GORDON, A., 2003, "The Brawniest retroflection", *Nature*, v. 421, pp. 904–905. doi: <10.1038/421904a>.

GRASSL, H., 2001, "The Ocean and Climate: Climate and Oceans". In: Siedler, G., Church, J., Gould, J. (Eds.), *Ocean Circulation and Climate: Observing and Modelling the Global Ocean*, ISBN 9780123918536, Academic Press, pp. 3–10.

GREGORY, J. M., DIXON, K. W., STOUFFER, R. J., et al., 2005, "A model intercomparison of changes in the Atlantic thermohaline circulation in response to increasing atmospheric CO2 concentration", *Geophysical Research Letters*, v. 32, n. 12. doi: <10.1029/2005GL023209>. Availability: <https://agupubs.onlinelibrary.wiley.com/doi/abs/10.1029/2005GL023209>.

GRIFFIES, S., BÖNING, C., BRYAN, F., et al., 2000, "Developments in ocean climate modeling", *Ocean Modelling*, v. 2, pp. 123–192. doi: <10.1016/S1463-5003(00)00014-7>.

GRIFFIES, S., GNANADESIKAN, A., DIXON, K., et al., 2005, "Formulation of an ocean model for global climate simulations", *Ocean Science*, v. 1, pp. 45–79. doi: <10.5194/os-1-45-2005>.

GRIFFIES, S., HARRISON, M., PACANOWSKI, R., et al., 2008, *A Technical Guide To Mom4*. Relatório Técnico No. 5., GFDL Ocean Group NOAA/Geophysical Fluid Dynamics Laboratory.

GRODZINS, M., 1957, "Metropolitan segregation", *Scientific American*, v. 197, n. 4, pp. 33–41. doi: <10.1038/scientificamerican1057-33>.

GRUBER, N., CLEMENT, D., CARTER, B. R., et al., 2019, "The oceanic sink for anthropogenic CO_2 from 1994 to 2007", *Science*, v. 363, n. 6432, pp. 1193–1199. doi: <10.1126/science.aau5153>. Availability: <https://science.sciencemag.org/content/363/6432/1193ter .

GUPTA, A. S., MUIR, L. C., BROWN, J. N., et al., 2012, "Climate Drift in the CMIP3 Models", *Journal of Climate*, v. 25, n. 13, pp. 4621–4640. doi: <10.1175/JCLI-D-11-00312.1>. Availability: <https://doi.org/10.1175/JCLI-D-11-00312.1>.

GUPTA, A. S., JOURDAIN, N. C., BROWN, J. N., et al., 2013, "Climate Drift in the CMIP5 Models", *Journal of Climate*, v. 26, n. 21, pp. 8597–8615. doi: <10.1175/JCLI-D-12-00521.1>. Availability: <https://doi.org/10.1175/JCLI-D-12-00521.1>.

HAGOS, S., LEUNG, R., RAUSCHER, S., et al., 2013, "Error Characteristics of Two Grid Refinement Approaches in Aquaplanet Simulations: MPAS-A and WRF", *Monthly Weather Review*, v. 141, pp. 3022–3036. doi: <10.1175/MWR-D-12-00338.1>.

HALTINER, G. J., WILLIAMS, R. T., 1980, "Numerical prediction and dynamic meteorology (2nd Edition)", *Quarterly Journal of the Royal Meteorological Society*, v. 110, n. 463, pp. 280–280. doi: <10.1002/qj.49711046321>. Availability: <https://rmets.onlinelibrary.wiley.com/doi/abs/10.1002/qj.49711046321>.

HANSEN, J., RUEDY, R., SATO, M., et al., 2010, "Global Surface Temperature Change", *Reviews of Geophysics*, v. 48 (12), pp. RG4004–. doi: <10.1029/2010RG000345>.

HARTMANN, D. L., 1994, *Global Physical Climatology*. 9780080571638. São Diego, Academic Press.

HODGES, K. I., LEE, R. W., BENGTSSON, L., 2011, "A Comparison of Extratropical Cyclones in Recent Reanalyses ERA-Interim, NASA MERRA,

NCEP CFSR, and JRA-25", *Journal of Climate*, v. 24, n. 18, pp. 4888–4906. doi: <10.1175/2011JCLI4097.1>. Availability: <https://doi.org/10.1175/2011JCLI4097.1>.

HODGSON, D. A., SIME, L. C., 2010, "Southern westerlies and CO2", *Nature Geoscience*, v. 3 (10), pp. 666–667. doi: <10.1038/ngeo970>.

HOESLY, R. M., SMITH, S. J., FENG, L., et al., 2018, "Historical (1750-2014) anthropogenic emissions of reactive gases and aerosols from the Community Emissions Data System (CEDS)", *Geoscientific Model Development*, v. 11, n. 1, pp. 369–408. doi: <10.5194/gmd-11-369-2018>. Availability: <https://www.geosci-model-dev.net/11/369/2018/>.

HOLLAND, M. M., BITZ, C. M., TREMBLAY, B., 2006, "Future abrupt reductions in the summer Arctic sea ice", *Geophysical Research Letters*, v. 33, n. 23. doi: <10.1029/2006GL028024>. Availability: <https://agupubs.onlinelibrary.wiley.com/doi/abs/10.1029/2006GL028024>.

HOUGHTON, J., 2004, *Global Warming*. ISBN 978-0521528740. New York, Cambrigde University Press.

HOUGHTON, J., 2009, *Global Warming*. ISBN 978-0521709163. New York, Cambrigde University Press.

HOUGHTON, R. A., 2010, "How well do we know the flux of CO2 from land-use change?" *Tellus B*, v. 62, n. 5, pp. 337–351. doi: <10.1111/j.1600-0889.2010.00473.x>. Availability: <https://onlinelibrary.wiley.com/doi/abs/10.1111/j.1600-0889.2010.00473.x>.

HUNKE, E., LIPSCOMB, W., 2010, "CICE: The Los Alamos sea ice model documentation and software user's manual version 4.0 LA-CC-06-012", *Tech. Rep. LA-CC-06-012*, (01).

HURK, B. V. D., BRACONNOT, P., EYRING, V., et al., 2013, "Assessing the Reliability of Climate Models, CMIP5". In: Asrar, G., Hurrel, J. (Eds.), *Climate Science for Serving Society: Research, Modelling and prediction Priorities*, ISBN 978-94-007-6691-4, Springer, pp. 237–248, Dordecht.

HURRELL, J. W., HOLLAND, M. M., GENT, P. R., et al., 2013, "The Community Earth System Model: A Framework for Collaborative Research", *Bulletin of the American Meteorological Society*, v. 94, n. 9, pp. 1339–1360. doi: <10.1175/BAMS-D-12-00121.1>. Availability: <https://doi.org/10.1175/BAMS-D-12-00121.1>.

HURTT, G. C., CHINI, L. P., FROLKING, S., et al., 2011, "Harmonization of land-use scenarios for the period 1500-2100: 600 years of global gridded annual land-use transitions, wood harvest, and resulting secondary lands", *Climatic Change*, v. 109, n. 1 (Aug), pp. 117. doi: <10.1007/s10584-011-0153-2>. Availability: <https://doi.org/10.1007/s10584-011-0153-2>.

IPCC, 2007, *Climate Change 2007: The Physical Science Basis. Working Group I Contribution to the Fourth Assessment Report of the Intergovernmental Panel on Climate Change*, v. 1. Cambridge, United Kingdom and New York, NY, USA, Cambridge University Press. Solomon, S. and Qin, D. and Manning, M. and Chen, Z. and Marquis, M. and Avery, K. and Tignor, M. and Miller, H. (eds.).

IPCC, 2013a, "Summary for Policymakers". In: *Climate Change 2013: The Physical Science Basis. Contribution of Working Group I to the Fifth Assessment Report of the Intergovernmental Panel on Climate Change*, book section SPM, p. 1–30, Cambridge, United Kingdom and New York, NY, USA, Cambridge University Press, a. ISBN: ISBN 978-1-107-66182-0. Availability: <www.climatechange2013.org>. Stocker, T.F. and Qin, D. and Plattner, G.-K. and Tignor, M. and Allen, S.K. and Boschung, J. and Nauels, A. and Xia, Y. and Bex, V. and Midgley, P.M. (eds.).

IPCC, 2013b, *Climate Change 2013 - The Physical Science Basis: Working Group I Contribution to the Fifth Assessment Report of the Intergovernmental Panel on Climate Change*. Cambridge, United Kingdom and New York, NY, USA, Cambridge University Press. Stocker, T.F., D. Qin, G.-K. Plattner, M. Tignor, S.K. Allen, J. Boschung, A. Nauels, Y. Xia, V. Bex and P.M. Midgley (eds.).

IPCC, 2019, *Glossary of acronyms and specialised terms on the IPCC-DDC website*. Availability: <http://www.ipcc-data.org/guidelines/pages/glossary/glossary_r.html>. Accessed in May, 27th 2019.

JENKINS, A., DUTRIEUX, P., JACOBS, S., et al., 2016, "Decadal Ocean Forcing and Antarctic Ice Sheet Response: Lessons from the Amundsen Sea", *Oceanography*, v. 29 (December). Availability: <https://doi.org/10.5670/oceanog.2016.103>.

JIANG, L.-Q., CARTER, B. R., FEELY, R. A., et al., 2019, "Surface ocean pH and buffer capacity: past, present and future", *Scientific Reports*, v. 9, n. 18624, pp. 11p. doi: <10.1038/s41598-019-55039-4>.

JOHANNESSEN, O. M., BENGTSSON, L., MILES, M. W., et al., 2004, "Arctic climate change: observed and modelled temperature and sea-ice variability", *Tellus A: Dynamic Meteorology and Oceanography*, v. 56, n. 4, pp. 328–341. doi: <10.3402/tellusa.v56i4.14418>. Availability: <https://doi.org/10.3402/tellusa.v56i4.14418>.

JOHNS, W. E., BEAL, L. M., BARINGER, M. O., et al., 2008, "Variability of Shallow and Deep Western Boundary Currents off the Bahamas during 2004–05: Results from the 26°N RAPID–MOC Array", *Journal of Physical Oceanography*, v. 38, n. 3, pp. 605–623. doi: <10.1175/2007JPO3791.1>. Availability: <https://doi.org/10.1175/2007JPO3791.1>.

JOHNSON, H. L., CESSI, P., MARSHALL, D. P., et al., 2019, "Recent Contributions of Theory to Our Understanding of the Atlantic Meridional Overturning Circulation", *Journal of Geophysical Research: Oceans*, v. 124, n. 8, pp. 5376–5399. doi: <10.1029/2019JC015330>. Availability: <https://agupubs.onlinelibrary.wiley.com/doi/abs/10.1029/2019JC015330>.

JONES, R. W., RENFREW, I. A., ORR, A., et al., 2016, "Evaluation of four global reanalysis products using in situ observations in the Amundsen Sea Embayment, Antarctica", *Journal of Geophysical Research: Atmospheres*, v. 121, n. 11, pp. 6240–6257. doi: <10.1002/2015JD024680>. Availability: <https://agupubs.onlinelibrary.wiley.com/doi/abs/10.1002/2015JD024680>.

KALNAY, E., KANAMITSU, M., KISTLER, R., et al., 1996, "The NCEP/NCAR 40-Year Reanalysis Project", *Bulletin of the American Meteorological Society*, v. 77, n. 3, pp. 437–472. doi: <10.1175/1520-0477(1996)077<0437:TNYRP>2.0.CO;2>. Availability: <https://doi.org/10.1175/1520-0477(1996)077<0437:TNYRP>2.0.CO;2>.

KAMPEL, M., SILVA JR, C., 1996, "Análise EOF da Confluência Brasil-Malvinas a partir de imagens AVHRR". In: *VIII Simpósio Brasileiro de Sensoriamento Remoto*, INPE: Instituto Nacional de Pesquisas Espaciais, pp. 775–780, Salvador.

KANAMITSU, M., EBISUZAKI, W., WOOLLEN, J., et al., 2002, "NCEP–DOE AMIP-II Reanalysis (R-2)", *Bulletin of the American Meteorological Society*, v. 83, n. 11, pp. 1631–1644. doi: <10.1175/BAMS-83-11-1631>. Availability: <https://doi.org/10.1175/BAMS-83-11-1631>.

KAY, J. E., DESER, C., PHILLIPS, A., et al., 2015, "The Community Earth System Model (CESM) Large Ensemble Project: A Community Resource for Studying Climate Change in the Presence of Internal Climate Variability", *Bulletin of the American Meteorological Society*, v. 96, n. 8, pp. 1333–1349. doi: <10.1175/BAMS-D-13-00255.1>. Availability: <https://doi.org/10.1175/BAMS-D-13-00255.1>.

KEELING, C. D., PIPER, S. C., BACASTOW, R. B., et al., 2001, *Exchanges of atmospheric CO_2 and $^{13}CO_2$ with the terrestrial biosphere and oceans from 1978 to 2000. I. Global aspects*. Relatório técnico, Scripps Institution of Oceanography SIO, 06. Availability: <https://escholarship.org/uc/item/09v319r9>. UC San Diego: Library – Scripps Digital Collection.

KEELING, R. F., KEELING, C. D., 2017. "Atmospheric Monthly In Situ CO_2 Data - Mauna Loa Observatory, Hawaii". http://doi.org/10.6075/J08W3BHW. doi: <10.6075/J08W3BHW>. In Scripps CO_2 Program Data. UC San Diego Library Digital Collections. Accessed in June, 8th 2020.

KIRTMAN, B., ANDERSON, D., BRUNET, G., et al., 2013, "Prediction from Weeks to Decades". In: Asrar, G., Hurrel, J. (Eds.), *Climate Science for Serving Society: Research, Modelling and prediction Priorities*, ISBN 978-94-007-6691-4, Springer, pp. 205–236, Dordecht.

KNUTTI, R., MASSON, D., GETTELMAN, A., 2013, "Climate model genealogy: Generation CMIP5 and how we got there", *Geophysical Research Letters*, v. 40, n. 6, pp. 1194–1199. doi: <10.1002/grl.50256>. Availability: <https://agupubs.onlinelibrary.wiley.com/doi/abs/10.1002/grl.50256>.

KOENIG, Z., PROVOST, C., PARK, Y.-H., et al., 2016, "Anatomy of the Antarctic Circumpolar Current volume transports through Drake Passage", *Journal of Geophysical Research: Oceans*, v. 121, n. 4, pp. 2572–2595. doi: <10.1002/2015JC011436>. Availability: <https://agupubs.onlinelibrary.wiley.com/doi/abs/10.1002/2015JC011436>.

LARGE, W. G., DANABASOGLU, G., DONEY, S. C., et al., 1997, "Sensitivity to Surface Forcing and Boundary Layer Mixing in a Global Ocean Model: Annual-Mean Climatology", *Journal of Physical Oceanography*, v. 27, n. 11 (11), pp. 2418–2447. doi: <10.1175/1520-0485(1997)027<2418:STSFAB>2.0.CO;2>. Availability: <https://doi.org/10.1175/1520-0485(1997)027<2418:STSFAB>2.0.CO;2>.

LAUVSET, S. K., CARTER, B. R., PÈREZ, F. F., et al., 2020, "Processes Driving Global Interior Ocean pH Distribution", *Global Biogeochemical Cycles*, v. 34, n. 1, pp. e2019GB006229. doi: <10.1029/2019GB006229>. Availability: <https://agupubs.onlinelibrary.wiley.com/doi/abs/10.1029/2019GB006229>. e2019GB006229 2019GB006229.

LAWRENCE, D., FISHER, R., KOVEN, C., et al., 2020, *Technical Description of version 5.0 of the Community Land Model (CLM)*. Relatório técnico, NCAR: National Center for Atmospheric Research, 03. Availability: <http://www.cesm.ucar.edu/models/cesm2/land/CLM50_Tech_Note.pdf>. Accessed in May, 14th 2020.

LAWRENCE, D. M., FISHER, R. A., KOVEN, C. D., et al., 2019, "The Community Land Model Version 5: Description of New Features, Benchmarking, and Impact of Forcing Uncertainty", *Journal of Advances in Modeling Earth Systems*, v. 11, n. 12, pp. 4245–4287. doi: <10.1029/2018MS001583>. Availability: <https://agupubs.onlinelibrary.wiley.com/doi/abs/10.1029/2018MS001583>.

LAZZARA, M. A., DWORAK, R., SANTEK, D. A., et al., 2014, "High-Latitude Atmospheric Motion Vectors from Composite Satellite Data", *Journal of Applied Meteorology and Climatology*, v. 53, n. 2 (02), pp. 534–547. doi: <10.1175/JAMC-D-13-0160.1>. Availability: <https://doi.org/10.1175/JAMC-D-13-0160.1>.

LENTON, T., FOOTITT, A., DLUGOLECKI, A., 2009, *Major Tipping Points in the Earth's Climate System and Consequences for the Insurance Sector*. Munich, Germany, Gland, Switzerland and Allianz SE.

LENTON, T., ROCKSTRÖM, J., GAFFNEY, O., et al., 2019, "Climate tipping points — too risky to bet against", *Nature*, v. 575 (11), pp. 592–595. doi: <10.1038/d41586-019-03595-0>.

LENTON, T. M., 2013, "Environmental Tipping Points", *Annual Review of Environment and Resources*, v. 38, n. 1, pp. 1–29. doi: <10.1146/annurev-environ-102511-084654>. Availability: <https://doi.org/10.1146/annurev-environ-102511-084654ater .

LENTON, T. M., 2020, "Tipping positive change", *Philosophical Transactions of the Royal Society B: Biological Sciences*, v. 375, n. 1794, pp. 20190123. doi: <10.1098/rstb.2019.0123>. Availability: <https://royalsocietypublishing.org/doi/abs/10.1098/rstb.2019.0123>.

LENTON, T., HELD, H., KRIEGLER, E., et al., 2008, "Tipping elements in the Earth's climate system", *Proceedings of the National Academy of Science*, v. 105, n. 6, pp. 1786–1793. doi: <10.1073/pnas.0705414105>.

LI, C., STORCH, J.-S., MAROTZKE, J., 2012, "Deep-ocean heat uptake and equilibrium response", *Climate Dynamics*, v. 40 (03). doi: <10.1007/s00382-012-1350-z>.

LI, H., WIGMOSTA, M. S., WU, H., et al., 2013, "A Physically Based Runoff Routing Model for Land Surface and Earth System Models", *Journal of Hydrometeorology*, v. 14, n. 3, pp. 808–828. doi: <10.1175/JHM-D-12-015.1>. Availability: <https://doi.org/10.1175/JHM-D-12-015.1>.

LIMEBURNER, R., WHITEHEAD, J., CENEDESE, C., 2005, "Variability of Antarctic bottom water flow into the North Atlantic", *Deep Sea Research Part II: Topical Studies in Oceanography*, v. 52, n. 3, pp. 495–512. doi: <https://doi.org/10.1016/j.dsr2.2004.12.012>. Availability: <http://www.sciencedirect.com/science/article/pii/S0967064504003054>. Direct observations of oceanic flow: A tribute to Walter Zenk.

LIQUE, C., JOHNSON, H., PLANCHEREL, Y., 2018, "Emergence of deep convection in the Arctic Ocean under a warming climate", *Climate Dynamics*, (08), pp. 3833–3847. doi: <10.1007/s00382-017-3849-9>.

LOHMANN, K., DRANGE, H., BENTSEN, M., 2009, "Response of the North Atlantic subpolar gyre to persistent North Atlantic oscillation like forcing", *Climate Dynamics*, v. 32, n. 2 (Feb), pp. 273–285. doi: <10.1007/s00382-008-0467-6>. Availability: <https://doi.org/10.1007/s00382-008-0467-6>.

LOZIER, M., LI, F., BACON, S., et al., 2019, "Meridional overturning circulation and the associated heat and freshwater transports observed by the OSNAP (Overturning in the Subpolar North Atlantic Program) Array from 2014 to 2016." *Duke Digital Repository*. doi: <https://doi.org/10.7924/r4z60gf0f>.

LOZIER, S. M., BACON, S., BOWER, A. S., et al., 2017, "Overturning in the Subpolar North Atlantic Program: A New International Ocean Observing System", *Bulletin of the American Meteorological Society*, v. 98, n. 4, pp. 737–752. doi: <10.1175/BAMS-D-16-0057.1>. Availability: <https://doi.org/10.1175/BAMS-D-16-0057.1>.

LUCARINI, V., RAGONE, F., 2011, "Energetics Of Climate Models: Net Energy Balance And Meridional Enthalpy Transport", *Reviews of Geophysics*, v. 49, n. 1. doi: <10.1029/2009RG000323>. Availability: <https://agupubs.onlinelibrary.wiley.com/doi/abs/10.1029/2009RG000323>.

LUO, Y., T, J., GUO, C., et al., 2018, "Atlantic deep water circulation during the last interglacial", *Scientific Reports*, v. 8 (03). doi: <10.1038/s41598-018-22534-z>.

LUTJEHARMS, J. R. E., VAN BALLEGOOYEN, R. C., 1988, "The Retroflection of the Agulhas Current", *Journal of Physical Oceanography*, v. 18, n. 11, pp. 1570–1583. doi: <10.1175/1520-0485(1988)018<1570:TROTAC>2.0.CO;2>. Availability: <https://doi.org/10.1175/1520-0485(1988)018<1570:TROTAC>2.0.CO;2>.

LUTJEHARMS, J., 2006, "The Agulhas Current", *Springer*, (01). doi: <10.1007/3-540-37212-1>.

MADEC, G., DELECLUSE, P., IMBARD, M., et al., 1998, *OPA 8 Ocean General Circulation Model - Reference Manual*. Relatório técnico, LODYC/IPSL Note 11.

MADEC, G., IMBARD, M., 1996, "A global ocean mesh to overcome the North Pole singularity", *Climate Dynamics*, v. 12, n. 6 (May), pp. 381–388. doi: <10.1007/BF00211684>. Availability: <https://doi.org/10.1007/BF00211684>.

MANABE, S., STOUFFER, R., 1995, "Simulation of abrupt climate change induced by freshwater input to the North Atlantic Ocean", *Nature*, v. 378, pp. 165–167. doi: <10.1038/378165a0>.

MANABE, S., STOUFFER, R. J., 1999, "The rôle of thermohaline circulation in climate", *Tellus A: Dynamic Meteorology and Oceanography*, v. 51, n. 1, pp. 91–109. doi: <10.3402/tellusa.v51i1.12308>. Availability: <https://doi.org/10.3402/tellusa.v51i1.12308>.

MANN, M. E., 2009, "Defining dangerous anthropogenic interference", *Proceedings of the National Academy of Sciences*, v. 106, n. 11, pp. 4065–4066. doi: <10.1073/pnas.0901303106>. Availability: <https://www.pnas.org/content/106/11/4065>.

MASSON-DELMOTTE, V., ZHAI, P., PÖRTNER, H.-O., et al., 2018, "Summary for Policymakers". In: *Global Warming of 1.5°C. An IPCC Special Report on the impacts of global warming of 1.5°C°above pre-industrial levels and related global greenhouse gas emission pathways, in the context of strengthening the global response to the threat of climate change, sustainable development, and efforts to eradicate poverty*, book section SPM, p. 1–24, World Meteorological Organization, Geneva, Switzerland, World Meteorological Organization. ISBN: ISBN 978-92-9169-151-7. Availability: <https://www.ipcc.ch/site/assets/uploads/sites/2/2019/06/SR15_Full_Report_High_Res.pdf>.

MATSUOKA, Y., KAINUMA, M., MORITA, T., 1995, "Scenario analysis of global warming using the Asian Pacific Integrated Model (AIM)", *Energy Policy*, v. 23, n. 4-5, pp. 357–371. Availability: <https://ideas.repec.org/a/eee/enepol/v23y1995i4-5p357-371.html>.

MAURITZEN, C., HÄKKINEN, S., 1997, "Influence of sea ice on the thermohaline circulation in the Arctic-North Atlantic Ocean", *Geophysical Research Letters*, v. 24, n. 24, pp. 3257–3260. doi: <10.1029/97GL03192>. Availability: <https://agupubs.onlinelibrary.wiley.com/doi/abs/10.1029/97GL03192>.

MCCARTHY, G., SMEED, D., JOHNS, W., et al., 2015, "Measuring the Atlantic Meridional Overturning Circulation at 26°N", *Progress in Oceanography*, v. 130, pp. 91–111. doi: <https://doi.org/10.1016/j.pocean.2014.10.006>. Availability: <http://www.sciencedirect.com/science/article/pii/S0079661114001694>.

MCDONAGH, E., KING, B., BRYDEN, H., et al., 2015, "Continuous Estimate of Atlantic Oceanic Freshwater Flux at 26.5°N", *Journal of Climate*, v. 28 (09), pp. 150901110021003. doi: <10.1175/JCLI-D-14-00519.1>.

MCGUFFIE, K., HENDERSON-SELLERS, A., 2001, "Forty Years of Numerical Climate Modelling", *International Journal of Climatology*, v. 21, pp. 1067–1109. doi: <10.1002/joc.632>.

MEINEN, C., SABRINA, S., PEREZ, R., et al., 2013, "Temporal variability of the Meridional Overturning Circulation at 34.5°S: Results from two pilot boundary arrays in the South Atlantic", *Journal of Geophysical Research*, v. 118 (12), pp. 1–18. doi: <10.1002/2013JC009228>.

MEINEN, C. S., SPEICH, S., PIOLA, A. R., et al., 2018, "Meridional Overturning Circulation Transport Variability at 34.5°S During 2009–2017:

Baroclinic and Barotropic Flows and the Dueling Influence of the Boundaries", *Geophysical Research Letters*, v. 45, n. 9, pp. 4180–4188. doi: <10.1029/2018GL077408>. Availability: <https://agupubs.onlinelibrary.wiley.com/doi/abs/10.1029/2018GL077408>.

MEINSHAUSEN, M., VOGEL, E., NAUELS, A., et al., 2017, "Historical greenhouse gas concentrations for climate modelling (CMIP6)", *Geoscientific Model Development*, v. 10, n. 5, pp. 2057–2116. doi: <10.5194/gmd-10-2057-2017>. Availability: <https://www.geosci-model-dev.net/10/2057/2017/>.

MEINSHAUSEN, M., SMITH, S. J., CALVIN, K., et al., 2011, "The RCP greenhouse gas concentrations and their extensions from 1765 to 2300", *Climatic Change*, v. 109, n. 1 (Aug), pp. 213. doi: <10.1007/s10584-011-0156-z>. Availability: <https://doi.org/10.1007/s10584-011-0156-z>.

MESSNER, S., STRUBEGGER, M., 1995, *User's Guide for MESSAGE III*. Iiasa working paper, IIASA: International Institute for Aplied Systems Analysis, IIASA, Laxenburg, Austria, July. Availability: <http://pure.iiasa.ac.at/id/eprint/4527/>.

MINNETT, P., ALVERA-AZCÁRATE, A., CHIN, T., et al., 2019, "Half a century of satellite remote sensing of sea-surface temperature", *Remote Sensing of Environment*, v. 233, pp. 111366. doi: <https://doi.org/10.1016/j.rse.2019.111366>. Availability: <http://www.sciencedirect.com/science/article/pii/S0034425719303852>.

MITCHELL, J. F. B., 1983, "The seasonal response of a general circulation model to changes in CO2 and sea temperatures", *Quarterly Journal of the Royal Meteorological Society*, v. 109, n. 459, pp. 113–152. doi: <10.1002/qj.49710945906>. Availability: <https://rmets.onlinelibrary.wiley.com/doi/abs/10.1002/qj.49710945906>.

MOSS, A. R., JOUANY, J.-P., NEWBOLD, J., 2000, "Methane production by ruminants: its contribution to global warming", *Ann. Zootech.*, v. 49, n. 3, pp. 231–253. doi: <10.1051/animres:2000119>. Availability: <https://doi.org/10.1051/animres:2000119>.

MOSS, R., BABIKER, M., BRINKMAN, S., et al., 2008, "Towards New Scenarios for Analysis of Emissions, Climate Change, Impacts, and Response Strategies. Technical Summary". In: *IPCC Expert Meeting Rep.*, ISBN 978-92-9169-125-8, p. 132p., 10.

MOSS, R. H., EDMONDS, J. A., HIBBARD, K. A., et al., 2010, "The next generation of scenarios for climate change research and assessment", *Nature*, v. 463 (Feb), pp. 747–756. doi: <10.1038/nature08823>. Availability: <https://doi.org/10.1038/nature08823>.

MUNTJEWERF, L., PETRINI, M., VIZCAINO, M., et al., 2020a, "Greenland Ice Sheet Contribution to 21st Century Sea Level Rise as Simulated by the Coupled CESM2.1-CISM2.1", *Geophysical Research Letters*, v. 47, n. 9, pp. e2019GL086836. doi: <10.1029/2019GL086836>. Availability: <https://agupubs.onlinelibrary.wiley.com/doi/abs/10.1029/2019GL086836>. e2019GL086836 10.1029/2019GL086836.

MUNTJEWERF, L., SELLEVOLD, R., VIZCAINO, M., et al., 2020b, "Accelerated Greenland Ice Sheet Mass Loss under High Greenhouse Gas Forcing as Simulated by the Coupled CESM2.1-CISM2.1", *Earth and Space Science Open Archive*, p. 40. doi: <10.1002/essoar.10501583.1>. Availability: <https://doi.org/10.1002/essoar.10501583.1>.

MURRAY, R., 1996, "Explicit Generation of Orthogonal Grids for ocean Models", *Journal of Computational Physics*, v. 126, pp. 251–273. doi: <0021-9991/96>.

MYHRE, G., SHINDELL, D., BRÉON, F.-M., et al., 2013, "Anthropogenic and Natural Radiative Forcing". In: *Climate Change 2013: The Physical Science Basis. Contribution of Working Group I to the Fifth Assessment Report of the Intergovernmental Panel on Climate Change*, book section 8, pp. 659–740, Cambridge, United Kingdom and New York, NY, USA, Cambridge University Press. Stocker, T.F. and Qin, D. and Plattner, G.-K. and Tignor, M. and Allen, S.K. and Boschung, J. and Nauels, A. and Xia, Y. and Bex, V. and Midgley, P.M. (eds.).

NAKICENOVIC, N., ALCAMO, J., GRUBLER, A., et al., 2000, *Special Report on Emissions Scenarios (SRES), A Special Report of Working Group III of the Intergovernmental Panel on Climate Change*. Cambridge, Cambridge University Press. Availability: <http://pure.iiasa.ac.at/id/eprint/6101/>.

NCAR/UCAR, 2016, *CCSM4.0 Public Release*. Availability: <http://www.cesm.ucar.edu/models/ccsm4.0/>. Accessed in August, 7th 2018.

NCAR/UCAR, 2019, *CESM2 Scientifically Validated Configurations*. Availability: <http://www.cesm.ucar.edu/models/cesm2/

scientifically-validated-cesm2.html>. Accessed in April, 16th 2019.

NEALE, R. B., GETTELMAN, A., PARK, S., et al., 2010, *Description of the NCAR Community Atmosphere Model (CAM 5.0)*. NCAR Technical Note NCAR/TN-486+STR, NCAR: National Center for Atmospheric Research. Availability: <http://citeseerx.ist.psu.edu/viewdoc/download?doi=10.1.1.422.3202&rep=rep1&type=pdf>.

NOAA-AOML, 2019, *Florida Current Transport Time Series and Cruises*. Availability: <https://www.aoml.noaa.gov/phod/floridacurrent/index.phpreater . Accessed in April, 16th 2019.

NORDHAUS, W., 1975, "Can We Control Carbon Dioxide?" *IIASA Working Paper, WP - Austria*, pp. 63–75.

NSIDC, 2018, *NSIDC Data Terminology*. Availability: <http://engineering.purdue.edu/~mark/puthesis>. Accessed in May, 21th 2018.

OLESON, K., YJ, D., GB, B., et al., 2004, *Technical Description of the Community Land Model (CLM)*. NCAR Technical Note NCAR/TN-461+STR, NCAR: National Center for Atmospheric Research, 05. Availability: <https://opensky.ucar.edu/islandora/object/technotes%3A393/datastream/PDF/view>.

OLESON, K. W., LAWRENCE, D. M., BONAN, G. B., et al., 2010, *Technical Description of version 4.0 of the Community Land Model (CLM)*. NCAR Technical Note NCAR/TN-478+STR, NCAR: National Center for Atmospheric Research, 04. Availability: <https://opensky.ucar.edu/islandora/object/technotes%3A493/datastream/PDF/view>.

O'NEILL, B. C., TEBALDI, C., VAN VUUREN, D. P., et al., 2016, "The Scenario Model Intercomparison Project (ScenarioMIP) for CMIP6", *Geoscientific Model Development*, v. 9, n. 9, pp. 3461–3482. doi: <10.5194/gmd-9-3461-2016>. Availability: <https://www.geosci-model-dev.net/9/3461/2016/>.

PACANOWSKI, R., GNANADESIKAN, A., 1998, "Transient response in a z-level ocean model that resolves topography with partial cells", *Monthly Weather Review*, v. 126, pp. 3248–3270. doi: <10.1175/1520-0493(1998)126<3248:TRIAZL>2.0.CO;2>.

PARK, J., SWEET, W., 2015, "Accelerated sea level rise and Florida Current transport", *Ocean Science Discussions*, v. 12 (04), pp. 551–572. doi: <10.5194/osd-12-551-2015>.

PASSOS, E., 2012. "Variabilidade sazonal da Circulação Oceânica associada à Água Central do Atlântico Sul". Monografia (Bacharel em Oceanografia), UERJ (Universidade do Estado do Rio de Janeiro), Rio de Janeiro, Brazil.

PEIXOTO, J., OORT, A., 1992, *Physics of Climate*. ISBN 978-0883187128. New York, American Institute of Physics.

PETERSON, R., STRAMMA, L., 1991, "Upper-level circulation in the South Atlantic Ocean", *Progress in Oceanography*, v. 26, pp. 1–73. doi: <10.1016/0079-6611(91)90006-8>.

PICKARD, G., 1974, *Oceanografia Física Descritiva: Uma introdução*. Rio de Janeiro, Rio de Janeiro: Fundação de Estudos do Mar.

PICKARD, G., EMERY, W., 1990, *Intoductory Descriptive Physical Oceanography*. 5ª ed. Oxford, Pergamon Press.

POND, S., PICKARD, G., 1983, *Introductory Dynamical Oceanography*. ISBN 978-0750624961. Nova Iorque, Pergamon Press Inc.

PRATHER, M., EHHALT, D., DENTENER, F., et al., 2001, "Atmospheric Chemistry and Greenhouse Gases". In: *Climate Change 2001: The scientific basis - Contribution of Working Group I to the Third Assessment Report of the Intergovernmental Panel on Climate Change (IPCC)*, v. 881, p. 50, Cambridge, Cambridge University Press, 01. ISBN: 0521-01495-6.

PRENTICE, I., FARQUHAR, G., FASHAM, M., et al., 2001, "The carbon cycle and atmospheric carbon dioxide". In: *Climate Change 2001: The scientific basis - Contribution of Working Group I to the Third Assessment Report of the Intergovernmental Panel on Climate Change (IPCC)*, p. 56, Cambridge, Cambridge University Press, 01.

RAHMSTORF, S., 1995, "Climate drift in an ocean model coupled to a simple, perfectly matched atmosphere", *Climate Dynamics*, v. 11, n. 8 (Oct), pp. 447–458. doi: <10.1007/BF00207194>. Availability: <https://doi.org/10.1007/BF00207194>.

RANDALLS, S., 2010, "History of the 2°C climate target", *Wiley Interdisciplinary Reviews: Climate Change*, v. 1, n. 4, pp. 598–605. doi: <10.1002/wcc.

62>. Availability: <https://onlinelibrary.wiley.com/doi/abs/10.1002/wcc.62eater .

RANGEL, R. H. O., 2019, *Avaliação do Impacto de um Novo Mínimo Solar e do Aumento da Concentração de CO_2 no Sistema Climático*. Ph.D. Thesis, Programa de Engenharia Civil, COPPE, Universidade Federal do Rio de Janeiro, Rio de Janeiro.

RAPID, 2019, *RAPID: Monitoring the Atlantic Meridional Overturning Circulation at 26.5°N since 2004*. Availability: <https://www.rapid.ac.uk/rapidmoc/index.php>. Accessed in April, 16th 2019.

RAPID-AMOC, 2019, *RAPID-AMOC: Monitoring the Atlantic Meridional Overturning Circulation*. Availability: <https://www.rapid.ac.uk/index.php>. Accessed in April, 16th 2019.

RAPID-WATCH, 2012, *RAPID-WATCH: Monitoring the Atlantic Meridional Overturning Circulation*. Availability: <https://www.rapid.ac.uk/index.php>. Accessed in April, 16th 2019.

RASCH, P. J., 2012, "The South Atlantic and Climate". In: Rasch, P. J. (Ed.), *Climate Change Modeling Methodology*, Springer.

REID, J. L., 1994, "On the Total Geostrophic Circulation of the North-Atlantic Ocean - Flow Patterns, Tracers, and Transports", *Progress in Oceanography*, v. 33, n. 1, pp. 1–92. doi: <10.1016/0079-6611(94)90014-0>. Availability: <http://www.sciencedirect.com/science/article/pii/0079661194900140>.

REID, J. L., 1989, "On the total geostrophic circulation of the South Atlantic Ocean: Flow patterns, tracers, and transports", *Progress in Oceanography*, v. 23, n. 3, pp. 149–244. doi: <https://doi.org/10.1016/0079-6611(89)90001-3>. Availability: <http://www.sciencedirect.com/science/article/pii/0079661189900013>.

REVELLE, R., 2013, "Introduction: The Scientific History of Carbon Dioxide". In: *The Carbon Cycle and Atmospheric CO2: Natural Variations Archean to Present*, cap. 01, pp. 1–4, Washington, D.C., American Geophysical Union (AGU). ISBN: 9781118664322. Availability: <https://agupubs.onlinelibrary.wiley.com/doi/abs/10.1029/GM032p0001>.

RINGLER, T., PETERSEN, M., HIGDON, R., et al., 2013, "A multi-resolution approach to global ocean modeling", *Ocean Modelling*, v. 69, pp. 211–232. doi: <10.1016/j.ocemod.2013.04.010>.

RINGLER, T. D., HEIKES, R. P., RANDALL, D. A., 2000, "Modeling the Atmospheric General Circulation Using a Spherical Geodesic Grid: A New Class of Dynamical Cores", *Monthly Weather Review*, v. 128, n. 7, pp. 2471–2490. doi: <10.1175/1520-0493(2000)128<2471:MTAGCU>2.0.CO;2>. Availability: <https://doi.org/10.1175/1520-0493(2000)128<2471:MTAGCU>2.0.CO;2>.

RINTOUL, S., 1991, "South Atlantic Interbasin Exchange", *Journal of Geophysical Research*, v. 96, pp. 2675–2692. doi: <10.1029/90JC02422>.

RIVIÈRE, G., 2011, "A Dynamical Interpretation of the Poleward Shift of the Jet Streams in Global Warming Scenarios", *Journal of the Atmospheric Sciences*, v. 68, n. 6, pp. 1253–1272. doi: <10.1175/2011JAS3641.1>. Availability: <https://doi.org/10.1175/2011JAS3641.1>.

ROBERTS, A., HUNKE, E., ALLARD, R., et al., 2018, "Quality control for community-based sea-ice model development", *Philosophical Transactions of the Royal Society A: Mathematical, Physical and Engineering Sciences*, v. 376 (09), pp. 20170344. doi: <10.1098/rsta.2017.0344>.

RODRIGUES, R. R., ROTHSTEIN, L. M., WIMBUSH, M., 2007, "Seasonal Variability of the South Equatorial Current Bifurcation in the Atlantic Ocean: A Numerical Study", *Journal of Physical Oceanography*, v. 37, n. 1 (01), pp. 16–30. doi: <10.1175/JPO2983.1>. Availability: <https://doi.org/10.1175/JPO2983.1>.

ROSENLOF, K., TERRAY, L., DESER, C., et al., 2013, "Changes in Variability Associated with Climate Change". In: Asrar, G., Hurrel, J. (Eds.), *Climate Science for Serving Society: Research, Modelling and prediction Priorities*, ISBN 978-94-007-6691-4, Springer, pp. 249–272, Dordecht.

RUSSEL, J., 2006, "The Southern Hemisphere Westerlies in a Warming World: Propping Open the Door to the Deep Ocean", *Journal of Climate*, v. 96, pp. 6382–6390. doi: <10.1175/JCLI3984.1>.

RUSSIL, C., NYSSA, Z., 2009, "The tipping point trend in climate change communication", *Global Environmental Change*, v. 19, pp. 336–344. doi: <10.1016/j.gloenvcha.2009.04.001>.

SANCHO, L., 2012. "Análise dos transportes advectivos de calor e volume na bacia do Atlântico Sul frente a cenários de mudanças climáticas". Monografia (Bacharel em Oceanografia), UERJ (Universidade do Estado do Rio de Janeiro), Rio de Janeiro, Brazil.

SANCHO, L., 2014, *Variação da extensão do gelo marinho e seu impacto sobre a Circulação Termohalina do oceano Atlântico*. Master Thesis, Programa de Engenharia Civil, COPPE, Universidade Federal do Rio de Janeiro, Rio de Janeiro.

SANCHO, L., 2020, *Evaluation of the Atlantic Meridional Overturning Circulation Under High CO_2 Emissions*. Ph.D. Thesis, Programa de Engenharia Civil, COPPE, Universidade Federal do Rio de Janeiro, Rio de Janeiro. In press.

SANCHO, L., ASSAD, L., LANDAU, L., 2015, "VOLUME AND HEAT TRANSPORTS ANALYSIS IN THE SOUTH ATLANTIC BASIN RELATED TO CLIMATE CHANGE SCENARIOS", *Revista Brasielira de Geofísica*, v. 33, n. 2, pp. 333–348. doi: <10.1590/rbgf.v33i2.724>.

SAUNDERS, K., ROBERTS, S., PERREN, B., et al., 2018, "Holocene dynamics of the Southern Hemisphere westerly winds and possible links to CO2 outgassing", *Nature Geoscience*, v. 11 (09). doi: <10.1038/s41561-018-0186-5>.

SCAIFE, A. A., 2016, *30-Second Meteorology: The 50 most significant events and phenomena, each explained in half a minute*. ISBN 1782403108. United Kingdom, Ivy Press Limited.

SCHEFFER, M., CARPENTER, S., FOLEY, J. A., et al., 2001, "Catastrophic shifts in ecosystems", *Nature*, v. 413, pp. 591–596. doi: <10.1038/35098000>. Availability: <https://doi.org/10.1038/35098000>.

SCHEFFER, M., BOLHUIS, J. E., BORSBOOM, D., et al., 2018, "Quantifying resilience of humans and other animals", *Proceedings of the National Academy of Sciences*, v. 115, n. 47, pp. 11883–11890. doi: <10.1073/pnas.1810630115>. Availability: <https://www.pnas.org/content/115/47/11883>.

SCHELLING, T. C., 1971, "Dynamic models of segregation", *The Journal of Mathematical Sociology*, v. 1, n. 2, pp. 143–186. doi: <10.1080/0022250X.1971.9989794>. Availability: <https://doi.org/10.1080/0022250X.1971.9989794>.

SCHINDLER, D. W., 1999, "The mysterious missing sink", *Nature*, v. 398 (03), pp. 105–107. doi: <10.1038/18111>. Availability: <https://doi.org/10.1038/18111>.

SCHMITTNER, A., 2005, "Decline of the marine ecosystem caused by a reduction in the Atlantic overturning circulation", *Nature*, v. 434 (03), pp. 628–633. doi: <10.1038/nature03476>. Availability: <https://doi.org/10.1038/nature03476>.

SCHMITZ, W. J., 1996, *On the world ocean circulation. Volume I, some global features/North Atlantic circulation*. Relatório técnico, Woods Hole Oceanographic Institution. Availability: <https://hdl.handle.net/1912/355>.

SCHMITZ JR., W. J., MCCARTNEY, M. S., 1993, "On the North Atlantic Circulation", *Reviews of Geophysics*, v. 31, n. 1, pp. 29–49. doi: <10.1029/92RG02583>. Availability: <https://agupubs.onlinelibrary.wiley.com/doi/abs/10.1029/92RG02583>.

SCHNEIDER, S. H., DICKINSON, R. E., 1974, "Climate modeling", *Reviews of Geophysics*, v. 12, n. 3, pp. 447–493. doi: <10.1029/RG012i003p00447>. Availability: <https://agupubs.onlinelibrary.wiley.com/doi/abs/10.1029/RG012i003p00447>.

SEN-GUPTA, P. K., 1935, "Photodissociation of Nitrous Oxide", *Nature*, v. 136 (Sep), pp. 513–514. doi: <10.1038/136513a0>. Availability: <https://doi.org/10.1038/136513a0>.

SENUM, G. I., GAFFNEY, J. S., 1985, "A Reexamination of the Tropospheric Methane Cycle: Geophysical Implications". In: *The Carbon Cycle and Atmospheric CO2: Natural Variations Archean to Present*, pp. 61–69, Washington, D.C., American Geophysical Union (AGU). ISBN: 9781118664322.

SIME, L. C., KOHFELD, K. E., QUÉRÉ, C. L., et al., 2013, "Southern Hemisphere westerly wind changes during the Last Glacial Maximum: model-data comparison", *Quaternary Science Reviews*, v. 64, pp. 104–120. doi: <https://doi.org/10.1016/j.quascirev.2012.12.008>. Availability: <http://www.sciencedirect.com/science/article/pii/S0277379112005215>.

SMEE, D., MOAT, B. I., RAYNER, D., et al., 2019, "Atlantic meridional overturning circulation observed by the RAPID-MOCHA-WBTS (RAPID-Meridional Overturning Circulation and Heatflux Array-Western Boundary Time Series) array at 26N from 2004 to 2018." *British Oceanographic Data Centre - Natural Environment Research Council, UK*. doi: <10.5285/8cd7e7bb-9a20-05d8-e053-6c86abc012c2>.

SMITH, G. C., ALLARD, R., BABIN, M., et al., 2019, "Polar Ocean Observations: A Critical Gap in the Observing System and Its Effect on Environmental Predictions From Hours to a Season", *Frontiers in Marine Science*, v. 6, pp. 429. doi: <10.3389/fmars.2019.00429>. Availability: <https://www.frontiersin.org/article/10.3389/fmars.2019.00429% textgreater .

SMITH, R., JONES, P., BRIEGLEB, B., et al., 2010, *The Parallel Ocean Program (POP) reference manual: Ocean component of the Community Climate System Model (CCSM) and Community Earth System Model (CESM)*. Relatório Técnico LAUR-10-01853, Los Alamos National Laboratory.

SPEER, K. G., ZENK, W., 1993, "The Flow of Antarctic Bottom Water into the Brazil Basin", *Journal of Physical Oceanography*, v. 23, n. 12, pp. 2667–2682. doi: <10.1175/1520-0485(1993)023<2667:TFOABW>2.0.CO;2>. Availability: <https://doi.org/10.1175/1520-0485(1993)023<2667:TFOABW>2.0.CO;2>.

SROKOSZ, M., BARINGER, M., BRYDEN, H., et al., 2012, "Past, Present, and Future Changes in the Atlantic Meridional Overturning Circulation", *Bulletin of the American Meteorological Society*, v. 93, n. 11, pp. 1663–1676. doi: <10.1175/BAMS-D-11-00151.1>. Availability: <https://doi.org/10.1175/BAMS-D-11-00151.1>.

STAMMER, D., WUNSCH, C., GIERING, R., et al., 2002, "Global ocean circulation during 1992-1997, estimated from ocean observations and a general circulation model", *Journal of Geophysical Research*, v. 107, n. C9, 3118, pp. 1–27. doi: <10.1029/2001JC000888>.

STAMMER, D., WUNSCH, C., GIERING, R., et al., 2003, "Volume, heat, and freshwater transports of the global ocean circulation 1993–2000, estimated from a general circulation model constrained by World Ocean Circulation Experiment (WOCE) data", *Journal of Geophysical Research: Oceans*, v. 108, n. C1, pp. 7–1–7–23. doi: <10.1029/2001JC001115>. Availability: <https://agupubs.onlinelibrary.wiley.com/doi/abs/10.1029/2001JC001115>.

STAMMER, D., KÖHL, A., VLASENKO, A., et al., 2018, "A pilot climate sensitivity study using the CEN coupled adjoint model (CESAM)", *Journal of Climate*, v. 31 (03), pp. 2031–2056. doi: <10.1175/JCLI-D-17-0183.1>.

STANIFORTH, A., THUBURN, J., 2012, "Horizontal grids for global weather and climate prediction models: a review", *Quarterly Journal of the Royal*

Meteorological Society, v. 138, n. 662, pp. 1–26. doi: <10.1002/qj.958>. Availability: <https://rmets.onlinelibrary.wiley.com/doi/abs/10.1002/qj.958% textgreater .

STEELE, M., MORLEY, R., ERMOLD, W., 2001, "PHC: A Global Ocean Hydrography with a High-Quality Arctic Ocean", *Journal of Climate*, v. 14, n. 9, pp. 2079–2087. doi: <10.1175/1520-0442(2001)014<2079:PAGOHW>2.0.CO;2>. Availability: <https://doi.org/10.1175/1520-0442(2001)014<2079:PAGOHW>2.0.CO;2>.

STEFFEN, W., RICHARDSON, K., ROCKSTRÖM, J., et al., 2020, "The emergence and evolution of Earth System Science", *Nature Reviews Earth and Environment*, v. 1, pp. 54–63. doi: <10.1038/s43017-019-0005-6>.

STEHFEST, E., VUUREN, D., KRAM, T., et al., 2014, *Integrated Assessment of Global Environmental Change with IMAGE 3.0. Model description and policy applications*. The Hague: PBL Netherlands Environmental Assessment Agency. Availability: <https://www.pbl.nl/sites/default/files/downloads/pbl-2014-integrated_assessment_of_global_environmental_change_with_image30_735.pdfater .

STEWART, R. H., 2008, *Introduction to Physical Oceanography*. ISBN 9781616100452. Texas, Texas University.

STOCKER, T., 2011, *Introduction to Climate Modelling*. ISSN: 1866-8348. ISBN: 978-3-642-00772-9. DOI: 10.1007/978-3-642-00773-6. e-ISSN: 1866-8356. e-ISBN: 978-3-642-00773-6. Verlag Berlim, Springer.

STOCKER, T., WRIGHT, D., 1991, "Rapid transitions of the ocean's deep circulation induced by changes in surface water fluxes", *Nature*, v. 351, pp. 729–732. doi: <10.1038/351729a0>.

STOCKER, T. F., WRIGHT, D. G., BROECKER, W. S., 1992, "The influence of high-latitude surface forcing on the global thermohaline circulation", *Paleoceanography*, v. 7, n. 5, pp. 529–541. doi: <10.1029/92PA01695>. Availability: <https://agupubs.onlinelibrary.wiley.com/doi/abs/10.1029/92PA01695>.

STOUFFER, R. J., YIN, J., GREGORY, J. M., et al., 2006, "Investigating the Causes of the Response of the Thermohaline Circulation to Past and Future Climate Changes", *Journal of Climate*, v. 19, n. 8, pp. 1365–1387. doi: <10.1175/JCLI3689.1>. Availability: <https://doi.org/10.1175/JCLI3689.1>.

STOUFFER, R. J., SEIDOV, D., HAUPT, B. J., 2007, "Climate Response to External Sources of Freshwater: North Atlantic versus the Southern Ocean", *Journal of Climate*, v. 20, n. 3, pp. 436–448. doi: <10.1175/JCLI4015.1>. Availability: <https://doi.org/10.1175/JCLI4015.1>.

STRAMMA, L., ENGLAND, M., 1999, "On the water masses and mean circulation of the South Atlantic Ocean", *Journal of Geophysical Research: Oceans*, v. 104, n. C9, pp. 20863–20883. doi: <10.1029/1999JC900139>. Availability: <http://dx.doi.org/10.1029/1999JC900139>.

SUNDQUIST, E. T., 2013, "Geological Perspectives on Carbon Dioxide and the Carbon Cycle". In: *The Carbon Cycle and Atmospheric CO2: Natural Variations Archean to Present*, pp. 55–59, Washington, D.C., American Geophysical Union (AGU). ISBN: 9781118664322. Availability: <https://agupubs.onlinelibrary.wiley.com/doi/abs/10.1029/GM032p0005>.

TALLEY, L., PICKARD, G., EMERY, W., et al., 2011, *Descriptive Physical Oceanography: An Introduction*. ISBN 978-0-7506-4552-2. Boston, Elsevier.

TOGGWEILER, J., RUSSELL, J., CARSON, S., 2006, "Midlatitude Westerlies, atmospheric CO2, and climate change during the ice ages", *Paleoceanography*, v. 21 (06). doi: <10.1029/2005PA001154>.

TOMCZAK, M., GODFREY, J., 1994, *Regional Oceanography: An Introduction*. ISBN 9781483287614. Inglaterra, Elsevier Science Ltd.

TOSTE, R., 2017, *Efeitos da Subida do Nível do Mar na Inundação Costeira na Costa Leste do Brasil Devido às Mudanças Climáticas*. Ph.D. Thesis, Programa de Engenharia Civil, COPPE, Universidade Federal do Rio de Janeiro, Rio de Janeiro.

TOSTE, R., ASSAD, L., LANDAU, L., 2018, "Downscaling of the global HadGEM2-ES results to model the future and present-day ocean conditions of the southeastern Brazilian continental shelf", *Climate Dynamics*, v. 51, pp. 143–159. doi: <10.1007/s00382-017-3911-7>. Availability: <https://doi.org/10.1007/s00382-017-3911-7>.

TRENBERTH, K., ANTHES, R., BELWARD, A., et al., 2013, "Challenges of a Sustained Climate Observing System". In: Asrar, G., Hurrel, J. (Eds.), *Climate Science for Serving Society: Research, Modelling and prediction Priorities*, ISBN 978-94-007-6691-4, Springer, pp. 13–50, Dordecht.

VAN MARLE, M. J. E., KLOSTER, S., MAGI, B. I., et al., 2017, "Historic global biomass burning emissions for CMIP6 (BB4CMIP) based on merging satellite observations with proxies and fire models (1750–2015)", *Geoscientific Model Development*, v. 10, n. 9, pp. 3329–3357. doi: <10.5194/gmd-10-3329-2017>. Availability: <https://www.geosci-model-dev.net/10/3329/2017/>.

VECCHI, G., SODEN, B., WITTENBERG, A., et al., 2006, "Weakning of tropical Pacific atmospheric circulation due to anthropogenic forcing", *Nature*, v. 441, pp. 73–76. doi: <10.1038/nature04744>.

VELLINGA, M., WOOD, R., 2002, "Global Climatic Impacts of a Collapse of the Atlantic Thermohaline Circulation", *Climatic Change*, v. 54 (01), pp. 251–267. doi: <10.1023/A:1016168827653>.

VUUREN, D., STEHFEST, E., ELZEN, M., et al., 2011, "RCP2.6: Exploring the possibility to keep global mean temperature increase below 2°C", *Climatic Change*, v. 109 (11), pp. 95–116. doi: <10.1007/s10584-011-0152-3>.

WALKER, G., 2006, "The tipping point of the iceberg", *Nature*, v. 441, pp. 802–805. doi: <10.1038/441802a>. Availability: <http://dx.doi.org/10.1038/441802a>.

WALKER, G., 1923, "Correlation in seasonal variations of weather, VIII. A preliminary study of world weather", *Memoirs of the India Meteorological Department*, v. 24, n. 4, pp. 75–131.

WALKER, J., KASTING, J., 1992, "Effect of fuel and forest conservation on future levels of atmospheric carbon dioxide", *Palaeogeography, Palaeoclimatology, Palaeoecology*, v. 97 (02), pp. 151–189. doi: <10.1016/0031-0182(92)90207-L>.

WALSH, J. E., CHAPMAN, W. L., FETTERER, F., et al., 2019, *Gridded Monthly Sea Ice Extent and Concentration, 1850 Onward, Version 2. G10010.* Relatório técnico, NSIDC: National Snow and Ice Data Center, Boulder, Colorado USA. Availability: <https://nsidc.org/data/G10010/versions/2>. Accessed in October, 7th 2019.

WDCGG, W., 2018, *WDCGG Map*. Availability: <https://gaw.kishou.go.jp/search>. Accessed in February, 20th 2020.

WITTENBERG, A. T., ROSATI, A., LAU, N.-C., et al., 2006, "GFDL's CM2 Global Coupled Climate Models. Part III: Tropical Pacific Climate and

ENSO", *Journal of Climate*, v. 19, n. 5, pp. 698–722. doi: <10.1175/JCLI3631.1>. Availability: <https://doi.org/10.1175/JCLI3631.1>.

WMO, 1975, *The Physical Basis of Climate and Climate Modeling*. Relatório Técnico No 16, World Meteorological Organization.

WMO, 2018, *WMO GREENHOUSE GAS BULLETIN*. Relatório Técnico No 14, World Meteorological Organization. Availability: <https://library.wmo.int/doc_num.php?explnum_id=5455er . The State of Greenhouse Gases in the Atmosphere Based on Global Observations through 2017.

WUNSCH, C., 2002, "What is the Thermohaline Circulation?" *Science*, v. 298, pp. 1179–1181. doi: <10.1126/science.1079329>.

YEAGER, S., DANABASOGLU, G., 2014, "The Origins of Late-Twentieth-Century Variations in the Large-Scale North Atlantic Circulation", *Journal of Climate*, v. 27, n. 9, pp. 3222–3247. doi: <10.1175/JCLI-D-13-00125.1>. Availability: <https://doi.org/10.1175/JCLI-D-13-00125.1>.

ZHANG, L., WU, L., 2012, "Can Oceanic Freshwater Flux Amplify Global Warming?" *Journal of Climate*, v. 25 (05), pp. 3417–3430. doi: <10.1175/JCLI-D-11-00172.1>.

ZHANG, S., 2011, "A Study of Impacts of Coupled Model Initial Shocks and State-Parameter Optimization on Climate Predictions Using a Simple Pycnocline Prediction Model", *Journal of Climate*, v. 24 (12), pp. 6210–6226. doi: <10.1175/JCLI-D-10-05003.1>.

ZHENG, Y., GIESE, B. S., 2009, "Ocean heat transport in Simple Ocean Data Assimilation: Structure and mechanisms", *Journal of Geophysical Research: Oceans*, v. 114, n. C11. doi: <10.1029/2008JC005190>. Availability: <https://agupubs.onlinelibrary.wiley.com/doi/abs/10.1029/2008JC005190>.

ZHU, Y., WEI, Z., WANG, Y., et al., 2014, "The annual mean sketches and climatological variability of the volume and heat transports through the inter-basin passages: A study based on 1 400-year spin up of MOM4p1", *Acta Oceanologica Sinica*, v. 33 (09), pp. 12–24. doi: <10.1007/s13131-014-0513-7>.